Naval Sea Systems Command

Naval Surface Warfare Center
Panama City Division

Multipass and Non-concentric Target Circular Synthetic Aperture Sonar (CSAS)

FINAL REPORT

SERDP Project Number: MR-2439

Dr. Jermaine L. Kennedy
Naval Surface Warfare Center Panama City Division
Code X11
110 Vernon Ave
Panama City Beach, Florida 32407-7001
email: jermaine.kennedy@navy.mil

Dr. Timothy M. Marston
Applied Physics Laboratory
University of Washington
1013 NE 40th Street
Seattle, Washington 98105-6698
email: Marston@apl.washington.edu

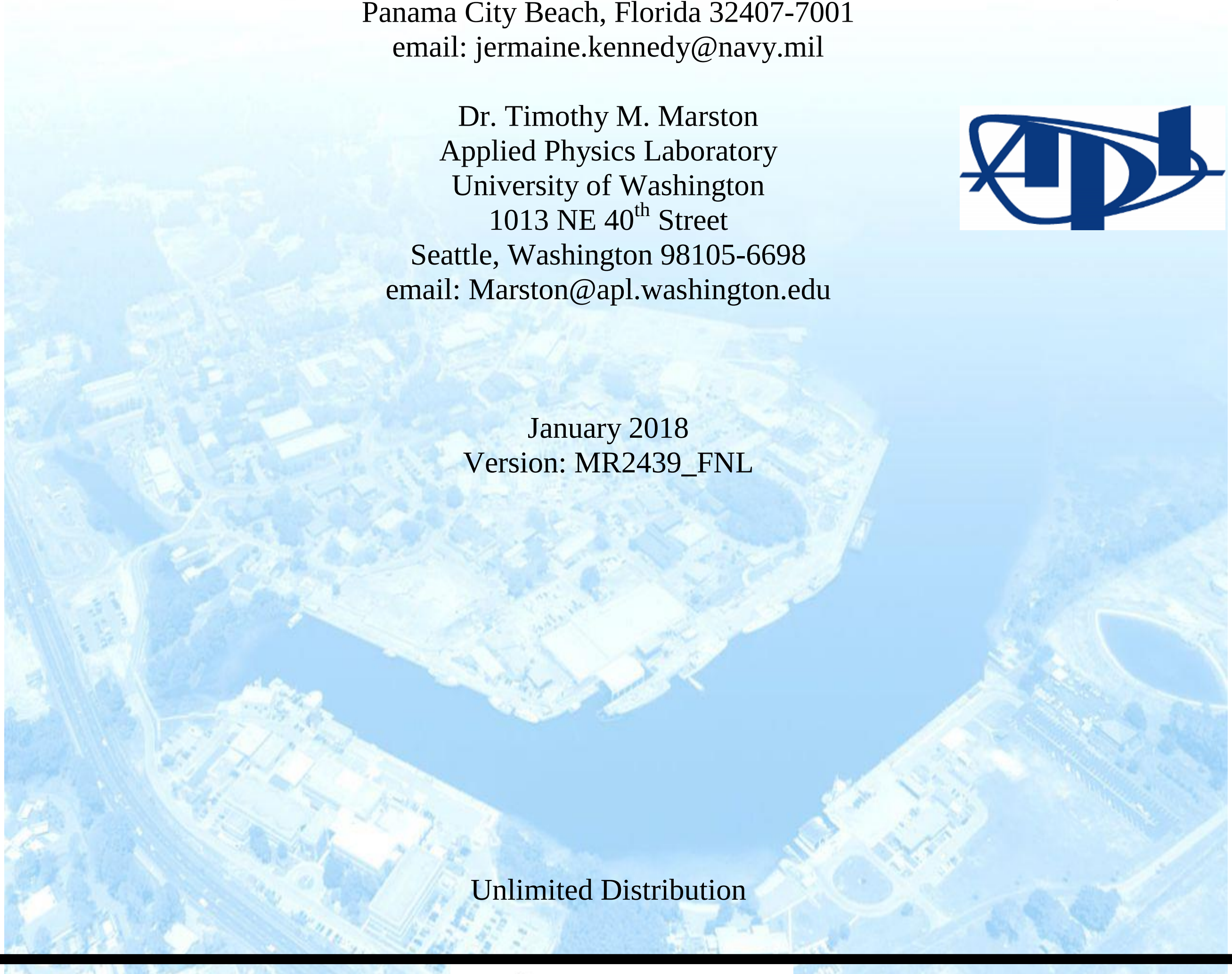

January 2018
Version: MR2439_FNL

Unlimited Distribution

REPORT DOCUMENTATION PAGE	*Form Approved* *OMB No. 0704-0188*

1. REPORT DATE *(DD-MM-YYYY)* 31-01-2018	**2. REPORT TYPE** SERDP Final Report	**3. DATES COVERED** *(From - To)* 14 MAR 2014 to 31 SEP 2017

4. TITLE AND SUBTITLE
Multipass and Nonconcentric Target Circular Synthetic Aperture Sonar (CSAS)

5a. CONTRACT NUMBER

5b. GRANT NUMBER

5c. PROGRAM ELEMENT NUMBER

6. AUTHOR(S)
Kennedy, Jermaine, L. (1)
Marston, Timothy, M. (2)

5d. PROJECT NUMBER
MR-2439

5e. TASK NUMBER

5f. WORK UNIT NUMBER

7. PERFORMING ORGANIZATION NAME(S) AND ADDRESS(ES)
(1) Naval Surface Warfare Center Panama City Division
110 Vernon Ave, Code X11
Panama City, FL 32407
(2) Applied Physics Lab.-UW
1013 NE 40th St.
Seattle, WA 98105

8. PERFORMING ORGANIZATION REPORT
MR-2439

9. SPONSORING / MONITORING AGENCY NAME(S) AND ADDRESS(ES)

SERDP Program Office
Dr. Herb Nelson (Munitions Response)
4800 Mark Center Drive, Suite 17D08
Alexandria, VA 22350

10. SPONSOR/MONITOR'S ACRONYM(S)
SERDP

11. SPONSOR/MONITOR'S REPORT NUMBER(S)
MR-2439

12. DISTRIBUTION / AVAILABILITY STATEMENT
Distribution A: Approved for public release; distribution is unlimited.

13. SUPPLEMENTARY NOTES
N/A

14. ABSTRACT
In SERDP project MR-2439 research was conducted to enable the in-situ measurement of the aspect and grazing angle dependent scattering response of unexploded ordnance (UXO), clutter, and science targets by conducting circular scans at different heights around identified concentric and non-concentric (i.e. off-center) targets. Methods were developed for coherently fusing the information from all circular scans to generate three-dimensional data products describing spatial reflectivity and impulse response of targets. Showing that these three dimensional (3D) dataproducts could be sampled in the 3D wavenumber spectrum to generate a series of two dimensional (2D) random orientation realizations that have use for target recognition training and/or testing was an additional objective.

15. SUBJECT TERMS
Circular Synthetic Aperture Sonar (CSAS) of UXO, Synthetic Aperture Sonar of UXO, underwater UXO

16. SECURITY CLASSIFICATION OF:			**17. LIMITATION OF ABSTRACT**	**18. NUMBER OF PAGES**	**19a. NAME OF RESPONSIBLE PERSON** Dr. Jermaine L. Kennedy
c. REPORT U	**b. ABSTRACT** U	**c. THIS PAGE** U	UU	150	**19b. TELEPHONE NUMBER** *(include area code)* 850-230-7311

TABLE OF CONTENTS

LIST OF TABLES

LIST OF FIGURES

Figure 5- The backscattered signal from the reference target after re-centering and azimuthal filtering to reduce noise. A curve fit for the estimated time delays is shown in red.

Figure 6- The reference target wavefronts following residual correction.

Figure 7- A point-cloud showing the locations of the receive array, estimated using the delays to the fiducial, and color-coded for the various stave heights: black = 4.3 m, magenta = 3.99 m, blue = 3.69 m, red = 3.39 m, and green 3.08 m.

Figure 8- Illustration of the beamforming procedure. The complex 3D sinogram depicted in (a) is beamformed in the vertical (i.e., z direction) dimension, and the result is shown in (b). The Fourier spectrum is computed in the range dimension and a polar-Cartesian transformation is performed, with the results shown in (c). The inverse two-dimensional Fourier transform is then computed for every height plane, resulting in the beamformed image (d).

Figure 9- Slice through vertically beamformed data at θ = 0°. The beamforming method on the left is projection slice beamforming and the method on the right is back-projection. The image features are similar (differences are a result of varying spectral weightings), but the back-projection image clearly suffers from a large number of imaging artifacts. The color-scale is in dB with respect to the brightest point.

Figure 10- The two dimensional spectrum of the images shown in the previous Fig. 9. Without compensating for sample density or frequency the spatial spectrum of a backprojected image will over weight low frequencies and spectral regions corresponding to elevated aperture sample density. The color-scale is in dB relative to the brightest point.

Figure 11- Three-dimensional spectrum (axes: $K_{x,y,z}$) of a proud 2-1 aluminum cylinder. This spectrum is equivalent to taking the Fourier-transform in the Z-dimension of the volumetric dataset depicted in Fig. 8(c).

Figure 12- Illustration of the relationship between array spacing relative to a target and the sample through the three-dimensional spectrum (with bounds illustrated by the blue curves) corresponding to each array point. The example on left is a linear array and the example on the right is a highly distorted non-linear array. Note that the linear array appears to result in a planar slice through the 3D spectrum.

Figure 13- Illustration of the conical and skewed-conic sampling of the three-dimensional spectrum caused by circular and non-concentric circular apertures.

Figure 14-	Representation of target aspect/grazing angle frequency response in spherical coordinates. This method of data representation makes data-projection very simple, but is less physically intuitive in how it relates to the aperture.
Figure 15-	Concentric (L) and non-concentric (R) 2-1 cylinders, both constructed from samples of same three-dimensional scattering function depicted in Fig. 11. The left figure simulates a target imaged from an 11 meter radius, 6 meter altitude scan, and the right figure assumes the target is shifted from the center by 6 meters, resulting in a maximum grazing angle of 45 degrees.
Figure 16-	Linear aperture simulations generated via image formation from planar slices through the three-dimensional spectrum. The planar slices are generated using simulated linear scan geometries. Range in the image is slant-range, and the images span a variety of grazing angles ranging from 15 to 45 degrees. The color-scale is in decibels (dB).
Figure 17-	Comparison of log-scale CSAS (L) and linear SAS (R) color plots for a span of 120 degrees, when captured at a steep grazing angle. Note the different spans of similar acoustic phenomena.
Figure 18-	A “pseudo-stripmap” image created from circular aperture data. This type of image was used both for rapid coordinate inversion and co-registration between multi-pass data. It is extremely rapid to compute, requiring a convolution operation in only one dimension.
Figure 19-	An illustration on the aperture division process carried out in the spectrum and the resulting translation estimates arranged as a two-dimensional matrix. A matrix of correlation coefficients is also generated that will be used as weights. The horizontal axes in all figures are slant range r normalized by scan radius R, and the vertical axis on the spectrum is azimuthal wavenumber K_θ normalized by the spatial nyquist rate $K_{nyq.}$ The vertical axes on the two other plots are the angle in degrees around the circular aperture.
Figure 20-	Illustration of range (A), height (B) and sampling (C) errors possible in a circular aperture geometry. Realistic situations often contain a combination of all three, though radial errors tend to be dominant and sampling errors tend to be insignificant.
Figure 21-	Quadratic error vs. normalized range for sample rate (“*smp*,” dashed line), radial (“*rad,”* solid), height (*“hght*,” x’s), and propagation speed (“*prp*,” dots).
Figure 22-	Example of Pseudo-stripmap autofocusing. A) shows the scene with injected, spatially variant errors. B) shows the scene after autofocusing using the technique

described in [19]. C) shows the pseudo-stripmap focusing results. The alternative solution was only capable of generating a locally focused result, vs. the pseudo-stripmap version which, by virtue of creating an actual 3D coordinate update, created a general focusing solution for the full scene.

Figure 23- Table and flowchart showing co-registration steps for AUV data.

Figure 24- Low resolution CSAS image generated by performing a polar-Cartesian coordinate transform on a Pseudo-stripmap image. Note that this type of image is low resolution in comparison to a standard CSAS image but spans all the way to the water column. A complementary image can be generated using the scattering beyond the radius.

Figure 25- Illustration of the model used for generating a fitting function to the measured delay data. The reference coordinate location has a nominal height H with respect to the ground-plane that may have a small error component δH. Coordinates of the matching array are described in terms of height relative to the reference H_c and range relative to the reference R_c. The vehicle is assumed to have separate vertical and horizontal velocities, $V_{H1,2}$ and $V_{R1,2}$.

Figure 26- Comparison of the residual phase error between the fitted model and the measured data using the non-linear least squares approach (top) and the extension that compensates for relative platform velocity (bottom). Note that rapid fluctuations on the left side of the graph are almost completely corrected in the model with velocity compensation.

Figure 27- The scan patterns used in the first multipass beamforming field experiment. The scans in (A) fix the radius at 30 meters and span 2.4 meters in altitude. The scans in (B) fix the altitude at 5.95 meters and span 8 meters in radius.

Figure 28- Example of a synthesized multipass array. The vertical samples are irregular as a result of the different vertical spacings between the multipass scans and the interferometric receiver arrays. Additional irregularity occurs because of currents and, for the bottom three scans, a GPS localization offset acquired during a resurfacing operation.

Figure 29- Underwater photographs of various targets deployed in the Gulf of Mexico off the shore of Panama City Beach, FL. The targets in this figure were scanned during the second set of tests conducted in June 2015.

Figure 30- An example scan showing the flight path of the AUV in Cartesian coordinates (right figure, blue line) and the location of the test-patches used for multilateration (right figure, red dots). The image snippets at left correspond to the test-patches.

Figure 31- The point-spread functions before (L) and after (R) an iteration of the multilateration procedure applied to the scan depicted in Fig. 30.

Figure 32- The radial, height, and angular corrections that are estimated from the iterated multilateration process and applied to the 3D coordinates of the SAS sonar platform.

Figure 33- CSAS image of a proud, vertically oriented plastic barrel on a limestone and coral sediment. Focus is achieved throughout the image excepting out-of-plane regions, in which case defocusing is due to being out of plane.

Figure 34- Zoomed in section of Fig. 33 showing the barrel.

Figure 35- Phase 2 (FY15) AUV-scan coregistration model. The parameters are h_s: the height of the reference sonar above the nominal ground-plane, h_1: the initial vertical baseline estimate between the reference and comparison scan, Δh: the vertical baseline error, R: the radial location of the reference scan, r_1: the initial radial baseline estimate, Δr: the radial error variable, c_1: the reference sound-speed, c_2: the sound speed of the medium at the time the second scan is taken and lastly h_D: the sediment height relative to the nominal ground-plane. Lowercase r denotes the coordinate radial direction, and lowercase h represents the coordinate vertical direction.

Figure 36- Top: phase measurements produced by patch-wise correlation. Middle: correlation coefficients for the patches. Bottom: radial displacement estimates measured by combining the phase estimates with coarse dislocation estimates found using the correlation peaks.

Figure 37- Top left: Original displacement data estimated via patch-wise correlation. Middle left: the displacement surface, reconstructed using the basis functions and estimated error parameters for the FY15 model incorporating bathymetry. Bottom left: the displacement surface, reconstructed using the basis functions and estimated parameters for a flat-bottom assumption. Middle right: the model – data residual for the FY15 model. Bottom right: the residual error for the flat-bottom model. The color scale is in meters.

Figure 38- The estimated error parameters for the full FY15 model (blue) and the flat-bottom model (red).

Figure 39- Left: array localization results using the flat-bottom model (blue) vs. incorporation of bathymetry (red). Right: the range-projected vertical beamforming results for the case in which a flat-bottom is assumed (top) vs. incorporation of bathymetry (bottom).

Figure 40- The simulated scattering distribution (A) and the results for different beamforming approaches. Plot (B) shows the result of one-dimensional Fourier analysis applied to the ideal, regularly sampled array, (C) shows the result of backprojection applied to the irregularly sampled experimental array shape, and (D) shows the wideband sparse result generated using the procedure described in this paper. The color scale is logarithmic and the dynamic range on all SAS images is 30 dB referenced to the brightest point.

Figure 41- A flowchart of the vertical mapdrift algorithm.

Figure 42- Slices through the full 3D image data cube (top and middle) and a rendered & zoomed 3D patch of the full image (bottom) for the case in which no vertical map-drift was applied (left) versus the case in which it was applied (right). The images at right show superior focus in the vertical dimension. Note that back-scattering angle is mapped to color in the above examples. The objects in the 3D zoomed images are roughly sand-dollar sized.

Figure 43- Example of a synthesized multipass array. The vertical samples are irregular as a result of the different vertical spacings between the multipass scans and the interferometric receiver arrays. Additional irregularity occurs because of currents and, for the bottom three scans, a GPS localization offset acquired during a resurfacing operation.

Figure 44- The latitude, longitude, and depth coordinates of a spiral scan from the phase-3, FY16 field experiments.

Figure 45- Flowchart of the navigation refinement process for spiral scans. Only the first loop of the scan is processed specifically as a “CSAS” scan. The rest of the array is incrementally built up from that first loop.

Figure 46- A snapshot of the alignment diagnosis window, actively updated in Matlab during the spiral scan alignment process.

Figure 47- A flowchart of the spiral scan beamforming process. The red green and blue point clouds represent different 5 degree chunks of aperture.

Figure 48- Illustration of the phase-center double localization (PCDL) principle of Telbaldini et al. [13], with sonar systems. For *N* sensor positions and *M* control point locations, an over-determined system of equations relating *MN* measurements to 2*N* + *M* position measurements (2 coordinate directions for the sensors and 1 coordinate direction for the position measurements) can be solved to within a rotation and translation.

Figure 49- Multipass barrel scene, viewed from different angles and at different times. The

sub-aperture images are shown on the left. The middle column shows the detected intensity changes, and the right hand side shows the interferogram between interferometric staves. The hypothesized gravity waves are circled in red.

Figure 50- Example of the autofocus algorithm applied to a 5 degree sub-aperture snippet of the high frequency steel barrel spiral scan set. The top image shows beamforming without the autofocus operation, the bottom image shows beamforming with the autofocus operation. Note the improved focusing of the sediment interface.

Figure 51- CSAS image *with* (A) and *without* (B) application of the NF-FF correction. The dotted white line shows the 5-meter radius mark and the center of the CSAS scan is close to the upper right corner.

Figure 52- Acoustic color of a solid 2-1 aluminum cylinder before (L) and after (R) KM filtering to remove multipath and clutter noise. A large increase in signal-to-noise ratio has been gained. The color scale gives the approximate absolute target strength in dB re 1m and the dynamic range is 30 dB.

Figure 53- The 3D beamformed image (L), and the same image with the direct path (red) and interface scattering (blue) contributions color-coded.

Figure 54- End-on perspective of the cylinder showing the specular glint (red), and the multi-path contributions out to second-order, for interface interactions. The specular glint does not strongly trace out the surface of the cylinder.

Figure 55- A single slice of data from the test pond, vertically beamformed using standard backprojection, on the left, and sparse beamforming on the right.

Figure 56- Backprojected 3D image (L) of 2-1 solid aluminum cylinder and the sparse version (R) demonstrating a very large resolution enhancement. Only 90 degrees of aperture are used in this image to make edge and end-on features maximally visible.

Figure 57- Top (L) and three-quarter (R) views of the solid aluminum cylinder.

Figure 58- End-on view of 3D image and a slice through the data-cube showing the specular glint, and using the multipath convention in [41], the path 1 & 2 (target – sediment, sediment – target reciprocal paths), and the path 3 (sediment – target – sediment) multipaths.

Figure 59- Comparison of the simulated 3D target with the data from the test pond, both end-on. Note the clear preservation of the multipath and specular signals in the experimental data. The simulated data is working with ~70 degrees of aperture, vs. the experimental which is only using ~ 3 degrees. Sparse processing is

enhancing the features to be distinctly visible despite the very narrow range of apertures.

Figure 60- Views of the 3D reconstruction of a 155mm howitzer shell, showing internal features and multi-path signals. M-FOCUSS with a P-norm of 0.6 was used for vertical resolution enhancement. Usage of joint-sparsity improved the SNR and coherent reconstruction.

Figure 61- Rendered images and projections of the volumetric data corresponding to the scans described in Table 1. Column 1) shows the linear scale three-quarter view volumetric images rendered using alpha blending, column 2) shows projections of the volumetric images onto the *XZ* plane, column 3) shows projections onto the *YZ* plane, and column 4) shows projections onto the *XY* plane. From top to bottom, the rows show: a) proud howitzer shell, altitude scan, b) proud howitzer shell, radial scan, c) oblique howitzer shell, altitude scan, d) oblique howitzer shell, radial scan, e) proud vertical steel barrel, radial scan, and f) proud 2-1 solid aluminum cylinder, radial scan. Fig. 61 can be found in [11] with additional information.

Figure 62- A standard CSAS image of an obliquely tilted UXO (L) and the Z-projection of the 3D image generated using multipass data synthesis (R).

Figure 63- A HF/LF composite, HF is in blue, LF is in red, showing direct and multi-path reflections in an image, and their corresponding manifestations in the acoustic color domain. The effect, which looks like a splitting of the broadside signal, is discussed more in [44].

Figure 64- Photograph of a 155 mm Howitzer shell (right) and the 3D volumetric acoustic image (left), showing the material boundaries at the front of the shell, the components of the end-cap, and a nylon rope tied around the center for diver manipulation (not in photo).

Figure 65- A gray scale, alpha-blended image of multipass data for a radial scan, beamformed in Z, showing the coupling of height to polar angle of a target relative to the current azimuthal angle.

Figure 66- Illustration of high-frequency image snippets produced using the multipass 2-1 aluminum cylinder data.

Figure 67- Three examples of imaging from the second field test, in which solution biasing due to bathymetric variation is unaccounted for during the coregistration process. The figure on the left, a howitzer shell, is difficult to interpret but features like edges are easily visible. In the center image, rings of a barrel appear fairly undistorted at the sediment but the distortion becomes significant near the top of

the barrel. The image on the right, of a lobster pot, is almost impossible to interpret.

Figure 68- 3D images of a plastic barrel with an internally suspended shot put, with (L) and without (R) performing co-registration with a height-prior used to de-bias the solution.

Figure 69- The coherently processed low-frequency 3D dataproduct from a multipass set, in this case containing a coral outcropping (red arrow) and a proud howitzer shell (white arrow). Image (A) shows the 3D image from a three-quarter view perspective, while (B) and (C) project the image onto the [X, Y], [Y, Z] and [X, Z] planes. Image (D) is a three-quarter view of the three-dimensional wavenumber spectrum of the image.

Figure 70- A high frequency three-quarter view (A) rendering of the rock and howitzer shell shown in Fig. 69, along with two slices (B and C) through the rock. Note that overhangs are well imaged using the 3D tomography approach.

Figure 71- 3D snippet of the howitzer shell scene, showing just the shell.
(A) is a three-quarter view, and image (B) is a horizontal planar slice through the image, showing the tip, the sides, the endcap, and material boundaries.

Figure 72- (A) a vertical slice through the image snippet showing a glint and its sub-sediment reflection, and (B and C) the three-dimensional wavenumber spectrum for the 3D snippet.

Figure 73- A CSAS scan of a scene containing a lobster pot. The complex structure of the rocky outcropping on which the lobster pot is located is also visible.

Figure 74- A zoomed view of the lobster trap in the previous image. The trap appears to be rectangular and the inlet portions, along with some of the netting, is visible in the top portion of the trap. It is also clearly divided into two chambers.

Figure 75- An VAA3D alpha-rendered image of the lobster-trap shown in Figs. 73 and 74, viewed from two perspectives. The arched top of the lobster trap is clearly visible.

Figure 76- Horizontal plane slices through the imagecube of the lobster trap. The images are arranged in order of descending height, beginning with the top left image and working clockwise around the set. The red arrow highlights some netting, the yellow arrow highlights the bait spike, and the blue arrow highlights the trap inlets.

Figure 77- Vertical slices perpendicular to the axis of the trap. The ordering is from the rear

to the front of the trap, beginning with the top left and moving clockwise around the figure. The red arrow highlights the net, which appears to pinch off towards one end of the trap. The yellow arrow shows the bait spike.

Figure 78- Vertical slices along the axis of the trap. The blue arrow highlights the circular trap inlet. The red arrow shows part of the netting.

Figure 79- A side view of the array used to scan the lobster pot. The array experiences drift to the left as it moves from the bottom of the array to the top.

Figure 80- The magnitudes of the complex lobster trap image (L) and the magnitudes of its 3D wavenumber spectrum. The spectrum is clearly asymmetric and thicker on the left side.

Figure 81- A slice through the 3D wavenumber spectrum (top). The sides of the array corresponding to the spectral regions are shown via the lines (note that they are opposite, which is due to the fact that these acoustic tomograms are formed by reflections from a scene rather than transmissions through a scene).

Figure 82- Three views of the plastic barrel target. Plot A shows a three-quarter view alpha-blended image, rendered in VAA3D. Plot B shows a vertical slice of the barrel, where the coloration corresponds to insonification angle – blue from the left and pink from the right. C is a snippet of a sub-aperture window of the CSAS scan. This is what an ordinary linear SAS image of the target would look like.

Figure 83- The left plot is a cutaway illustration of the target, showing the barrel, the concrete filling (gray) and the shotput (circle). Hypothesized scattering mechanisms are numbered. The center plot is a slice through the tomogram formed from a 5 degree arc of the aperture for simple comparison with the figure on the left. The figure on the right is the standard SAS image of the target (the range dimension is to the right).

Figure 84- 3D acoustic image of a tire with color-encoded backscattering angle, and a photograph of the same target captured by a diver.

Figure 85- A cutaway illustration of the target (L) with the hypothesized dominant scattering mechanisms numbered, and the a cutaway of the target on the right with the same scattering mechanisms labeled. The scattering to the left is in a purple hue, though likely mechanism 5 is hidden beneath contribution 2 from the opposing direction.

Figure 86- A complex scene shaped by rock and coral formations. A) shows the 3D view and B – D) show slices through the image cube.

Figure 87- Four sub-aperture quick looks at the Buzzard’s Bay Helldiver. The target is

LIST OF ACRONYMS

2D: Two Dimensional
3D: Three Dimensional
APL-UW: The Applied Physics Laboratory, University of Washington
ATR: Automatic Target Recognition
AUV: Autonomous Underwater Vehicle
BOSS: Buried Object Scanning Sonar
CAT: Computer Aided Tomography
CSAR: Circular Synthetic Aperture Radar
CSAS: Circular Synthetic Aperture Sonar
CTD: Conductivity Temperature Depth
dB: Decibels
DLR: German Aerospace Center
DoD: Department of Defense
FOCUSS: Focal Underdetermined System Solver
FPB: Fast Polar Backprojection
FFBP: Fast Factorized Backprojection
FFI: Norwegian Defence Research Establishment
FFT: Fast Fourier Transform
FY: Fiscal Year
GPS: Global Positioning Satellite
HF: High Frequency
IFFT: Inverse Fast Fourier Transform
INS: Inertial Navigation System

kHz: kiloHertz
KM: wavenumber (*k*)-Moment
LF: Low Frequency
LHS: Left Hand Side
MIP: Maximum Intensity Projection
MR: Munitions Response
MUST: Multi Sensor Towbody
NUDFT: Non Uniform Discrete Fourier Transform
NSWC PCD: Naval Surface Warfare Center, Panama City Division
ONR: Office of Naval Research
PCDL: Phase center double localization
RHS: Right Hand Side
ROI: Region of Interest
RPC: Redundant Phase Center
SAR: Synthetic Aperture Radar
SAS: Synthetic Aperture Sonar
SNR: Signal to Noise Ratio
SERDP: Strategic Environmental Research and Development Program
TIER: Targets In Environment Response
UXO: Unexploded Ordnance
WSU: Washington State University

KEYWORDS

Circular Synthetic Aperture Sonar of UXO, Synthetic Aperture Sonar of UXO, underwater UXO

ACKNOWLEDGEMENT

This report was prepared under contract to the Department of Defense Strategic Environmental Research and Development Program (SERDP). The publication of this report does not indicate endorsement by the Department of Defense, nor should the contents be construed as reflecting the official policy or position of the Department of Defense. Reference herein to any specific commercial product, process, or service by trade name, trademark, manufacturer, or otherwise, does not necessarily constitute or imply its endorsement, recommendation, or favoring by the Department of Defense.

ABSTRACT

Objectives: In SERDP project MR-2439 research was conducted to enable the in-situ measurement of the aspect and grazing angle dependent scattering response of unexploded ordnance (UXO), clutter, and science targets by conducting circular scans at different heights around identified concentric and non-concentric (i.e., off-center) targets. Methods were developed for coherently fusing the information from all circular scans to generate three-dimensional data products describing spatial reflectivity and impulse response of targets. Showing that these three dimensional (3D) dataproducts could be sampled in the 3D wavenumber spectrum to generate a series of two dimensional (2D) random orientation realizations that have use for target recognition training and/or testing was an additional objective.

Technical Approach: The primary signal processing challenges of this project were 1) the precision, data-driven alignment of synthetic aperture data captured over a very large multi-dimensional array consisting of multiple circles or, in our final implementation, a corkscrew like spiral aperture, and 2) the coherent fusion of the data captured by the multi-dimensional array into a three-dimensional data-product from which useful spatial and frequency response information about targets could be gathered. To address these challenges a crawl-walk-run approach was taken. In the first year highly controlled multi-pass circular scans were conducted via a sonar system mounted on a tower and traversing a circular rail in a controlled pond environment. Basic multi-pass data fusion (e.g., 3D beamforming) and concentricity correction algorithms were developed using this dataset. In the second year a dual band sonar system mounted on a REMUS 600 autonomous underwater vehicle (AUV) conducted multipass circular scans of varying types in both benign and complex uncontrolled ocean environments. Finally, in the last year of the project the same sonar system was used to test a more efficient means of conducing multipass circular scans. Using this method a much larger sampling of the multidimensional scattering response of targets could be captured in the same amount of time as in previous methods, but the signal-processing approach for fusing the data had to be completely reworked.

Results: Results demonstrated that not only is 3D multipass synthetic aperture sonar feasible, but is extremely doable in field conditions and for objects the size of UXO. 3D impulse response data showing both rigid and elastic structural response information was readily extractable from 3D low-frequency image data products. It was further demonstrated that by appropriately sampling the 3D wavenumber spectrum, realizations of the target from random orientations could be generated.

Benefits: 3D multipass processing has a number of potential uses, ranging from high certainty target and environment classification and characterization to classifier training and performance analysis. Additionally, many of the 3D synthetics aperture sonar (SAS) signal processing techniques developed in this project (e.g., 3D autofocus procedures and 3D region-of-interest

impulse response extraction) could potentially be extended to work with 3D downlooking SAS systems used for funding buried targets.

OBJECTIVE

The Department of Defense (DoD) and the Strategic Environmental Research and Development Program (SERDP) have identified a need for the development of systems with the ability to detect and identify submerged UXO. Circular synthetic aperture sonar (CSAS) has been demonstrated to be an extraordinarily powerful tool for a variety of sonar based object classification/identification tasks, potentially including UXO detection. CSAS data products include high-resolution imagery and data ideally suited for acoustic frequency response vs. angle ("acoustic color") based target recognition. Research efforts aimed at modeling the acoustic response of targets in marine environments have identified several hurdles that must be overcome to maximize the effectiveness of response-based classification. These include response sensitivity to environmental parameters, attenuation and modification of features with aspect angle, and the coupling of structural modes to grazing angle which occurs in linear scan systems or, alternatively, in circular scan systems when a target is non concentric (SERDP projects MR-2230, 2231, & 1665). The insonification of targets over both a broad set of aspect and grazing angles makes multipass CSAS an ideal approach for addressing these difficulties. The primary objective of this project is to create methods for the coherent fusion of CSAS data collected at multiple radii or altitudes, with the intention of generating datasets that could be used for accurate target classification, model parameter adjustment, or to train recognition algorithms using environmentally relevant data. In support of the primary objective, methods for processing the co-registered data to reduce clutter, correct for near-field effects, and extrapolate/interpolate between multi-pass datasets to simulate target responses from arbitrary scan paths will be developed.

BACKGROUND

In an underwater environment, acoustic UXO detection has many benefits, such as range, area coverage rate, shape and structural information, insensitivity to water quality, and the maturity of acoustic transducer technology. Regarding UXO detection, of primary concern are the precise locations, the distribution density, munitions type, and state (i.e., intact or fragmented). With this information the level of threat can be assessed and methods for remediation planned. Acoustic technology may be used to gather this type of information, however there may not be a single acoustic sensor or sensing modality that optimally provides all of this information. For example, some acoustic sensing methods are optimized for large area coverage rates. Detection and classification performance may be reduced, but the area covered is extremely large. In contrast, other systems may have very high performance from a classification or detection standpoint, but may not be able to scan as large of an area. In this project, Circular Synthetic Aperture sonar was investigated as a method for both detecting and characterizing UXO, and it falls under the latter category of acoustic sensing methods.

Circular synthetic aperture sonar is the application of medical tomographic imaging techniques to sonar data collected around an approximately circular trajectory. Tomographic theory of image reconstruction was first systematically addressed by Bracewell in his seminal paper in radio astronomy demonstrating a solution to the Radon transform by applying what is known as the projection-slice theorem [1]. With the development of efficient and fast computers this technique was later applied very successfully to X-ray imaging in the medical industry and became known as Computer Aided Tomography (i.e., "CAT" scans). In 2005, two research groups simultaneously published papers relating to the application of tomographic imaging for coherent acoustic beamforming [2,3]. Ferguson and Wyber [2] describe a series of beamforming algorithms and the results of applying them to simulated and real datasets collected on a turn-table. Friedman et. al. [3] describes the platform velocity requirements that need to be met, to capture the broadside response of cylindrical targets of various sizes in the insonified region, as well as area coverage-rate considerations for CSAS operations. A paper that clearly defines the relationship between CSAS and various other synthetic aperture imaging methods (e.g., stripmap and spotlight) from a wavenumber perspective was published several years later by Ferguson and Wyber [4].

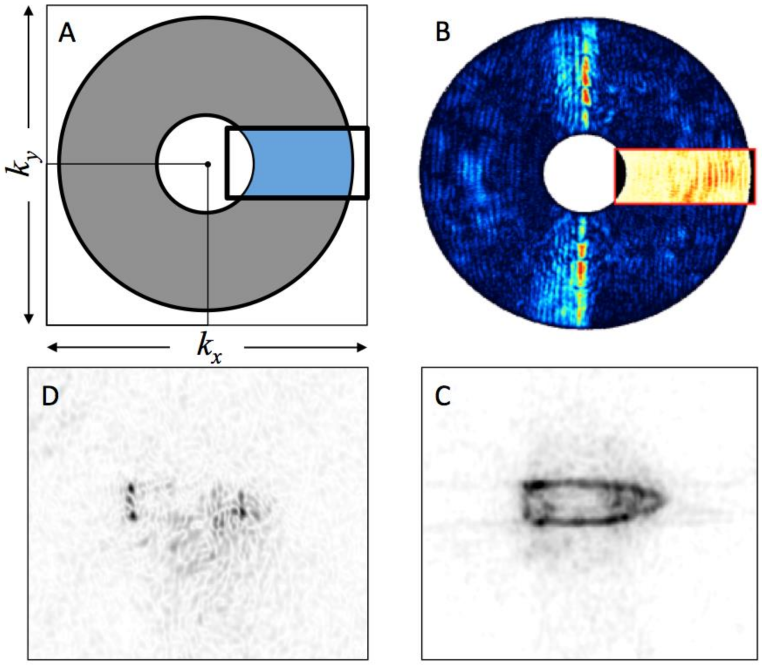

Figure 1. An illustration of the relationship between CSAS and linear SAS from a wavenumber sampling standpoint. The gray annulus in Fig. 1A depicts the wavenumber coverage of a CSAS scan. In contrast, the bounded subset shows the sampled region for a linear SAS system. Fig. 1B shows a real example of the spatial spectrum captured for a 155 mm Howitzer shell. The corresponding CSAS image is shown in Fig. 1C. An equivalent linear SAS image is generated in Fig. 1D from the bounded subset highlighted in Fig. 1B. Notice that the CSAS image is significantly easier to interpret.

In [4] the wavenumber coverage for a circular SAS scan was shown to be a spectral annulus, and a linear SAS scan was shown to be a sampled portion along the annulus. This difference is graphically illustrated here in Fig.1, which compares the differences for a theoretical system with finite bandwidth and beamwidth. The spectral annulus for a CSAS system has a width that is dependent on the bandwidth of the system. Its ring-like nature around the origin of the spatial spectrum is an indication of the number of look-angles created by the CSAS beamforming operation: a full 360 degrees. In contrast, linear SAS wavenumber coverage is limited to a rectangular sampled region, where the rotation around the center depends on the look-angle to a given target. (In a target-centered coordinate system the sampled region will rotate based on the sonar look angle. In contrast, in a sonar-centered coordinate system the sampled region will remain fixed and the spectrum will rotate around the origin based on the orientation of the target relative to the sonar).

The enhanced wavenumber coverage and range of aspects associated with CSAS scans results in both higher resolution images, lower speckle noise, and more spectral information regarding the aspect-dependency of the frequency response of targets. Furthermore, unlike spotlight beamforming in SAR applications, the CSAS imaging modality requires no active beam-steering, and CSAS scans can be conducted with no hardware modifications. All that is required is a modification of the scan path of the sonar and the processing applied to the collected data.

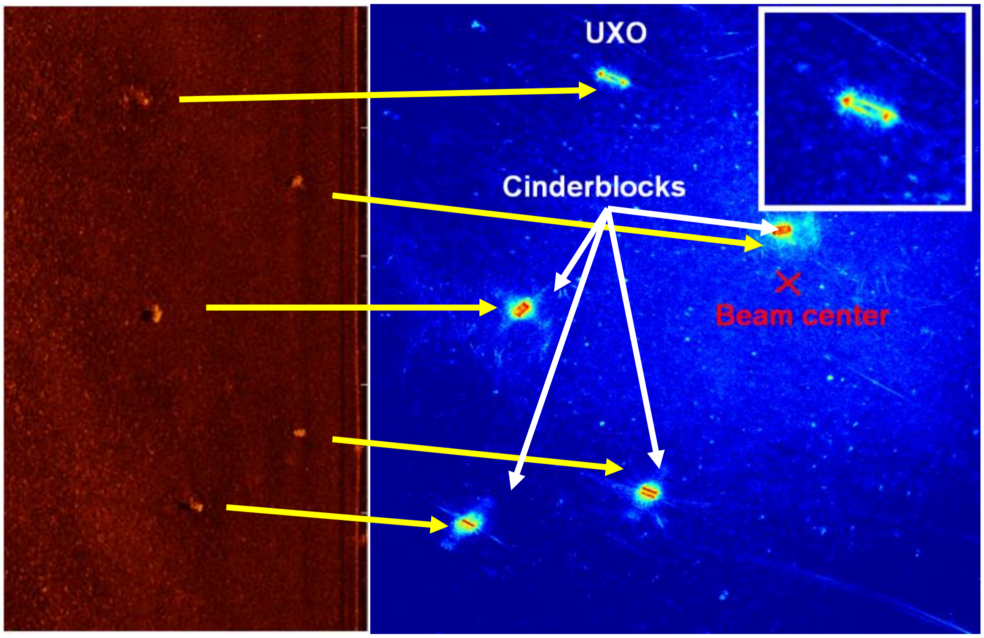

Figure 2. A comparison of the high-frequency linear scan (left) with a low frequency CSAS scan of the same region.

Data used in the first wave of CSAS papers was primarily gathered using the inverse configuration (i.e., a fixed sonar with targets on a rotating turn-table), which avoided most of the implementation difficulties of CSAS; e.g., extreme focus sensitivity to both navigation and focusing plane errors. Follow-on AUV based demonstrations required the placement of transponders near targets to overcome this sensitivity. The imagery obtained from these transponder-augmented experiments was clearly superior to the analogous linear-scan results (see, for example, *Circular synthetic aperture sonar w/controllable focus* [5]). The requirement for transponders, however, posed a severe limitation from an operational standpoint. Interest was generated in other sonar research groups and CSAS was next investigated by the Norwegian defense institute (FFI). FFI produced the first published attempt at generating CSAS imagery without the use of a navigation reference (see *Callow et. al*, [6]), which was a major improvement from an operational standpoint. The image quality, though, was inferior to the previous beacon-based approaches. A follow-up paper later published by the same group attempted to demonstrate an optimal way for fusing four strip-map images observing the same object from the cardinal directions [7]. While admittedly not demonstrating CSAS image reconstruction, the described algorithm could be viewed as supplementary to the autofocus technique published in the previous paper.

The first description of a process for successfully generating well focused CSAS imagery from a freestanding AUV was published in the proceedings of EUSAR12 [8]. The process uses correlations between "sub-apertures" (e.g., limited angle sub-samples of the spectral annulus) to generate a coherent spectral focusing solution for a corrupted CSAS image. Some of the results can be seen in images published in Sternlicht *et al.* [9]. If open literature reflects the state of the field, there have been no successful field demonstrations of coherently beamforming acoustic data across separate scans using either the linear or circular geometries, prior to this project. Synthesis of data captured from multiple *circular* scans would have the benefit of enabling in-situ measurements of the scattering response of UXO, not only as a function of aspect angle but also of grazing angle. Multipass CSAS scans would have the simultaneous benefit of generating high resolution 3D imagery of targets and sampling a three-dimensional volume of the wavenumber response. The former could be used for high fidelity target or environment characterization, and the latter could be sampled to generate realizations of UXO targets at both random orientations and ranges for classification algorithm training and/or testing.

Multipass aperture synthesis comes with a number of challenges however. No standard approach currently exists for synthesizing a multidimensional aperture composed of independently conducted scans. Considering that SAS processing typically requires navigation errors to be on the order of $\lambda/8$ or less, (λ = sonar center frequency wavelength), and that sound-speed inhomogeneity may be non-trivial in many environments, there are some significant signal processing hurdles that need to be overcome to make multipass CSAS processing robust. From a beamforming standpoint, the multi-dimensional aperture will no doubt be irregularly sampled, and possibly undersampled in the vertical dimension, and methods for addressing this problem must also be addressed. Furthermore, the approach towards synthesizing an aperture from even a single circle is still in need of maturation, with the methods current at the time of project conception failing or underperforming in difficult environments. Lastly, given a three-dimensional multi-pass CSAS dataproduct, how can the wavenumber spectrum be exploited to generate independent target realizations? All these issues are addressed by this project.

MATERIALS AND METHODS

Project MR-2439 took a crawl-walk-run approach to the development of multipass imaging operations, beginning with experiments conducted in a highly controlled environment and moving to progressively less controlled and more difficult environments and more realistic imaging scenarios. This section will give an outline of the procedures used (and challenges overcome) for multipass imaging in each stage of the project, ranging from initial tests using a rail system in a controlled environment, to the final tests using AUV's performing corkscrew scans in uncontrolled environments. It is arranged in two parts: The first concerns test pond processing in a controlled environment, and the second concerns processing data acquired autonomous underwater vehicles (AUV), captured in uncontrolled environments. The second part will be further divided into three project phases: *Phase 1*, in which multi-pass algorithms were constructed using previously available circular scans, *Phase 2* in which the first sets of multipass scans from an AUV were acquired and beamforming techniques developed, and *Phase 3*, in which spiral scans were exploited to further improve the results of field tests.

Controlled Data Acquisition

In year 1 of the project (FY14), data collection was initiated utilizing an underwater circular rail system [10]. A custom fabricated 22 meter diameter circular rail system with a mobile trolley was deployed in the 9 million gallon freshwater Pond Acoustic Test Facility (ATF) at Naval Surface Warfare Center Panama City Division. This enabled variables like sonar altitude, scan radius, target type, orientation, non-concentricity, and sediment type to be precisely controlled and/or known. Figure 3 shows an aerial view of the ATF with a schematic of the circular rail system superimposed, showing its placement location within the test pond.

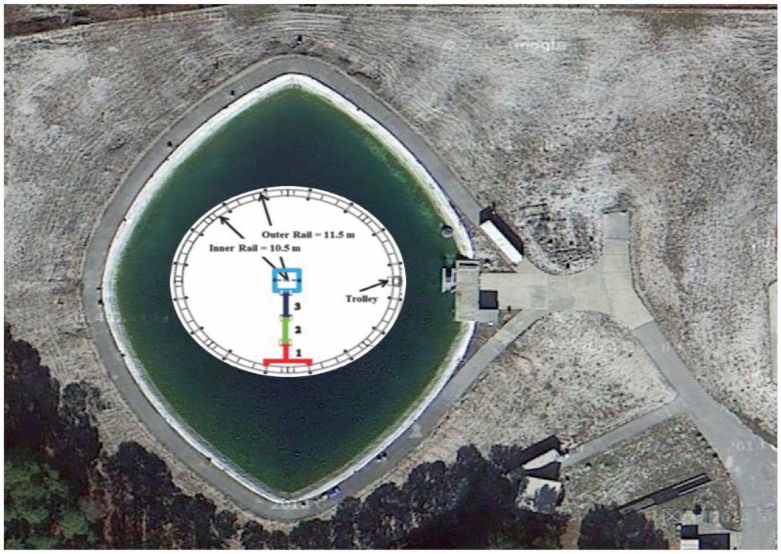

Figure 3. Aerial view of the 9 million gallon freshwater Pond Acoustic Test Facility (ATF) at Naval Surface Warfare Center Panama City Division (NSWC PCD) with a schematic of the circular rail system superimposed.

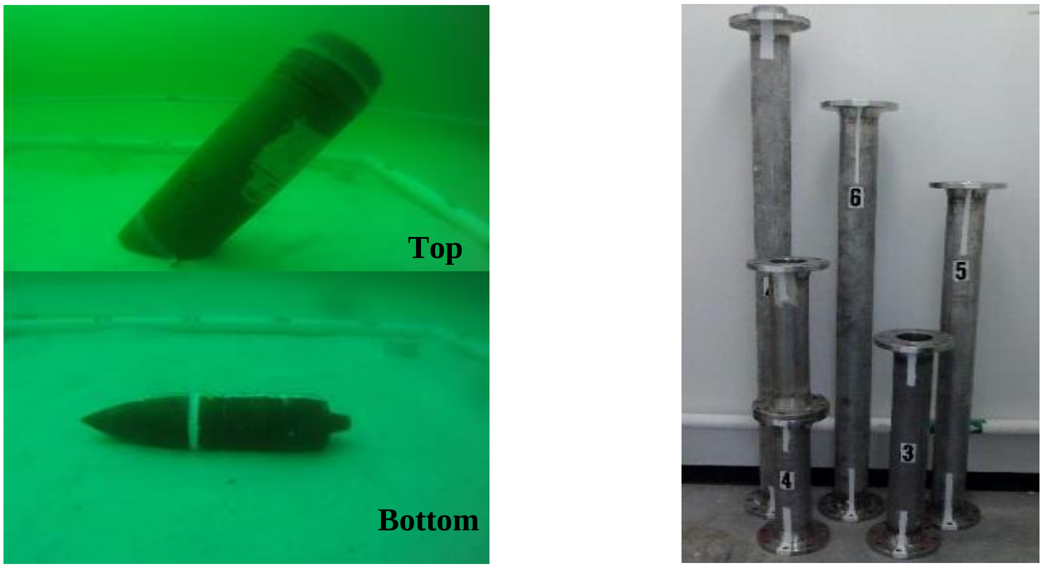

(a) **(b)**

Figure 4. (a) Underwater photograph of a tilted inert 155mm howiter (top) and proud 100 mm UXO (bottom) at the center of the circular rail system in the Freshwater Acoustic Test Pond Facility at Naval Surface Warfare Center Panama City Division. (b) Photograph of the tower staves used to alter the sonar height.

The circular rail apparatus was instrumented with an underwater acoustic sonar projector and array which were used to acquire 360 degrees of acoustic backscatter information from targets deployed in various configurations on a water-sediment interface (Fig. 4a). A detailed description of the circular rail apparatus and measurement instrumentation can be found in literature [10]. Multipass datasets were collected for various types of inert unexploded ordnances (UXO's) and replica UXO's. To gathers datasets at varying altitude, 5 custom staves were fabricated with varying lengths (Fig. 4b). Each stave enables target insonification from a different altitude and hence grazing angle. With the current set of staves, altitudes of 4.3 m, 3.99 m, 3.69 m, 3.39 m, and 3.08 m can be achieved. The corresponding insonification grazing angles for these altitudes are 21.35º, 19.91º, 18.51º, 17.12º, and 15.64º. Measurements of the backscattering response of targets in various orientations relative to the sediment were made for all of these grazing angles. Additionally, targets were insonified with different levels of non-concentricity (i.e., distance from the origin of the circular aperture) and clustering densities (i.e., inter-target spacing).

Though the circular rail system was intended to provide a platform in which phase error was not a significant variable, a small amount of settling occurred beneath the rail supports. The long lever arm formed by the tower resulted in platform settling having a large impact on the phase and timing of the signal to the target, and motion error became non trivial, highly distorting CSAS images produced by the test pond. Data-driven motion estimation was hindered by the fact that the data was severely undersampled in azimuth. Ordinarily this would not be a problem, as the sample in tomographic imaging is determined by the size of the imaged object [11] and the targets were small enough to be sufficiently sampled. Under sampling did, however, prevent effective data-driven navigation using sediment scattering. To mitigate the problem, a shotput was half-buried in the vicinity of the target. The isotropic nature of the backscattering from a shotput made it a useful motion fiducial. Autofocusing studies for synthetic aperture radar operations have noted that more than one focusing point is necessary to fully solve for the motion of a platform [12], [13], however in the rail system the angular location of the tower was well known and the array motion was constrained to move along an equidistant arc circling the base of the platform. These constraints reduce the variables in the motion estimation problem so that the delays to a single motion fiducial become sufficient for estimating the 3D location of the array elements. Figures 5 and 6 show the backscattered signal before and after correction (the envelope is shown prior to correction and the wavefronts are shown after correction and dynamic range compression). Figure 7 shows a point-cloud of the receive array locations, estimated using the delays measured to the fiducial.

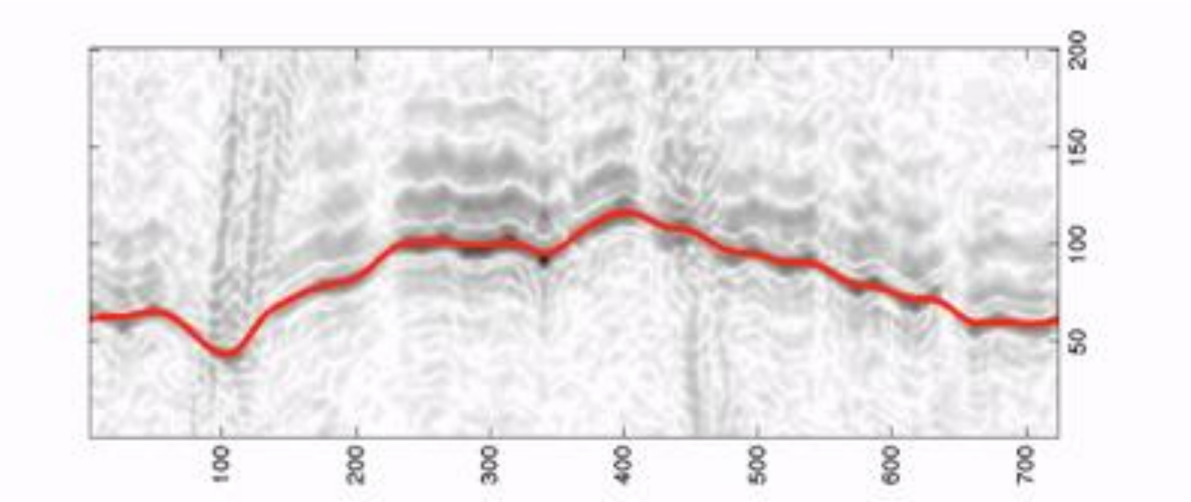

Figure 5. The backscattered signal from the reference target after re-centering and azimuthal filtering to reduce noise. A curve fit for the estimated time delays is shown in red.

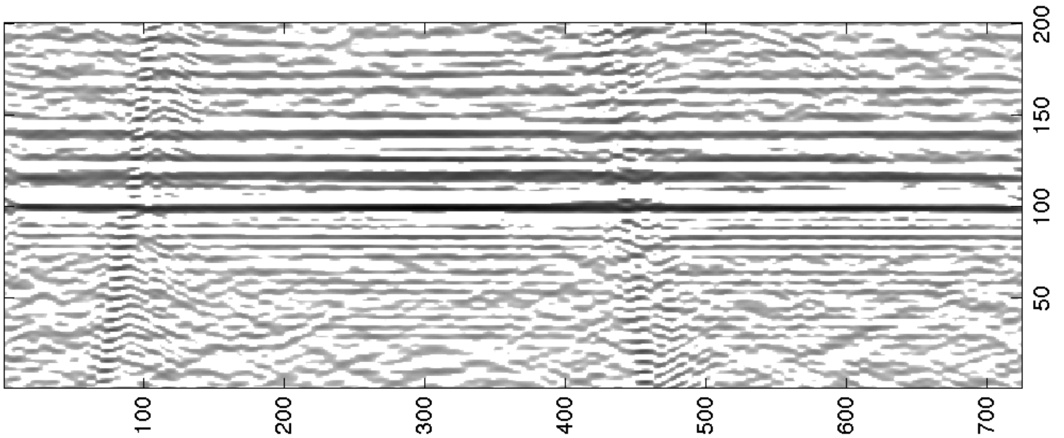

Figure 6. The reference target wavefronts following residual correction.

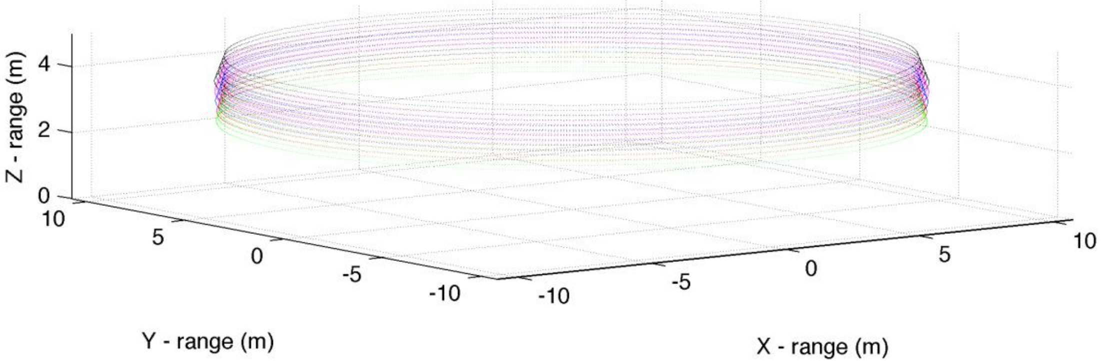

Figure 7. A point-cloud showing the locations of the receive array, estimated using the delays to the fiducial, and color-coded for the various stave heights: black = 4.3 m, magenta = 3.99 m, blue = 3.69 m, red = 3.39 m, and green 3.08 m.

The coordinates for the array solved via the time delays to the fiducial were used in subsequent beamforming experiments.

NSWC PCD Test Pond Data Processing: Fast Nearfield to Farfield Transformation

Raw SAS data is not an image but rather samples of projections through a reflectivity function. They must be coherently combined to generate a reflectivity map, i.e., a sonar image. The process of generating a sonar image from raw data is called beamforming. Some types of beamforming operations are “general,” meaning they work for essentially arbitrary array geometries. These operations have drawbacks, however, one of which being that they are very slow. Other techniques, such as Fourier algorithms like the Omega-k [14] and, for CSAS imaging, projection slice [2], [5], imaging techniques are very fast and very accurate provided that the scan geometry matches the geometry assumed by the beamformer. For CSAS imaging, however, Fourier based projection slice imaging and other techniques based on medical tomographic algorithms assume planar wavefronts. This assumption is valid for very small targets near the center of a circular scan, but for targets with any significant size, wavefront curvature causes major distortion. For SAS systems this distortion is frequently observable for practical geometries and targets [15]. Fortunately, a transformation enabling efficient Fourier-based beamforming for circular synthetic aperture data has been developed and a simple derivation can be found in [15]:

$$\Psi_{FF}(\theta,t) = F^{-(2)}\left[\frac{\left|H_n^{(1)}(kR)\right|}{H_n^{(1)}(kR)} F^{(2)}[\Psi_{NF}(\theta,t)]_n e^{j\left(kR-\frac{\pi}{2}n-\frac{\pi}{4}\right)}\right] \qquad (1)$$

where Ψ_{NF} is the nearfield (original) backscattered acoustic data collected along a circular path, Ψ_{FF} is the farfield converted data, k is monostatic wavenumber, R is the radial diameter, n is the azimuthal Fourier component, $H_n^{(1)}$ represents the nth-order Hankel function of the first type, and $F^{(2)}$ and $F^{-(2)}$ represent the forward and inverse two-dimensional Fourier Transforms. This transformation makes the signals from the scatterers in the scene appear as if their ray-paths are all parallel (i.e., a nearfield to farfield transformation). Expression (1) contains Hankel functions, which are computationally expensive to compute for large matrices, however. Qualitative observation of the phase correction shows that it varies smoothly and should be representable by a simple series expansion. The asymptotic expression for the argument of the Hankel function is known [16]:

$$\arg\left[H_n^{(1)}(kR)\right] \approx kR - \frac{\pi}{2}n - \frac{\pi}{4} - \frac{4n^2-1}{2(4kR)} + \frac{(4n^2-1)(4n^2-25)}{6(4kR)^3} + \cdots \qquad (2)$$

Recognizing that the Hankel functions in (1) can be expressed as the conjugate of the argument, the listed terms in eq. (2) can be substituted into 1), resulting in:

$$\Psi_{FF}(\theta,t) \approx F^{-(2)}\left[F^{(2)}[\Psi_{NF}(\theta,t)]_n e^{j\left(\frac{4n^2-1}{2(4kR)} - \frac{(4n^2-1)(4n^2-25)}{6(4kR)^3}\right)}\right] \qquad (3)$$

The second term in the exponent reduces error at very wide angles, however for most CSAS systems only the first term is necessary for reconstruction. The fast approximation in (3) was developed near the start of this project and subsequently, because of its effectiveness and efficiency, applied to all instances of Fourier CSAS beamforming performed in this project, test-pond or otherwise. Examples will be shown in the results section.

NSWC PCD Test Pond Data Processing: Clutter Reduction as a Wavenumber Filter

In-situ response estimation requires that acoustic signals from adjacent, significant scatterers be rejected to prevent signal contamination. Based on the success of image-isolation methods developed for linear and/or circular SAS [17, 18], a holographic modification for CSAS beamforming was proposed. Upon more careful consideration of the decluttering problem a more efficient alternative was developed. This technique, which generates a mask in the wavenumber-moment domain, will be called the *KM* (i.e., wavenumber *k* and moment *M*) filter and the steps are described below:

1) Apply the appropriate delays to artificially "re-center" the object of interest, e.g., delay a target by:

   $$t_{del}(\theta) = \frac{R - \sqrt{R^2 + R_t^2 - 2RR_t\cos(\theta - \theta_t)}}{c/2}, \qquad (4)$$

   where R is the circle radius, R_t is the distance of the object from the circle center, and θ_t is its angular offset. Note that this is only an approximate re-centering algorithm, but that it is sufficient for pushing acoustic data into a convenient location of the wavenumber spectrum for filtering.

2) Compute the two-dimensional Fourier spectrum of the backscattered acoustic data, and its associated wavenumber values: $k_{r\_max} = \pm\mathrm{pi}/\delta r$, $k_{\vartheta\_max} = \pm\mathrm{pi}/\delta\theta$, where $\delta r = c/(2 * f_s)$, and f_s is the sample rate assuming the data is real and un-modulated, and $\delta k_r = 2/(c\ t_{max})$, $\delta k_\vartheta = 1$.

3) Compute aspect insonification angle:

   $$\Theta = \tan^{-1}\left[\frac{k_r}{k_\theta}\right], \qquad (5)$$

   for each sample of the wavenumber spectrum.

4) Define a limiting angle Θ_{lim} that corresponds to the maximum angle insonified over the region for which the acoustic signal is to be isolated. This angle is:

$$\Theta_{lim} = \sin^{-1}\left[\frac{R_{patch}}{R}\right], \tag{6}$$

where R_{patch} is the size of the region around the target (possibly the target dimensions) for which the acoustic backscattering response is to be preserved.

5) Define an insonification mask in wavenumber space that limits the span of receivable aspect angles to those corresponding to the finite size of the target region. This can be done by applying the following sigmoid function to the two-dimensional aspect angle map Θ defined over the sampled wavenumber space:

$$M(\Theta) = \frac{1}{\left(\sqrt{1+e^{\sigma(\Theta-\Theta_{lim})}}\sqrt{1+e^{-\sigma(\Theta+\Theta_{lim})}}\right)}, \tag{7}$$

where σ is a parameter that determines the steepness of the filter cutoff that occurs at Θ_{lim}.

6) Multiply mask M(Θ) with the complex data spectrum, and compute the inverse Fourier transform to return to the original data domain.

7) Define upper and lower time-limits corresponding to the patch boundaries. The lower time limit will correspond to the patch radius, but the upper limit will be larger to preserve resonance signals, e.g:

$$t_{low} = 2(R - R_{patch})/c\ , \tag{8}$$

$$t_{high} = 2(R + R_{patch})/c + \mathrm{t}_{decay}\ . \tag{9}$$

8) Zero all data arriving before t_{low} or after t_{high}.

9) Undo the delays applied in step 1).

A major advantage of the proposed method vs. competing image isolation methods is that separate bounds can be set for the temporal leading and trailing edge of the mask. Secondly, determining the mask boundaries is very simple, as the only parameters are R_{patch}, the radius of the patch to be isolated, σ, the filter cutoff strength, and t_{decay}, estimated target resonance decay time. Lastly, the filter cutoff strength can be determined independently from the decay time, enabling better noise reduction for signals having long decay times.

The general outline of this process was developed under ONR grant #11517317, however the details of implementation, in particular how the wavenumber filter relates to insonification aspect angle and the bounding conditions for the wavenumber filter were developed in SERDP project MR-2439. This type of filtering is now used extensively for acoustic feature and signal extraction in the test-pond and results will be shown in the results and discussion section.

3D Beamforming

To evaluate potential beamforming techniques, target simulations drawing on other modeling work (e.g., SERDP sponsored MR-2505 Target-in-environment TIER modeling) were used to provide a performance baseline. Using the axiscat finite element model and rapid environmental simulation tool (see project MR-2505), sets of synthetic datasets were generated to evaluate basic three-dimensional data-processing strategies. The volumetric image domain and its complex three-dimensional spectrum were chosen as the ideal domains to work in because of their potential uses for target de-cluttering and the intuitive means by which they allow data and path projection interpretations. Alternate methods are possible, however, especially with regard to the method by which path-projection occurs and these will be discussed.

As in the two-dimensional case, generalized beamforming algorithms can be used to create 3D volumetric images simply by backprojecting to voxels (i.e., 3D pixels). The problem, however, is that this approach to beamforming is computationally burdensome: backprojection from an array with N samples to a datacube with N voxels per dimension has a computational burden of N^4 in the volume imaging case. Two methods were devised to reduce this burden. The first method beamforms data in the vertical dimension, which has a computational efficiency of N (array elements) x M_r (range samples) x M_h (height samples). Following this computation, Fourier based methods are applied to each horizontal slice.

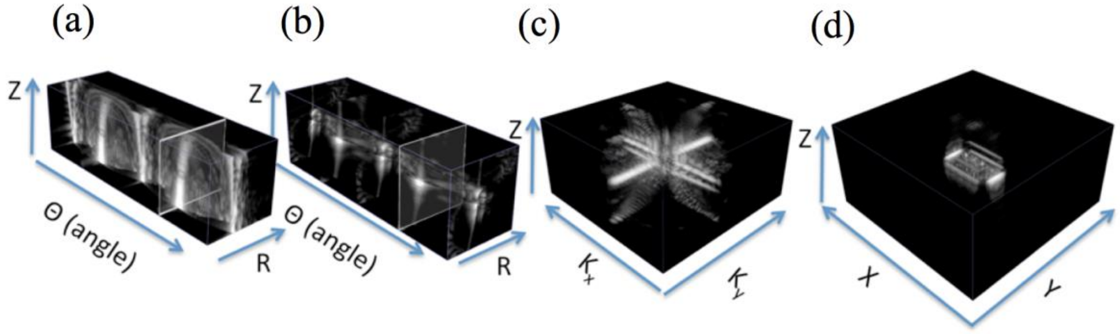

Figure 8. Illustration of the beamforming procedure. The complex 3D sinogram depicted in (a) is beamformed in the vertical (i.e., z direction) dimension, and the result is shown in (b). The Fourier spectrum is computed in the range dimension and a polar-Cartesian transformation is performed, with the results shown in (c). The inverse two-dimensional Fourier transform is then computed for every height plane, resulting in the beamformed image (d).

The relative computational efficiency is approximately NM_rM_h. The second half of the data-processing (e.g., Fourier processing) takes an insignificant amount of time compared to the first half. An added advantage of this method is that the nearfield to farfield approximation, which assumes planar scattering, is now exact for each image height plane.

Additionally, artifacts from under-sampling exist. The second approach considered for 3D beamforming further improves the computational efficiency, and can even improve the beamforming results, but is primarily applicable if the spatial dimensions of the imaging patch are much smaller than the circle radius. This approach back-propagates the data to a polar format in the vertical dimension. The projection slice imaging approach is then applied to each plane in the range-height dimensions. This has certain advantages for the case in which the data is undersampled in the vertical dimension (from a standard SAS perspective – tomographic sample requirements still remain, see [11]). The downside is that it is only applicable to local patches. Example comparisons between standard backprojection and this approach are shown in the following figures.

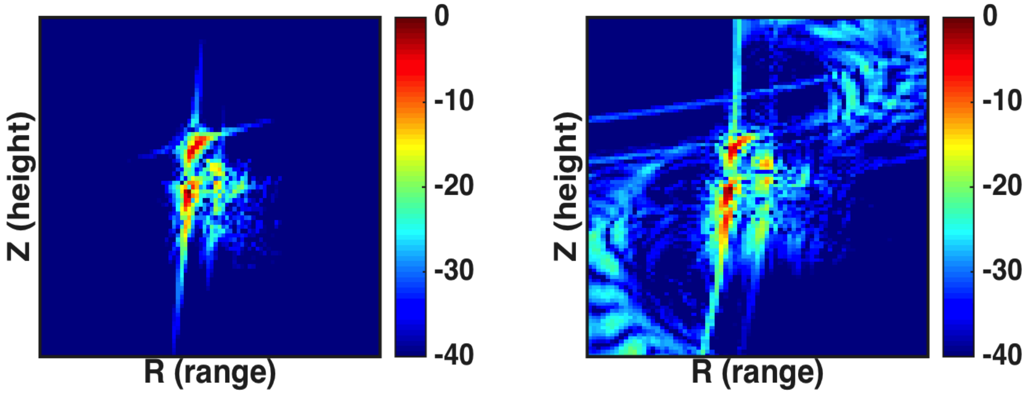

Figure 9. Slice through vertically beamformed data at θ = 0°. The beamforming method on the left is projection slice beamforming and the method on the right is back-projection. The image features are similar (differences are a result of varying spectral weightings), but the back-projection image clearly suffers from a large number of imaging artifacts. The color-scale is in dB with respect to the brightest point.

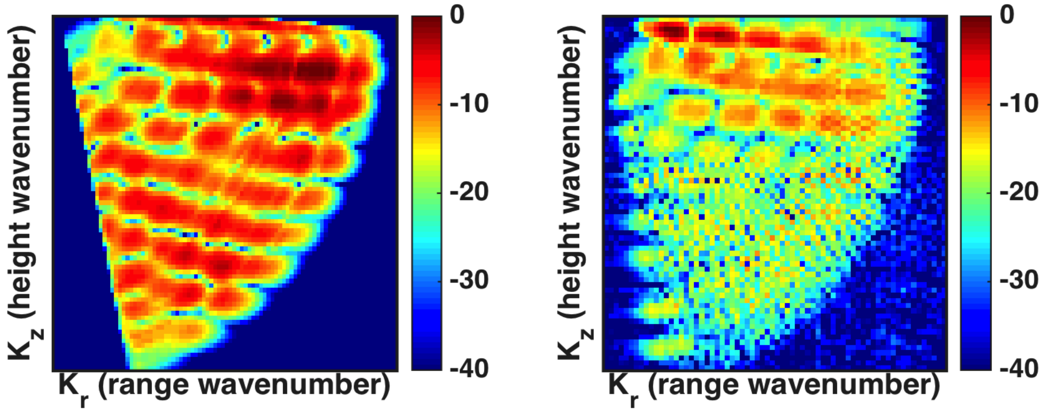

Figure 10. The two dimensional spectrum of the images shown in the previous Fig. 9. Without compensating for sample density or frequency the spatial spectrum of a backprojected image will over weight low frequencies and spectral regions corresponding to elevated aperture sample density. The color-scale is in dB relative to the brightest point.

Trajectory Projection

Assuming experimental or synthetic data has been captured and processed so that a well sampled volumetric region of the wavenumber spectrum exists, it can be processed to resemble data observed by from arbitrary scan patterns, so long as the observation angles are supported by the sampled region of wavenumber space. This projection capability enables, for example, artificial re-centering to remove grazing angle as a scan variable, or the simulation of linear scan snapshots of targets at random orientations, which has the potential to be useful for target recognition algorithm testing and/or training.

Consider the volumetric image of the three-dimensional scattering function shown in Fig. 11, which was constructed from a TIER simulation of a proud cylinder, and corresponds to datasets shown in Fig. 8 – 10:

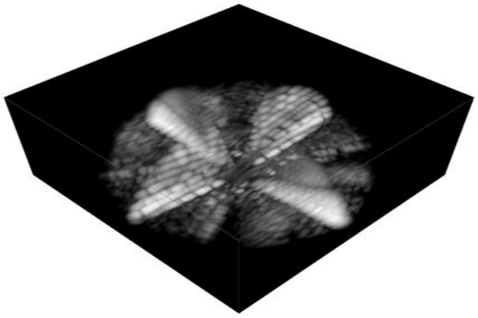

Figure 11. Three-dimensional spectrum (axes: $K_{x,y,z}$) of a proud 2-1 aluminum cylinder. This spectrum is equivalent to taking the Fourier-transform in the Z-dimension of the volumetric dataset depicted in Fig. 8(c).

The previous image was generated using the projection slice method to preserve spectral calibration. A simulated target signal acquisition along an arbitrary scan pattern can be sampled from this data, and the spectral sampling of this arbitrary scan can be represented as a series of rays in spherical coordinates as illustrated in Fig. 12:

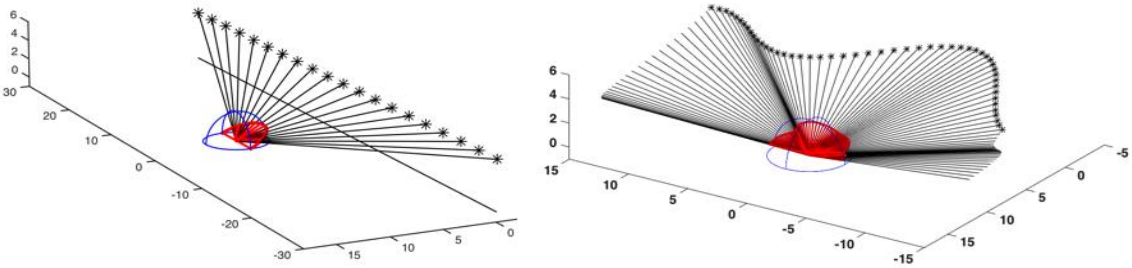

Figure 12: Illustration of the relationship between array spacing relative to a target and the sample through the three-dimensional spectrum (with bounds illustrated by the blue curves) corresponding to each array point. The example on left is a linear array and the example on the right is a highly distorted non-linear array. Note that the linear array appears to result in a planar slice through the 3D spectrum.

A concentric circle looks like a symmetrical cone, whereas a non-concentric circle looks like a skewed cone as shown in Fig. 13:

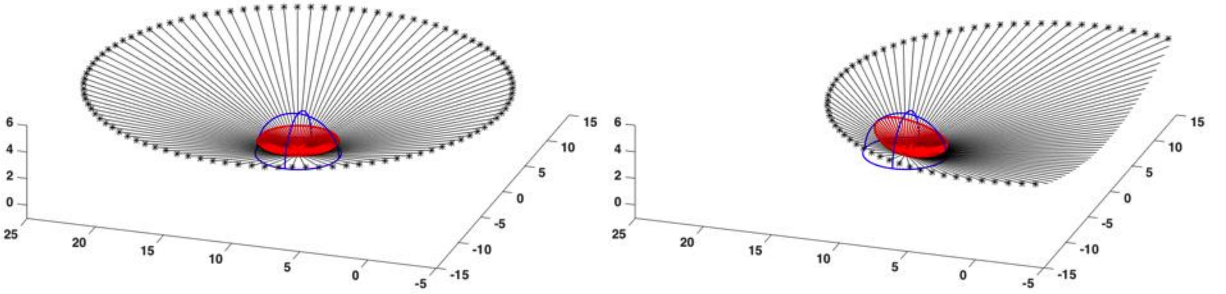

Figure 13. Illustration of the conical and skewed-conic sampling of the three-dimensional spectrum caused by circular and non-concentric circular apertures.

If a multi-pass dataset is captured in situ it is therefore possible to simulate observations from a variety of angles, or to sample the data in such a way that certain variables are consistent between model and observation (e.g., ensure a constant grazing angle vs. aspect). To demonstrate this with volumetric spectral data captured in the field is one of the goals of this project.

An alternative method for path projection that is simpler but provides less physical insight is to represent the data directly in a spherical coordinate frame rather than Cartesian coordinate frame:

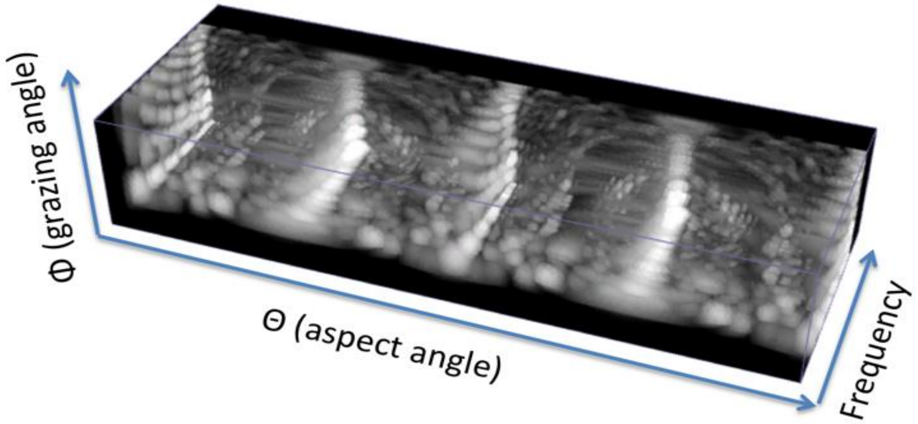

Figure 14. Representation of target aspect/grazing angle frequency response in spherical coordinates. This method of data representation makes data-projection very simple, but is less physically intuitive in how it relates to the aperture.

In this domain, data-projection may be accomplished simply by sampling at the correct aspect and grazing angles, and back-propagating data from each of these array points the appropriate distance to intersect with the scan path. This is a particularly convenient method for applying simulated phase error, and examples for application to AUV captured data are shown later in this document. Examples with TIER data, are shown below.

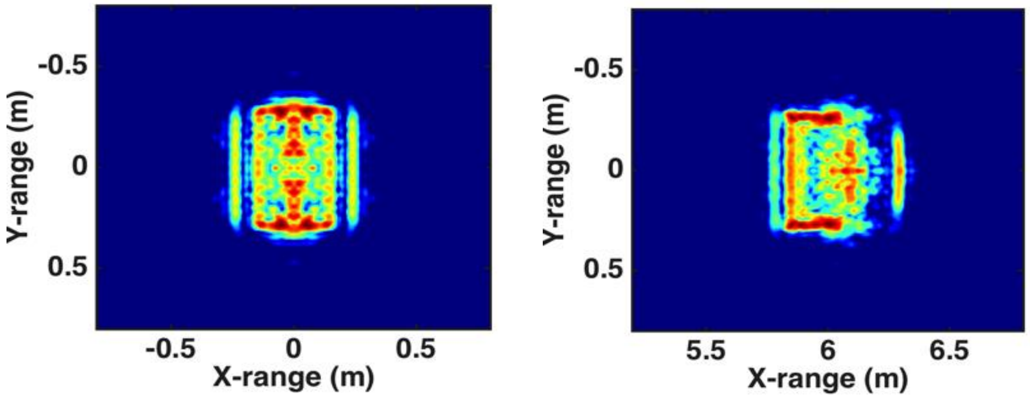

Figure 15. Concentric (L) and non-concentric (R) 2-1 cylinders, both constructed from samples of same 3D scattering function depicted in Fig. 11. The left figure simulates a target imaged from an 11 meter radius, 6 meter altitude scan, and the right figure assumes the target is shifted from the center by 6 meters, resulting in a maximum grazing angle of 45 degrees.

Despite the target being perfectly concentric in the scan data, a simulation of a non-concentric target could be generated. The fact that the three-dimensional scattering function has been sampled enables this alternate projection. The reverse could theoretically be accomplished (i.e., a non-concentric target could be projected to the center), and this is the theoretical basis for artificial target “re-centering” using sub-sampling of the three dimensional wavenumber spectrum.

Acquisition simulations from linear trajectories can also be sub-sampled from circular multipass data using this method. Examples are shown in Fig. 16.

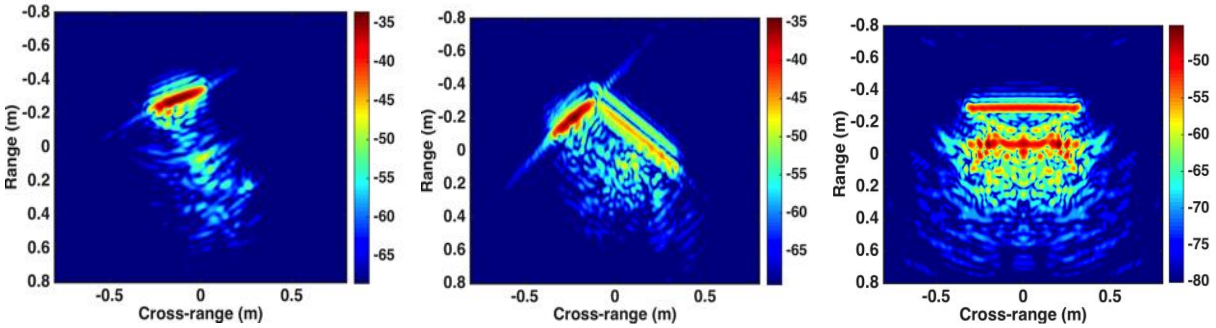

Figure 16. Linear aperture simulations generated via image formation from planar slices through the three-dimensional spectrum. The planar slices are generated using simulated linear scan geometries. Range in the image is slant-range, and the images span a variety of grazing angles ranging from 15 to 45 degrees. The color-scale is in decibels (dB).

One point of interest from observation of these projections is that both the acoustic image and associated acoustic color plot can vary a large amount over the spanned range of aspect angles, if the grazing angle changes significantly. An example of this difference is shown in Fig. 17.

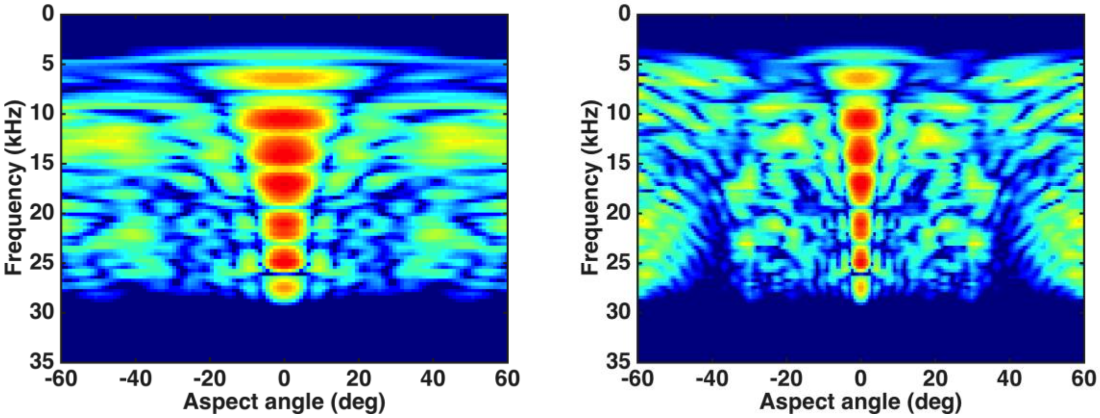

Figure 17. Comparison of log-scale CSAS (L) and linear SAS (R) color plots for a span of 120 degrees, when captured at a steep grazing angle. Note the different spans of similar acoustic phenomena.

The potential ramifications for target recognition is that the models produced by finite element simulations assume constant grazing angle with aspect, but this assumption can break down in a significant manner in linear scans, especially at steep grazing angles, due to the coupling of the acoustic response to variation in grazing angle. More examples, applied to real data scans, are shown in the results section of this document.

AUV Based Field Experimentation

The previous section outlines methods that were developed in the initial year of the project to address basic multipass processing issues such as efficient 3D beamforming, nearfield phase and amplitude correction, and clutter reduction for acoustic signal isolation. Ultimately, however, it was the intention of the project to move out of a test-pond environment and into an uncontrolled environment in which an AUV was used as the sonar platform so that in-situ measurements of the 3D wavenumber responses of targets could be measured in real, UXO contaminated environments. This extension is accompanied by a whole set of additional challenges that will be addressed in this portion of the methods section of this document. The main challenges to AUV multipass processing are 1) Navigation error correction (due to the stringent requirement of phase error being $\leq \lambda/8$ radians for coherent processing), 2) Beamforming with an irregularly sampled (and potentially undersampled) array in the vertical dimension, and 3) acquisition methodology, i.e., what is the best scan pattern for acquiring 3D wavenumber spectra data.

In this project, a number of methods were proposed and tested, some of which were significantly less effective though all, excepting the most recent developments, have been documented in previous project interim reports and peer-reviewed papers. For completeness, each of these "phases" of development will be discussed in subsequent subsections, however emphasis will be given to the most recent procedures because these have are not captured in any of the interim reports previously submitted to SERDP.

Phase 1.0 Methods (FY14): CSAS Data Navigation and Coregistration

The multipass scans conducted in this research are all composed of a set of circular scans. The non-linearity and length of circular apertures generally require that further navigation refinement be applied to produce well focused imagery from even a single circle. This project began, therefore, with addressing the issue of circular scan navigation refinement, prior to tackling the difficulties with aperture synthesis between circular scans.

The first approach to navigation refinement tested in project MR-2439 was a method coined "pseudo-stripmap" imaging. This approach, conceived in ONR grant 11517317, attempts a three-dimensional navigation refinement parameter inversion using the range variance of local quadratic phase error measurements. A paper describing the approach [19] was published in the bi-annual proceedings the European Symposium on Synthetic Aperture Sonar and Synthetic Aperture Radar. To summarize the approach the sonar data, coarsely compensated using standard SAS micronavigation, is imaged in the range and angular dimensions using a one-dimensional compressional filter applied in the azimuthal dimension of the sonar. An example is shown in the following figure.

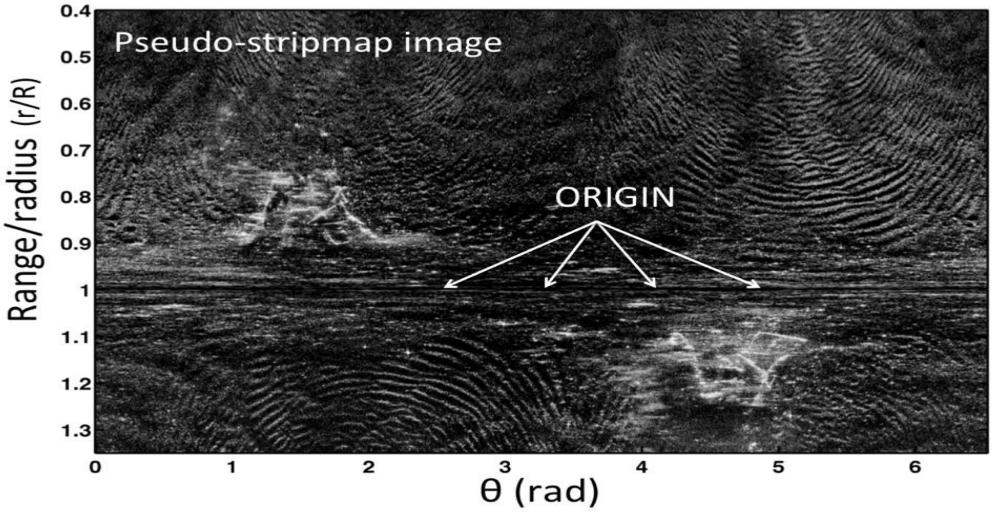

Figure 18. A "pseudo-stripmap" image created from circular aperture data. This type of image was used both for rapid coordinate inversion and co-registration between multi-pass data. It is extremely rapid to compute, requiring a convolution operation in only one dimension.

The angular spectrum of the azimuthally focused image is divided in half to generate images having divergent aspect angles (e.g., Fig. 19). Patch-wise correlations are then used to estimate the local translational offsets in the azimuthal dimension (i.e., angular dimension for CSAS scans), relating the squinted images. These translational measurements are arranged in a two-

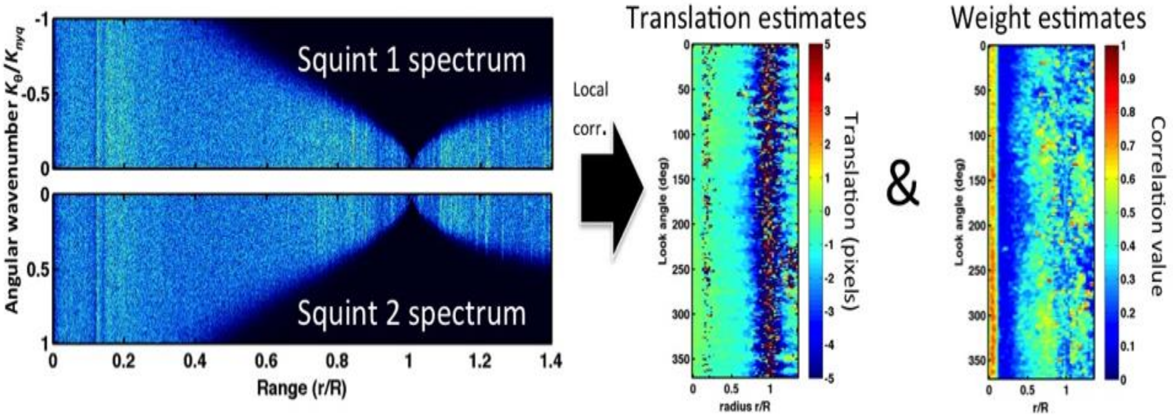

Figure 19. An illustration on the aperture division process carried out in the spectrum and the resulting translation estimates arranged as a two-dimensional matrix. A matrix of correlation coefficients is also generated that will be used as weights. The horizontal axes in all figures are slant range *r* normalized by scan radius *R*, and the vertical axis on the spectrum is azimuthal wavenumber K_θ normalized by the spatial nyquist rate $K_{nyq.}$ The vertical axes on the two other plots are the angle in degrees around the circular aperture.

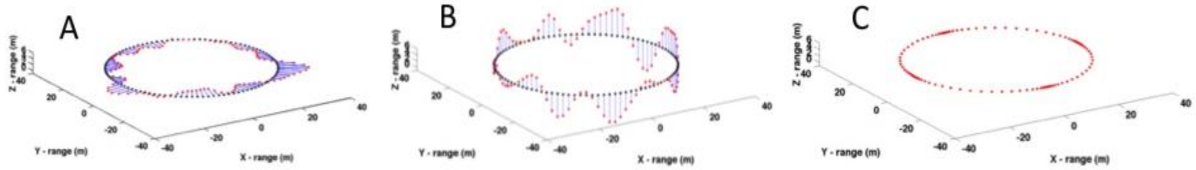

Figure 20. Illustration of range (A), height (B) and sampling (C) errors possible in a circular aperture geometry. Realistic situations often contain a combination of all three, though radial errors tend to be dominant and sampling errors tend to be insignificant.

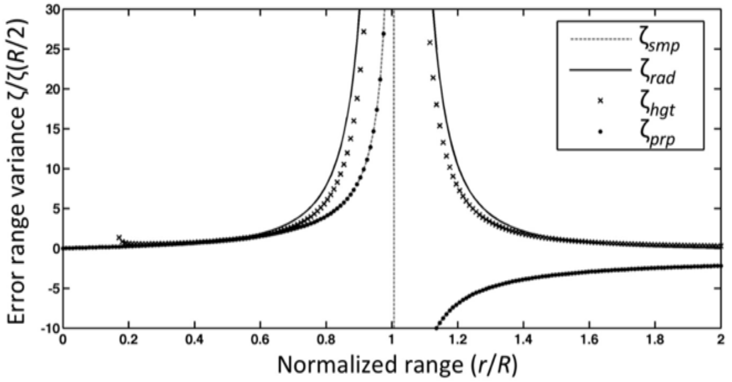

Figure 21. The quadratic phase error *range dependencies* (normalized by the values at half of the scan radius *R*) vs. slant range (normalized by *R*) for errors in sample rate ("*smp,*" dashed line*)*, radius ("*rad,"* solid), height (*"hgt*," x's), and propagation speed ("*prp*," dots). Combinations of these bases form the rows of the matrix in the center panel of Fig. 19.

dimensional matrix and the local quadratic phase error is directly proportional to the measured local translational offsets in the azimuthal direction between squints. To make a navigation refinement, the measurements of quadratic phase error are decomposed into a set of basis modeling the range dependency for distinct types of navigation errors. The types of navigation errors are shown in Fig. 20 and corresponding quadratic phase error range dependencies are shown in Fig. 21.

The range dependencies for perturbations in each dimension are linearized (see [19]) and used to form a basis set into which the matrix of translational values are be decomposed. The correlations between squinted images also result in a quality map (Fig. 19), which is used to initialize the weights in the inversion process. Following navigation estimation the vehicle coordinates are updated and the process is iterated to convergence (typically 3 or 4 times but varies depending on the vehicle motion statistics or bottom backscattering properties).

There were both advantages and disadvantages to this approach. For example, in contrast to many point-based SAR phase error correction methods frequently used for circular aperture phase error correction (see, e.g., [20], [21]), or in SAS (Generalized cone paper [22]), this method can fix spatial variance issues by virtue of providing a multi-dimensional navigation correction, vs. a simple 2D phase correction filter that works only locally. This is demonstrated in the subsequent figure, in which azimuthal and radial navigation errors cause a high degree of spatial variance that require a navigation correction vs. a spatial phase filter to refocus data:

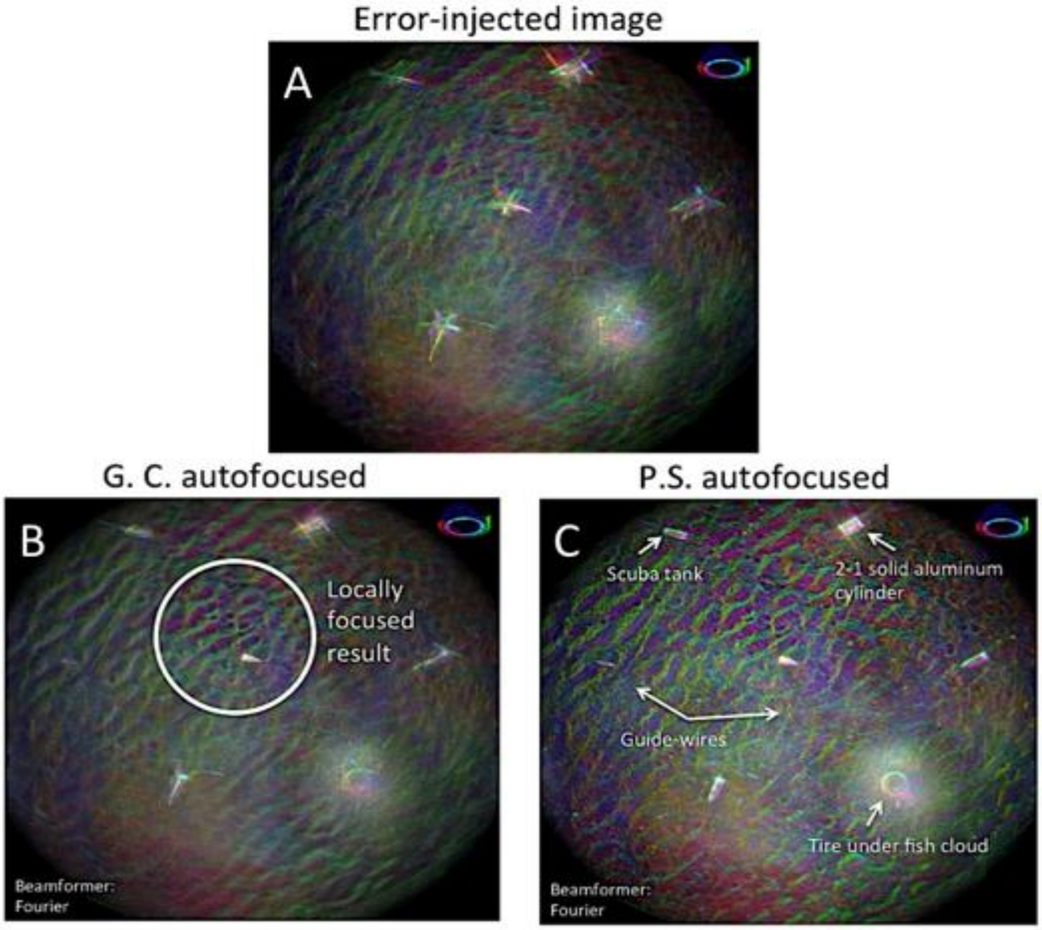

Figure 22. Example of Pseudo-stripmap autofocusing. A) shows the scene with injected, spatially variant errors. B) shows the scene after autofocusing using the technique described in [19]. C) shows the pseudo-stripmap focusing results. The alternative solution was only capable of generating a locally focused result, vs. the pseudo-stripmap version which, by virtue of creating an actual 3D coordinate update, created a general focusing solution for the full scene.

The primary disadvantages, which ended up being crucial points of failure, were that pseudo-stripmap autofocusing failed under high crabbing or crab-variance CSAS scan scenarios, (an inherent limitation of the 1D azimuthal focusing scheme), and that, upon closer inspection, the range dependencies for the quadratic phase errors introduced by the different aperture perturbations are not a linearly independent set. Any two of the three basis are linearly independent, but not the set of all three. As a result, the inversion is completely ill-posed. Error from the height basis can potentially be eliminated, because it tends to be known with much more certainty than the other errors (by virtue of having an absolute reference, e.g., depth), but even small height errors can still have significant ramifications on focus, and this just an inherent limitation of the technique when formulated as in [19]. For these reasons, the process was abandoned in favor of *multilateration*, which will be discussed more in the description of *phase 2*.

During phase 1 a model for circular scan navigation alignment was developed that wasn't significantly altered until phase 3 of the project. Even though multipass apertures capable of generating 3D data were not available in phase 1, multiple circular scans had been conducted around targets by AUV's in severe, uncontrolled environments and these were used to develop the co-registration approach depicted in the following flow chart.

Step	AUV data coregistration
1	INS and RPC-based vehicle micronavigation for 3D vehicle position estimation for each scan
2	Pseudo-stripmap autofocusing for navigation refinement of reference and repeat-pass data
3	Low-resolution CSAS image generation
4	Coarse rotation and translation alignment
5	Repeat-pass data re-centering
6	Angular co-registration refinement
7	Semi-fine range co-registration
8	Fine range co-registration
9	Repeat for each pass, updating reference when baseline crosses threshold

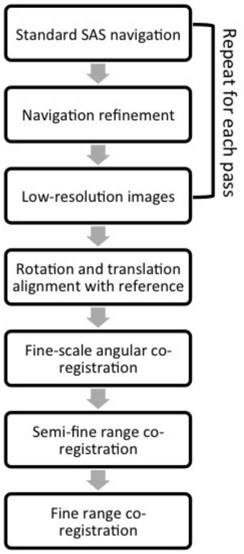

Figure 23. Table and flowchart showing co-registration steps for AUV data.

The procedure can be summarized as follows. The multipass scan is broken into a set of discrete circles. For each circle, standard SAS micronavigation methods (e.g., Belletini and Pinto [23] or [24]) are applied to arrive at an initial estimate for 3D navigation coordinates, and the autofocus method of choice (e.g., pseudo-stripmap autofocus in phase 1, multilateration in phase 2), is used to refine the 3D navigation estimates. A low-resolution intensity image, (pseudo-stripmap image in phase 1, see example below, or a projection slice image in phase 2), is then generated for each scan.

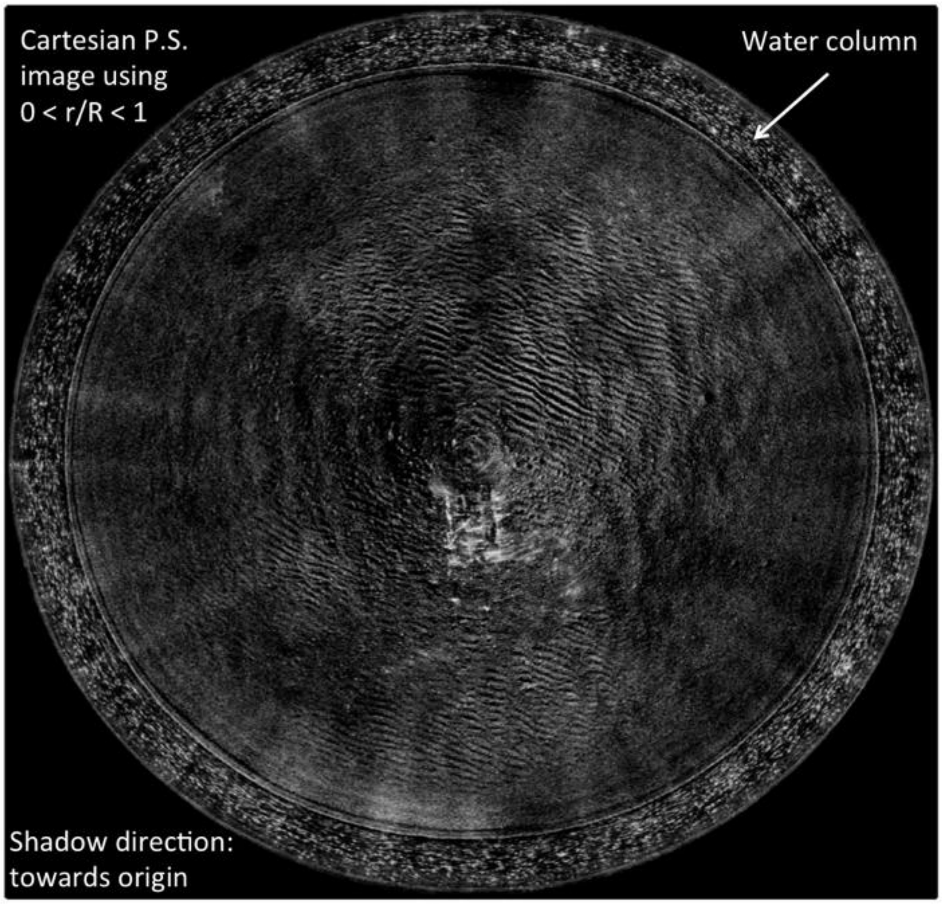

Figure 24. Low resolution CSAS image generated by performing a polar-Cartesian coordinate transform on a Pseudo-stripmap image. Note that this type of image is low resolution in comparison to a standard CSAS image but spans all the way to the water column. A complementary image can be generated using the scattering beyond the radius.

A lumped translation and rotation estimate relating adjacent scans is found using these low resolution intensity images. The navigation estimates for each scan are adjusted to compensate for these coarse translation and rotation alignment errors. A reference scan is picked (the middle scan for a set), data is projected to the ground-plane assuming the current coordinate estimates, and local, patch-wise correlations like the type done in redundant phase center micronavigation [23], [24] are used to find the local azimuthal, range, and height offsets between scans. This is done by fitting the measured offsets to a linearized model relating the significant parameters of the co-registration problem to the observed patch offsets. More detail on the procedure can be found in the FY14 interim report for project MR-2439, but the model used for navigation alignment in phase 1 is shown below:

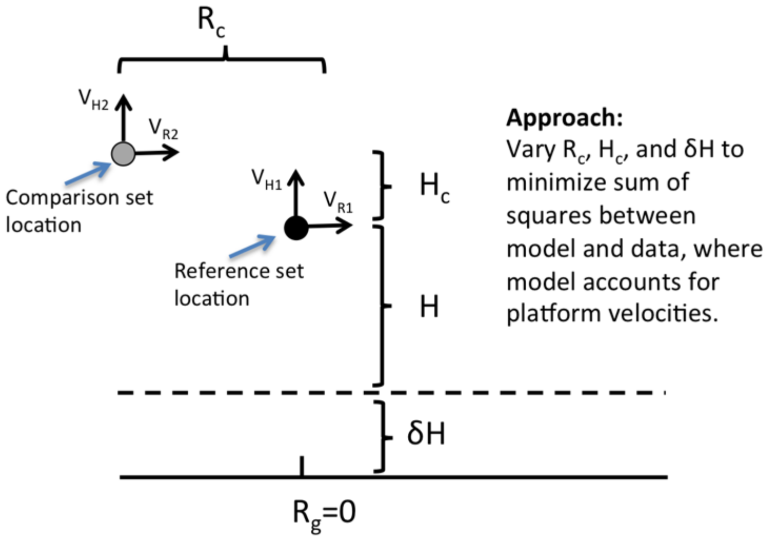

Figure 25. Illustration of the model used for generating a fitting function to the measured delay data. The reference coordinate location has a nominal height *H* with respect to the ground-plane that may have a small error component *δH*. Coordinates of the matching array are described in terms of height relative to the reference H_c and range relative to the reference R_c. The vehicle is assumed to have separate vertical and horizontal velocities, $V_{H1,2}$ and $V_{R1,2}$.

Assuming the data received at the reference scan is backscattered data sampled regularly in time, each sample corresponds to some ground-plane range r_s. Given initial estimates R_{c0}, H_{c0} from the translation / rotation procedure, an approximate equation relating the previously defined model to the true parameters R_c, H_c, δH is:

$$D + [\tilde{r}_s - r_s] - \left[\frac{R_{c0} - \sqrt{r_s^2 - (H+\delta H_0)^2}}{\tilde{r}_s} R_{c0} + \frac{H+\delta H_0+H_{c0}}{\tilde{r}_s} H_{c0} + \frac{H+H_{c0}-\chi\zeta+(\zeta^2+1)\delta H_0}{\tilde{r}_s}\delta H_0\right] + \left[\frac{H+\delta H_0}{c}(V_{H2} - V_{H1}) + \frac{\sqrt{r_s^2 - (H+\delta H_0)^2}}{c}(V_{R2} - V_{R1})\right] = \frac{R_{c0} - \sqrt{r_s^2 - (H+\delta H_0)^2}}{\tilde{r}_s} R_c + \frac{H+\delta H_0+H_{c0}}{\tilde{r}_s} H_c + \frac{H+H_{c0}-\chi\zeta+(\zeta^2+1)\delta H_0}{\tilde{r}_s}\delta H, \tag{10}$$

where

$$\tilde{r}_s = \sqrt{\left(\sqrt{r_s^2 - (H+\delta H_0)^2} - R_{c0}\right)^2 + (H+\delta H_0+H_{c0})^2}, \tag{11}$$

$$\zeta = \frac{H+\delta H_0}{\sqrt{r_s^2 - (H+\delta H_0)}}, \tag{12}$$

$$\chi = \zeta\delta H_0 + \sqrt{r_s^2 - (H+\delta H_0)^2} - R_{c0}\ . \tag{13}$$

In (10) *D* is the delay measurement matrix. The terms in the first and second brackets are expressions that alter the inverse problem so that rather than updating the basis after each iteration to minimize the residual, the full values of R_c, H_c, and δH are fit at each iteration. This creates good convergence properties when the basis are updated at each iteration and the system is solved with added navigation constraints. It is noticeable that the terms in the second bracket are equal to the RHS (right hand side) of the equation with the initial values plugged in. The values in the first two brackets are very similar, which means that the values in D still dominate the results. The terms in the last bracket on the LHS are velocity related. Noticeably, it is the velocity difference between the vehicles rather than their absolute velocities that significantly affect the phase. It is important to note that in this model the velocities do not have to be assumed constant and may vary as a function of time, though in the tested cases allowing for this did not significantly affect the residual. Lastly, the velocity terms were significant in the data used to develop coregistration procedures in Phase 1 because of the severity of the wave action experienced by the platform. In subsequent multipass experiments, however, the velocity term was less significant, and bathymetric height variance, un-modeled in (10 – 13), became a significant point of model breakdown. Compensation for this, and the updated model will be discussed in the section describing Phase 2.

Finally, the RHS of (10) contains the basis functions which are updated at each iteration, where R_{c0}, H_{c0}, and δH_0 are the values from the previous iteration. The best fit values in a weighted least-squares sense can be found for R_c, H_c, and δH using simple matrix inversion using the known values for r_s, initial values for R_{c0}, H_{c0}, and δH_0 (δH_0 is initialized at zero), H, and other relevant sonar and environment constants (*c*, sample rate, etc.). With the above formula, however, the values can be solved for as a whole system (i.e., co-registration for all aperture locations simultaneously), allowing navigation constraints to be added in the angular dimension. This can be expressed using a regularized weighted inversion:

$$[\psi_i^T[W(r,\theta) \circ \psi_i] + \lambda\chi^T\chi]^{-1}[W(r,\theta) \circ \psi_i]^T S = C_{i+1} \tag{14}$$

where ψ_i is a matrix with the basis functions calculated at the i$^{\text{th}}$ iteration, χ is a regularization matrix that penalizes platform motion that is unrealistic given vehicle mass and motion characteristics, $\circ$ is the Hadamard product and superscript ^{T} represents the transpose operator. The level of regularization is determined by the parameter λ. For each iteration of *i* the basis functions are updated by the value of the previous iteration results:

$$\psi_{i\_rng} = \frac{R_{ci} - \sqrt{r_s^2 - (H + \delta H_i)^2}}{\tilde{r}_{s\_i}}, \tag{15}$$

$$\psi_{i\_hgt} = \frac{H + \delta H_i + H_{ci}}{\tilde{r}_{s\_i}}, \tag{16}$$

$$\psi_{i\_bth} = \frac{H + H_{ci} - \chi\zeta + (\zeta^2 + 1)\delta H_i}{\tilde{r}_{s\_i}}, \tag{17}$$

These basis are arranged in a sparse manner, with a corresponding weighting matrix:

$$\psi_i = \begin{bmatrix} \psi_{i\_rng\,n} & & \cdots & \psi_{i\_hgt\,n} & & \cdots \\ \psi_{i\_rng\,n+1} & \vdots & \cdots & \psi_{i\_hgt\,n+1} & \vdots & \cdots \\ \vdots & 0 & \cdots & \vdots & 0 & \cdots \\ \psi_{i\_rng\,N} & 0 & \cdots & \psi_{i\_hgt\,N} & 0 & \cdots \\ 0 & \psi_{i\_rng\,n} & \cdots & 0 & \psi_{i\_hgt\,n} & \cdots \\ 0 & \psi_{i\_rng\,n+1} & \cdots & 0 & \psi_{i\_hgt\,n+1} & \cdots \\ \vdots & \vdots & \cdots & & \vdots & \cdots \\ & \psi_{i\_rng\,N} & \cdots & & \psi_{i\_hgt\,N} & \cdots \\ \vdots & \vdots & \vdots & \vdots & \vdots & \vdots \end{bmatrix} \tag{18}$$

$$W = \begin{bmatrix} W(r_n,\theta_m) & & \cdots & W(r_n,\theta_m) & & \cdots \\ W(r_{n+1},\theta_m) & \vdots & \cdots & W(r_{n+1},\theta_m) & \vdots & \cdots \\ \vdots & 0 & \cdots & \vdots & 0 & \cdots \\ W(r_N,\theta_m) & 0 & \cdots & W(r_N,\theta_m) & 0 & \cdots \\ 0 & W(r_n,\theta_{m+1}) & \cdots & 0 & W(r_n,\theta_{m+1}) & \cdots \\ 0 & W(r_{n+1},\theta_{m+1}) & \cdots & 0 & W(r_{n+1},\theta_{m+1}) & \cdots \\ \vdots & \vdots & \cdots & & \vdots & \cdots \\ & W(r_N,\theta_{m+1}) & \cdots & & W(r_N,\theta_{m+1}) & \cdots \\ \vdots & \vdots & \vdots & \vdots & \vdots & \vdots \end{bmatrix} \tag{19}$$

These matrixes are plugged into eq. (14) and re-solved each iteration, updating the basis and the solution. A demonstration of the effect of including velocity corrections on the total model-data residual are shown in Fig. 26. As previously mentioned, however, relative velocity between platforms was not the dominant source of coregistration error in subsequent multipass processing experiments and the model was adjusted accordingly in later project phases.

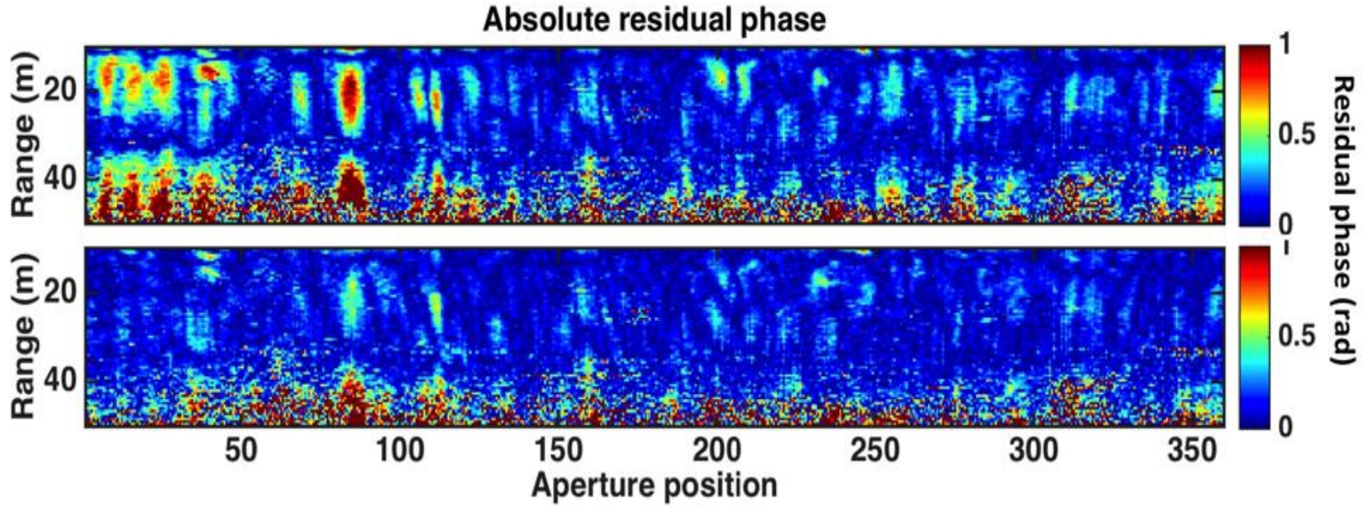

Figure 26. Comparison of the residual phase error between the fitted model and the measured data using the non-linear least squares approach (top) and the extension that compensates for relative platform velocity (bottom). Note that rapid fluctuations on the left side of the graph are almost completely corrected in the model with velocity compensation.

Phase 2.0 Methods (FY15): Navigation Refinement, Coregistration Model, and 3D Beamforming Updates

In phase 2 of the project, actual AUV multipass scans became available. The experiments are described in detail in [11] and the publically available FY15 SERDP interim report for MR2439 ([25]), but the experiments will be summarized here.

Two AUV-based multipass SAS field experiments for 3D imaging and spectrum acquisition were conducted in uncontrolled environments in phase 2 (~FY15). The utilized SAS system has two operational frequency bands: a high frequency band with a center frequency in the hundreds of kilohertz and a low frequency band with a center frequency in the tens of kilohertz. The SAS system was mounted on a REMUS 600 autonomous underwater vehicle [26]. The first field test, conducted off the coast of Panama City Beach, Florida in December of 2014, was performed in 20 meters of total water depth, over a flat sediment composed primarily of fine sand and small shell fragments. Two different scan patterns were utilized. The first pattern used circular scans with a constant radius of 30 meters altitudes that varied between 4.3 meters and 6.9 meters in altitude, in steps of 0.3 meters. The second pattern, which was designed to be more compatible with tow body systems, fixed the altitude at 6 meters and varied the radii between 27 and 35 meters in increments of 1 meter.

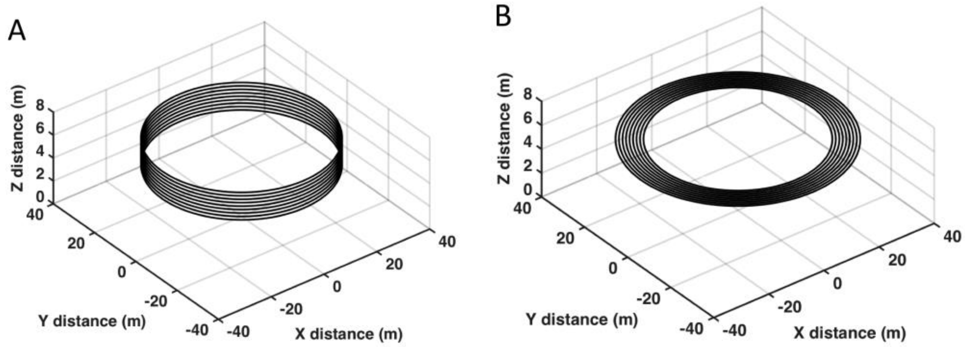

Figure 27. The scan patterns used in the first multipass beamforming field experiment. The scans in (A) fix the radius at 30 meters and span 2.4 meters in altitude. The scans in (B) fix the altitude at 5.95 meters and span 8 meters in radius.

In total, both scan types used 9 individual circular scans to form the full aperture. The presence of two parallel receive arrays separated by a vertical baseline on board the SAS system (typically used for interferometry) resulted in two vertical samples per scan, for a total of 18 sample points per multi-pass set. Fig. 28 is an example of an experimental realization of a vertical multipass set.

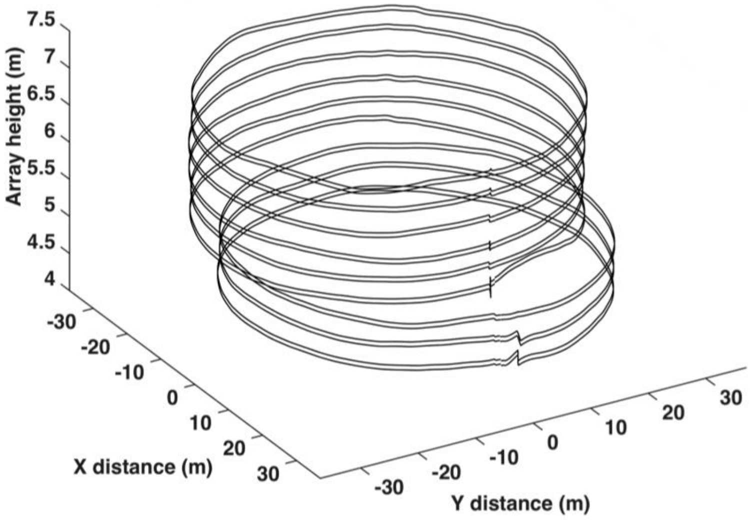

Figure 28. Example of a synthesized multipass array. The vertical samples are irregular as a result of the different vertical spacings between the multipass scans and the interferometric receiver arrays. Additional irregularity occurs because of currents and, for the bottom three scans, a GPS localization offset acquired during a resurfacing operation.

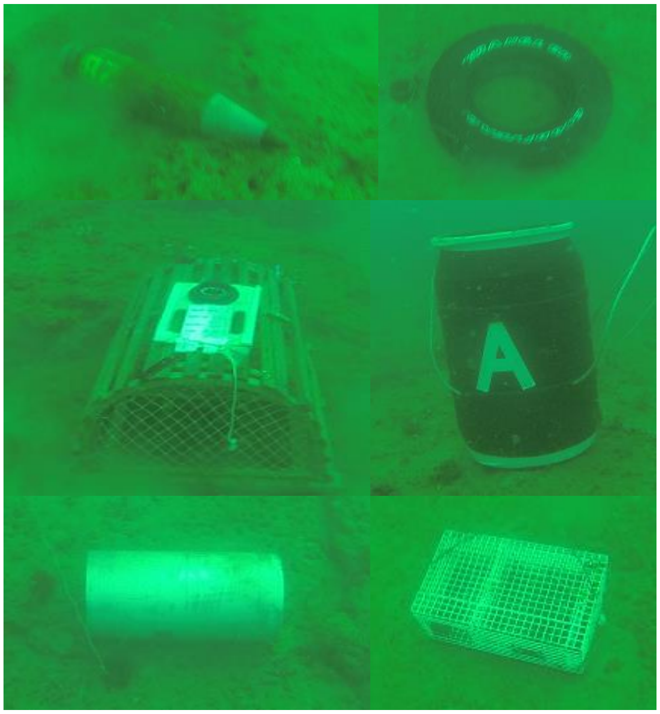

Figure 29. Underwater photographs of various targets deployed in the Gulf of Mexico off the shore of Panama City Beach, FL. The targets in this figure were scanned during the second set of tests conducted in June 2015.

The second test, also conducted off the coast of Panama City Beach, Florida, was performed in June of 2015. In this test the sediment was predominately limestone, rock and coral, some of which can be seen adjacent to the targets in Fig. 29. In the results section of this document, the 3D acoustic imaging results for these targets will be shown. Inclement weather prior to the tests caused dynamic currents which reduced platform stability. As in the first test, no strong static currents were present at the test site and large AUV crabbing was not an issue. The additional complexity of the bathymetry, however, played a significant role in algorithm development, which will be discussed in this section.

Targets were deployed in primarily in the proud configuration (i.e., on top of the sediment), however in the first set of scans, partially buried and obliquely buried configurations were used for some targets because the sandy sediment made this a possibility. The target inventory consisted of howitzer shells, a 2 foot by 1 foot diameter solid aluminum cylinder, steel and plastic barrels with the axis positioned vertically (the plastic barrel had a shotput suspended inside to test the visualization of internal features), and additional targets such as lobster traps (wooden and wire) and a tire. Not all of the circular trajectory scans were performed successfully, in some cases due to a navigation error and in some cases due to glitches in the software used to activate sonar signal transmission. Additionally, some targets appeared to have migrated from their originally deployed positions (possibly due to tidal currents) and were completely missed.

Subsequent subsections will describe the updates to the navigation refinement procedure, coregistration model, and beamforming approach used to synthesize the data from the various scans.

Phase 2.1: Multilateration

The principle behind multilateration is that the location of a signal source can be estimated by inverting an over-determined system of equations formed from the relative positions of, and time delays to, a set of receivers. In [12] it was shown that measurements of circular SAR focusing aberrations at a series of dispersed control points can be related by the multilateration principle to aperture coordinate errors in three dimensions. The current research has extended the ideas in [12] to make the navigation inversion more robust by adding appropriate regularization and adaptive weighting schemes to the navigation error inversion process, as well as specifically incorporating into the inversion process parameters accounting for positional errors in the multilateration control points. The latter, specifically, is a major improvement to the original formulation in [12] that increases the reliability of the routine in the areas of complex bathymetry that some of the scans took place. Additionally, the algorithm was extended to handle the high crab-angles encountered by SAS systems.

The full multilateration process, including equations for the linearized inversion routines, is described in detail in the FY15 interim report [25], however the following figures give an overview of the process, which consists of: 1) choosing a set of “control points”, at which point spread functions are estimated via map-drift measurements between sub-apertures (see Fig.’s 30 and 31). 2) the set of phase errors are related to 3D navigation refinements and control point position refines via an over-determined set of linearized equations. 3) the linear system is inverted to estimate the refinements, which are applied to the scan coordinates (Fig. 32), and the process is iterated to convergence.

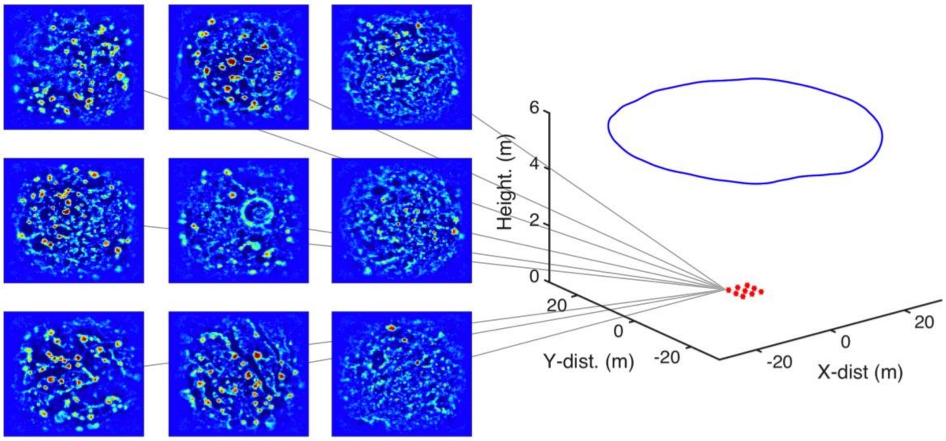

Figure 30. An example scan showing the flight path of the AUV in Cartesian coordinates (right figure, blue line) and the location of the test-patches used for multilateration (right figure, red dots). The image snippets at left correspond to the test-patches.

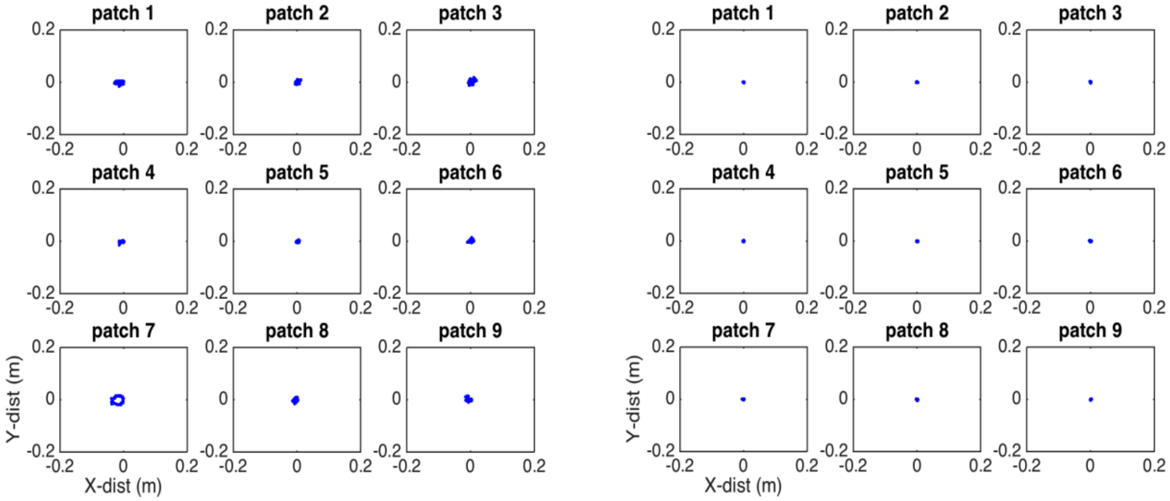

Figure 31. The point-spread functions before (L) and after (R) an iteration of the multilateration procedure applied to the scan depicted in Fig. 30.

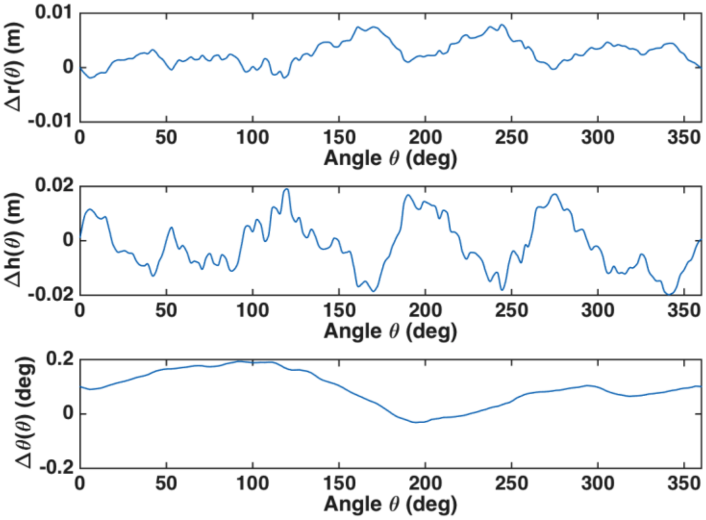

Figure 32. The radial, height, and angular corrections that are estimated from the iterated multilateration process and applied to the 3D coordinates of the SAS sonar platform.

The following figure gives an example of a CSAS image focused using this multilateration procedure. Of significance is the fact that the image remains in focus even at very large radii, which was the primary failing point for spectral correction methods like those described in ([20], [22]).

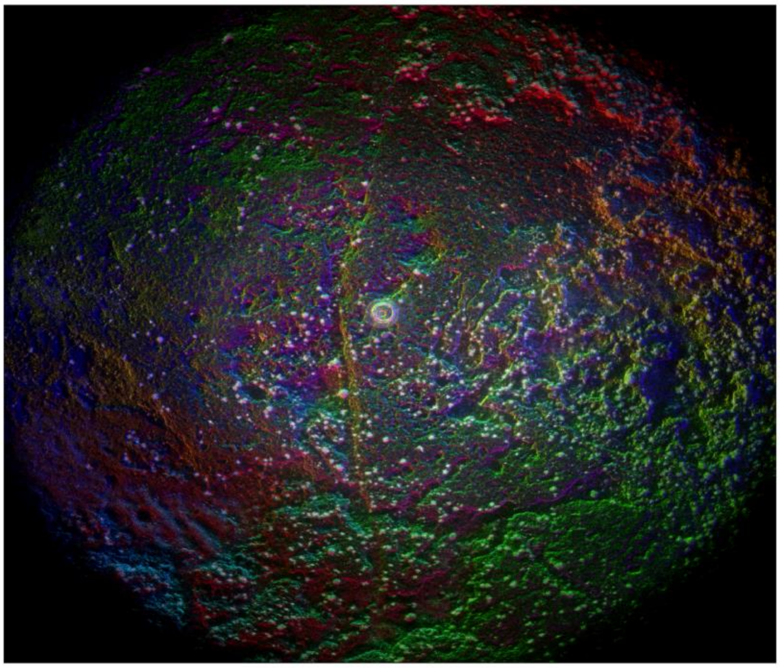

Figure 33. CSAS image of a proud, vertically oriented plastic barrel on a limestone and coral sediment. Focus is achieved throughout the image excepting out-of-plane regions, in which case defocusing is due to being out of plane.

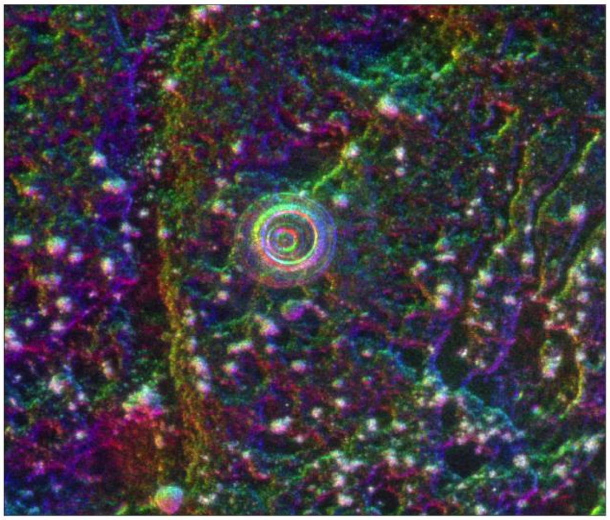

Figure 34. Zoomed in section of Fig. 33 showing the barrel.

Phase 2.2: Coregistration Model Updates

The variables in the Phase 1 model (Fig. 25), are the height H_c and radial R_c differences between the reference and comparison sets as well as a general model error for the height of the sonar above the sediment, δH. The sonar used for field experiments is interferometric, which means that a coarse estimate for the bathymetry of the insonified scene can be obtained. Bathymetry was found to strongly bias the coregistration results of the data from the second set of field experiments and the model was updated to incorporate the bathymetry into the coregistration process. The updated FY15 model, which can be found in [27] and FY15 interim report [25] is:

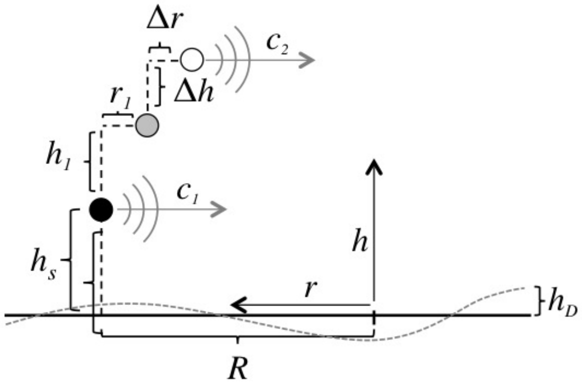

Figure 35. Phase 2 (FY15) AUV-scan coregistration model. The parameters are h_s: the height of the reference sonar above the nominal ground-plane, h_1: the initial vertical baseline estimate between the reference and comparison scan, Δh: the vertical baseline error, R: the radial location of the reference scan, r_1: the initial radial baseline estimate, Δr: the radial error variable, c_1: the reference sound-speed, c_2: the sound speed of the medium at the time the second scan is taken and lastly h_D: the sediment height relative to the nominal ground-plane. Lowercase r denotes the coordinate radial direction, and lowercase h represents the coordinate vertical direction.

Significant changes include the assumption of initial radial and height baselines r_1 and h_1, (initialized as the nominal radial and/or height difference between scans programmed into the vehicle objective), the reformulation of the location of the origin at the center of the cylindrical coordinate system, the inclusion of the bathymetry h_D, and a new variable, c_2, an independent sound-speed for the comparison scan. Presumably, c_2 should not vary significantly between scans, however due either to inaccuracies and drift in the onboard CTD or inhomogeneities in the water column, the average sound speeds measured at each scan varied enough to bias localization estimates between scans if left unaccounted. Unlike the FY14 model, the FY15 model did not include velocity terms because the relative platform velocities between scans did not vary significantly enough in the tested datasets to warrant their inclusion.

To summarize the new co-registration process, which is also done in [27], both the reference and comparison scan data sets are interpolated to the nominal ground-plane height $h = 0$, and interpolated as well to a uniform grid in the angular dimension, allowing coherent comparison between scans. These scans are then patch-wise correlated to generate a set of data products, which include complex phases, coherence measurements, and displacement measurements in units of meters. The displacements are found using the phase and locations of the correlation peaks. Examples of these data products are shown in in Fig. 36:

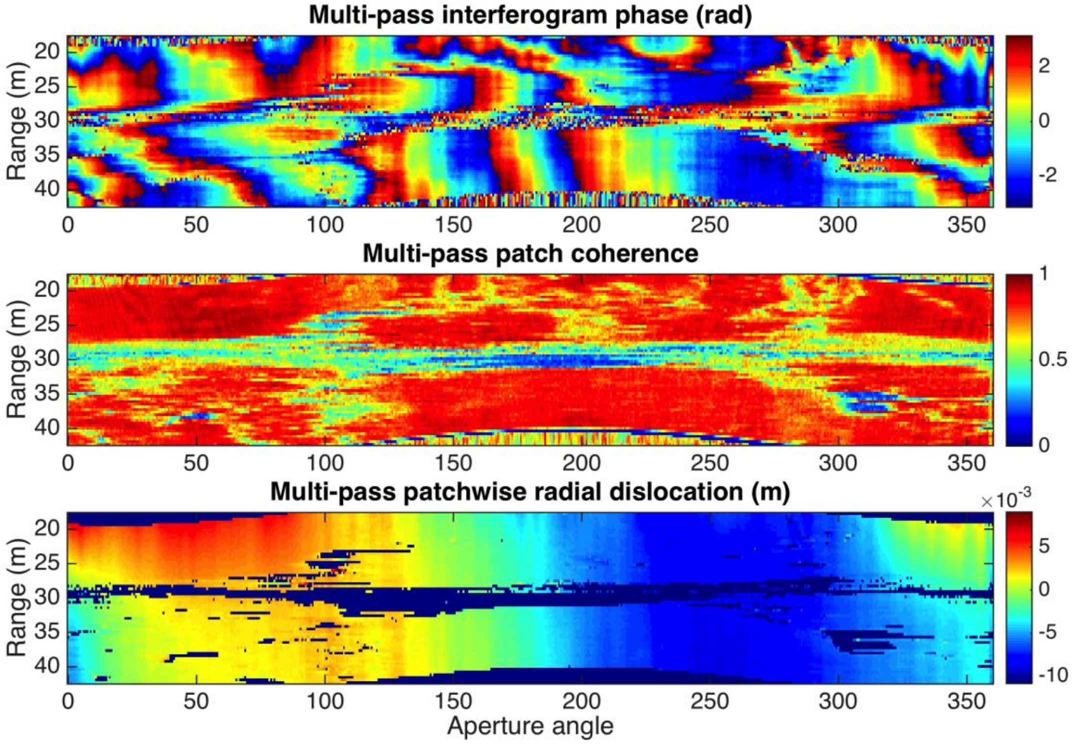

Figure 36. Top: phase measurements produced by patch-wise correlation. Middle: correlation coefficients for the patches. Bottom: radial displacement estimates measured by combining the phase estimates with coarse dislocation estimates found using the correlation peaks.

As done in Phase 1, regression is used to fit the displacement map in Fig. 36 to a set of basis functions. The derivation and linearization of the mathematical model associated with the displacement map in Fig. 31 can be found in Sec. IIIB of [11], and the final linearized description of the model, expanded around initial error estimates Δr, Δh, and σ (where $\sigma = c_1/c_2 - 1$) is:

$$\rho_{cor}(r_g) \approx \psi + \psi_0 + \zeta_{\Delta r}(r_g)(\Delta r - \Delta r_0) + \zeta_{\Delta h}(r_g)(\Delta h - \Delta h_0) + \zeta_{\sigma}(r_g)(\sigma - \sigma_0)\ , \tag{20}$$

$$\zeta_{\sigma}(r_g) = \frac{(r_g + r_1 + \Delta r_0)^2 + (h_S - h_d(r_g) + h_1 + \Delta h_0)^2}{\psi_0}\ , \tag{21}$$

$$\zeta_{\Delta r}(r_g) = \frac{(r_g + r_1 + \Delta r_0)(1 + 2\sigma_0)}{\psi_0}\ , \tag{22}$$

$$\zeta_{\Delta h}(r_g) = \frac{(h_S - h_d(r_g) + h_1 + \Delta h_0)(1 + 2\sigma_0)}{\psi_0}\ , \tag{23}$$

$$\psi(r_g) = \sqrt{r_g^2 - 2h_S h_d(r_g) + h_d(r_g)^2} + r_1, \tag{24}$$

$$\psi_0(r_g) = -\sqrt{(1 + 2\sigma_0)\left((r_g + r_1 + \Delta r_0)^2 + (h_S - h_d(r_g) + h_1 + \Delta h_0)^2\right) - (h_S + h_i)^2}\ . \tag{25}$$

In eq. (20) – (35), $\rho_{cor}(r_g)$ is the residual radial displacement at some aperture location (experimentally corresponding to a column from the displacement data at the bottom of Fig. 36), $\zeta_{\Delta r,\Delta h,\sigma}$ are the basis vectors, ψ and ψ_0 are terms that become important when the expansion is not around zero, and the other terms are explained in the caption of Fig. 35. Regression begins by initializing Δr_0, Δh_0, and σ_0 to zero, (in which case ψ and ψ_0 cancel), and performing a weighted least-squares fit with the basis functions:

$$\begin{bmatrix} \Delta\tilde{r} \\ \Delta\tilde{h} \\ \tilde{\sigma} \end{bmatrix} = \left(\begin{bmatrix} \zeta_{\Delta r} \\ \zeta_{\Delta h} \\ \zeta_{\sigma} \end{bmatrix} \cdot \left[(w \circ \zeta_{\Delta r})^T \quad (w \circ \zeta_{\Delta h})^T \quad (w \circ \zeta_{\sigma})^T \right] \right)^{-1} \cdot \begin{bmatrix} (w \circ \zeta_{\Delta r})^T \\ (w \circ \zeta_{\Delta h})^T \\ (w \circ \zeta_{\sigma})^T \end{bmatrix} \cdot \rho_{cor}^T, \tag{26}$$

where w is the weighting function for the data, (determined via the patch correlation coefficients), $\circ$ is the Hadamard product, superscript ^{T} represents the transpose operator and $\Delta\tilde{r}$, $\Delta\tilde{h}$, and $\tilde{\sigma}$ are the error values fitted from the i^{th} row of radial displacements.

Following initial data fitting the estimates of the error values determine the new expansion points, i.e., $\Delta r_0 = \Delta\tilde{r}$, $\Delta h_0 = \Delta\tilde{h}$, and $\sigma_0 = \tilde{\sigma}$. Using these new values the basis are recalculated and eq. (26) is re-evaluated. A full technical description of the process is described in Section IIIB of [11], which includes methods for adaptively determining the values of the weighting function w

as well as methods for coupling the estimates from adjacent aperture points to allow additional information about the likelihood of the behavior of the SAS platform to inform the estimates for the error variables and the weights.

The inclusion of bathymetric data into the regression process in the FY15 model is a major advantage over the FY14 process, which assumed a flat sediment. To illustrate, the displacement data in Fig. 36 was fit using both the flat bottom assumption in one case and in another case the full FY15 model that incorporates bathymetry. In Fig. 37, the data is shown (Fig. 37, top left) along with the surface reconstructions for the data generated using the basis that assume a flat bottom or incorporate bathymetry. Furthermore, the residual errors between the dataset and the individual models are shown for both instances as well.

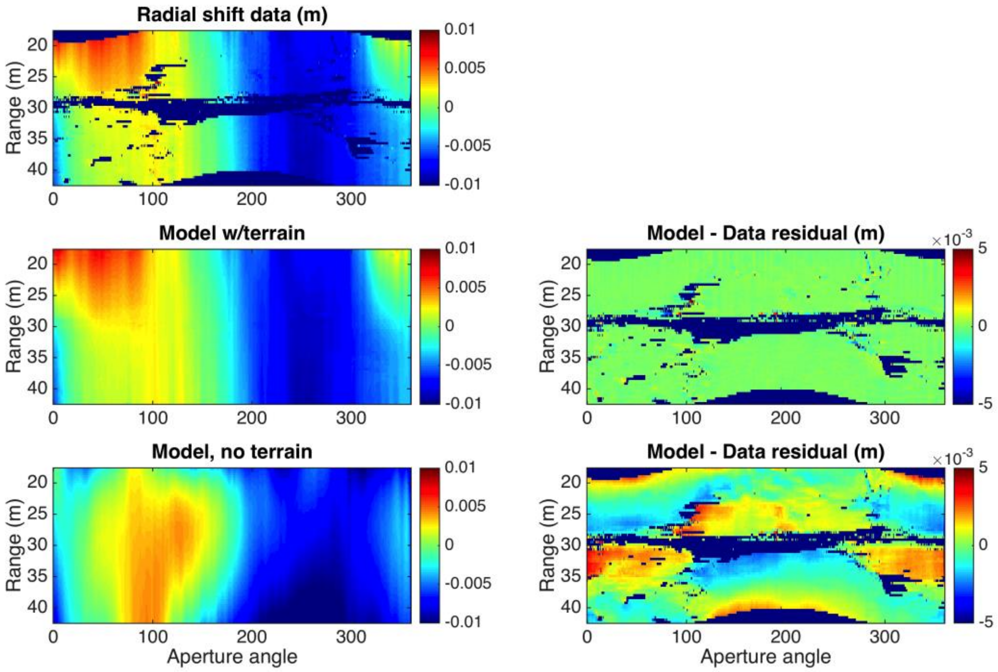

Figure 37. Top left: Original displacement data estimated via patch-wise correlation. Middle left: the displacement surface, reconstructed using the basis functions and estimated error parameters for the FY15 model incorporating bathymetry. Bottom left: the displacement surface, reconstructed using the basis functions and estimated parameters for a flat-bottom assumption. Middle right: the model – data residual for the FY15 model. Bottom right: the residual error for the flat-bottom model. The color scale is in meters.

The contrast between the methods is stark: the residual for the model incorporating bathymetry is much smaller. Qualitatively, the model generated by the parameter fits also appears much more like the original data (compare the middle left and top left images in Fig. 37). The difference also manifests in the estimated error parameters, which are shown in Fig. 38.

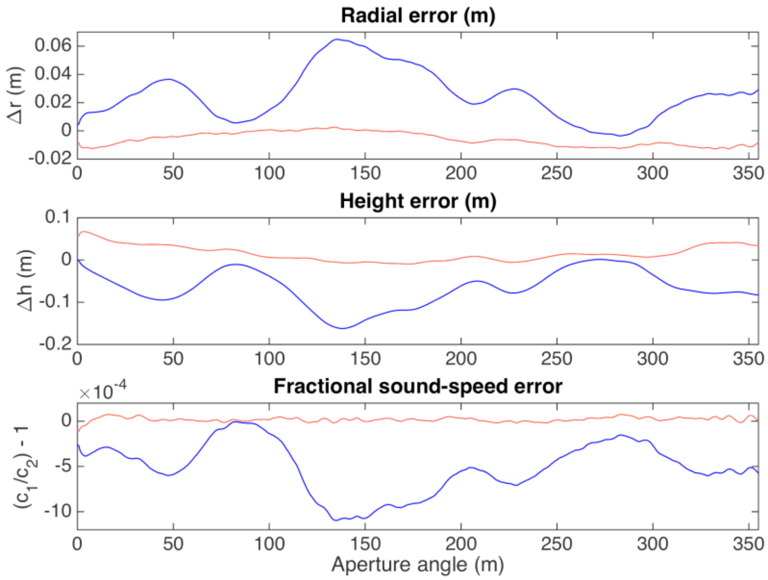

Figure 38. The estimated error parameters for the full FY15 model (red) and the flat-bottom model (blue).

Not only are the estimated parameters very different, but also the standard deviations of the flat-bottom estimates are much higher:

	Model w/bathymetry	Model, flat bottom
Δ*r*, standard dev.	0.47×10^{-2}	1.76×10^{-2}
Δ*h*, standard dev.	1.84×10^{-2}	4.22×10^{-2}
σ, standard dev.	0.24×10^{-4}	2.82×10^{-4}

Table 1. Standard deviations of the vectors of the estimated parameters for the models incorporating bathymetry verses assuming a flat bottom.

The fact that a model of one form gives both a lower residual and simultaneously produces a series of coefficients across all samples that are less complex is indicative of a better model. The contrast is especially apparent in the case of the standard deviation of the estimated sound-speed bias, which has been reduced by over an order of magnitude.

Finally, the inclusion of terrain into the coregistration process prevents coregistration and aperture localization errors from propagating throughout the array and biasing the locations of the aperture coordinates. This affects the measurements of the estimated grazing angle and the coherent processing of the data, which is illustrated in Fig. 39.

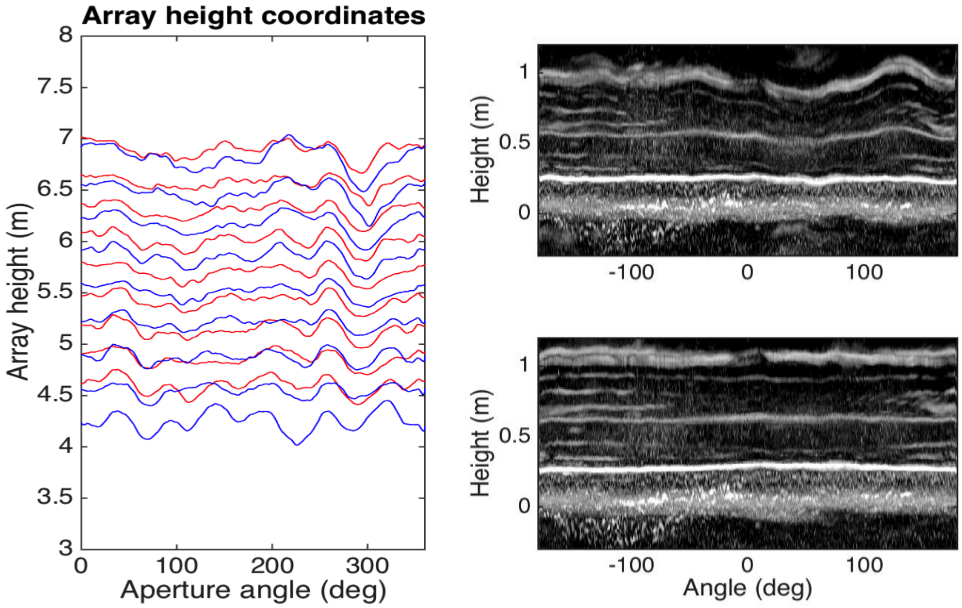

Figure 39. Left: array localization results using the flat-bottom model (blue) vs. incorporation of bathymetry (red). Right: the range-projected vertical beamforming results for the case in which a flat-bottom is assumed (top) vs. incorporation of bathymetry (bottom).

The final result has a big effect on the coherently synthesized estimate for the vertical scattering profile of a target, and correspondingly, the angle of incidence between each scan and the target.

One may reasonably ask why, given the size of the errors, beamforming is even possible in the flat-bottom case. The reason is that the flat-bottom assumption causes a systematic error that roughly affects all aperture coordinates at a given angle θ equally, i.e., the array is expanded or contracted. Rather than adding phase noise, this causes a contraction or expansion in the height dimension of the vertically beamformed image, as is clearly visible in the top right image of Fig. 39.

More details on the coregistration process, as well as the effect of bathymetry on the multipass aperture synthesis can be found in Section III of [11] as well as [27].

Phase 2.3: Sparse Beamforming in the Z Dimension and Autofocus

3D backprojection and Fourier imaging methods were previously discussed in this document for use with TIER and pond data. Modification was necessary prior to application to AUV captured data because the multipass array was both undersampled and irregularly sampled. Though both previously mentioned beamforming algorithms can accommodate irregular sampling schemes, the undersampling causes unacceptably high side-lobe problems for backprojection, and the variation in grazing angle limits the practicality of the Fourier equivalent if scenes of any appreciable size are going to be generated. As a result, a process based on sub-banding, and leveraging joint-sparsity between bands was formulated to give the flexibility of backprojection with greatly improved side-lobe response resulting from undersampling. Relative to standard SAR tomography algorithms, the method developed in this project excels at dealing both with wideband data (i.e., data in which the de-ramped data can still exhibit a large amount of range-cell migration from target signatures at the extrema of the supported height span), *and* for which a large span of grazing angles may exist in a single imaged 3D scene. (Extant SAR tomography algorithms can deal with both of these cases, e.g., [28] for large scenes that exhibit no range-cell migration following deramping, or [29] for wideband imaging with migration, but applied to only a very small region of a scan. The author is unaware, however, of a compressive sensing beamforming framework in SAR that deals with both situations simultaneously). The developed process is described in full detail in [11], but will be described in brief, here.

Assume signals from a set of U coregistered multipass scans (typically $U = 9*2 = 18$, where the factor of 2 comes from the presence of interferometric channels, from the phase 2 field experiments) have been projected to a common height plane, evenly sampled in the ground range dimension r_g. The heights of the corresponding multipass arrays are $h_{ar}^{(1,2,3,\ldots,U)}$, and the data is sub-banded into M bands. To beamform the irregularly sampled narrow-band signals a set of M sensing matrices corresponding to each sub-band and relating the phase of the received signals to scatterer height is assembled:

$$A^{(m)} = \begin{bmatrix} e^{-j2k_m\Psi\left(h_{ar}^{(1)},\, h_t^{(1)}, r_g\right)} & e^{-j2k_m\Psi\left(h_{ar}^{(1)},\, h_t^{(2)}, r_g\right)} & \cdots & e^{-j2k_m\Psi\left(h_{ar}^{(1)},\, h_t^{(V)}, r_g\right)} \\ e^{-j2k_m\Psi\left(h_{ar}^{(2)},\, h_t^{(1)}, r_g\right)} & e^{-j2k_m\Psi\left(h_{ar}^{(2)},\, h_t^{(2)}, r_g\right)} & & \\ \vdots & & \ddots & \\ e^{-j2k_m\Psi\left(h_{ar}^{(U)},\, h_t^{(1)}, r_g\right)} & & & e^{-j2k_m\Psi\left(h_{ar}^{(U)},\, h_t^{(V)}, r_g\right)} \end{bmatrix}. \tag{27}$$

In (27) $h_t^{(V)}$ where $V = 1,2,3,\ldots, V$ represents the altitudes of the complex scattering amplitudes in the solution vector, j is the imaginary unit, k_m denotes acoustic wavenumber $2\pi f_m/c$ and f_m is the center frequency of the m^{th} subband, $m = 1,2\ldots M$. $A^{(m)}$ is the m^{th} matrix of an M-length set of matrices each having size U x V. The function Ψ is the de-ramping delay resulting from ground-plane projection with the range biasing term, (i.e., the average delay to the array as a function of h_t and r_g), subtracted:

$$\Psi\left(h_{ar}^{(u)},\, h_t^{(v)}, r_g\right) = d_{dr}\left(h_{ar}^{(u)},\, h_t^{(v)}, r_g\right) - 2\left(\sqrt{{r_g}^2 + \left(\tilde{h}_{ar} - h_t^{(v)}\right)^2} - \sqrt{{r_g}^2 + \tilde{h}_{ar}^2}\right). \tag{28}$$

$$d_{dr}\left(h_{ar}^{(u)},\, h_t^{(v)}, r_g\right) = 2\sqrt{r_g^2 + \left(h_{ar}^{(u)} - h_t^{(v)}\right)^2} - 2\sqrt{r_g^2 + \left(h_{ar}^{(u)}\right)^2}\,, \tag{29}$$

In (28) $\tilde{h}_{ar}$ is the average height of the synthetic array at the currently evaluated azimuthal location θ along the multipass aperture. In both the experiments and simulations $r_g \gg \tilde{h}_{ar}$. The subtraction of the second term in (28) prevents the beamforming algorithm from performing an approximate range-bias correction that is discontinuous in frequency, which can result in side lobe artifacts in the range dimension. For a given range cell the m^{th} subband vertical complex scattering coefficients $\alpha^{(v,m)}$ can be related to the m^{th} column of subbanded, deramped data $S^{(u,m)}$ via:

$$A^{(m)} \begin{bmatrix} \alpha^{(1,m)} \\ \alpha^{(2,m)} \\ \vdots \\ \alpha^{(V,m)} \end{bmatrix} = \begin{bmatrix} S^{(1,m)} \\ S^{(2,m)} \\ \vdots \\ S^{(U,m)} \end{bmatrix}. \tag{30}$$

Compressive sensing literature presents a variety of methods to estimate the solution vector $\alpha^{(m,v=1,2\ldots V)}$ for the currently relevant case in which $V >> U$ and the solution vector is sparse. (For a more detailed look at the requirements for application of compressive sensing to synthetic aperture tomography problems see Zhu and Bamler [28]). In this paper an approach based on the regularized FOCUSS algorithm [30] is taken. More specifically, the joint sparse extension is exploited because of the assumed common sparsity structure that the M solution vectors $\alpha^{(m,v=1,2\ldots V)}$ will have regardless of the frequency subband. The regularized joint sparse M-FOCUSS algorithm, described in [31] calculates a series of solution vectors with common sparsity profile by iterating:

$$c_k^{(v)} = \left(\sum_{m=1}^{M}\left(\alpha_k^{(v,m)}\right)^2\right)^{1/2} , \tag{31}$$

$$W_{k+1} = diag\left(\left(c_k^{(1\ldots V)}\right)^{1-\frac{p}{2}}\right), \tag{32}$$

$$\tilde{A}_{k+1} = \tilde{A}_k W_{k+1} , \tag{33}$$

$$\alpha_k^{(1\ldots V,1\ldots M)} = W_{k+1}\tilde{A}_{k+1}^T\left(\tilde{A}_{k+1}\tilde{A}_{k+1}^T + \gamma I\right)^{-1} S^{(1\ldots U,1\ldots M)} , \tag{34}$$

where k is the current iteration, $\tilde{A}$ is a hypothetical sensing matrix that relates each measurement column to each solution column, I is the identity matrix, γ is a regularization parameter, (determined empirically in the present case), and $0 < p \leq 1$ is the chosen norm-like "diversity measure" for which the solution is minimized. For $k = 1$, W is initialized as the identity matrix I. Intuitively, at each iteration the algorithm determines a set of weights for the rows of the sensing matrix using the chosen diversity parameter p applied to the 2-norm $c_k^{(v)}$ of the rows of the previous iteration's $V \times M$ solution matrix. A new solution is calculated using the sensing matrix with the updated weights. Though M-FOCUSS was developed for the multiple measurement vector (MMV) problem in which a single sensing matrix $\tilde{A}$ relates the measurement vectors to the solution vectors, from (31-34) it can be seen that the weights are strictly a function of the solution vectors $\alpha_k^{(1\ldots V,1\ldots M)}$ and the assumption of a single sensing matrix is not necessary for the algorithm to operate as long as the joint sparsity assumption holds. In the present case we assume the sparsity structure is independent of frequency, however from (27) we have M sensing matrices relating the columns of the measurement matrix to the solution matrix. Therefore, in the present case (33) and (34) are calculated via a *for*-loop that solves $\alpha_{k+1}^{(1\ldots V,m)}$ for each $A_{k+1}^{(m)}$:

for m = 1:

$$A_{k+1}^{(m)} = A_k^{(m)} W_{k+1}$$

$$\alpha_{k+1}^{(1\ldots V,m)} = W_{k+1} {A_{k+1}^{(m)}}^T \left(A_{k+1}^{(m)} {A_{k+1}^{(m)}}^T + \gamma I\right)^{-1} S^{(1\ldots U,m)} \tag{35}$$

Following estimation of the vertical scattering profiles for each range cell of the subbanded dataset, a Fourier transform in the range dimension is computed for each subband and a full spectrum representation of the scattering response for the patch is attained by recombining the subbands:

$$\tilde{\alpha}(h_t,k) = \left[\mathcal{F}_r\left\{\alpha^{(1)}(h_t,r)\right\},\ \mathcal{F}_r\left\{\alpha^{(2)}(h_t,r)\right\},\ \dots,\ \mathcal{F}_r\left\{\alpha^{(M)}(h_t,r)\right\}\right]. \tag{36}$$

Range bias is corrected by reapplying as a height dependent linear phase the h_t dependent delays previously subtracted from Ψ. Incorporating this correction, the beamformed scattering profile can be recovered by performing an inverse Fourier transform in range:

$$\hat{\alpha}(h_t,r) = \mathcal{F}_k^{-1}\left\{\tilde{\alpha}(h_t,k)e^{jk\left(\sqrt{{r_g}^2+(\tilde{h}_{ar}-h_t)^2}-\sqrt{{r_g}^2+\tilde{h}_{ar}^2}\right)}\right\}. \tag{37}$$

The matrix $\hat{\alpha}(h_t,r)$ now represents the beamformed scattering profile, free of range bias. To demonstrate the algorithm it is applied to the simulated sediment and target distribution depicted in Fig. 40(A). A realistic scan pattern like the type used in the field experiments was used to simulate the data for the beamforming algorithm demonstration. Using a diversity factor of $p = 0.8$, $f_{SUB} \approx 5$ kHz, $\gamma = 0.01$, 50% overlap between subbands and a hardwired limit of 5 M-FOCUSS iterations the sparse image in Fig. 40(D) was obtained. For comparison purposes the result of applying one-dimensional Fourier analysis on a fully sampled, regular aperture is shown in Fig. 40(B), (note that this is impossible with the field data, because it requires almost three times as many vertical aperture points), and the result of generalized backprojection such as the type described for TIER data is shown in 40(C) (where the realistic sampling is again used).

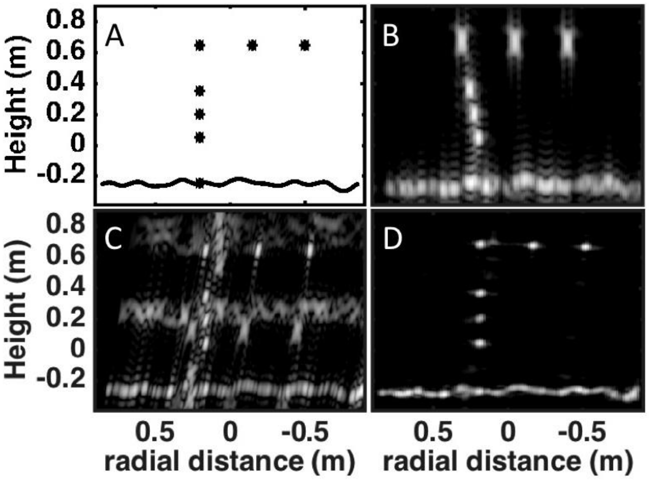

Figure 40. The simulated scattering distribution (A) and the results for different beamforming approaches. Plot (B) shows the result of one-dimensional Fourier analysis applied to the ideal, regularly sampled array, (C) shows the result of backprojection applied to the irregularly sampled experimental array shape, and (D) shows the wideband sparse result generated using the procedure described in this paper. The color scale is logarithmic and the dynamic range on all SAS images is 30 dB referenced to the brightest point.

In Fig. 40(B) the range bias in the one-dimensional Fourier beamforming example is highly visible and manifests as a strong slant in the leading edge of the barrel. A reduction in resolution resulting from range cell migration can also be seen. Generalized backprojection corrects range bias and maintains a higher resolution, as can be seen in Fig. 40(C), but it suffers from high grating lobe levels due to under-sampling. In contrast, the sparse processing result shown in Fig. 40(D) maintains both high resolution and low grating lobe levels.

This vertical beamforming process was used for all subsequent 3D beamforming processes in both phase 2 and phase 3, with the caveat that in phase 3, as will later be discussed, the order of the beamforming operation changed. In phase 2, the data was first beamformed in the vertical dimension, and Fourier beamforming was applied at each height bin to resolve the image spatially in the horizontal dimensions. This was critical for the purpose of applying 3D *autofocus* routines. Autofocus routines were necessary in phase 2, because the whole navigation solution, being tied to the reference scan, would experience collective drift in the vertical dimension equivalent to the height error of the reference scan. This could result in severe blurring in the *z*-dimension, when forming the final three-dimensional image.

To counter this problem the data was beamformed in the Z-dimension and scene shifts in the vertical dimension were tracked by correlating adjacent, vertically beamformed slices of the data around the aperture and integrating the vertical shifts. The integrated shifts were converted to a three-dimensional phase correction. Intuitively, the solution would only require a two-dimensional correction, e.g., a phase correction that is dependent on azimuth (or θ, the angular position around the circular aperture), and the height correction. Phase corrections applied in this manner, however, don't account for the change in total range to the scene center caused by a shift in height without a corresponding shift in ground-range toward the center. A 3D phase correction function is used to account for the height shift while preserving the same slant range to the center of the scene. More information on the autofocus algorithm, called *vertical mapdrift*, can be found in [30]. The following flowchart graphically depicts the process of the algorithm:

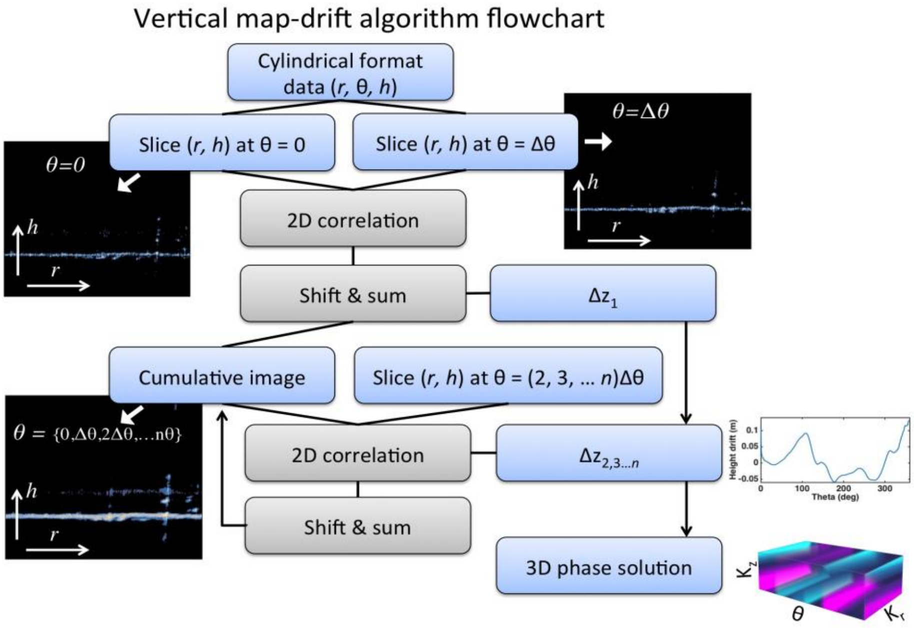

Fig. 41. A flowchart of the vertical mapdrift algorithm.

The following figure shows a zoomed in patch of sediment, imaged in three dimensions, with and without the application of 3D mapdrift. The coloring of the data indicates the dominant backscattering angle. The corrected image shows much greater focus in the vertical dimension, though the resolution in the horizontal dimensions is approximately the same.

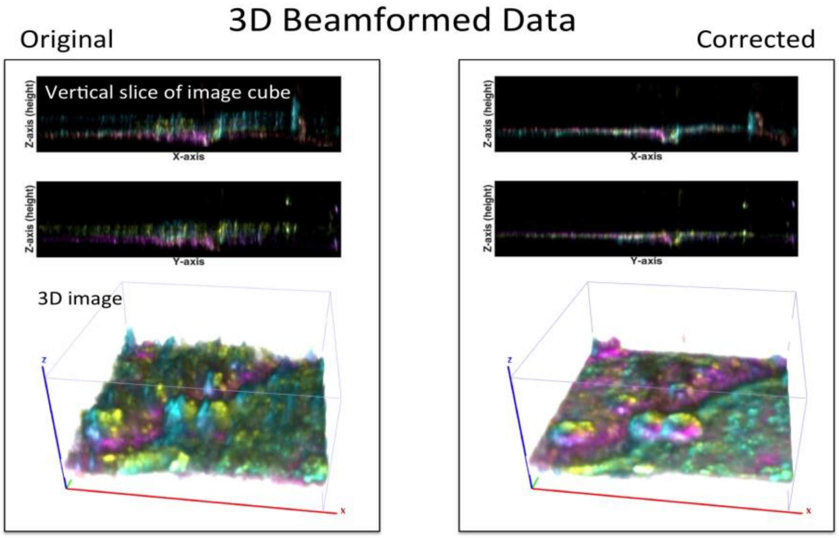

Figure 42. Slices through the full 3D image data cube (top and middle) and a rendered & zoomed 3D patch of the full image (bottom) for the case in which no vertical map-drift was applied (left) versus the case in which it was applied (right). The images at right show superior focus in the vertical dimension. Note that back-scattering angle is mapped to color in the above examples. The objects in the 3D zoomed images are roughly sand-dollar sized.

The signal processing in phase 3, which emphasized imaging large scenes, took a very different approach toward beamforming which was not amenable to this form of autofocus. The techniques used for autofocusing the dataproducts in phase 3 will be described in later portions of this materials and methods section.

Phase 3.0 Spiral Scan Processing: Overview

The signal processing prior to phase three had focused primarily on demonstrating the feasibility of multipass aperture processing. The demonstrations were extremely successful (see discussion in results section), so in the last year of the project (FY16) the emphasis of the project shifted to testing modifications both of the multipass data acquisition method and the signal processing, to improve all of the following: scan completion time, signal processing efficiency and robustness, target wavenumber coverage, and beamforming image size.

The method tested with the intention of solving most of these problems was to use a single, continuous corkscrew shaped scan pattern, rather than combining a set of discrete circles. There were several advantages to this approach, including a major hidden one: in the previous approach in which discrete circles were used, the AUV had to perform almost three circles to stabilize at a particular altitude and scan radius. Furthermore, halfway through most of the scans, the AUV would surface and get a new GPS lock. Error in the GPS localization would often cause a discontinuity in the final multipass aperture, as can be seen in the example shown in the figure below:

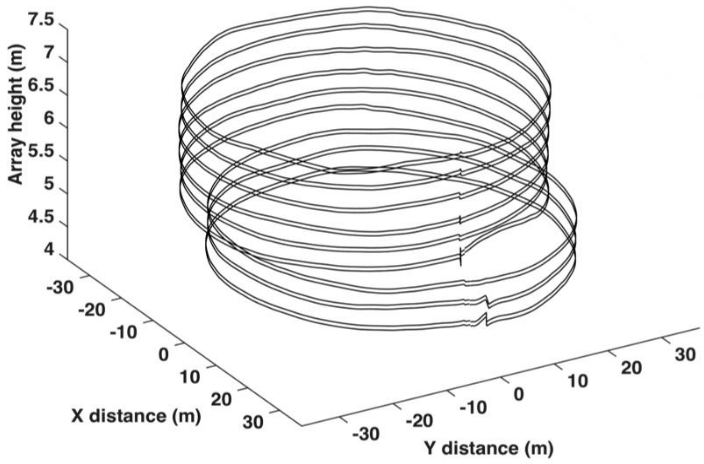

Figure 43. Example of a synthesized multipass array. The vertical samples are irregular as a result of the different vertical spacings between the multipass scans and the interferometric receiver arrays. Additional irregularity occurs because of currents and, for the bottom three scans, a GPS localization offset acquired during a resurfacing operation.

The bottom three pairs of scans (each pair composed of the upper and lower receive arrays of the SAS) are clearly offset from the top six, and the GPS re-localization partway through the scan was hindering rather than aiding localization.

In contrast, the spiral scan pattern requires no loitering time at a particular altitude or radius. No GPS fix is acquired part way through the scan, and the end result is that the same number of scans and equivalent sampling in the wavenumber spectrum can be completed over 3X faster. Where the old 9-pass scans would require a full hour to complete, in the same amount of time 28 loops were being scanned with the spiral methodology. Fig. 44 is an example of one of the new, 28-loop spiral scans conducted in this case around a sunken airplane:

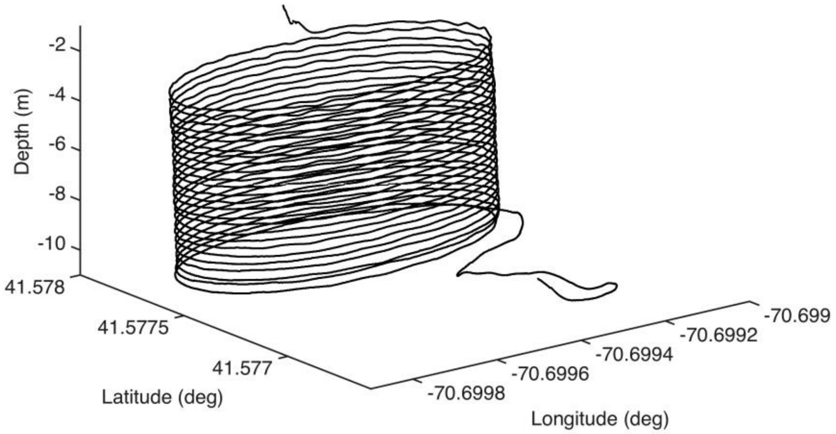

Figure 44. The latitude, longitude, and depth coordinates of a spiral scan from the phase-3, FY16 field experiments.

This greatly improved the wavenumber coverage of scanned targets, enabling more features of the 3D wavenumber response (particularly grazing angle target strength dependencies) to be observed. The usage of a scan with very different properties to those used in the FY15 field trials was taken as an opportunity to re-write the navigation, beamforming, and autofocus routines to better exploit multipass data. The following subsections will discuss the specifics of the spiral scan signal processing methods.

Phase 3.1 Spiral Scan Processing: Navigation Refinement

Another major advantage of spiral scans, from a navigation standpoint, is the continuous nature of the multipass aperture. In the previous coregistration approach, each scan was processed like a normal circular aperture, e.g., standard INS and micronavigation approaches were applied to get an initial estimate of the vehicle coordinates. This was followed by multilateration, which refined the coordinates to focus the scene. To combine scans, low resolution images were formed for each scan, and were translationally and rotationally aligned with the arbitrarily determined “reference” scan, and this coarse alignment was followed by a ground-plane projection and fine alignment operations for each scan.

In stark contrast to this block post-processing approach, the new method starts with the first loop of the spiral and incrementally builds up the aperture by adding additional, short segments onto the end of the current set. The coordinates of these small segments are refined to coherently align with previous scans. By incrementally adding segments the full aperture is gradually built up until the coordinates of the full aperture have been determined.

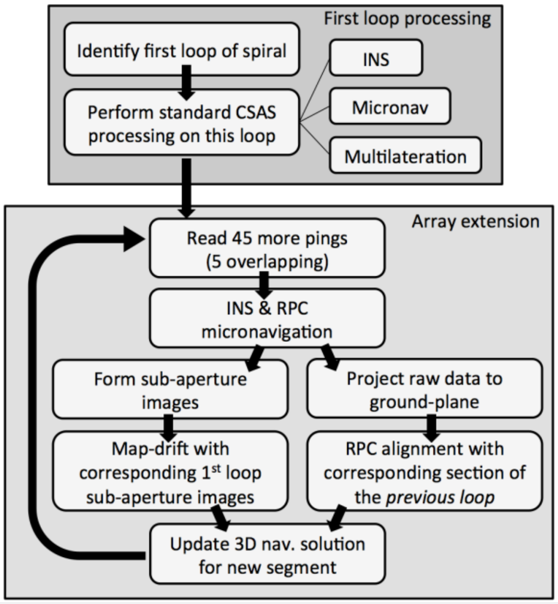

Figure 45. Flowchart of the navigation refinement process for spiral scans. Only the first loop of the scan is processed specifically as a “CSAS” scan. The rest of the array is incrementally built up from that first loop.

This process 1) prevents each loop of the spiral from having to be independently autofocused and rotationally aligned with a reference, and 2) is both faster and less memory intensive. The actual process is illustrated via a flow chart in Fig.45.

As can be seen from the figure, only the first loop is processed as a CSAS scan. All subsequent loops are added by incrementally appending small segments (e.g., 30 pings worth) onto the end of the current navigation solution. To refine the coordinates of the segments, standard INS-augmented redundant phase center micronavigation is performed. The data is then backprojected to the ground plane but not beamformed (i.e., it is stretched to be sampled evenly in the ground range vs. evenly in the slant range). Two alignment operations are then performed and a navigation solution is solved that simultaneously resolves the observed shifts from both alignment operations.

The first alignment operation is performed via a standard, coherent, patchwise correlation between the ground-plane projected raw data from the new segment and the overlapping data from the previous loop. When solving for the coordinates of the second loop, this means the data from the first loop, however for later portions of the aperture, this may mean that the overlapping portion of the 5th loop corresponding to the new segment in the 6th is used.

The azimuth and range shifts of estimated by these patch correlations could be used to directly refine the micronavigation estimates, but they have low stability, meaning that integration drift can propagate quickly through the array as loops are added. To add stability, a second set of alignments are exploited. These alignments come from alignment of the intensity images generated via sub-apertures of the new segment and the corresponding overlapping region of the very first loop. Coherent decorrelation occurs pretty fast over the array, but the authors have found that even at fairly large grazing angle changes, corresponding sub-aperture images correlate well enough to get basic alignment fixes that preserve solution stability over the course of the array. Sub aperture images are generated by taking sub-regions of the segment and performing projection-slice imaging over those regions. The intensity images formed by these patches are correlated against the corresponding patches from the first loop and azimuthal and range shifts are estimated.

The final navigation solution for the new segment, (excluding autofocus refinements that are found at a later stage in the processing), is found by solving for coordinate adjustments that simultaneously fit, in a least squares sense, the observed shifts both from the incoherent sub-aperture comparisons with the first loop and the coherent patch-wise comparison with the previous loop. This solution has both long-term stability due to the comparison with the original scan, and high accuracy due to the comparison with the data from the previous scan.
Each correlation results in a correlation coefficient, which can be viewed as a quality metric. In the current Matlab implementation, as array extension progresses, the sub-aperture shifts in the azimuth and range dimensions are continuously updated, along with the image correlation coefficients. These figures are useful for both diagnosing the alignment results and observing both temporal and grazing angle effects on image decorrelation in synthetic aperture imagery, an area of active study in SAS research circles. An example of these plots are shown below, for a spiral scan part way through the alignment process.

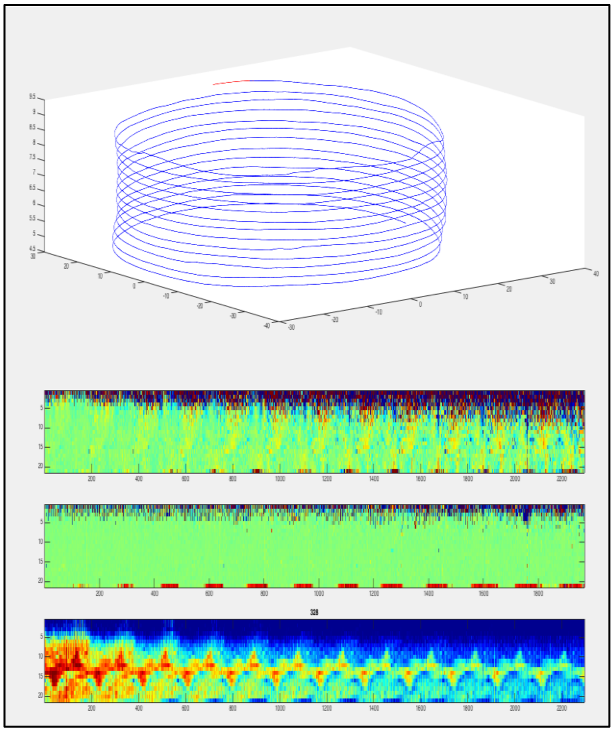

Figure 46. A snapshot of the alignment diagnosis window, actively updated in Matlab during the spiral scan alignment process.

In the previous figure, the top plot shows the scan coordinates. The aligned portion of the scan is shown in blue and the current segment that has just been added to the array is shown in red. The plot below, (the top of the three matrix plots beneath the scan coordinates), shows the residual azimuthal shifts between the first loop and current segment, following alignment. The middle matrix plot shows the range shifts, and the bottom matrix plot shows the patch correlation values. Each plot uses the Matlab "jet" color scale, where blue is low, red is high, and green is in the middle. For the alignment plots, green indicates no shift and is good. For the correlation plot, blue indicates low coherence. Areas of ranging from light blue to red tend to have high enough correlation to produce usable shift estimates for stability enforcement.

Phase 3.2 Spiral Scan Processing: Beamforming

The previous approach for beamforming was very memory intensive. The data for each independent circle was read into memory. The data for each scan was interpolated to ground plane coordinates, and then azimuthally low-pass filtered and decimated to make the memory requirements manageable for subsequent beamforming. Not only was the memory budget for this type of operation un-manageable for a scan with three times the number of loops, but the azimuthal filtering and decimation limited the beamwidth of the system, reducing the effective radius over which a meaningful multi-aspect image could be generated. As a result, all the 3D imaging results for phase 2 multipass imaging are shown for relatively small patches (typically 3 x 3 x 2 or 6 x 6 x 2 meter image cubes). This size limitation is problematic for a number of reasons. First, the target localization relative to the sonar platform may be off by more than this amount. If the scene is always imaged at the center of the scan then the target may be completely missed. Secondly, the area coverage rate for the 3D imaging operation becomes very poor. A whole target field may need to be evaluated, vs. a single target. Some objects of interest may even be at larger scales than the entire target scene. Lastly, the horizontal plane Fourier imaging utilized by the phase 2 beamforming approach tends to break down for larger radii circular scans anyway, due to the narrow-beam motion compensation assumptions implicit in the ground-plane stretching process.

The spiral SAS beamformer resolved these issues by changing the beamformer type for horizontal plane imaging to a more general beamforming solution called fast-polar backprojection (FPB [32], closely related to the popular fast-factorized backprojection (FFBP) algorithm described in many places in the literature [33], [34]), which, in the new approach is applied prior to beamforming in the vertical dimension. This new approach resolves several of the previously mentioned drawbacks to the phase 2 method. FPB is a generalized beamformer, meaning that it doesn't make the simplistic narrow beam motion compensation assumptions that the previously used Fourier algorithm does. As a result, wider radii images can be imaged with very fine resolution. Additionally, it achieves an orders-of-magnitude speed relative to ordinary generalized backprojection by beamforming discrete sub-apertures first into polar coordinates,

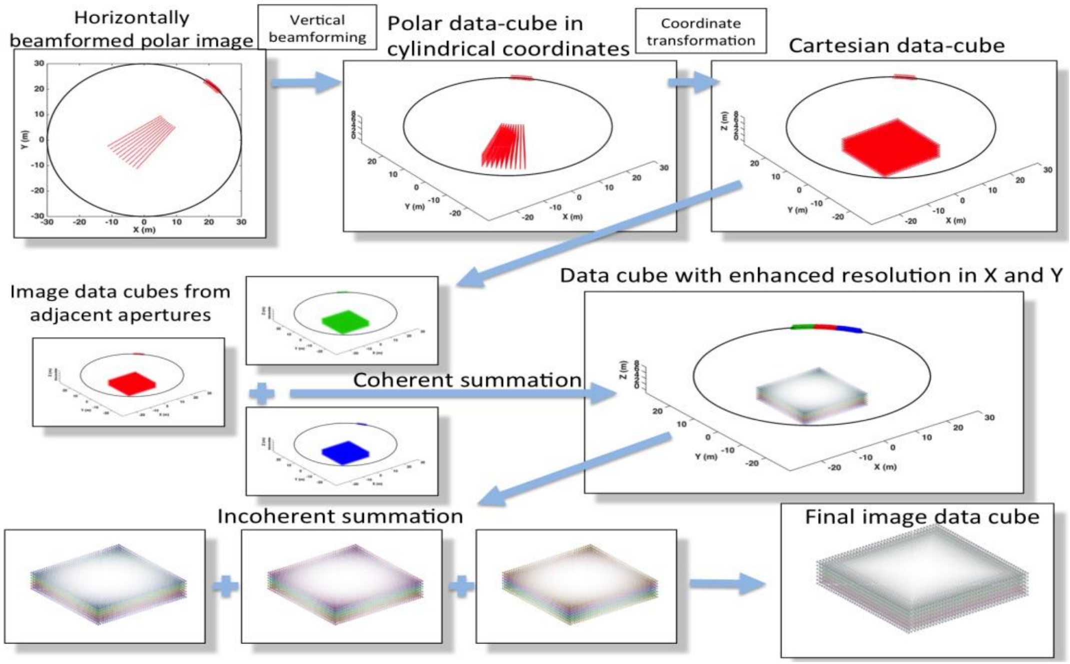

Figure 47. A flowchart of the spiral scan beamforming process. The red green and blue point clouds represent different 5 degree chunks of aperture.

before combining in Cartesian coordinates. For discrete sub-apertures, polar coordinates tend to be a much more efficient representation of fully sampled SAS image data than Cartesian coordinates, causing a reduction in computational complexity. From a memory management standpoint, this is perfect for imaging large datasets, because it means that only an azimuthally limited portion of the full multipass scan need be stored in memory at any given time to perform the sub-aperture imaging process.

Like the navigation process, the FBP algorithm, optimized in this case for circular aperture processing, incrementally builds up an image. A flowchart of the 3D spiral beamforming algorithm can be found in Fig. 47. The beamformer operates by dividing the circular multipass aperture into 5 degree chunks. These chunks are individually backprojected to form an image in the ground-plane, in polar coordinates, like the top left block of the flow chart. This is done for the corresponding 5 degree chunk of each loop in the aperture, so that a stack of 28 polar coordinate sub-aperture images are generated. This stack is then beamformed in the vertical dimension, resulting in a 3D image in cylindrical coordinates. This complex (i.e., phase preserving) cylindrical coordinate image is then coordinate transformed to the Cartesian coordinates of the final image, which has been sampled densely enough to prevent spatial aliasing for beamwidths as wide as 15 degrees for the sonar high frequency band, and for the entire circular aperture at the low band. The beamforming and coordinate transformation operations are done for the next two 5-degree aperture chunks. The chunks are then combined to form a coherent image incorporating 15 degrees of aperture. For the low frequency beamforming process, this coherent summation process continues around the aperture. At high frequencies, every time a 15 degree coherent chunk is made, it is incoherently combined with the results of previous apertures to form a despeckled 3D image datacube. Large scenes would require on the order of approximately $1*10^4$ x $1*10^4$ x 250 = $2.5*10^{10}$ pixels. At single precision (32 bits per complex pixel) this datacube would require approximately 100 GB of memory, which is unfeasible using the current data processing system. As a result, the data was heavily decimated to produce a lower resolution but despeckled incoherent 3D high frequency image cube. As mentioned previously, the low frequency data was processed coherently through the whole aperture, to make 3D acoustic wavenumber response measurements of targets.

Phase 3.3 Spiral Scan Processing: Autofocus

Because data is horizontally beamformed prior to imaging, and also because the full aperture raw data is never stored in memory at any given time, the vertical mapdrift algorithm cannot be used to correct bulk array altitude or tilt errors in the current spiral SAS imaging framework. The final autofocusing step in this process resolves these residual errors prior to imaging in the vertical dimension by leveraging in series two autofocusing techniques: “Phase-Center Double Localization” (PCDL), the multipass navigation error reduction technique of Telbaldini et al., [13], modified slightly to optimize the process for SAS data, and generalized sharpness maximization by gradient descent, which has been explored in many other places [35], [36], [37], and applied to SAR tomography in [38].

Conceptually, the autofocus approach developed by Telbaldini is very similar to both redundant phase center navigation and also the multilateration described by [12]: both use time-of-flight error to a set of control points (phase is a proxy for time in [13]) to form an overdetermined set of equations from which sensor position errors are solved. The idea is illustrated in Fig. 48:

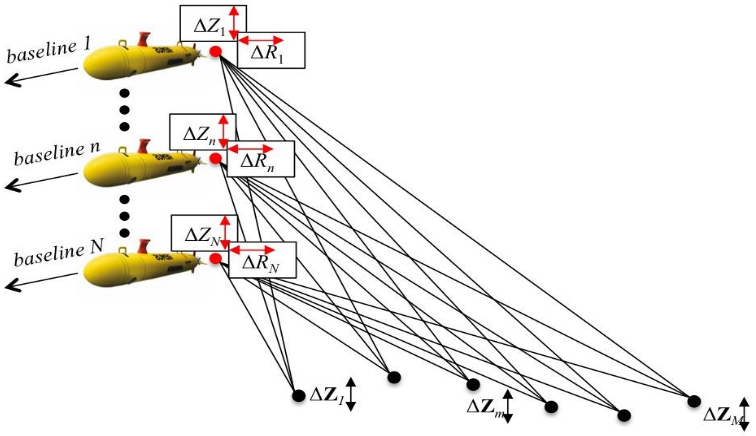

Figure 48. Illustration of the phase-center double localization (PCDL) principle of Telbaldini et al. [13], with sonar systems. For *N* sensor positions and *M* control point locations, an over-determined system of equations relating *MN* measurements to 2*N* + *M* position measurements (2 coordinate directions for the sensors and 1 coordinate direction for the position measurements) can be solved to within a rotation and translation.

The major conceptual difference (implementation, purpose, coordinate directions for solutions, etc. diverge significantly) is that in both: 1) Telbaldini et al. [13] and 2) Kennedy and Marston; [25] it is recognized that the system of equations formed between the delay measurements and variables in the problem can support solving for both the sensor position errors *and* position errors in the control points. If *N* vertical baselines are present in the multipass aperture, and *M* control points are available, then an over-determined system is formed if $NM > pN + qM$, where p is the number of sensor position variables, (2 in [13], 3 in [25]) and q is the number of control point position variables (1 in both [13] and [25]). Note that the system being overdetermined does not necessarily imply, even in the ideal case of high signal SNR, that the solution is well posed, which can be affected by factors like the spacing of control points.

Implementation of the PCDL algorithm is very similar to the version described in [13] with a couple exceptions. In [13] the interferogram phases formed between baselines are used as a proxy for time delay measurements. The inherent delay ambiguities caused by the modulo-2π phase wrapping problem precludes effective usage of fast linear methods for solving the linearized system of equations relating time-delays to position corrections. In contrast, the delay measurements used in the current project are found via local patch correlations between sets of baselines, and the utilized sonar system has broad enough bandwidth that the exact wrapping can frequently be resolved. As a result, a linear system can be assembled solved just like eq. (14) with helpful weighting and regularization terms included.

Secondly, in [13], a “master” scan and a master point are used to resolve the rotation and translation ambiguities. In the present paper, the presence of interferometric staves with high roll accuracy resolves the rotational problem. No reference scan is used, however; the average shift of the array in the height dimensional is penalized via regularization, and the total translation in the range dimension is limited by assuming the control-point locations have no error in that dimension.

As in [13], the delay estimates are weighted, in the present case by observation of the correlation coefficient amplitude between observation pairs. In [13], weighting is biased to favor adjacent pairs to accommodate potential issues with volumetric targets, however in all the tested environments for the SAS case, the sediment interface from which scattering measurements were made were sufficiently localized in altitude to prevent this specific weighting from being a necessity.

Other issues were frequently present, however. The correlation coefficient tends to bias high, resulting in outliers not always being sufficiently de-weighted. Additionally, the fractional bandwidth of the system allows the modulo-2π error to be resolved most of the time but not always, causing additional outliers. To reduce the effect of these, the weighting was refined using an iterative reweighted least squares (IRLS) approach similar to the one described in [11], namely, the residual was computed after the first solution was found, and the weights updated based on the size of the residual. Tebaldini et al. also note that solutions for adjacent slices of data in azimuth can be computed efficiently by initializing them using the solution from the previous scan. In the current approach, however, the set of corrections along the azimuthal direction are simultaneously solved for in a 5-degree aperture chunk and smoothness (i.e., second-order-difference) regularization is applied to the azimuthal variation of the sensor and control point altitude position correction terms to give a similar result. It was also occasionally observed, perhaps due to the low grazing angles of the sonar system, that wildly and unrealistically varying estimates for control point height could result from the inversion of the system of equations. To avoid this issue, a small degree of regularization was applied both to the height of the control points and the local variation of the height of the control points.

It is also worth noting that the computational time necessary to perform the previous computations is negligible compared to both the horizontal and vertical beamforming operations for the data. For each 5-degree data cube, with range x azimuth x height dimensions typically on the order of 1000’s x 100’s x 10’s, the whole iterative reweighting and solution estimation process typically takes on the order of 30 seconds using the current processing system.
The final autofocusing step is included to account for the fact that the previously described autofocus method may be somewhat under-parameterized, meaning that certain physical processes may produce phase errors that cannot be modeled or corrected using the previous approach. Examples would include errors caused by the relative velocities of the platform, sound-speed profile variation in both the horizontal and vertical planes, and local sound-speed inhomogeneities. An example of a sound-speed inhomogeneity causing noticeable effect on both the phase and amplitude of sections of a multipass scan are shown below, in which gravity waves travelling across a sharp temperature gradient are visible:

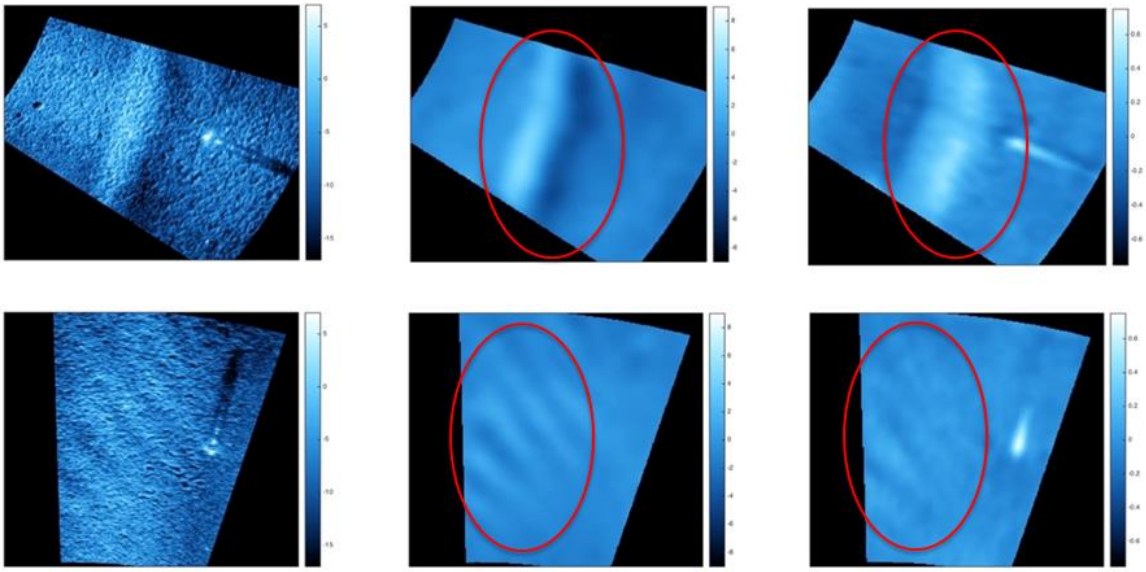

Sub-aperture image (dB scale)

Detected intensity changes (dB scale)

Interferogram (rad)

Figure 49. Multipass barrel scene, viewed from different angles and at different times. The sub-aperture images are shown on the left. The middle column shows the detected intensity changes, and the right hand side shows the interferogram between interferometric staves. The hypothesized gravity waves are circled in red.

The gravity waves in the previous figure can be seen to propagate in a particular direction and with a particular speed when viewed as a sub-aperture movie. Furthermore, the effect is not confined to the intensity but also manifests in the phase, which implies that focus could be affected. Some form of non-parametric solution is more useful for phase correction in these cases. In the present case, this correction is provided by a sharpness maximization approach [35], [37]. Sharpness maximization (or entropy minimization) algorithms are non-parametric and can efficiently find phase solutions for maximizing focus, especially in cases for which focused and raw data form a Fourier pair. Though the present system is wideband, this is still approximately true in the vicinity of the sediment interface, and in conjunction with a non-uniform discrete Fourier Transform (NUDFT) in the height dimension a reasonable solution can be found relatively rapidly. In the present implementation the phase solution is found via gradient descent (as in [35]) and is constrained to vary slowly in the azimuthal and range dimensions.

For the combined autofocusing procedure, the second part of the algorithm (sharpness maximization) results in a phase correction that is directly applied to the data. The first part of the algorithm, PCDL, results in a coordinate correction that is used to re-define the locations of the array elements prior to vertical beamforming. It is not used to directly modify the matrix fed into the vertical beamforming algorithm. Fig. 50 is an example of a maximum-intensity projection through a beamformed datacube with and without the application of the previous autofocusing operation:

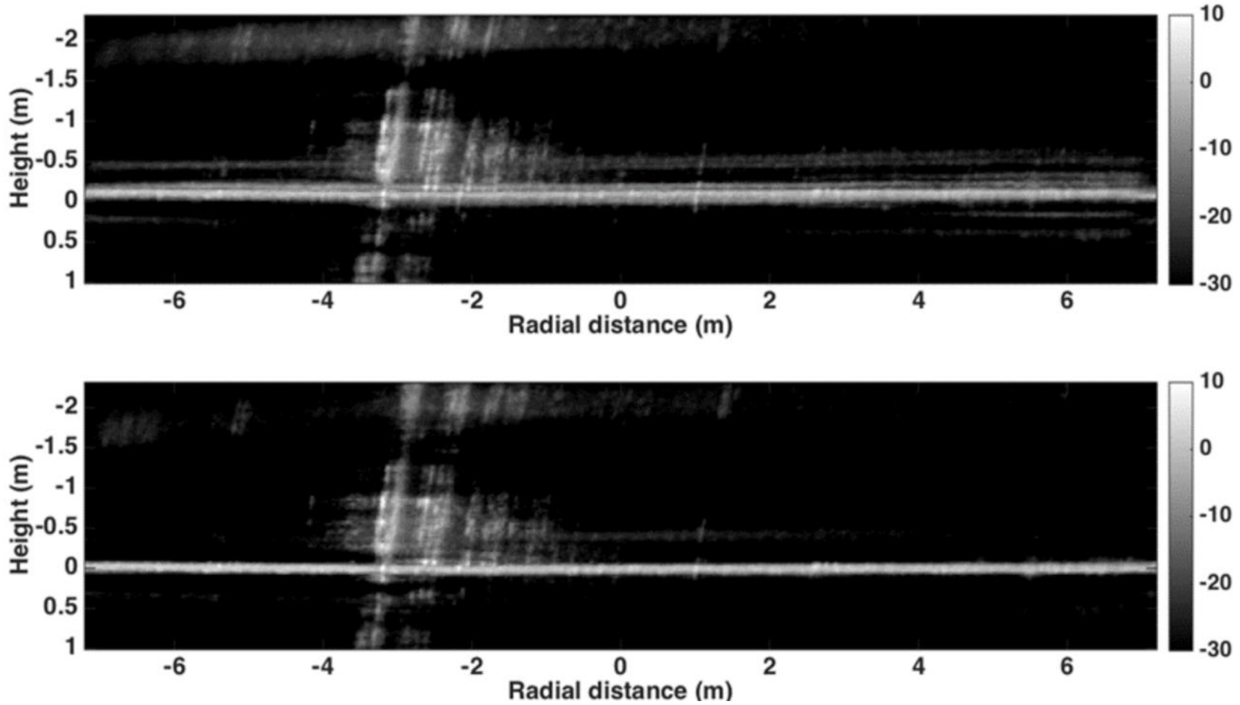

Figure 50. Example of the autofocus algorithm applied to a 5 degree sub-aperture snippet of the high frequency steel barrel spiral scan set. The top image shows beamforming without the autofocus operation, the bottom image shows beamforming with the autofocus operation. Note the improved focusing of the sediment interface.

RESULTS AND DISCUSSION

The previous portion of this document discussed the different methods investigated in this project for generating data products such as 3D images and wavenumber spectra, and sub-sampling spectra to generate single-pass target realizations. It divided the research into two threads: one thread dealing with controlled experiments in a test-pond and comparisons with idealized finite-element simulations, and a second thread dealing with processing data captured from at-sea field experiments conducted using an AUV in an uncontrolled environment. This second thread was divided into three phases: phase 1, roughly corresponding to FY14, dealt with practical approaches to co-registration between multiple scans. Phase 2, roughly corresponding to FY15, refined the phase 1 coregistration to account for the observed realities of multipass apertures (e.g., the significance of bathymetry to the coregistration result), and developed better approach for handling wide-band beamforming in the sparse and irregularly sampled vertical aperture case. The last phase of the project, corresponding to FY16, dealt with the testing of a more efficient technique for constructing multipass apertures, and the new beamforming and autofocusing techniques developed to accommodate this new approach.

In this portion of the document, the experimental results obtained from both threads and all three phases will be shown and discussed. It will begin with a discussion of the results obtained from the controlled experiments, and progress to the results of the field experiments acquired in Phase

2 and Phase 3. (Phase 1 multipass processing results aren't discussed because multipass apertures suitable for 3D beamforming were not yet available).

NSWC PCD Controlled Test Pond Experiments and Modeling Results

The test-pond experiments were designed to provide a controlled platform to test specific aspects of the project, namely, clutter reduction routines for isolating the structural response of targets from clutter and improve the SNR, test the nearfield-to-farfield conversion algorithm, and provide a platform for testing 3D beamforming of broadband data. The results for each of these goals will be shown in this section.

Nearfield to Farfield Conversion Algorithm Results

The nearfield-to-farfield algorithm was a great success, and with the polynomial based approximation for the phase argument in [15], very efficient. The small scene size relative to the scan radius, the relatively low frequency, and the lack of strong sediment texture make the effects of the correction difficult to see in the test pond data. When applied to the high frequency data, however, the effects become immediately obvious, and an example is shown in Fig. 51.

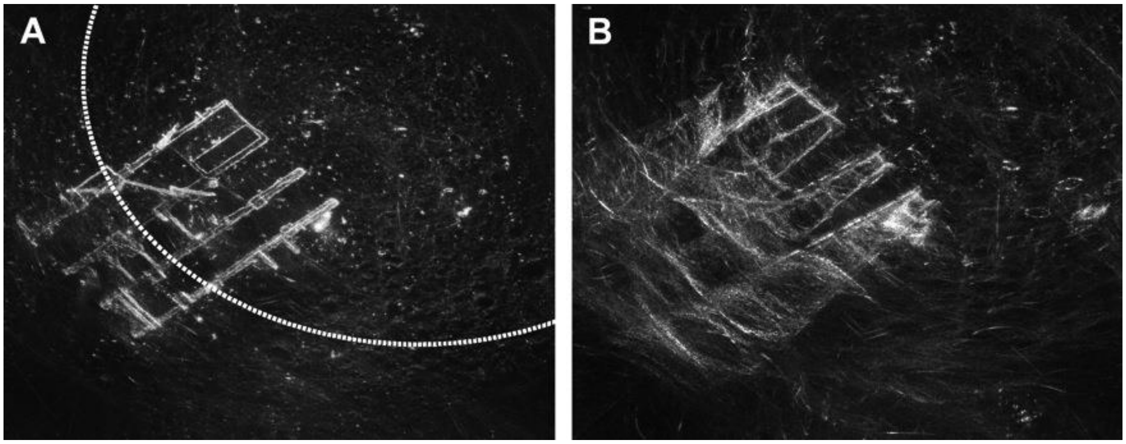

Figure 51. CSAS image *with* (A) and *without* (B) application of the NF-FF correction. The dotted white line shows the 5-meter radius mark and the center of the CSAS scan is close to the upper right corner.

Fig. 51. shows that this nearfield correction is highly effective for circular aperture systems. Its usage is now standard for all instances of rapid, small-patch beamforming at both high and low frequencies, and was used throughout the remainder of the project for every instance of Fourier based CSAS imaging, ranging from evaluation of multilateration control points to focusing the individual height-planes of vertically beamformed datacubes in Phase 2.

Noise Reduction and the KM-Filter Results

Fig. 52 shows the acoustic color spectrum for an example pond scan of a proud, solid 2-1 aluminum cylinder before and after the wavenumber-moment (*"KM-filter"*) filter was applied to isolate the signal data:

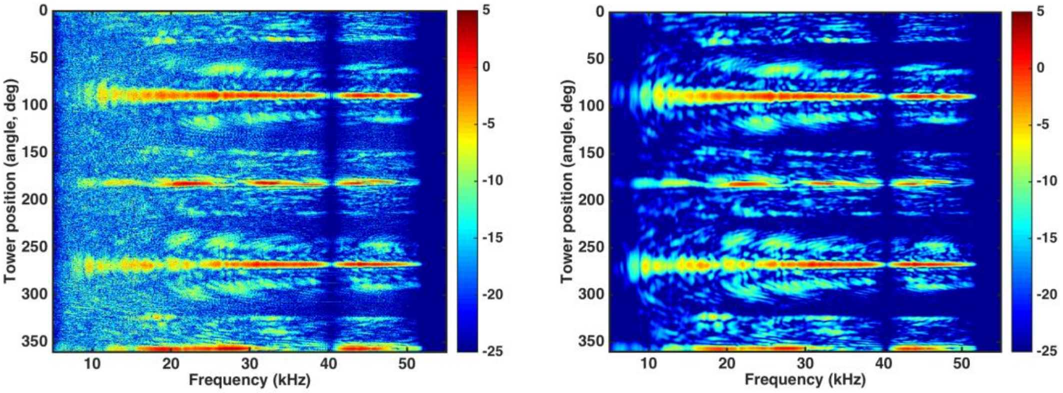

Figure 52. Acoustic color of a solid 2-1 aluminum cylinder before (L) and after (R) KM filtering to remove multipath and clutter noise. A large increase in signal-to-noise ratio has been gained. The color scale gives the approximate absolute target strength in dB re 1m and the dynamic range is 30 dB.

Two instances of the filter were applied: the first was applied to remove the signal from the scattering rod. The second filter was applied to remove multipath and sediment scattering from the signal from the target. The signal level is improved in some cases by over 10dB and certain features, especially low level elastic features below ~15 kHz, benefit greatly from this process. For all instances of acoustic color extraction in test pond data, this procedure was utilized.

3D Beamforming Results

The image presented in Fig. 53 was generated from simulated TIER data [39] using the projection-slice combination method described in the technical approach. Two TIER simulations were done: a free-field simulation and a proud simulation. By taking the difference between these simulations, the direct-path and multipath contributions can be isolated. These contributions were individually colored, with red representing the direct-path contributions, and blue representing the multipath contributions.

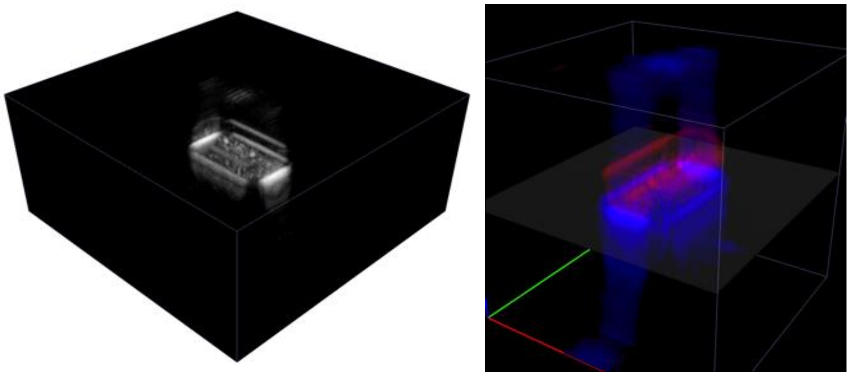

Figure 53. The 3D beamformed image (L), and the same image with the direct path (red) and interface scattering (blue) contributions color-coded.

The target in the simulation is a solid 60 cm x 30 cm aluminum cylinder, proud on a flat, sandy interface. The simulation contains scans conducted at constant slant-range distances of 10 meters and aperture heights spanning 1 to 9.75 meters in increments of 0.25 meters. Of significant note is that the curved surface of the cylinder is not imaged well and most of the backscattered energy is focused to a line along the broad-side face of the receiver. This is particularly noticeable from an end on aspect view as shown in Fig. 54.

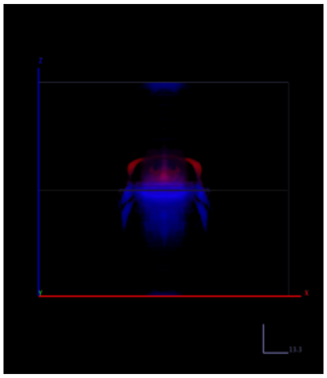

Figure 54. End-on perspective of the cylinder showing the specular glint (red), and the multi-path contributions out to second-order, for interface interactions. The specular glint does not strongly trace out the surface of the cylinder.

The primary broadside glint does not appear distributed around the surface. Additionally, the single and double – interface interaction paths image *below* the sediment, as coincides with experimental work accomplished previously at WSU [41]. The end-on corner reflector, strongly visible as the blue vertical streak in Fig. 53 generates a very dominant reflection that is vertically smeared, with the peak appearing almost directly at the surface of the interface.

Sparse imaging was used to enhance the resolution of volumetric images generated using multi-pass circular scans around a targets in the test pond. Fig. 55 shows a single slice of rail data in the vertical dimension, showing beamforming results using a sparse beamformer vs. standard backprojection:

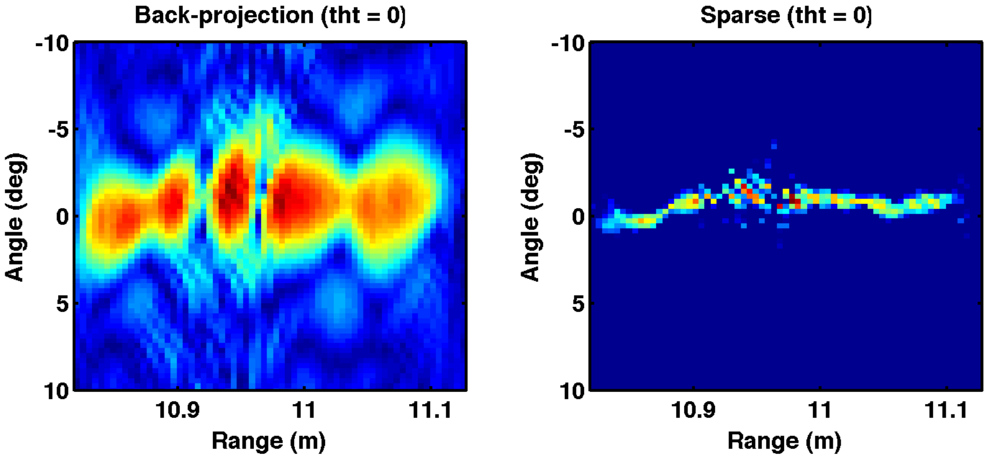

Figure 55. A single slice of data from the test pond, vertically beamformed using standard backprojection, on the left, and sparse beamforming on the right.

The algorithm used to generate the plots in Figs. 55-57 was essentially an early version of the more refined approach described previously in the methods section of this paper. The image provided in Figs. 56 and 57 shows a voxel-based representation of the beam-formed image for a proud, solid 2-1 aluminum cylinder generated using both back-projection and sparse imaging:

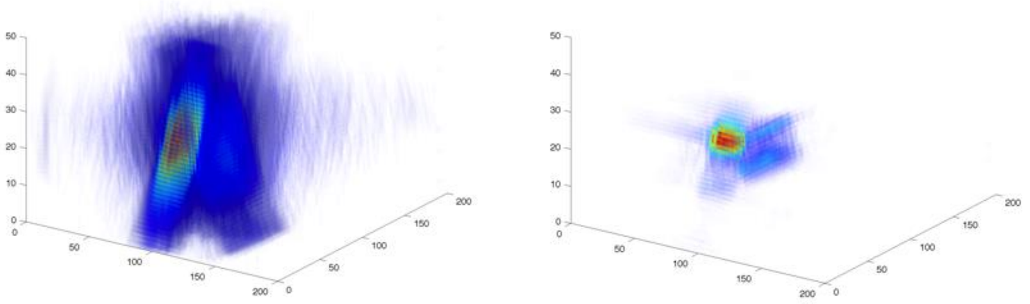

Figure 56. Backprojected 3D image (L) of 2-1 solid aluminum cylinder and the sparse version (R) demonstrating a very large resolution enhancement. Only 90 degrees of aperture are used in this image to make edge and end-on features maximally visible.

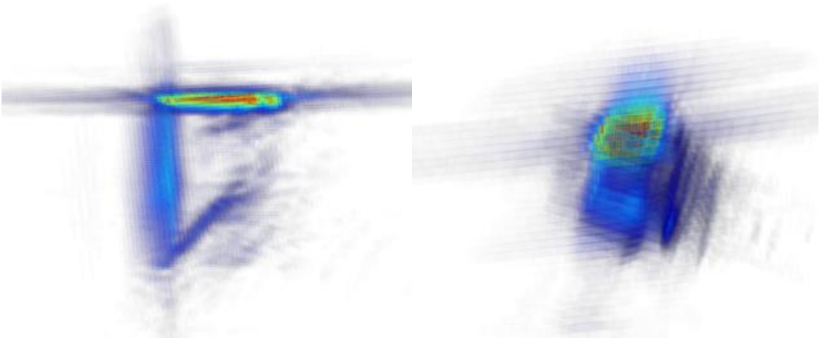

Figure 57. Top (L) and three-quarter (R) views of the solid aluminum cylinder.

In the previous examples only 90 degrees of the aperture were beamformed, to increase the clarity of the elastic features of the image (note the face-crossing feature). Similar to the simulation, the broadside glint images to a linear glint along the face of the target.

An end-on view of the target shows that the specular, single and double sediment interaction features also appear in the experimental data as shown in the following figures:

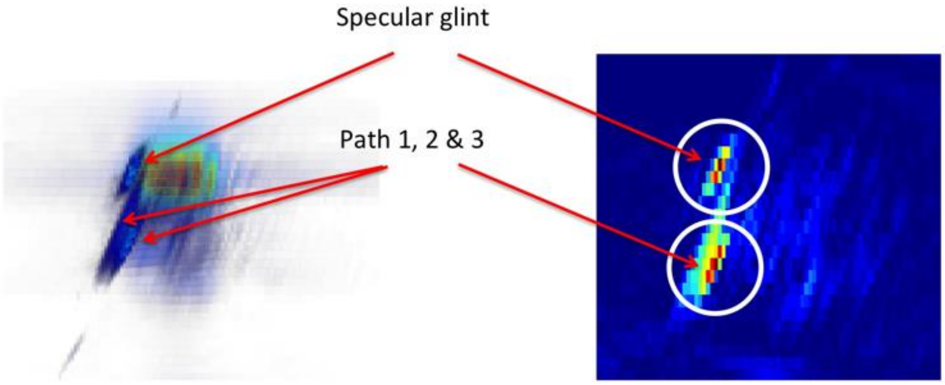

Figure 58. End-on view of 3D image and a slice through the data-cube showing the specular glint, and using the multipath convention in [41], the path 1 & 2 (target – sediment, sediment – target reciprocal paths), and the path 3 (sediment – target – sediment) multipaths.

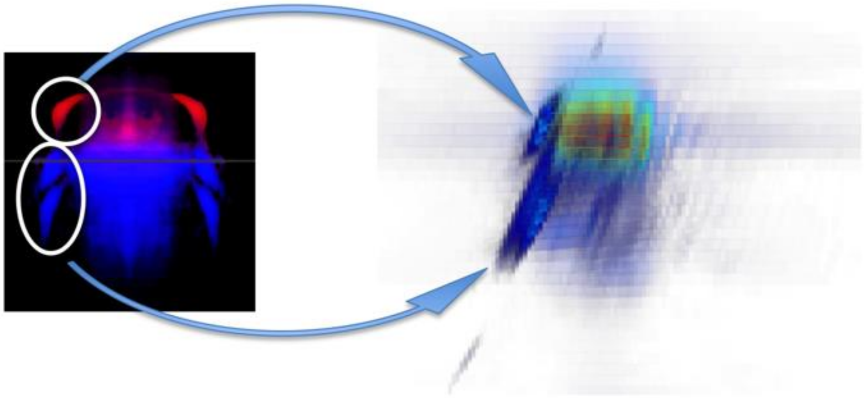

Figure 59. Comparison of the simulated 3D target with the data from the test pond, both end-on. Note the clear preservation of the multipath and specular signals in the experimental data. The simulated data is working with ~70 degrees of aperture, vs. the experimental which is only using ~ 3 degrees. Sparse processing is enhancing the features to be distinctly visible despite the very narrow range of apertures.

The examples from the previous figures are excellent confirmation that the realistic levels of noise and phase errors in the pond-collected data are not causing the sparse processing algorithm to distort key response features describing the target. Additional 3D images of UXO are depicted in Fig. 60.

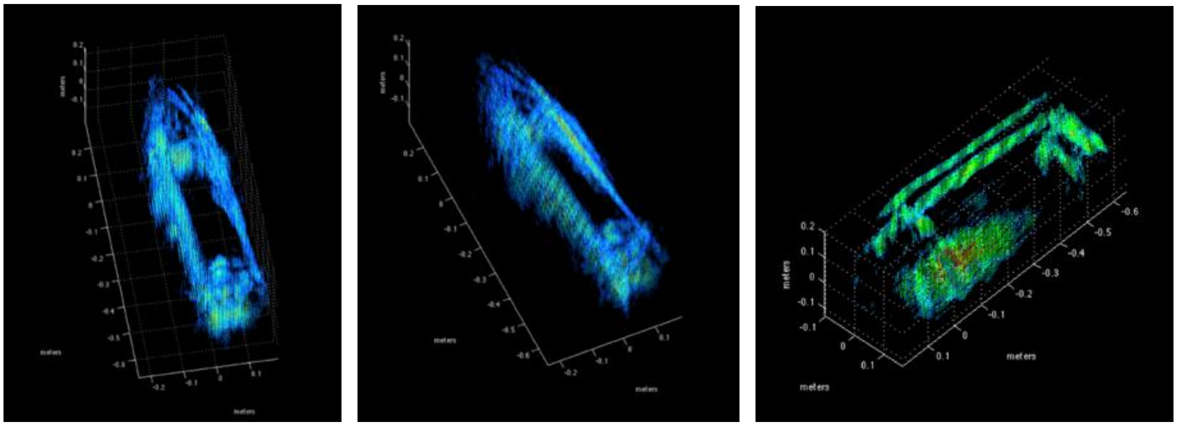

Figure 60. Views of the 3D reconstruction of a 155mm howitzer shell, showing internal features and multi-path signals. M-FOCUSS with a P-norm of 0.6 was used for vertical resolution enhancement. Usage of joint-sparsity improved the SNR and coherent reconstruction.

Further examples of test-pond processing can be found, with more detail given of the results, in the FY14 interim report of project MR-2439.

AUV Field Experiment for Multipass Aperture Synthesis (FY14 – FY15)

The results of the first two AUV experiments performed in uncontrolled ocean environments will be described here, with focus being on image domain data products. Image domain products are important because they are both intuitive to interpret and most difficult to make. They are very sensitive to parameters such as phase and beamforming errors, and in general the quality of an image domain data product decays more rapidly than the magnitude of the 3D wavenumber spectrum (directly related to acoustic color), if some aspect of beamforming or navigation refinement failed. In short, if a high quality image is successfully generated, a 3D high quality wavenumber spectrum can also be generated, but the image is easier to evaluate for defects.

Field Test #1 (December 2014)

Table 2 shows a list of all the targets and the scan patterns that were completed for each target in the first set of field experiments, completed in December of 2014 using the REMUS AUV, dual-band SAS system, and scan patterns described previously in the materials and methods section. The table below shows the target and the number and type of scans acquired for it in this first experiment.

Target	Radial scans	Altitude scans
Proud Howitzer Shell	9	9
Oblique Howitzer Shell	9	9
Steel Barrel	6	0
2-1 cylinder	8	0

Table 2. A list of the scanned targets and the number of scans completed for the radial and altitude types. The AUV malfunctioned after 6 scans around the steel barrel, and no altitude scans exist for either the steel barrel or the proud, solid 2-1 aluminum cylinder.

As mentioned previously, the environment in this set of scans was flat and sandy, and from a navigation standpoint was not incredibly challenging. Therefore, even though the environment was “uncontrolled,” it provided a gentle and ideal environment for initially testing AUV based multipass beamforming algorithms.

Fig. 61 is a visualization of each of the targets in table 2 for the different scan configurations. The images in the left hand column are “alpha-rendered” images (images in which pixels have opacities and ray-tracing is used to generate an image) generated in VAA3D [42], [43] and viewed from a three-quarter perspective. The three columns on the right hand side are intensity projections through the *x*, *y*, and *z* dimensions, and generated in Matlab. The coloration of the data corresponds to the dominant backscattering angle.

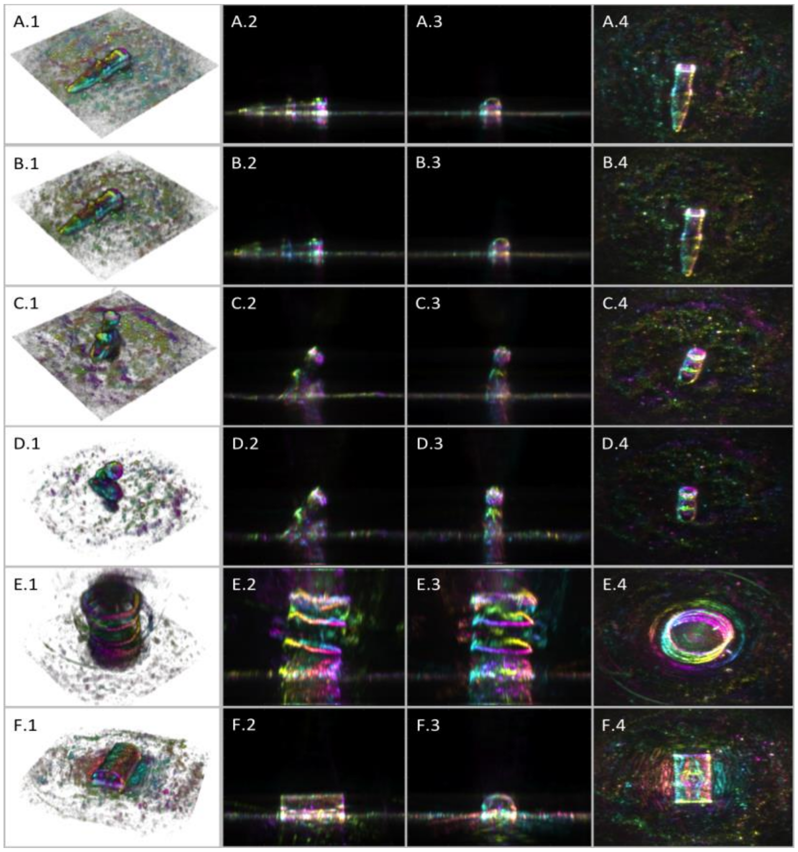

Figure 61. Rendered images and projections of the volumetric data corresponding to the scans described in Table 1. Column 1) shows the linear scale three-quarter view volumetric images rendered using alpha blending, column 2) shows projections of the volumetric images onto the *XZ* plane, column 3) shows projections onto the *YZ* plane, and column 4) shows projections onto the *XY* plane. From top to bottom, the rows show: a) proud howitzer shell, altitude scan, b) proud howitzer shell, radial scan, c) oblique howitzer shell, altitude scan, d) oblique howitzer shell, radial scan, e) proud vertical steel barrel, radial scan, and f) proud 2-1 solid aluminum cylinder, radial scan. Fig.61 can be found in [11] with additional information.

Note that the barrel still images extremely well despite the fact that only two-thirds of the scans around the target were successfully completed. Furthermore, it was confirmed that for small image patches the two scanning approaches (vertical and radial) give almost identical results (e.g., compare row A with row B, and row C with row D). The target orientation relative to the sediment (e.g., proud, partially buried, oblique, etc.) can be precisely determined from the 3D images in Fig. 61, indicating that the high-frequency 3D image data-products can be used as ground-truth position data for low-frequency model - vs. - data comparisons, which could be useful for evaluating target simulation methods.

Additionally, rows *C* and *D* illustrate an interesting and powerful property of broad-band 3D imaging, namely, that multipaths collapse to the same horizontal plane locations. This is illustrated more specifically in Figs. 62 and 63:

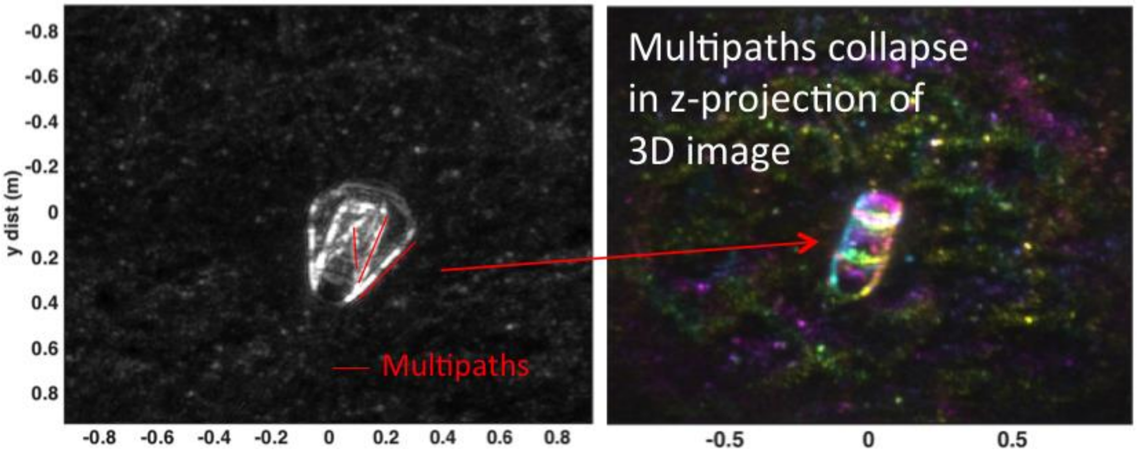

Figure 62. A standard CSAS image of an obliquely tilted UXO (L) and the Z-projection of the 3D image generated using multipass data synthesis (R).

In the previous figure, the image on the left, an ordinary CSAS scan, cannot resolve the correct spatial location of the multipaths because a single scan cannot resolve their locations in the z-dimension and hence are mapped to an erroneous location resulting from the static height-plane assumption of the CSAS image. In contrast, the multipass scan is able to appropriately map the location of the multipath phenomena in *x*, *y*, and *z* dimensions, and the resulting projection through the datacube in the z-dimension, (which ordinary SAS images are meant to be an approximation of,) collapses the features on top of each other correctly. The distribution of the multipath features can be seen more distinctly, along with their respective spectral manifestations, in the composite image shown in the next figure:

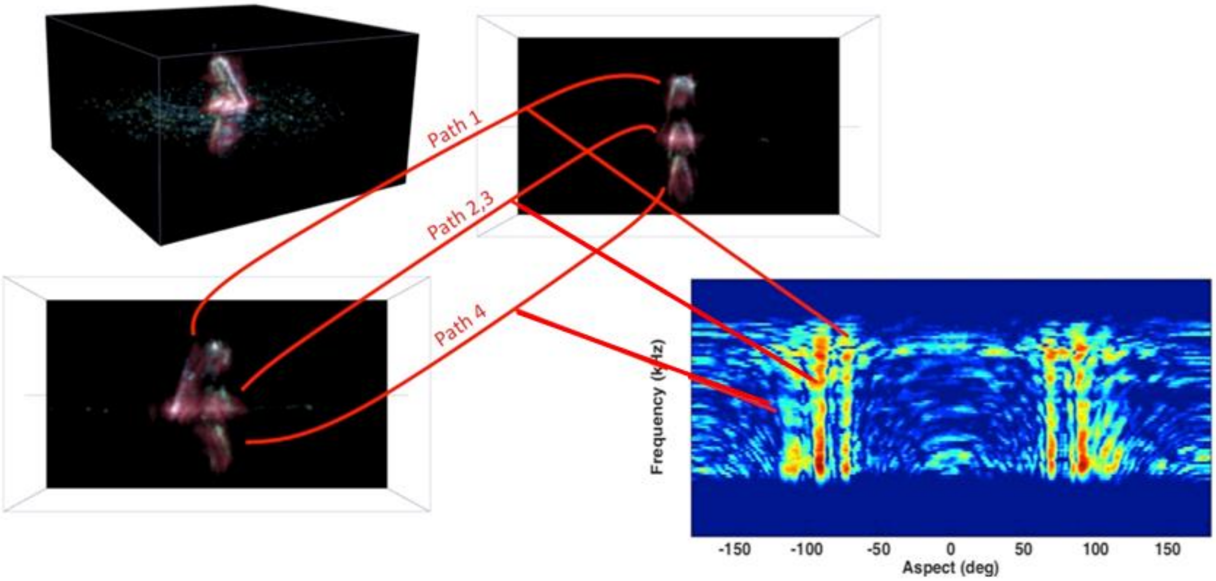

Figure 63. A HF/LF composite, HF is in blue, LF is in red, showing direct and multi-path reflections in an image, and their corresponding manifestations in the acoustic color domain. The effect, which looks like a splitting of the broadside signal, is discussed more in [44].

As noted in [44], multipath features of an oblique (i.e., tilted with respect to an interface) cylindrical object have different dominant aspect angles associated with each feature, and converge to the same location as the tilt moves to zero.

The actual resolution of the examples in Fig. 61 are remarkably high given the range to the targets (~30 meters in the examples). The following shows an enlargement of the alpha-rendered image of the proud howitzer shell alongside a photograph of the same target for reference.

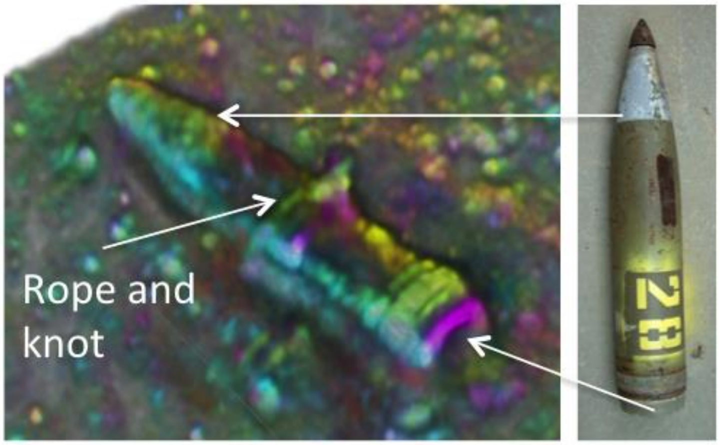

Figure 64. Photograph of a 155 mm Howitzer shell (right) and the 3D volumetric acoustic image (left), showing the material boundaries at the front of the shell, the components of the end-cap, and a nylon rope tied around the center for diver manipulation (not in photo).

Despite the center frequency being relatively high (low hundreds of kilohertz), the material boundaries at the front of the shell are visible. Other details, such as the rope tied around the shell to aid in diver manipulation, and the rings of the end-cap are also clearly visible. The same target was scanned using both the radial and vertical scan patterns. In Fig. 61, the image pairs from rows A and B, and C and D, show the results for imaging the same target using the two types of scan patterns shown in Fig. 27: fixed radius scans varying in altitude, and fixed altitude scans varying in radius. Both of these scan patterns provide insonification over a range of grazing angles and sample the 3D spectrum over a sufficient volume to produce images focused in all three dimensions.

A major difference between the two, however, is the vertically stacked set of circles can be described as a circular aggregation of vertical line scans, and the radial set of concentric scans can be described as a circular aggregation of horizontal spokes radiating from the center of the circular scan. This is an important difference, because in the first case, the array formed by the samples at some location around the array θ is *vertically axisymmetric*. By virtue of this symmetry, the phase signature of any individual scatterer insonified by the array is uncoupled from the horizontal polar angle of the scatterer to the array at any given location around the array θ.

In contrast, the radial scan pattern is not axisymmetric in *z* at any location θ around the array, and thus the phase signature of a scatterer is directly coupled to the horizontal polar angle to the array sample at θ. Practically, this manifests as an erroneous height estimate for off-axis scatterers, and this is visualized in the figure below, which shows data beamformed in the Z dimension for a set of radial (i.e., constant height with varying radius) scans:

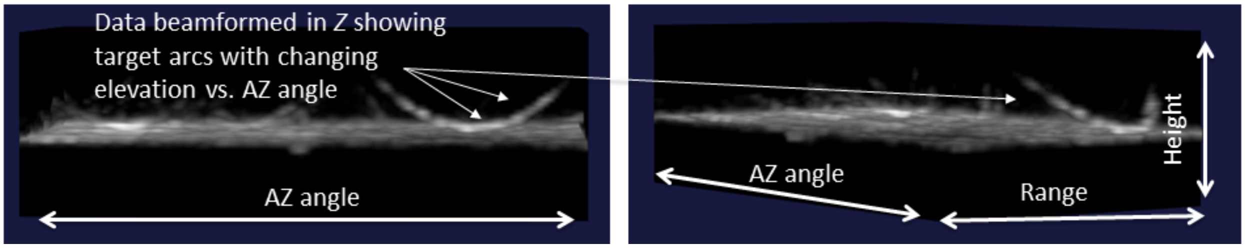

Figure 65: A gray scale, alpha-blended image of multipass data for a radial scan, beamformed in Z, showing the coupling of height to polar angle of a target relative to the current azimuthal angle.

As can be seen from the previous scan, target arcs are visible, and depending on the azimuthal location the target arcs will have a varying altitude. This will obviously cause defocusing in the *z* dimension following beamforming in the horizontal plane, and thus, for large scenes spanning a wide range of sonar beam angles, radial scans are not as readily compatible with Fourier beamforming because the coordinate directions of the scan can’t be decoupled. The systematic nature of the height / azimuth coupling implies that a simple spectral correction may exist to compensate for the radial scan geometry, however that was never computed in this project, and the radial scan pattern was abandoned in favor for the cylindrical (i.e., vertically stacked with constant radius) scan pattern because of the separability of the vertical and horizontal beamforming operations.

The next figure demonstrates the generation of multiple realizations of targets along different sampling axes by wavenumber sub-sampling, as described in *3D Beamforming* section of the materials and methods portion of this document:

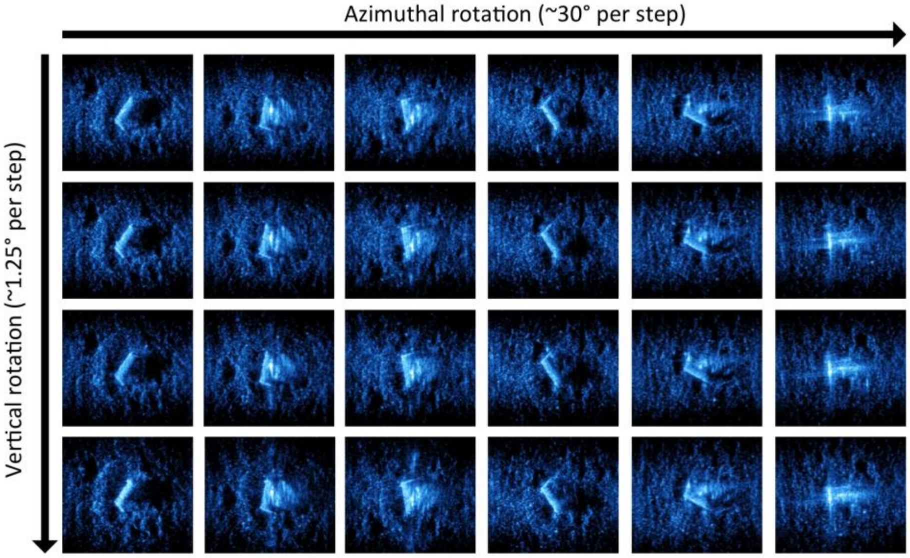

Figure 66. Illustration of high-frequency image snippets produced using the multipass 2-1 aluminum cylinder data.

In the previous figure, the target orientation is changed to span both grazing and aspect angle variables over ~140 degrees in aspect and ~6 degrees in grazing angle. The span of angles in the vertical dimension is short, limiting the observable change of behavior in that dimension, however phase 3 (FY16) experiments, which will be discussed later in this document, extended this range almost by a factor of ~3.

Field Test #2 (July 2015)

The coregistration algorithms applied to the data from the first field test made no use whatsoever of interferometric height-maps for mitigating solution biasing or vertical map-drift to reduce smearing in the z-dimension. The original algorithm worked well primarily due to the fact that the seafloor was very flat and ocean conditions were benign, making motion compensation relatively simple. Still, even in some of the first examples (e.g., the barrel), there were indications of problems, like the rings of the barrel not being perfectly circular or having strange and presumably non-physical bends in them.

These effects became much more pronounced in the 2015 field experiments. In this set of experiments, inclement weather and wave action caused larger trajectory perturbations, and the sediment bathymetry significantly biased the coregistration solutions. When the algorithms from the first field test were applied to data from the second field test, the following results were obtained for a howitzer shell, a plastic barrel, and a lobster pot:

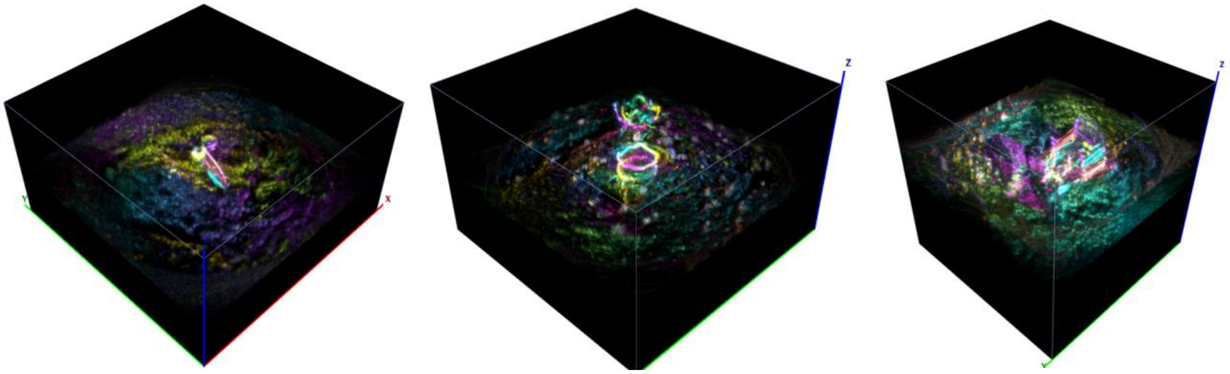

Figure 67. Three examples of imaging from the second field test, in which solution biasing due to bathymetric variation is unaccounted for during the coregistration process. The figure on the left, a howitzer shell, is difficult to interpret but features like edges are easily visible. In the center image, rings of a barrel appear fairly undistorted at the sediment but the distortion becomes significant near the top of the barrel. The image on the right, of a lobster pot, is almost impossible to interpret.

These biasing errors motivated the development of a solution [27] discussed in the methods portion for compensating for bathymetry during the coregistration process. This compensation resulted in significant improvements to image quality and distortion reduction. The barrel, beamformed using the bathymetry biased and unbiased solutions, is shown in the figure below:

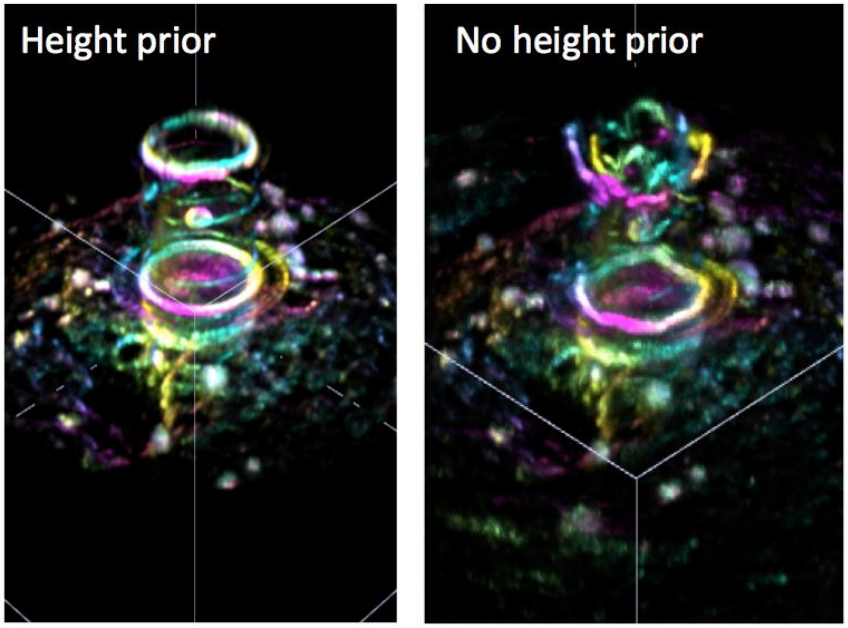

Figure 68. 3D images of a plastic barrel with an internally suspended shot put, with (L) and without (R) performing co-registration with a height-prior used to de-bias the solution.

The uninterpretable image on the right of Fig. 67 also resolves well with a height prior and application of vertical mapdrift (*Materials and Methods*, *Phase 2.3 section*), and becomes one of the primary beamforming examples used in later portions of this document.

Scans of many targets were attempted in the second field test, however due to combined AUV navigation and target localization inaccuracies, and potentially target migration due to currents, many of these were missed. Table 3 shows a table of targets including which scans were processed for 3D imaging, and which were not due to target localization issues.

Target	Sediment	Localization	Imaged?
Crab pot	Sand ripples	Missed	No
Proud howitz. shell	Coral and rock	Partial beam	Yes
Proud howitz. shell	Sand ripples	Missed	No
Plastic Barrel	Coral and rock	Full beam	Yes
Plastic Barrel	Sand ripples	Missed	No
Steel Barrel	Sand ripples	Missed	No
Car tire	Rock	Full beam	Yes
Lobster trap	Rock	Full beam	Yes
Table lamp	Sand ripples	Full beam	No
Unknown	Rock	Missed	Yes

Table 3: Target list for experiment 2, showing target type, sediment, localization, and whether or not the dataset was imaged. A localization attempt is considered “missed” if the target of interest is outside of the high-frequency beam for over 50% of the scan. A full beam localization means that the target is insonified over the entire aperture, and partial beam means that it is in the beam for most of the scan but not the full scan.

Results for the imaged targets will be discussed in the ensuing portion of this section.

Proud Howitzer Shell on Rock and Coral

Fig. 69 shows an example 3D image and 3D wavenumber spectrum for the scene containing a howitzer shell (marked by white arrow) and a large coral outcropping (marked by red arrow).

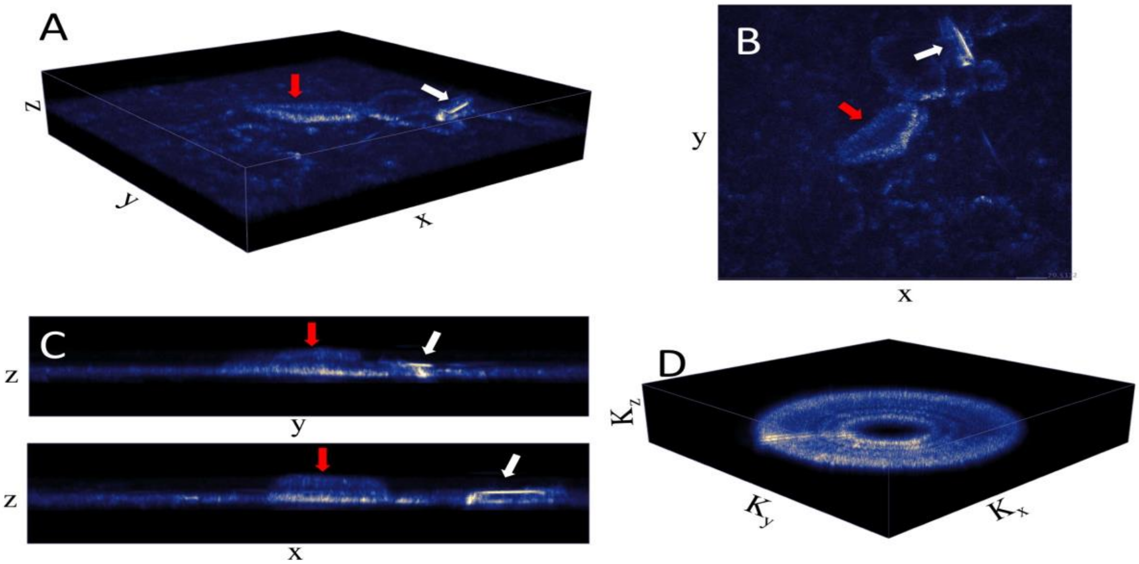

Figure 69. The coherently processed low frequency 3D dataproduct from a multipass set, in this case containing a coral outcropping (red arrow) and a proud howitzer shell (white arrow). Image (A) shows the 3D image from a three-quarter view perspective, while (B) and (C) project the image onto the [X, Y], [Y, Z] and [X, Z] planes. Image (D) is a three-quarter view of the three-dimensional wavenumber spectrum of the image.

The 3D volumetric images in Fig. 69 are the magnitudes of the coherent data-products. High frequency incoherent sub-aperture averaging procedures and aspect-to-color mapping are applied to Fig. 70 for the rock and howitzer shell. In comparison to the high-frequency data-product for the same scene, the low-frequency image has relatively low vertical resolution, as can be seen by comparison with the high frequency version shown below.

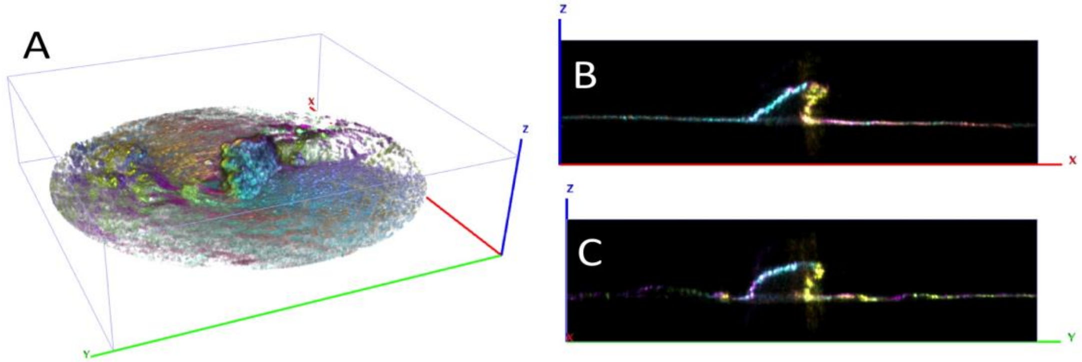

Figure 70. A high frequency three-quarter view (A) rendering of the rock and howitzer shell shown in Fig. 69, along with two slices (B and C) through the rock. Note that overhangs are well imaged using the 3D tomography approach.

Fig. 71 shows zoomed views of the low-frequency image of the target, captured from the 3D dataset shown in Fig. 69.

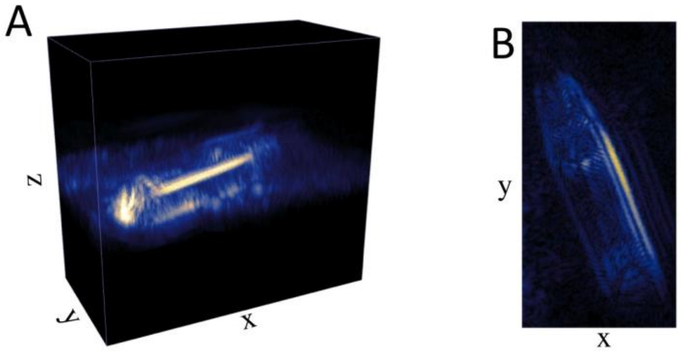

Figure 71. 3D snippet of the howitzer shell, showing just the shell. Image (A) is a three-quarter view, and image (B) is a horizontal planar slice through the image, showing the tip, the sides, the endcap, and material boundaries.

In Fig. 71 it can be seen that one side of the howitzer shell is much brighter than the other. This is a result of the non-concentricity of the target. The target was outside of the high-frequency sonar beam for much of the aperture, and hence doesn't image well in the HF data. In contrast, the low-frequency captures the full outline and both sides of the target because of the wider beamwidth, but one side is much brighter than the other.

If the 3D wavenumber spectrum is computed from the 3D snippet containing just the howitzer shell, the wavenumber spectrum of the target becomes much more visible, and this is shown in figure 72.

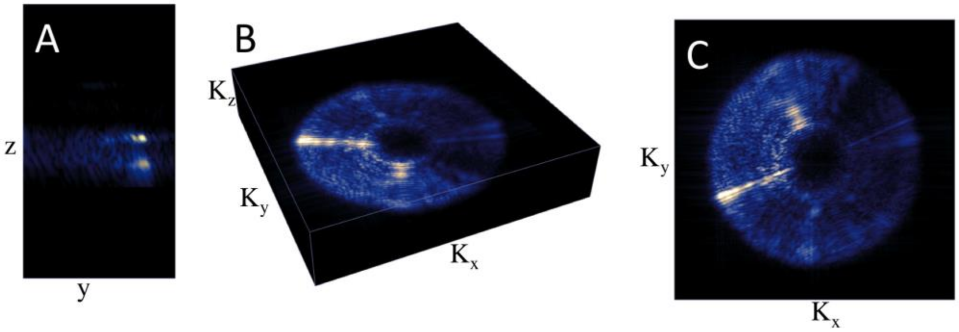

Figure 72. (A) a vertical slice through the image snippet showing a glint and its sub-sediment reflection, and (B and C) the three-dimensional wavenumber spectrum for the 3D snippet.

In Fig. 72 a vertical slice through the specular edge-glint is shown to highlight its relation to a wavenumber domain phenomenon. The specular glint in Fig. 72(A) (the bright, well-focused glint) is accompanied by a reflection below the sediment. This phenomenon is well known in other literature (see e.g., [41] and [45]). In the wavenumber spectrum, the presence of the glint causes an interference fringe that manifests as a series of evenly spaced nulls in the vertical direction for the narrow glint feature, that are visible in Fig. 72(B). These nulls are a three-dimensional visualization of the sweeping null phenomenon described in [41], [45], and this is probably the first experiment to visually tie these concepts together (i.e., associates the sweeping null phenomenon in [41] with the interference pattern manifesting in the 3D wavenumber domain). The grazing angle changes the angle of the sampled slice through the interference pattern and hence the frequency at which the null appears in the sampled response.

Lobster Trap Results

Fig. 73 is a high frequency, single-pass image of a scene containing a lobster pot on a rocky outcropping. For scale, the trap is about 0.8 meters long.

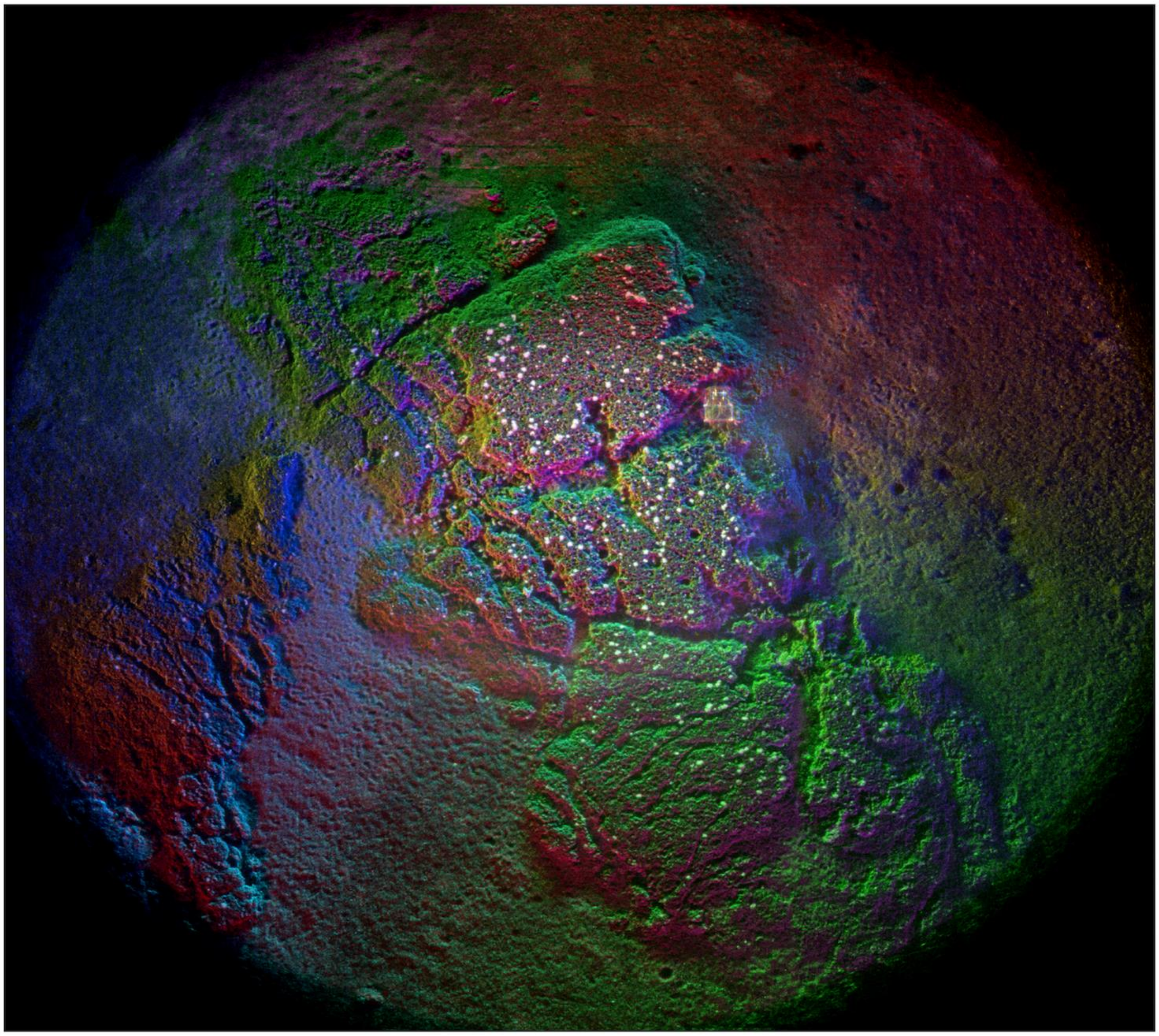

Figure 73. A CSAS scan of a scene containing a lobster pot. The complex structure of the rocky outcropping on which the lobster pot is located is also visible.

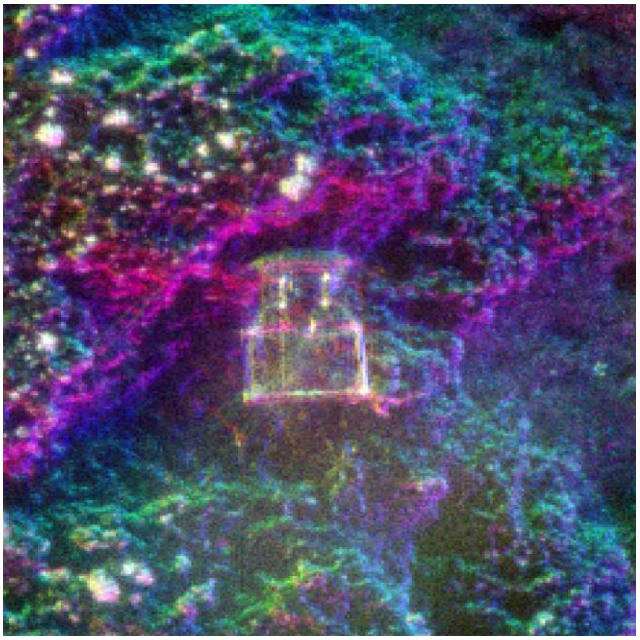

Figure 74. A zoomed view of the lobster trap in the previous image. The trap appears to be rectangular and the inlet portions, along with some of the netting, is visible in the top portion of the trap. It is also clearly divided into two chambers.

As shown previously in Fig. 67, this target failed to produce an interpretable 3D image when bathymetry compensation was neglected. Fig. 75, however, shows the results of the imaging with both bathymetric compensation and vertical map-drift. Rather than using a color-by-aspect scheme, the target has been colored in orange and the sediment in blue to maximize contrast.

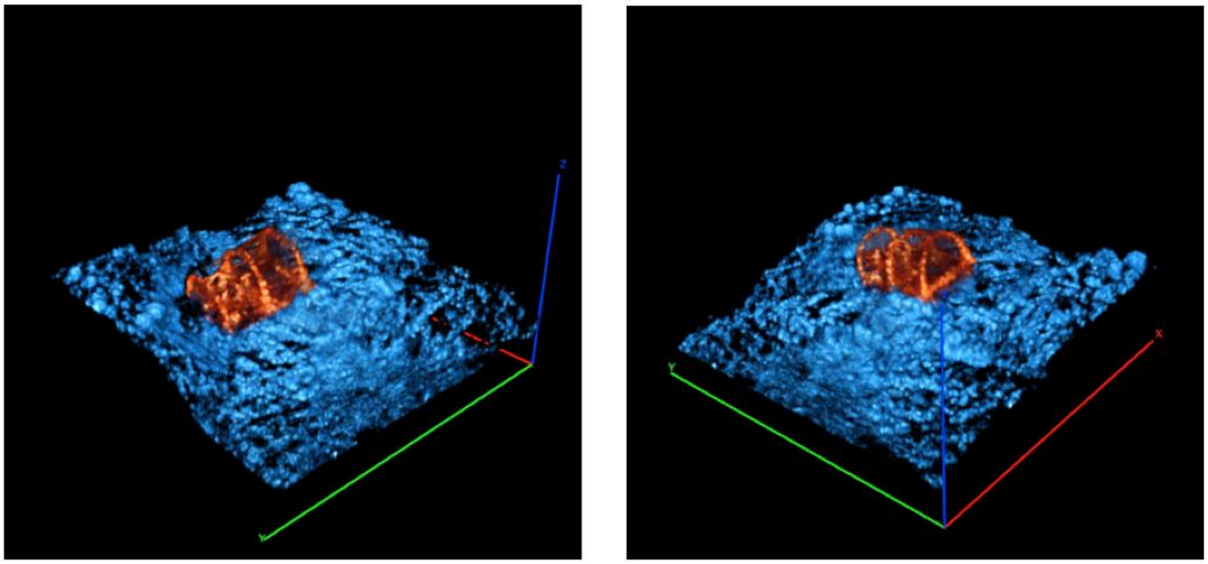

Figure 75. An VAA3D alpha-rendered image of the lobster-trap shown in Figs. 73 and 74, viewed from two perspectives. The arched top of the lobster trap is clearly visible.

From Fig. 75 it can be discerned that the trap is a lobster trap with a curved top. The target, made of wooden slats, is acoustically permeable and a number of interior features can be seen. These are revealed in the following plots which show a set of horizontal slices through the datacube, highlighting significant internal features of the lobster trap.

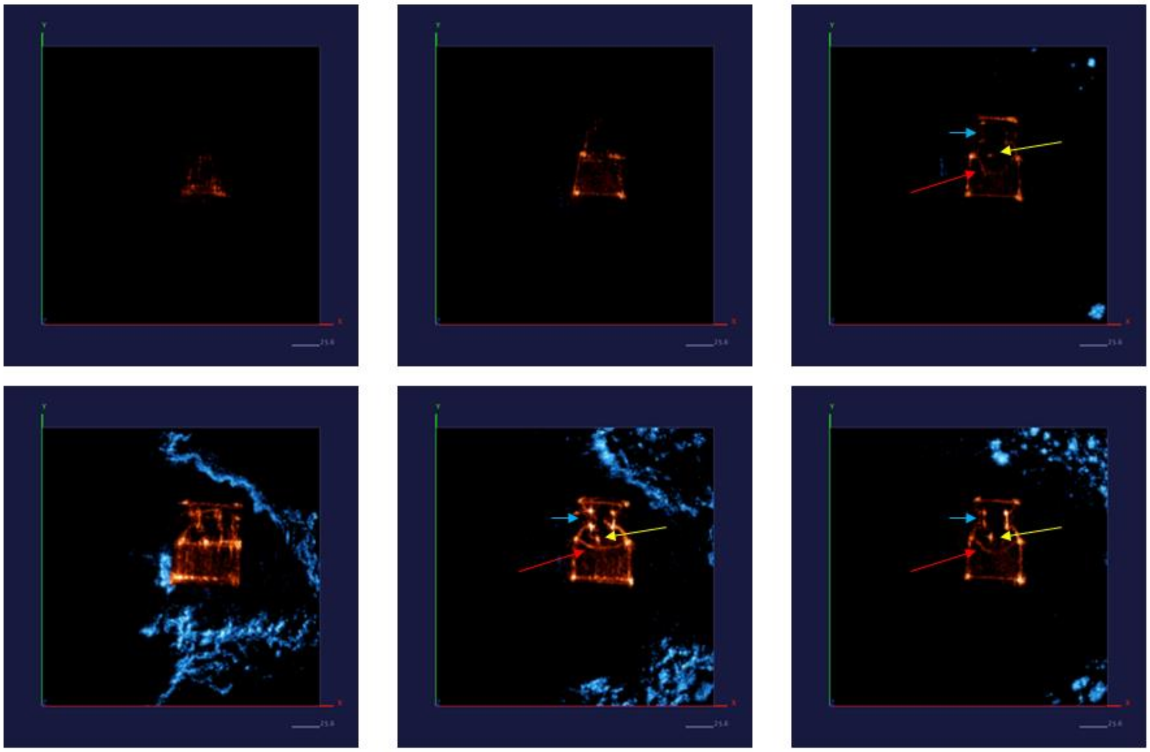

Figure 76. Horizontal plane slices through the imagecube of the lobster trap. The images are arranged in order of descending height, beginning with the top left image and working clockwise around the set. The red arrow highlights some netting, the yellow arrow highlights the bait spike, and the blue arrow highlights the trap inlets.

In the previous figure, internal features such as a bait spike and netting are easily visible inside of the lobster trap. The next figure shows vertical slices through the trap.

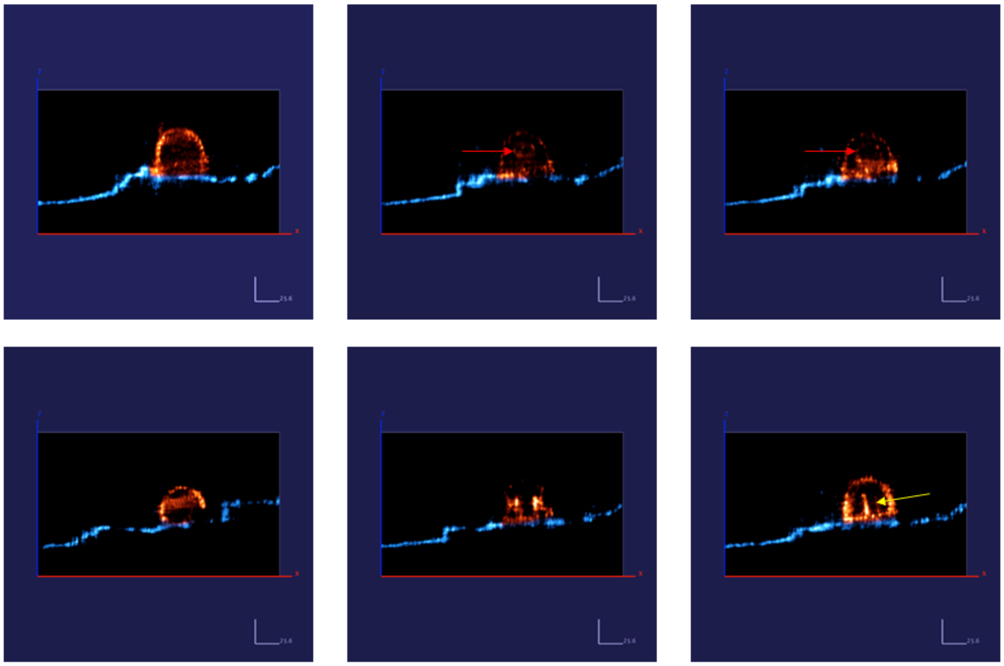

Figure 77. Vertical slices perpendicular to the axis of the trap. The ordering is from the rear to the front of the trap, beginning with the top left and moving clockwise around the figure. The red arrow highlights the net, which appears to pinch off towards one end of the trap. The yellow arrow shows the bait spike.

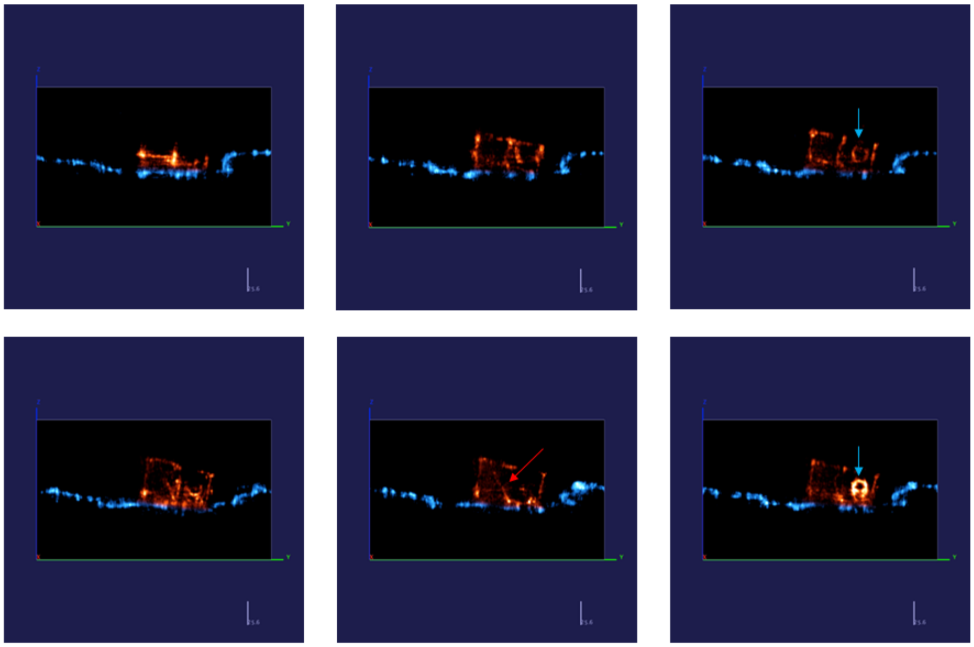

Figure 78. Vertical slices along the axis of the trap. The blue arrow highlights the circular trap inlet. The red arrow shows part of the netting.

The vertical slices also reveal information about the target, such as the shape of the trap inlets (rings), the vertical extent of the bait spike, and the slope of the net. The arched shape of the target and the individual slats composing the exterior of the trap can also be discerned. Another interesting aspect of this scan is that it sloped in one direction due to navigation drift. The AUV did *not* resurface mid scan in this second set, which prevented the large glitches of the first set from occurring. In Fig. 79 the multipass array is viewed from the side, enabling visualization of the drift which manifests as a slant in the array as a function of height.

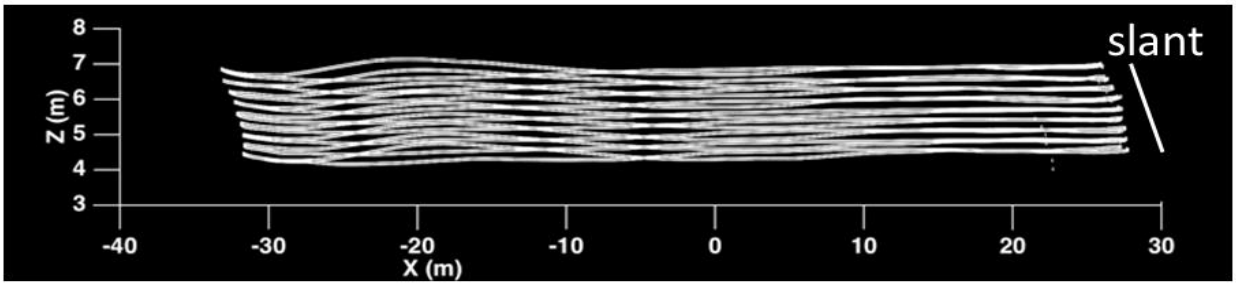

Figure 79. A side view of the array used to scan the lobster pot. The array experiences drift to the left as it moves from the bottom of the array to the top.

The vertical wavenumber coverage provided by the scan should be proportional to the range of grazing angles captured by the scan. For the scan depicted in the previous figure, the array tilt should produce an asymmetry in the wavenumber domain: the side slanting toward the object contains a broader range of grazing angles, which should correspond to extended vertical wavenumber coverage. The side slanting away from the target, however, should have reduced coverage.

In fact, this is verified when the 3D wavenumber spectrum of the scene is computed. The figure below shows the 3D Fourier pair of the complex image and 3D spectrum (magnitudes):

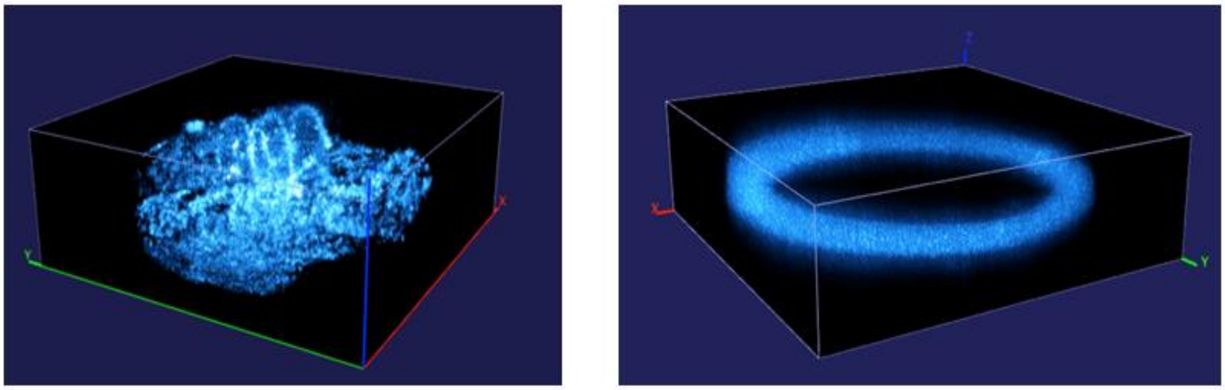

Figure 80. The magnitudes of the complex lobster trap image (L) and the magnitudes of its 3D wavenumber spectrum. The spectrum is clearly asymmetric and thicker on the left side.

If the 3D wavenumber spectrum is sliced in the plane corresponding to the direction of array tilt, the following figure is obtained.

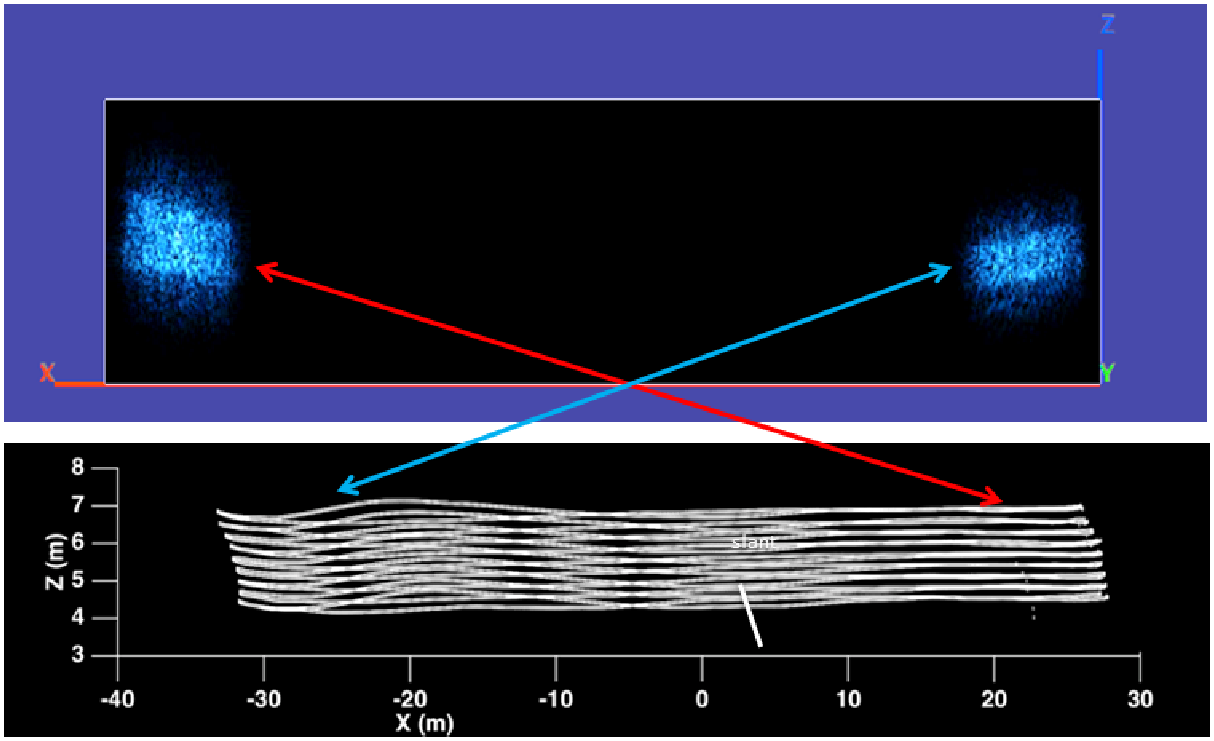

Figure 81. A slice through the 3D wavenumber spectrum (top). The sides of the array corresponding to the spectral regions are shown via the lines (note that they are opposite, which is due to the fact that these acoustic tomograms are formed by reflections from a scene rather than transmissions through a scene).

As predicted, the portion of the array slanting toward the target appears to sample a broader range of the wavenumber spectrum in the vertical dimension than the opposing side. This observation has ramifications for effective spectral coverage, i.e., a conical aperture may be a useful way for producing 3D images in shallow water environments where water depth may prohibit the usage of a very tall aperture.

Plastic Barrel Results

Another target that was scanned was an 85 centimeter tall barrel composed of black ABS plastic. The bottom 20 cm of the barrel was filled with concrete, and a solid steel track-and-field shotput was hung approximately 30 cm from the top of the barrel. The barrel was flooded. The purpose of suspending the shotput was to test the acoustic permeability of the target and see if tomographic imaging could resolve the object inside the barrel. Fig. 82, an image of the same target, shows that it imaged very successfully once a bathymetric prior was included in the scan coregistration process.

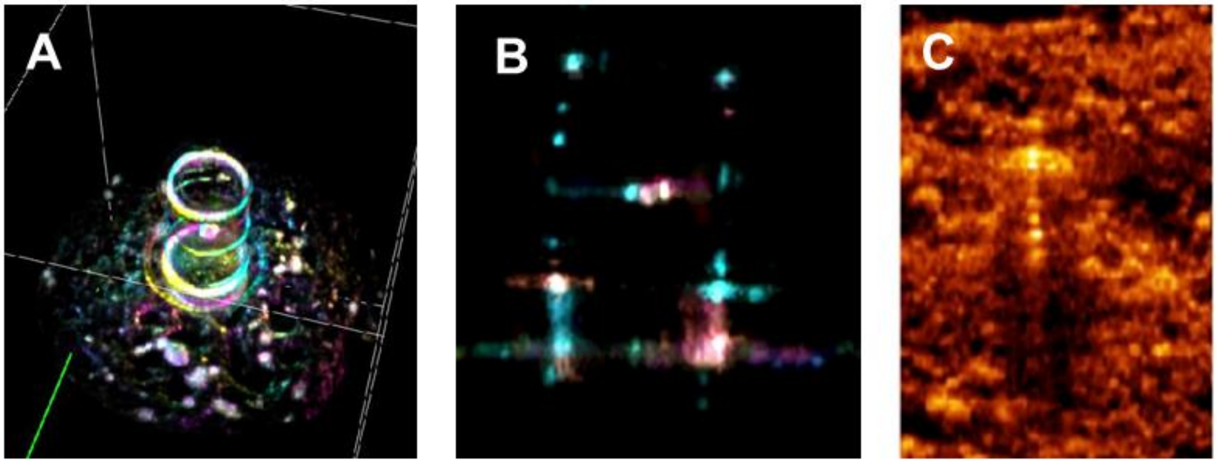

Figure 82. Three views of the plastic barrel target. Plot A shows a three-quarter view alpha-blended image, rendered in VAA3D. Plot B shows a vertical slice of the barrel, where the coloration corresponds to insonification angle – blue from the left and pink from the right. C is a snippet of a sub-aperture window of the CSAS scan. This is what an ordinary linear SAS image of the target would look like.

The previous figures show three views of the target. Three features of significance are 1) the shotput is clearly visible in the target, however it doesn't appear like a sphere – instead, just a glint from the side is visible. This makes sense, given that the range of aspect angles in the scan is relatively small (~6 degrees) and only a small segment of the radius would be imaged. Fig. 83 shows a cutaway schematic of the target and scattering features visualized acoustically in different manners.

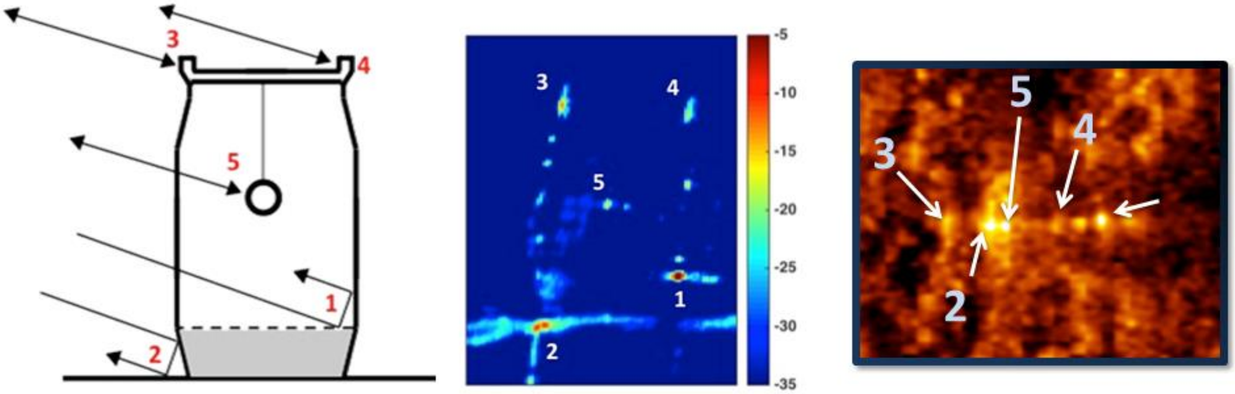

Figure 83. The left plot is a cutaway illustration of the target, showing the barrel, the concrete filling (gray) and the shotput (circle). Hypothesized scattering mechanisms are numbered. The center plot is a slice through the tomogram formed from a 5 degree arc of the aperture for simple comparison with the figure on the left. The figure on the right is the standard SAS image of the target (the range dimension is to the right).

In Fig. 83, the dominant scattering mechanisms for the target are numbered from strongest to weakest, and their source is hypothesized in the schematic. The most dominant feature appears to be a corner scattering mechanism formed between the top of the concrete and the *back* side of the barrel. Ironically, the brightest feature is an internal feature for this particular object. The next brightest scatterer is the corner scatterer formed between the sediment and the front side of the barrel. Next is the corner scattering from the top of the barrel, and lastly, the scattering from the suspended shotput.

For this particular target the impedance discontinuity provided by the plastic barrel was so low that imaging the internal features was not a challenging operation. In fact, the barrel itself produced very little shadowing. A steel barrel with a similarly suspended shotput was an intended target, but was poorly localized, and hence no results can be shown. In Phase 3 of the project, however, a steel barrel with an internally suspended shotput was scanned and results are shown later in this document.

Additional discussion of the scattering from this object and others can be found in [46].

Car Tire Results

Fig. 84 shows the 3D imaging results for a tire, along with a photograph taken by a diver of the same target. The rim of the tire was removed, so there was no bright, high impedance reflection. Furthermore, there was very little rough surface scattering from the tire, and most of the signature from the target was dominated by corner scattering.

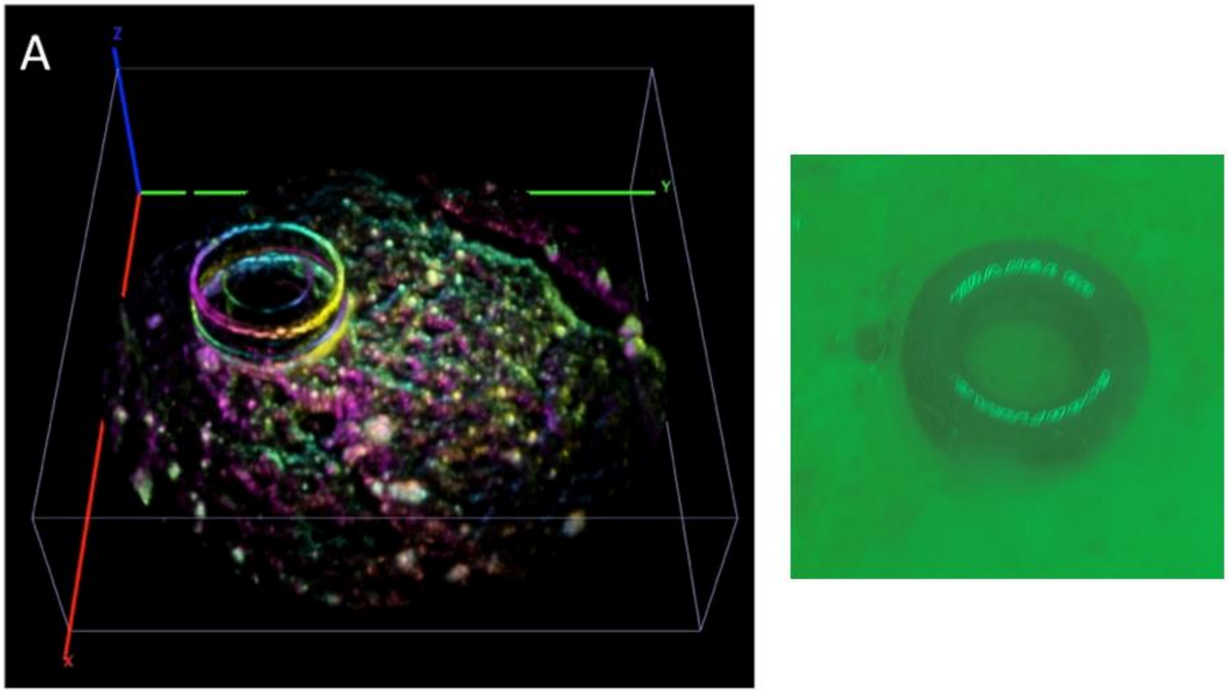

Figure 84. 3D acoustic image of a tire with color-encoded backscattering angle, and a photograph of the same target captured by a diver.

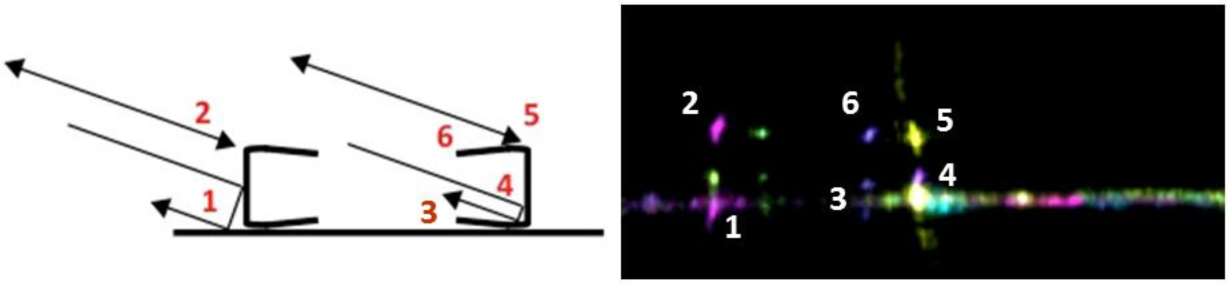

Figure 85. A cutaway illustration of the target (L) with the hypothesized dominant scattering mechanisms numbered, and the a cutaway of the target on the right with the same scattering mechanisms labeled. The scattering to the left is in a purple hue, though likely mechanism 5 is hidden beneath contribution 2 from the opposing direction.

The sediment appears to be partially visible beneath the tire, however a subsequent follow up experiment could try to place an object inside the tire or include the rim, to test how effectively objects inside of tires can be imaged.

Complex Sediment Results

The last example to be shown is a region of complex sediment structure and bathymetry. Though there was no target present in the field of view of the sonar, the sediment structure itself was sufficiently complex to form an interesting acoustic image. The imaging results are shown in the figure below:

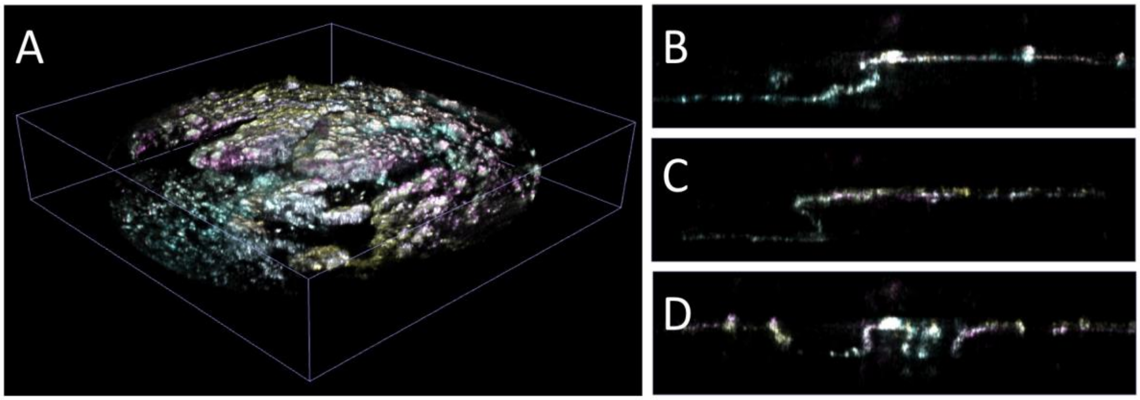

Figure 86. A complex scene shaped by rock and coral formations. A) shows the 3D view and B – D) show slices through the image cube.

The previous figure illustrates some potential advantages and drawbacks of 3D multipass aperture processing from a localization standpoint. Some of the formations are actually overhangs (e.g., Fig. 86C). A 3D image constructed from low grazing angles has the potential for observing objects beneath overhangs and places where occlusions (or observation) from above may be impossible. Another example of where this type of imaging could be useful would be imaging a black smoker or burst oil pump, where the flow or temperature above the feature may prevent the kind of close range microbathymetry measurements normally used to create high resolution 3D acoustic images. On the other hand, for deep cracks or holes, the low grazing angles prevent acoustic energy from penetrating to the bottom of the crevices. The solution to this problem is to image at higher grazing angles.

AUV Spiral Scans: Field Tests #3 and #4 (July 2016 & May 2017)

In July of 2016, scans were conducted around a number of objects of interest to test a new acquisition method: spirals. The AUV control specialist at Woods Hole reprogrammed the REMUS 600 firmware to increase altitude at a constant rate of time. Combined with a set of circular apertures, this functionality produced spiral scan patterns like the type shown previously in Fig. 44 (*Materials and Methods, Phase 2.3 section*). In the July 2016 experiments, the initial plan was to collect both regular and spiral scans around each target for comparison. The superiority of the spiral scans became apparent after the very first scan, and due to time limitations not a single instance of the previous scanning methodology was ever repeated again. The location of the experiments was Buzzards Bay near Woods Hole, and the dominant sediment reported by divers was an elbow-length layer of mud over sand. The divers were able to locate regions that were more sandy for placement of certain targets (see following table). The follow up experiment in May of 2017, in which several additional targets were scanned, took place in the same location. The following table lists the targets and scan conditions for these two sets of field experiments.

Target	Sediment	Localization	Imaged?	Set
Airplane	Mud	Halted	2D	Set 1, day 1
Airplane (CCW)	Mud	Full beam	2D	Set 1, day 1
Airplane (CW)	Mud	Full beam	3D	Set 1, day 1
Steel Barrel	Mud	Halted	2D	Set 1, day 1
Steel Barrel	Sand	Full beam	3D	Set 1, day, 1
UXO pile	Mud	Full beam	3D	Set 1, day 2
Howitzer shell	Mud	Full beam	3D	Set 1, day 2
Proud 2-1 al. cyl.	Mud	Partial beam	3D	Set 1, day 2
Flush 2-1 al. cyl.	Mud	Partial beam	3D	Set 1, day 2
Missed boat (stern)	Unknown	Missed	2D	Set 1, day 2
Missed boat (bow)	Unknown	Missed	2D	Set 1, day 2
6 ft. step ladder	Mud	Full beam	3D	Set 2
Bicycle	Mud	Full beam	3D	Set 2
Boat (bow)	Mud	Full beam	3D	Set 2
Boat debris	Mud	Full beam	3D	Set 2

Table 4: The target and condition list for the second set of experiments.

Between both experiments, 15 spiral scans were attempted, 13 of which were successfully completed. The very first scan, around an airplane, had an inter-loop spacing that was wider than the previous scans (50 cm vs. the typical 30 cm). Extending the spacing between scans too far can have a negative impact upon reconstruction (see vertical sampling constraints, [11]). Upon discovery, the scan was halted and the vertical spacing reprogrammed to be 30 cm. The airplane was then scanned twice, once in a counter-clockwise spiral, and a second time in the clockwise orientation.

The only other scan that was halted was the scan around a steel barrel placed on mud. Due to time constraints only one more target could be scanned that day and this target was abandoned in favor of another steel barrel with an internally suspended shotput.
Of the thirteen completed scans, only two missed their targets. These were of the bow and stern debris from the wreck of an abandoned sailboat. These were missed because of poor GPS coordinates supplied for the wreck, and were later successfully scanned in the second set. Despite missing the targets, the sediment that was scanned was highly unusual and useful for testing other facets of this project which will be discussed later in this document. In subsequent sections, the results for each of the targets will be discussed.

Curtis SB2C Helldiver Airplane

In 1947 a pilot was making practice bombing runs with a Curtiss SB2C Helldiver airplane when the engine stalled. The pilot safely ditched the plane in Buzzard's bay, and it wasn't rediscovered until the early 2000's [47]. Since its rediscovery, various institutions have used this plane as a test target for different sonar systems, to demonstrate imaging capability. The first three attempted spirals were conducted around this airplane. As mentioned previously, the first scan had an improper spacing and was prematurely halted, however the second set of scans were successfully completed. The following images were generated by a CSAS data quick-look code written to evaluate the placement of the object relative to the scan.

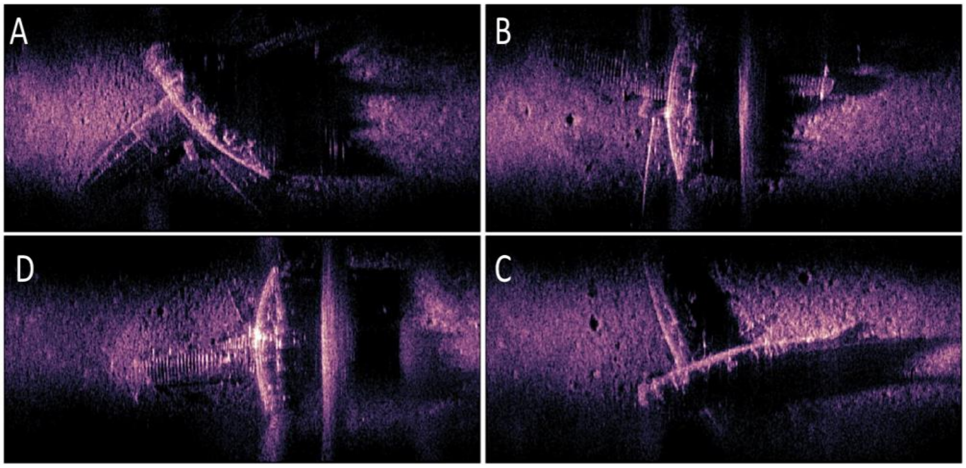

Figure 87. Four sub-aperture quick looks at the Buzzard's Bay Helldiver. The target is almost perfectly in the beam.

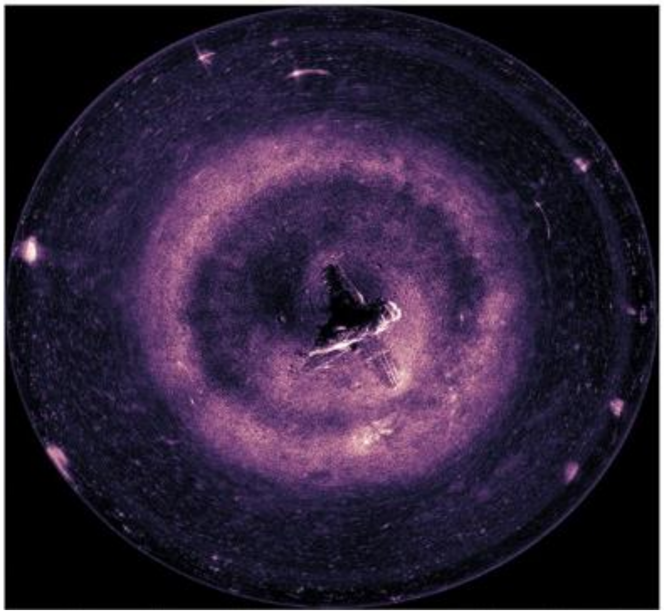

Figure 88. A full radius pseudo-stripmap image (*Materials and Methods*, Phase *2.1 section*) of the airplane projected to Cartesian coordinates, showing the localization of the airplane relative to the aperture.

Following generation of the quick looks, an ordinary CSAS image was generated to evaluate the focus quality of data in the Buzzards Bay environment. Data quality was good, but the large variation in height caused a lot of out-of-plane defocusing in the image of the aircraft.

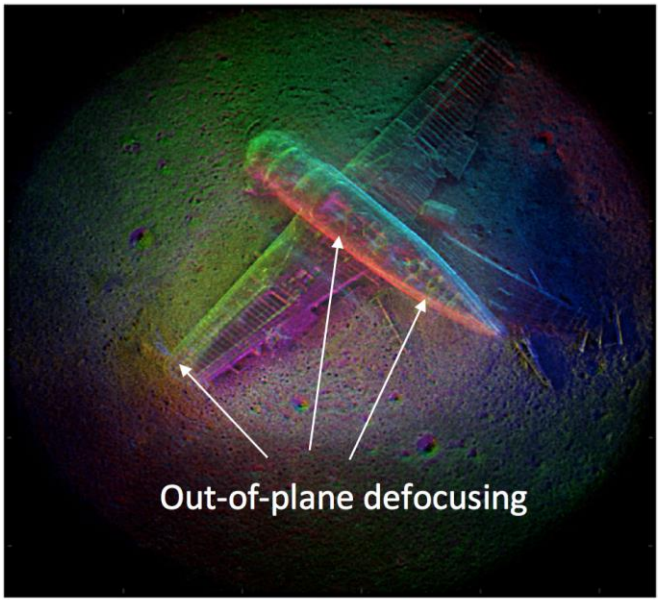

Figure 89. A standard CSAS image of the hell-diver. The height plane for the image is located at the level of the sediment so the features of the airplane, which extend above the sediment, are out of focus.

The Helldiver data was the first spiral scan data processed, and this data was used to develop and test the spiral-scan incremental coregistration algorithm and fast-polar-backprojection based 3D beamformer previously described in the methods portion of this document. Fig. 90 shows one of the first 15-degree 3D sub-apertures generated from this dataset. At this point in the processing, a full aperture 3D image had not yet been made.

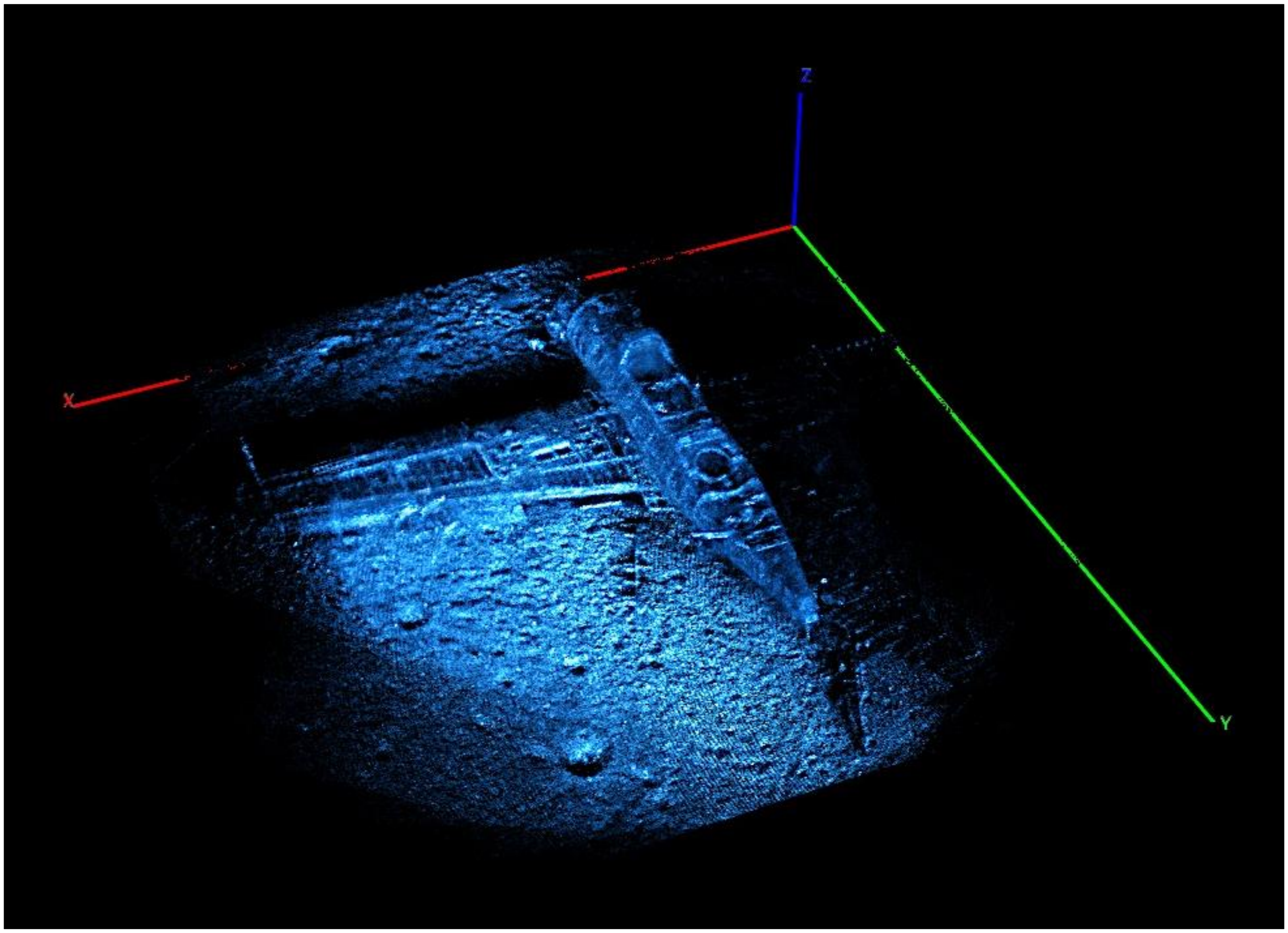

Figure 90. One of the initial sub-aperture images of the airplane generated using a 15 degree partial aperture around the multipass array. The appearance of sub-apertures are very similar to the illumination of a scene by a flashlight from a single direction. Image rendered in VAA3D.

The 15 degree sub-aperture images generated around the aperture were incoherently combined to form a full aperture despeckled high frequency image of the airplane. At low frequencies the sub-apertures were coherently combined, vs. incoherently for the high frequency scans. For spiral scans, the aspect-dependent coloration scheme was abandoned in favor of an altitude dependent coloration scheme. The result of this applied to the high frequency airplane image is shown in Fig. 91.

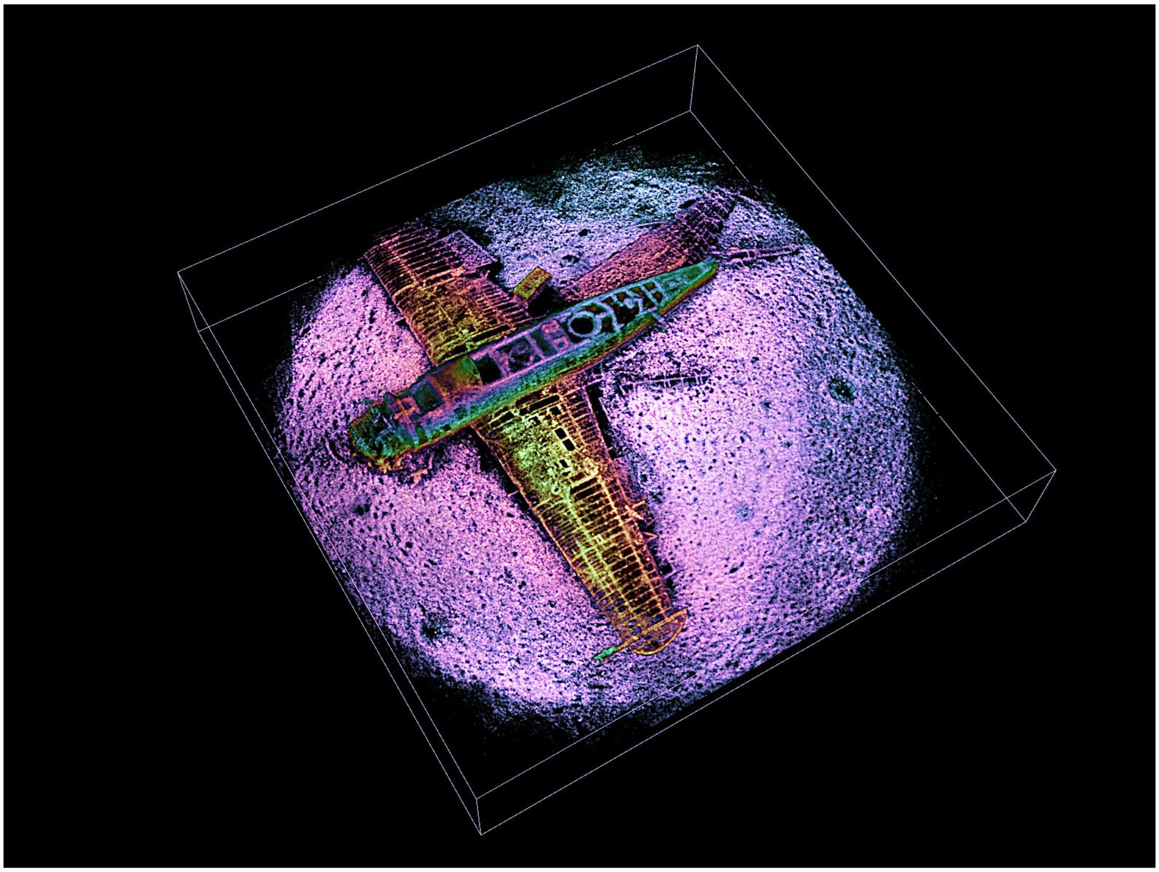

Figure 91. The full aperture high-frequency image of the Helldiver, with height-dependent coloring. Rendered in VAA3D.

Significantly in Fig. 91, many of the finer features located on the top of the airplane that were out of focus in the ordinary CSAS image (Fig. 89) are perfectly in focus in the 3D image. This occurs for the exact same reason that the multipath mechanisms for the tilted howitzer shell mapped to the wrong locations in the ordinary CSAS image in Fig. 62, but mapped to the correct location in the 3D image: by resolving the height of a scatterer its location in the *x* and *y* dimensions are correctly resolved as well.

As was done with the lobster trap, the plane can be sliced like a 3D medical CAT scan to observe various features of the target. For example, taking a slice through the wing allows the Pitot tube to be observed.

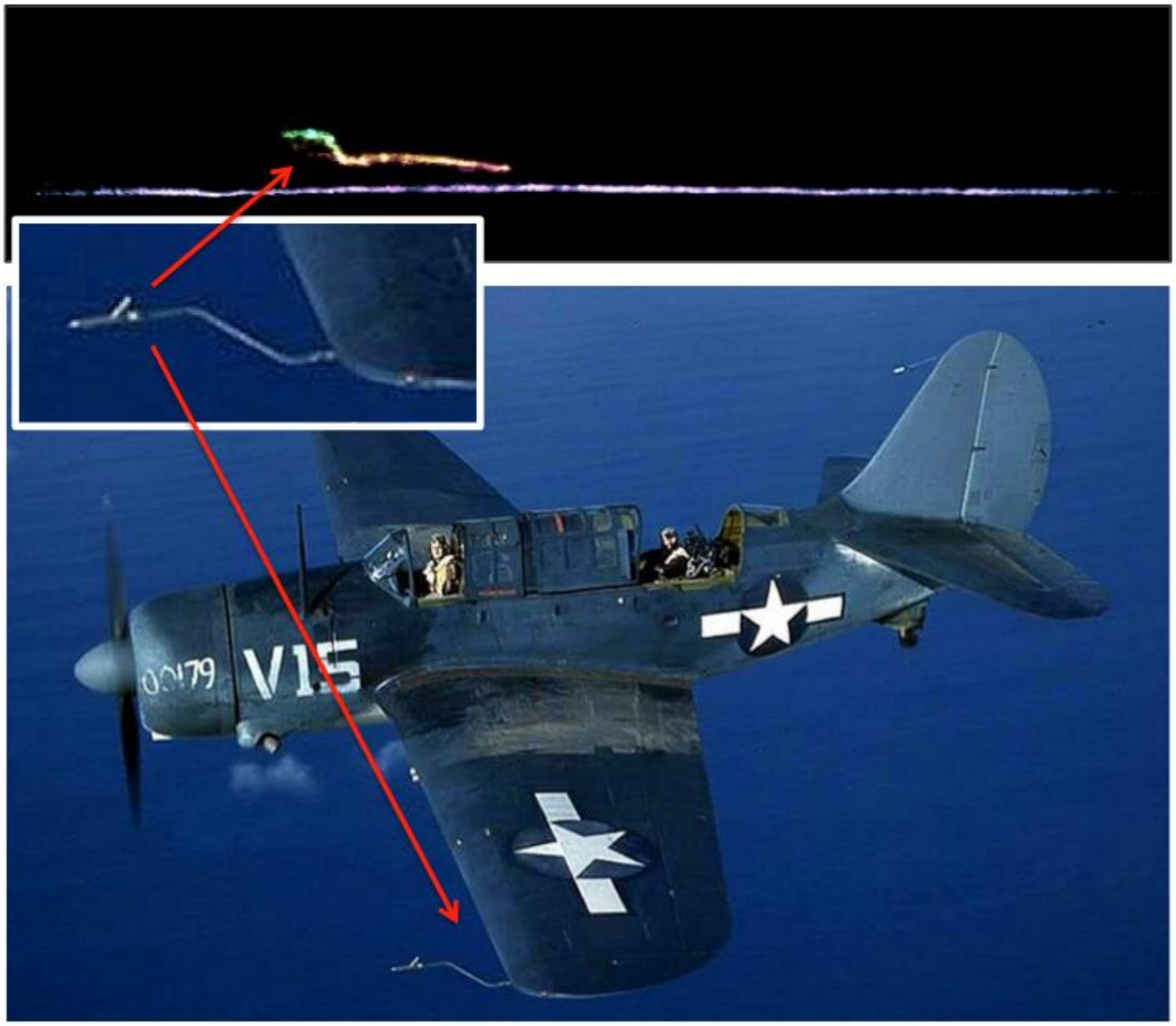

Figure 92. A slice of the tomogram showing the Pitot tube of the helldiver, and a corresponding image from the internet of the same type of plane (https://www.newenglandaviationhistory.com/tag/curtis-sb2c-helldiver/) confirming the design and presence on the left wing.

A certain degree of hull penetration was also achieved with the high frequency system. The crossbars of the wing appear to be visible through the wing as shown in the following slices:

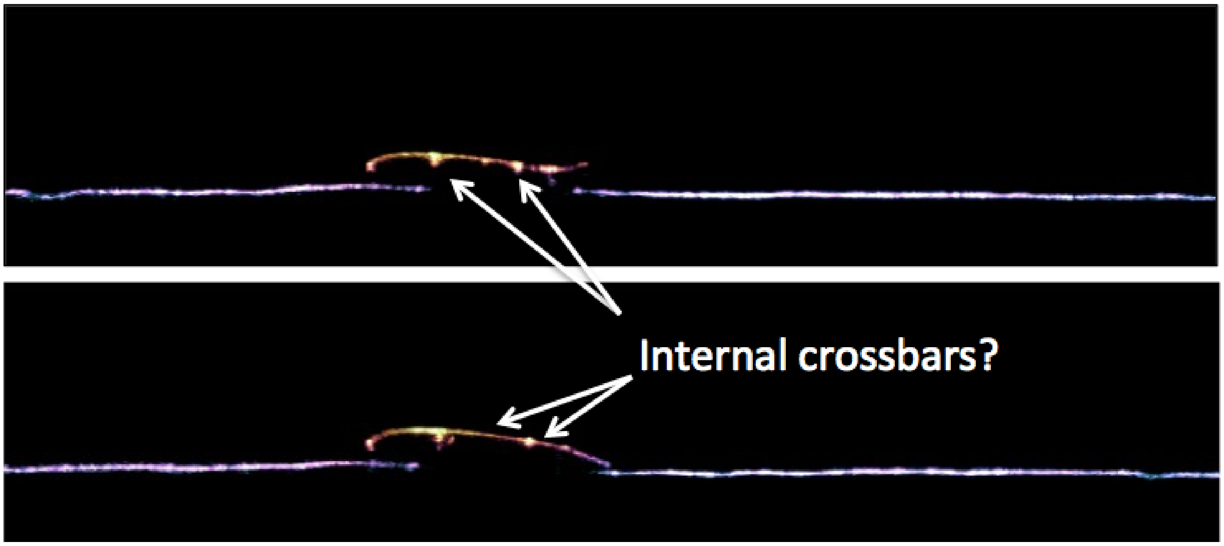

Figure 93. Additional slices through the wings, showing what appear to be cross bars.

Low frequency images for the target were also generated. It was found that, with the extended apertures generated by the spiral scans, the resolution of low frequency images in the vertical dimension was reasonably good and a number of features could be resolved. The coloration scheme used to represent low frequency images in all subsequent scans is a red hue, and these are frequently combined with blue shaded high frequency images to form composite high-frequency, low-frequency scans. The following figures compare maximum intensity projections in the vertical dimension of the low and high frequency (monochrome) images of the helldiver, showing the difference in type of features resolved.

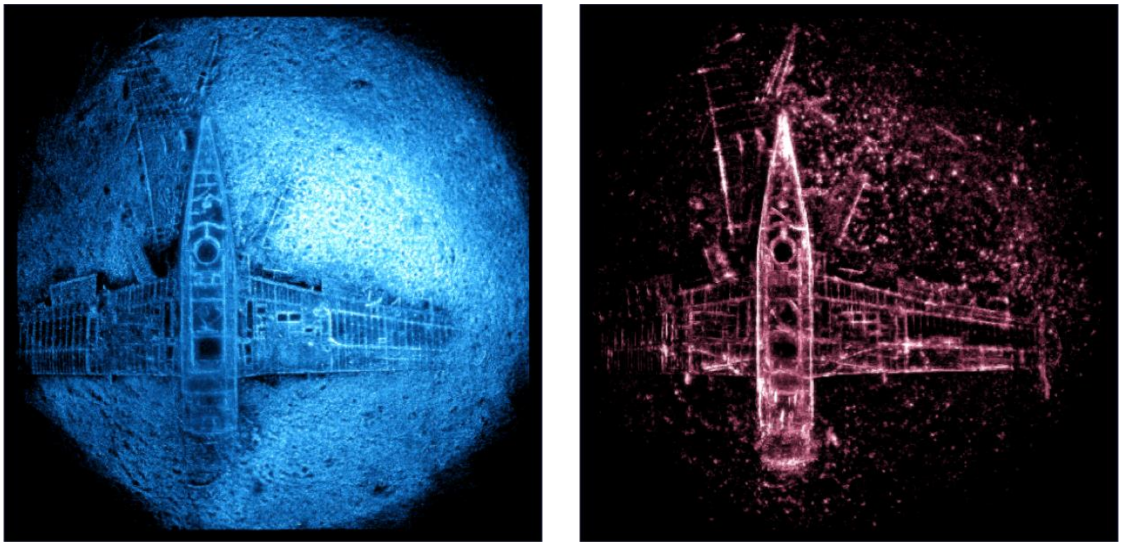

Figure 94. A side-by-side comparison of a high frequency MIP projection through the image cube (L) and a low frequency projection (R).

In the previous figure it can be seen that a vertical maximum intensity projection through the 3D beamformed data shows improved focusing of areas on the plane having significantly different height than the sediment, similar to the result in Fig. 95. The low frequency image clearly resolves different features of the wing and fuselage of the airplane, as well as resolving other objects suspended in the mud surrounding the plane.

A 3D alpha rendered perspective of the plane shows that, vs. the high frequency image, the low frequency image seems to be composed more of lines. It is unclear if these are internal features like cross bars or fuel lines, or if these are simply coherent glints from the sides of the plane.

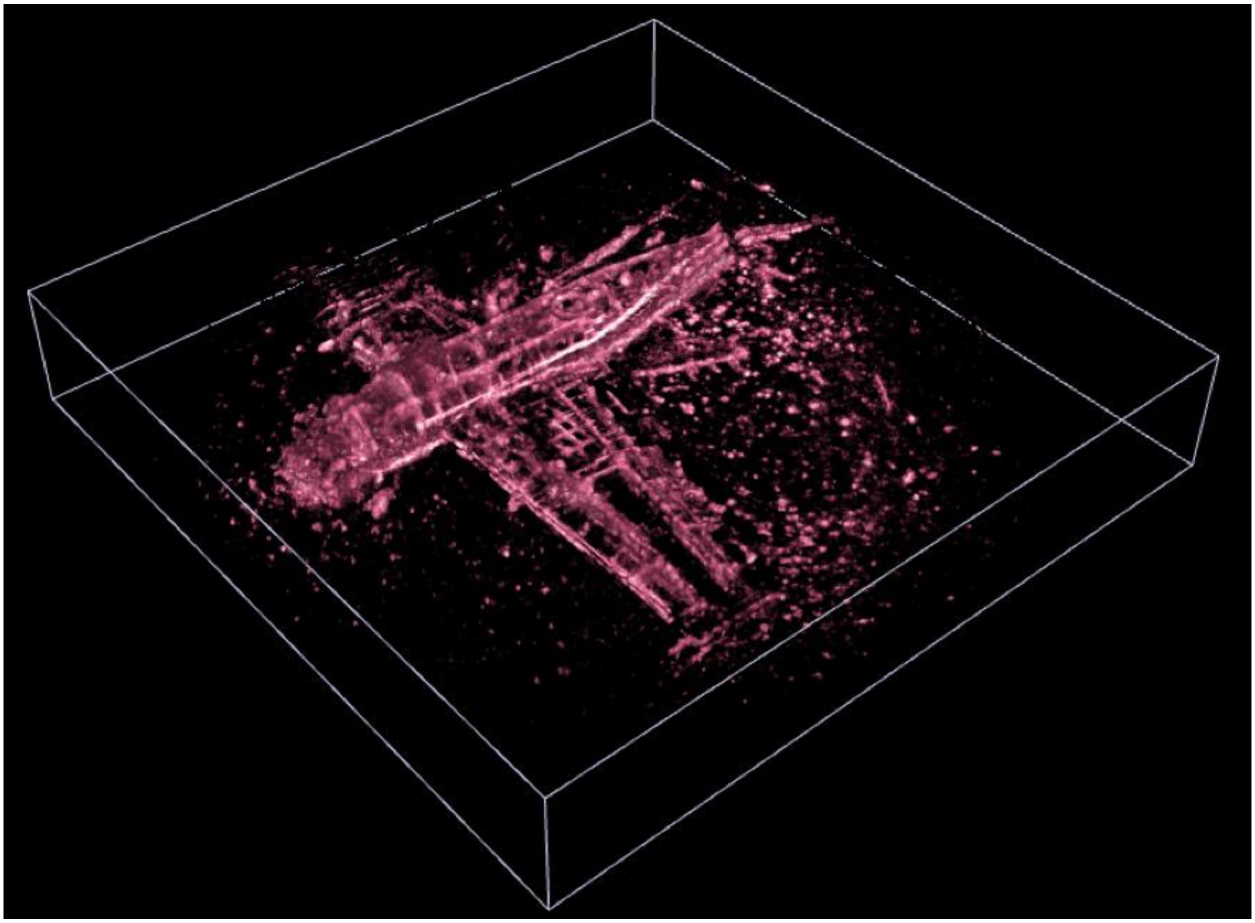

Figure 95. A low frequency alpha-rendered image of the airplane.

The previous image can be blended with the high frequency image to form a multicolor composite which can be useful for identifying low and high frequency features and discrepancies.

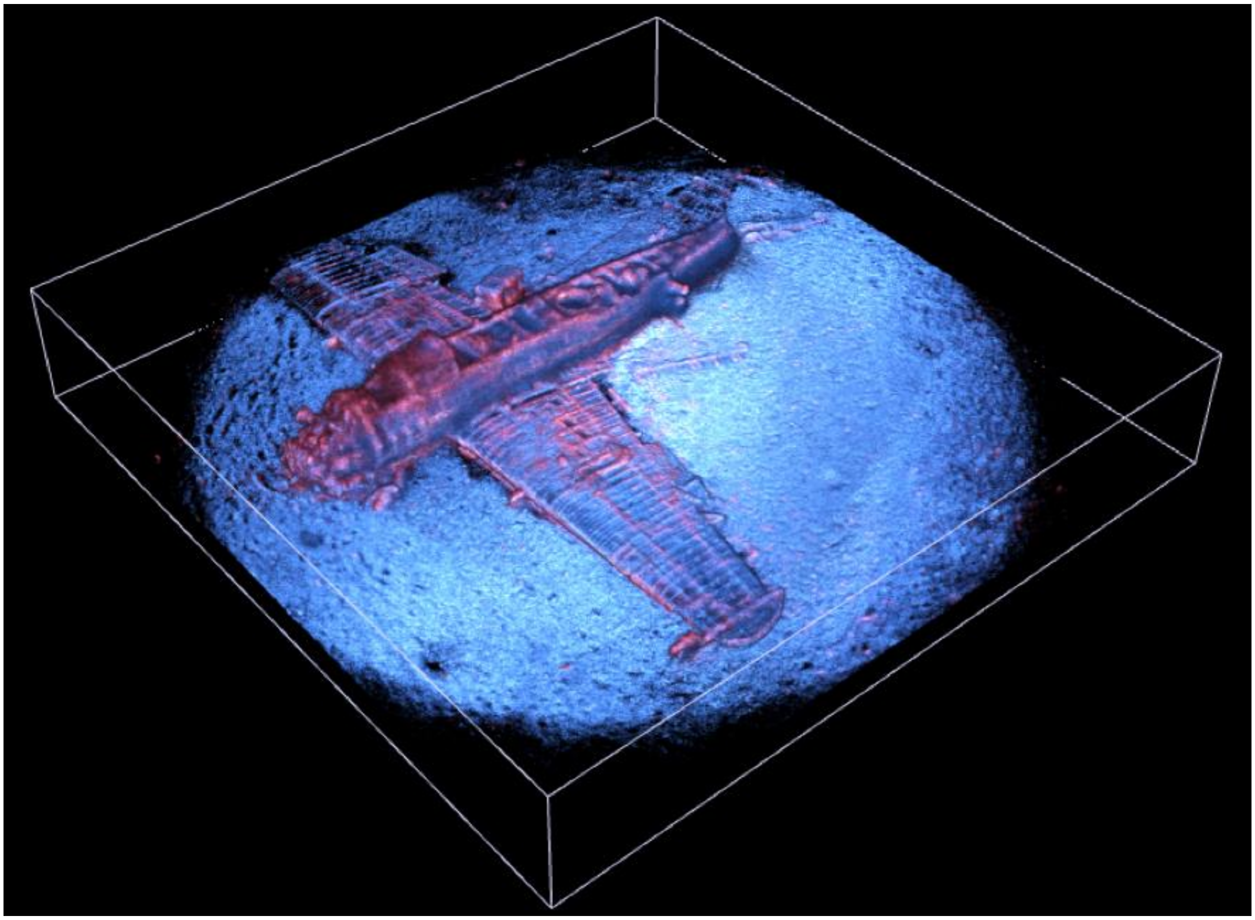

Figure 96. A multicolor low and high frequency combination image of the airplane.

The high frequencies are more sensitive to rough surface scattering from the surfaces of the aircraft and the result has a sort of skin-over-wireframe effect. These composite images are used for many of the subsequent examples of data processing.

Steel Barrel on Sand Results

The next object scanned was an 88 cm tall steel barrel on sand. As was done previously in the case of the plastic barrel dataset, this steel barrel had a shotput suspended internally from the lid. One of the purposes of this test was to determine if the shotput could be successfully imaged and if it would be visible at both high and low frequencies. The following figure is a high frequency image of the full barrel scene, approximately 15 meters per side:

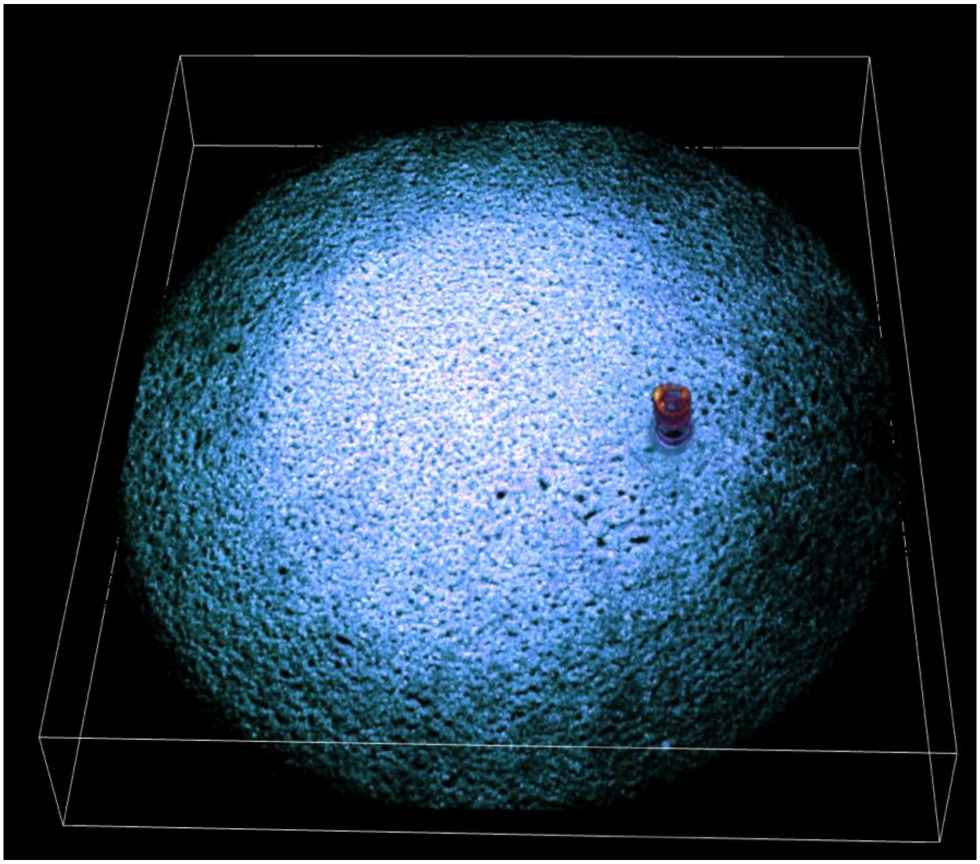

Figure 97. High frequency barrel scene

The following figures show a zoomed snippet containing the barrel and a slice through the barrel, showing that the target is indeed visible inside the barrel, however it is not as prominent as it was with the plastic barrel. The rings of the barrel are also very visible.

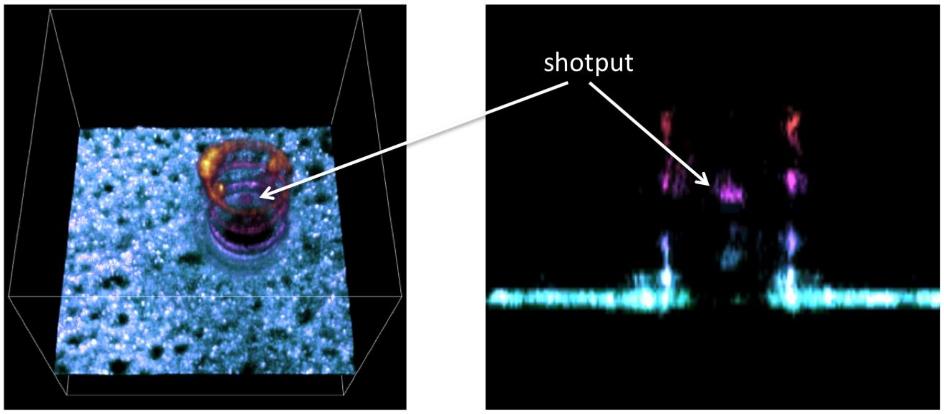

Figure 98. A zoomed image of the barrel and a slice, showing the shotput. The cause of the phenomena below the shotput is unknown but may possibly be a multipath reflection off of the top of the concrete filling at the bottom of the target.

The next figure compares a slice through the 3D image cube of just the top of the barrel, vs. the standard 2D CSAS image of the barrel. Many features in the tomogram are visible that were impossible to distinguish in the standard 2D CSAS image, due to being hidden by more dominant scattering from other features of the barrel.

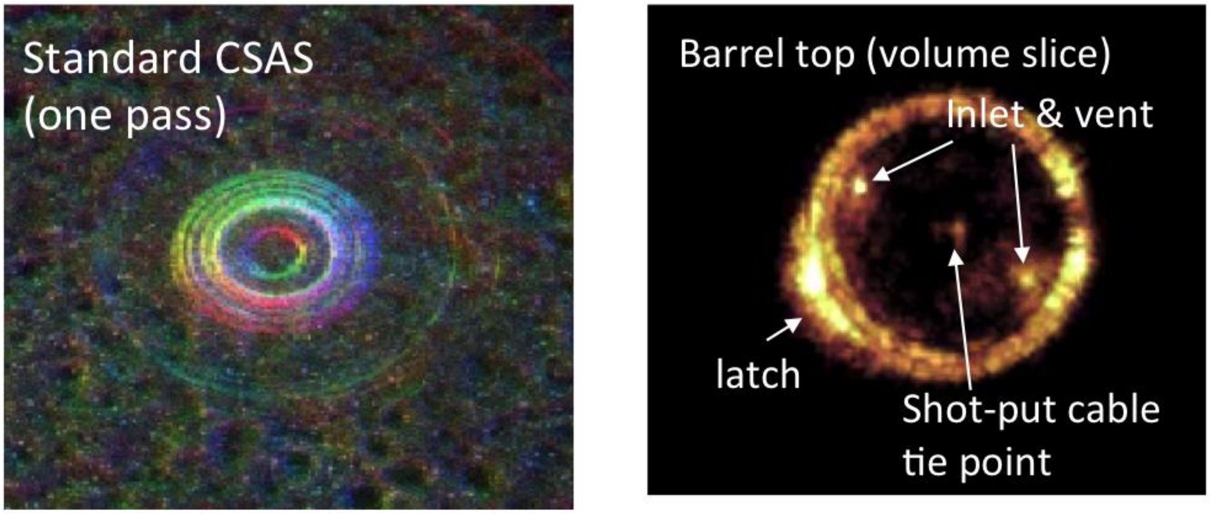

Figure 99. A standard CSAS image of the barrel (L) and a slice through the top of the tomogram on the right, showing a number of features that are difficult to spot in the standard image.

The low frequency image of the target was subsequently combined with the high frequency for comparison and to see if the shotput showed up any more strongly in the barrel. The following maximum intensity projection images show the full composite scene from side and tilted views. Blue corresponds to the high frequency band and red corresponds to the low frequency band.

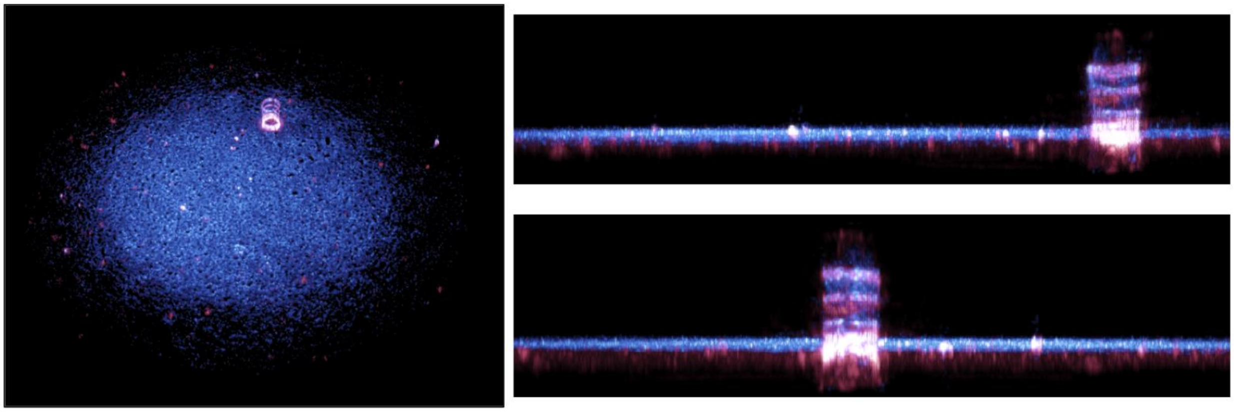

Figure 100. Tilted and side-view HF/LF composite maximum intensity projection (MIP) images. Discrete objects suspended in the mud layer are clearly visible in the low frequency data.

The next figure shows various cutaways of a zoomed image of the target which is alpha rendered to give the voxels opacity.

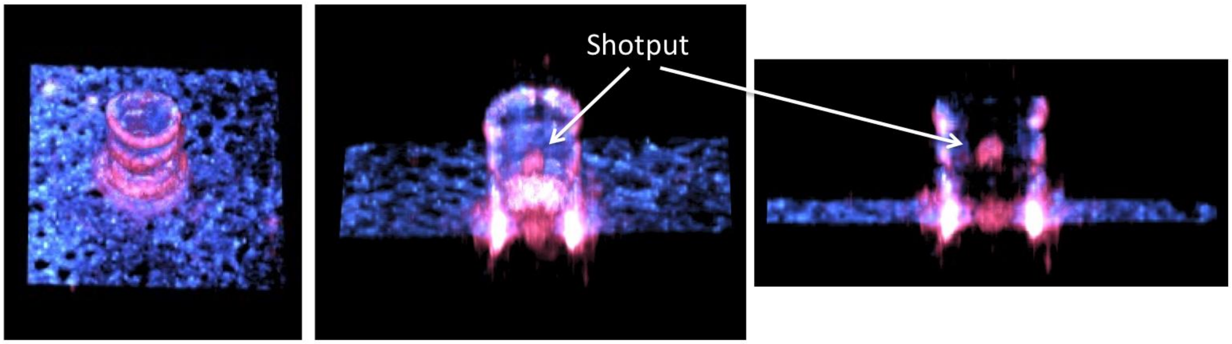

Figure 101. Tilted alpha-rendered image showing various cutaways of the barrel. The shotput on the inside of the barrel is visible.

In the previous figure, the cutaways show that the shotput is very visible. The red shading of the shotput indicates that the backscattering is dominated by low frequencies, which are able to penetrate the interior of the barrel better than the high frequencies.

UXO Cluster Results

A set of four UXO of varying types were placed in cluster, to test the ability of CSAS acoustic imaging to localize and discriminate targets in close proximity. The following images are 2D snippets of the cluster, imaged using a single CSAS scan and a sub-aperture *windowed to simulate a linear scan acquisition.*

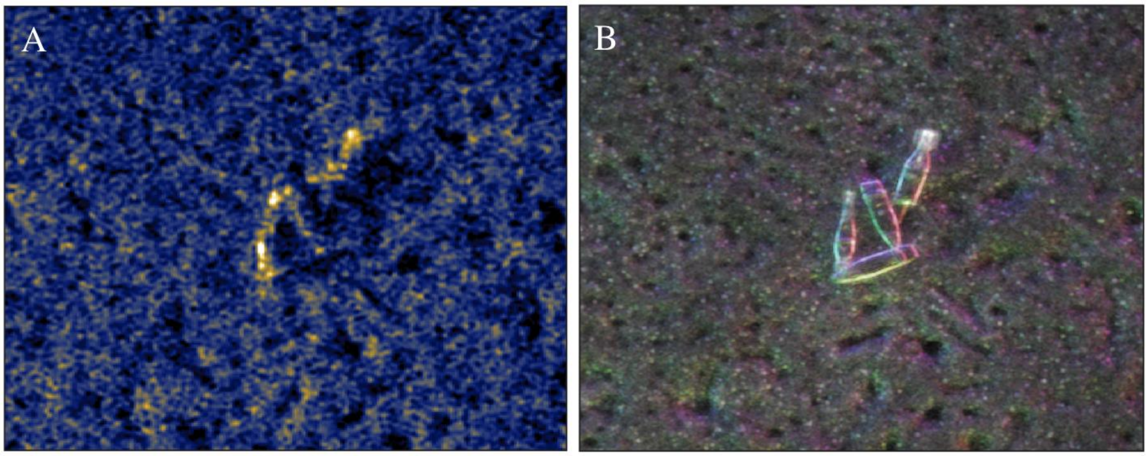

Figure 102. A partial aperture CSAS image, filtered to match the spectral coverage of a linear scan (L) and a full aperture CSAS scan (R). The particular method of aspect coloration in this figure is described in [48].

The multiple orientations of the targets made it very difficult to find a single sub-aperture in which prominent, identifiable features from all targets were visible. The previous figure represents the best aperture the authors could find, with 3 of the four target edges being visible, and a glint and shadow from the bottom target being slightly visible, though without additional knowledge from the CSAS scan it would be difficult to tell that a target was located in that position. The smooth surfaces of these targets, and their partial exposure contribute to the difficulty in finding a good linear aperture image of these targets. The figure below shows an HF image of the full scene, with a zoom of the cluster. Their state of partial burial is apparent in the image.

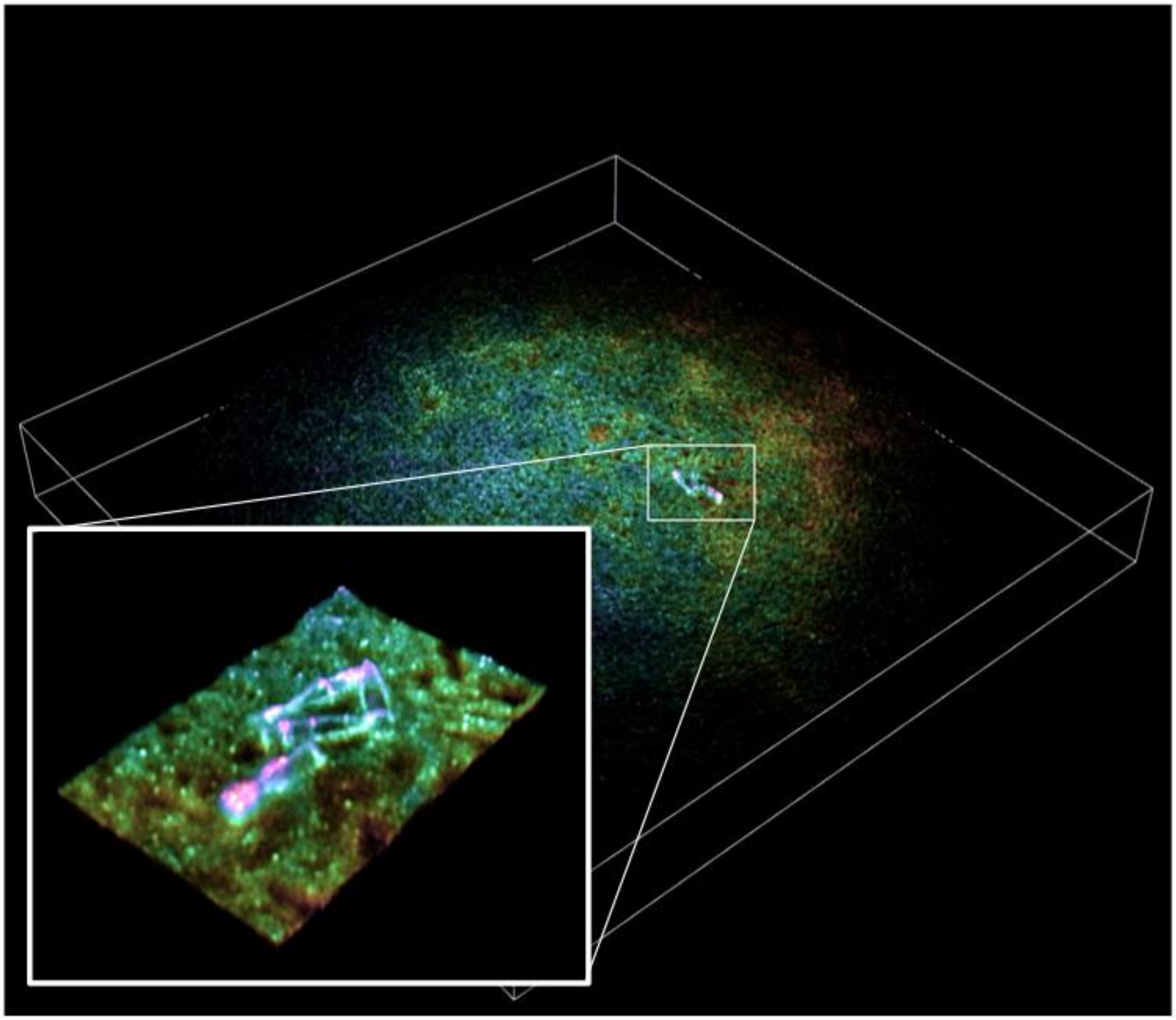

Figure 103. 3D multipass image of the UXO cluster showing their state of partial burial in the mud.

Partially Exposed Howitzer Shell Results

A 155 mm Howitzer shell was placed by the divers with specific instructions to be partially buried in the mud (less than 50%) with the nose end tilting up. Motivation for this placement came from this configuration being frequently encountered in previous scans of real UXO in a mud environment. The following shows the 3D high frequency image of the UXO and a zoomed snippet, showing the orientation of the target relative to the sediment:

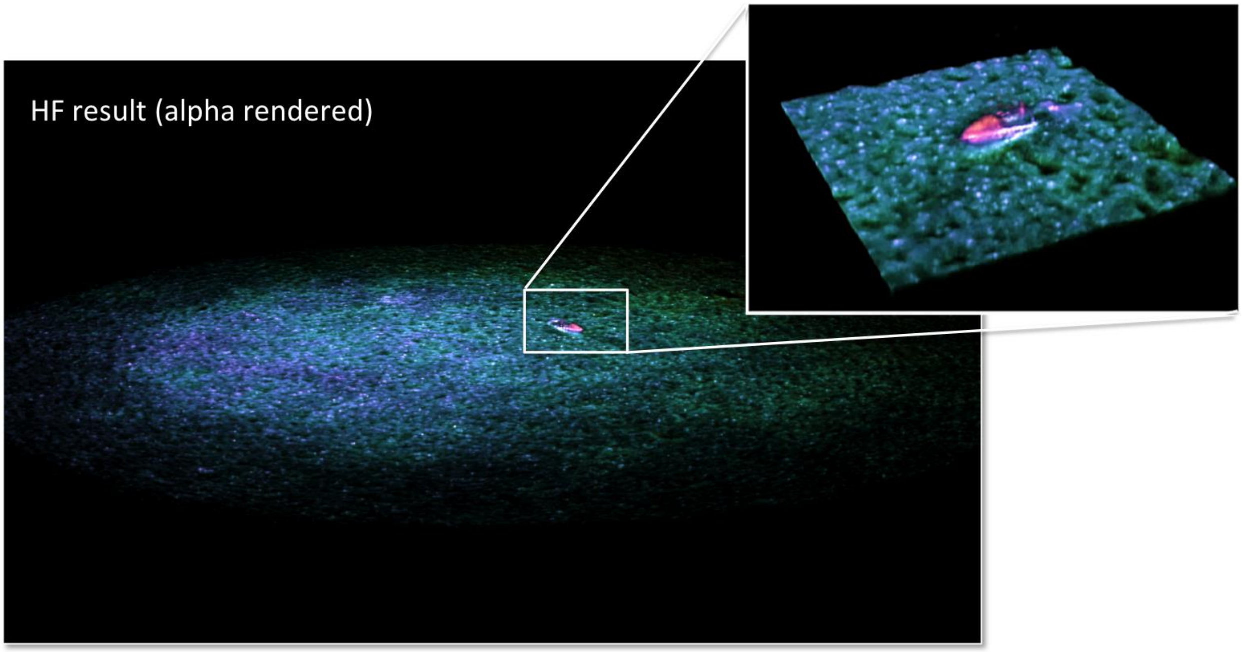

Figure 104. A partially buried UXO with the nose tilted up. The nose cone at the front end of the UXO exhibits extensive scattering due to the nose cone having a larger amount of surface roughness from the rest of the body and different structural properties.

Unlike examples tilted in sand, the target tilted in mud does not seem to have as strong multipath backscattering contributions. There are some contributions visible in the low frequency however, as shown in the next image:

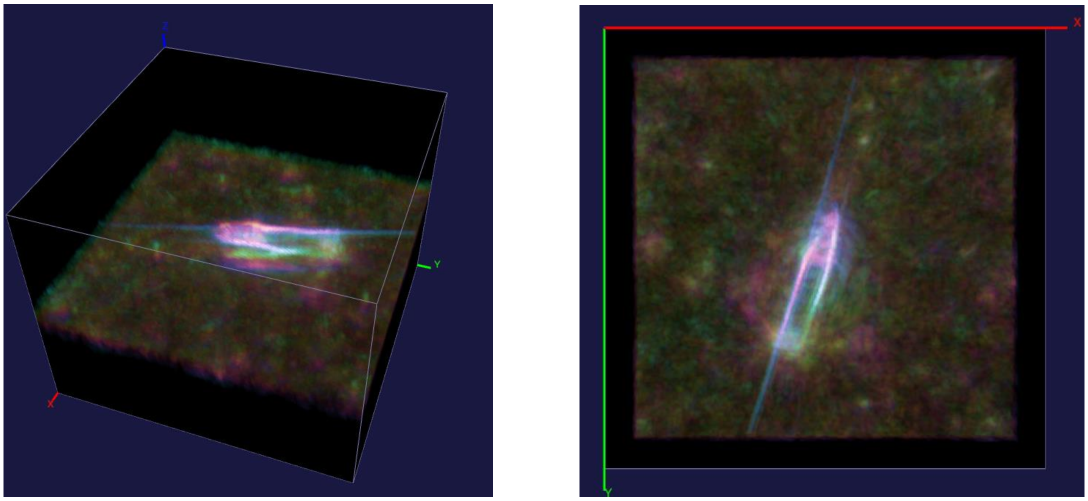

Figure 105. 3D LF MIP's of the UXO target. Color corresponds to height. The streak on the left side of the target is a result of a slight aperture misregistration in the region corresponding to the glint. A faint halo around the target indicates the presence of elastic scattering.

The back end of the target is largely hidden in the HF image due to burial, but all edges of the target are visible in the LF. The distinct nose-cone portion of the target visible in the HF is also visible in the LF image. Furthermore, multipath scattering seems more prominent in the LF, though it still has a diminished level relative to the direct backscattering. The dominance of the direct backscattering component gave rise to the hypothesis that the complex free-field data may correlate well with this experimental data, provided orientation is accounted for. To test this hypothesis, the complex wavenumber response corresponding to an approximately constant grazing angle was extracted. The following figure, also shown in the last MR-2439 in-progress report, shows the extracted data in both the angle-frequency and angle-time domains:

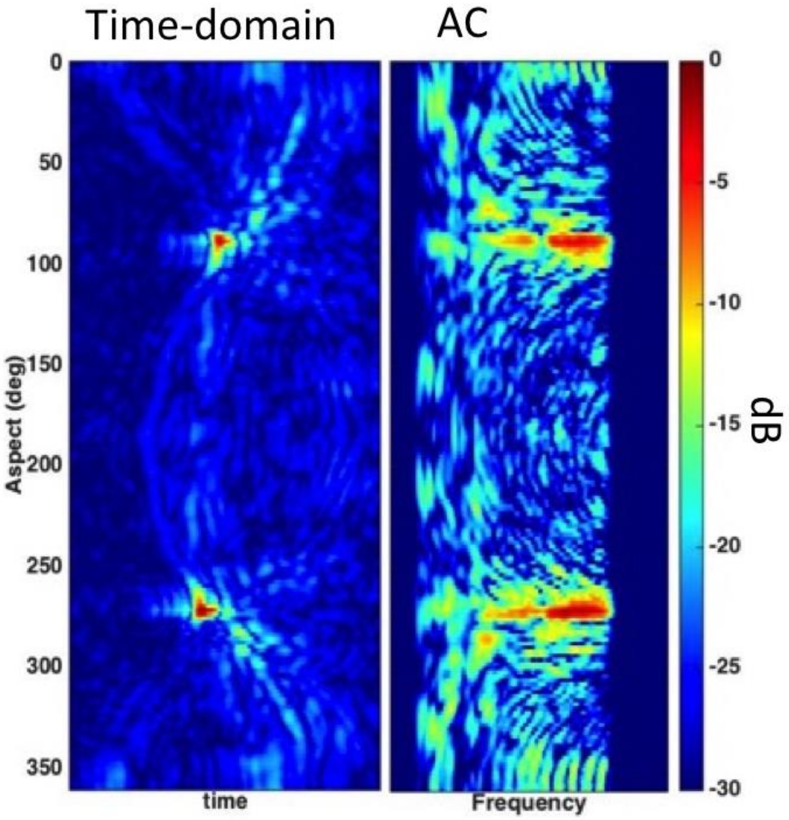

Figure 106. The extracted time-vs.-aspect data (L) and frequency-vs.-aspect (R) data for the partially buried, nose-up howitzer shell.

A question has arisen, in the past, as to whether or not elastic effects are dominant, or even significant in partially buried targets due to sediment damping and attenuation. If the previous response is compared to the response of a rigid finite-element model for a target of the same geometry, however, it becomes immediately apparent that much of what is being observed is elastic:

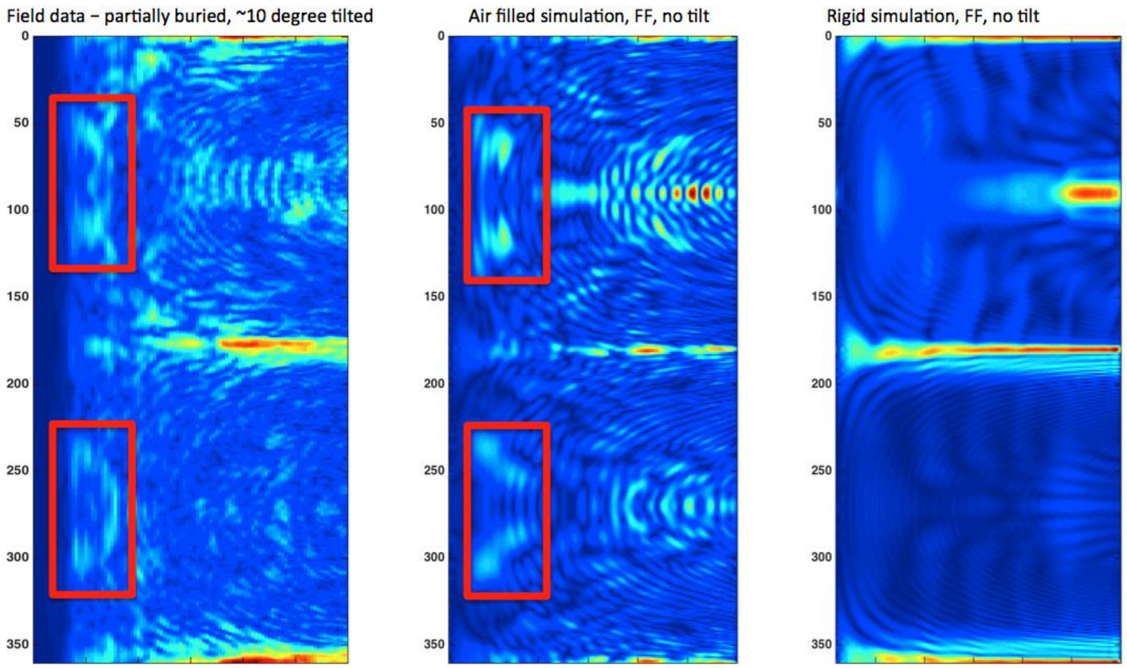

Figure 107. Field data (left), free-field, un-tilted finite element simulation data (middle), and free-field, un-tilted rigid target finite element simulation data (right). Prominent elastic mechanisms that are present in both the real data and finite element simulation are completely absent in the rigid model simulation.

If this is the case, then it was hypothesized that the experimental data should correlate more closely with the simulations including elastic responses than the purely rigid model. To test the hypothesis, the extracted field data and simulations were converted to the time-vs.-angle domain. The datasets were windowed to have matching duration and frequency domain support, and resampled to have equal spacing in the angle domain between 0 and 360 degrees. Two-dimensional cross correlation evaluated using the two dimensional Fast Fourier Transform was used to compare the datasets:

$$Corr_{I_1,I_2} = MAX\left\{\frac{\left|iFFT^{(2)}\left(FFT^{(2)}(I_1(x,y))*conj\left(FFT^{(2)}(I_2(x,y))\right)\right)\right|}{\sqrt{\sum_{x,y} I_1(x,y)*conj(I_1(x,y))}*\sqrt{\sum_{x,y} I_2(x,y)*conj(I_2(x,y))}}\right\} \qquad (38)$$

In (38) $FFT^{(2)}$ and $iFFT^{(2)}$ represent the forward and inverse two dimensional Fast Fourier Transform operations, the *conj*() represents the complex conjugate of the values inside the parentheses, and $I_{1,2}$ are the complex time-vs.-aspect datasets being compared. In (38) the denominator normalizes the peak so that the value lies between 0 and 1, where a value of 1 means the datasets are identical and zero means perfectly incoherent (which never occurs in reality). Because the complex signals were correlated, the correlation value is sensitive to the phase of these components. Object translation within the image domain region of interest manifests as a sinusoidal delay across azimuth with an arbitrary phase and amplitude depending on the length and direction in the time-vs.-aspect domain, and therefore has a big impact on the correlation component if left unaccounted. Cross-correlation were therefore maximized over translation and also over the tilt-angle of the target, which equates to a different sub-sampling of the 3D wavenumber response of the free-field model. The correlation score is invariant to rotation in aspect, however, as well as static time delay errors. The following table lists the resulting correlation scores for different FE models:

Model	Correlation score
Air-filled howitzer shell, with end cap	0.45
Water-filled howitzer shell, no end cap	0.40
Rigid howitzer shell model, with end cap	0.38
Water-filled howitzer shell, with cap	0.34
Rigid 2-1 al. cylinder	0.33
Elastic 2-1 al. cylinder	0.29

Table 5. Correlation results between field data and different FE models

A number of observations can be made from the previous test. It is shocking, for example, that the simulation data for the air filled howitzer shell correlated so well with the experimental data, given that the simulation was in the free field and the experimental data was in a real environment with multipath contributions and various extra sources of noise and attenuation. The experimental data was also only clutter calibrated, (i.e., the spectrum was pre-whitened using random backscattering from sediment and objects), which means that the relative levels between bands could possibly diverge from the true values. Secondly, elastic effects played a major contributing factor to the final correlation scores, despite being partially buried. Lastly, the aluminum cylinder model also showed a surprisingly high correlation, possibly because the broadside feature has a similar width to the Howitzer shell. When elastic features were enabled for the cylinder, however, the similarity decreased, probably due to the fact that the elastic mechanisms in these objects are very different.

Lastly, a Matlab routine for training set generation was applied to this dataset to demonstrate the construction of multiple realistic target realizations at high frequencies. Ordinarily, sonar systems perform wide area surveys using straight-line patterns and only observe objects over a limited range of aspect angles and at discrete ranges (range is associated with grazing angle). The acoustic backscattering response of objects can vary a huge amount, depending on the aspect and grazing angles of observation, [39.]. To be robust, target recognition algorithms must be cognizant of the different acoustic manifestations a target may have, given these angles as variables. In this project, these targets have already been scanned over a continuous range of aspect and grazing angles, and it is therefore possible to sub-sample the spectrum to generate a library of target realizations showing the different possible target manifestations for wide area survey systems scanning using linear apertures. It is further possible to modify these target realizations using common sources of focusing error that occur in wide area systems such as quadratic phase error ([49], [50], etc.]), which occurs with low levels of motion error or sound-speed error, or background noise level, which can change depending on water depth and ambient noise. Using these four variables, (aspect angle, grazing angle, quadratic phase error, noise level), a large set of target realizations were generated with random realizations along these variable axes. A few of the results are shown in the figure below:

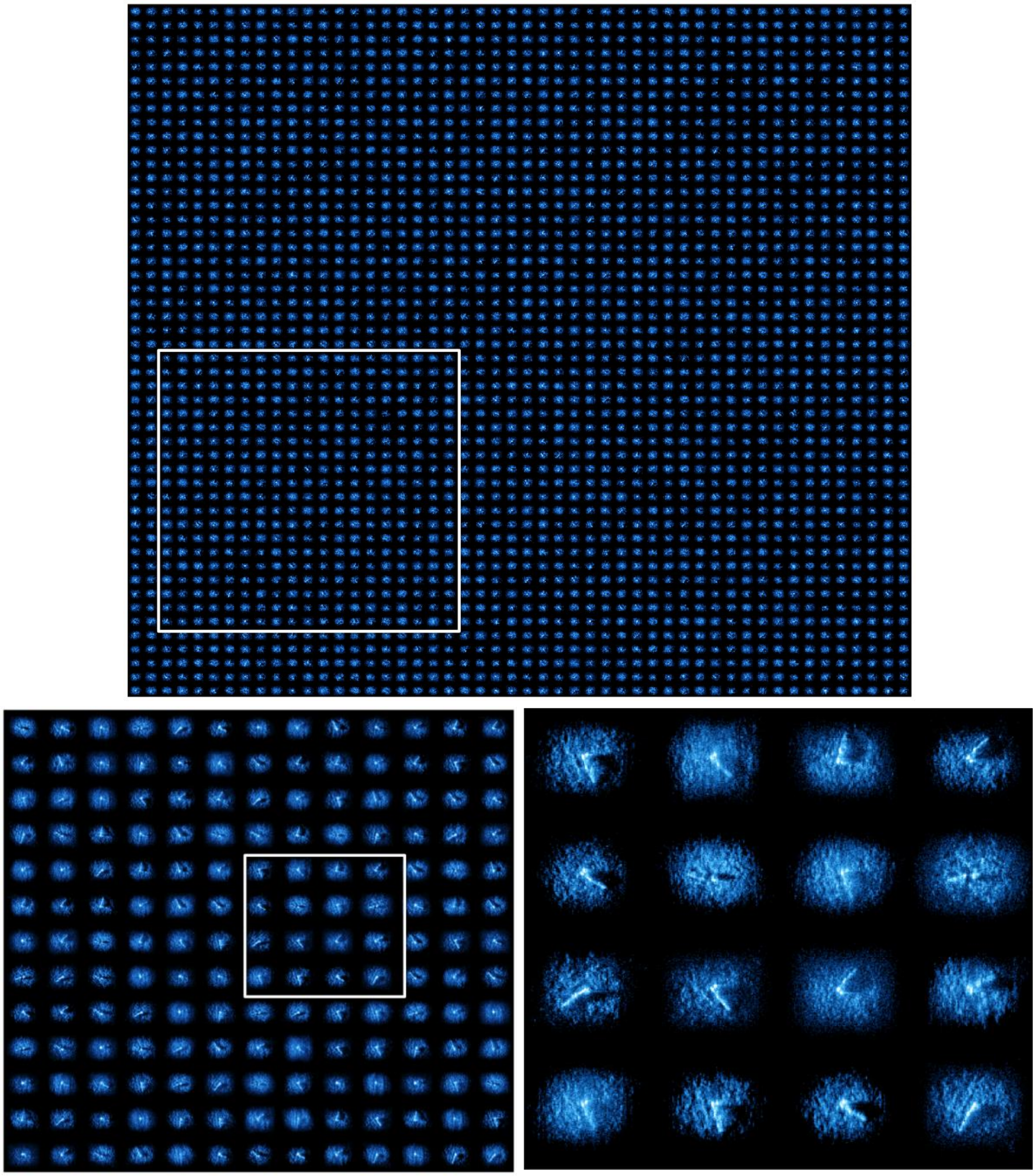

Figure 108. Target realizations for grazing angle (changes shadow length), aspect angel (target rotation), noise floor, and quadratic phase error (a common synthetic aperture defocusing effect). The top figure shows the full generated set of realizations. The bottom left plot is a zoom of the box in the top figure. The bottom right plot is a zoomed plot of the box in the bottom left.

The kind of libraries shown in the previous figure are useful for studying the performance of classifiers, especially determining which aspect angles, or which values or combination of values along the library generation axes cause significant drop or increases in target recognition performance. This kind of performance analysis can be used to determine, for example, both the number and orientation of passes necessary in a wide area survey to bring the probability of detection up to a minimum threshold. The usage of these libraries for ATR algorithm performance analysis is outside the scope of the current project, but research for how to effectively use this kind of training library for performance analysis is ongoing in other projects. Additionally, other research has shown that these kind of libraries are useful for training deep-learning based classifier networks, which typically require an enormous number of examples [51]. In the present case, rather than relying on unrealistic permutations to increase the number of training samples, rotational variation can be made with actual data instances.

Proud 2-1 Aluminum Cylinder on Mud Results

Divers positioned a 2-1 solid aluminum cylinder, of length 60 cm and diameter 30 cm, in a muddy environment. Attempts were made to make the cylinder proud, however because of the mud it inevitably sank, in this case approximately 10 centimeters, into the sediment. The following figure is a combined HF/LF ~15 x 15 meter maximum intensity projection image of the scene, where, as in previous cases, high frequencies are shown in blue and low frequencies are shown in red.

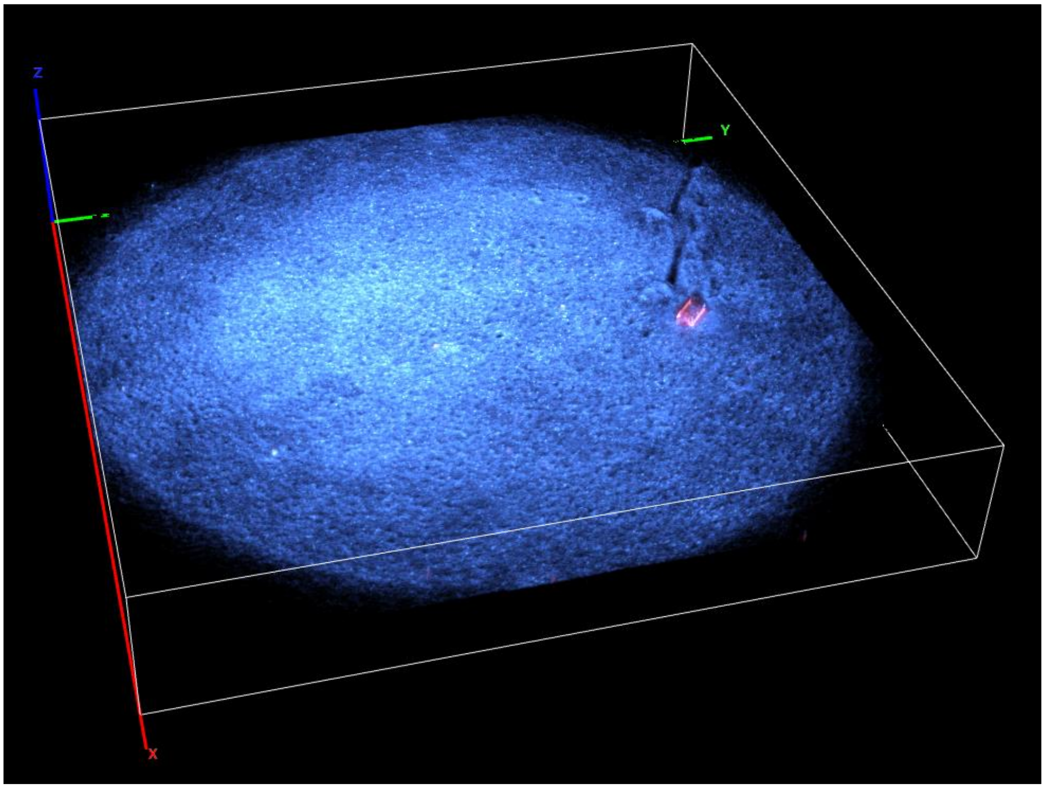

Figure 109. Scene containing a 2-1 solid aluminum cylinder.

Scour marks near the target indicate that it was dragged, perhaps by a diver, several meters. Additionally, the target is a not in the center of the beam and only received partial insonification from the high frequency beam, resulting in poor HF image reconstruction. The LF data captured all of the edges of the target, however, due to its wider beam coverage. The following alpha-rendered snippets show the object from different angles.

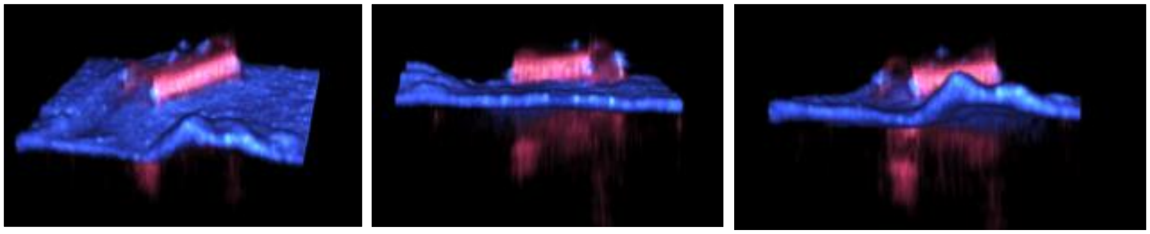

Figure 110. A zoomed in snippet of the target, viewed from different directions.

From Fig. 110 it can be seen that some of the scouring is almost as thick as the target. The broadside glints of the target are the brightest thing. Multipath from the target images beneath the sediment layer in the LF data, and corner scattering enables the circular ends of the target also to be faintly visible in the LF data.

Wavenumber response extraction was tested using this particular target. To test the effectiveness of wavenumber response extraction from the complex 3D LF image of the target a cuboid region surrounding the target was extracted. This region is shown in the figure below:

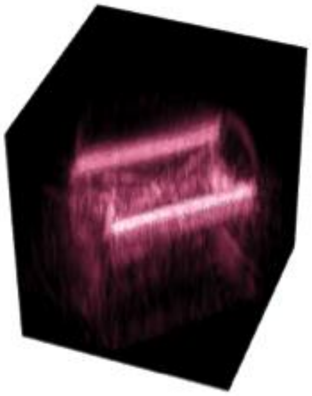

Figure 111. The extracted 3D region around the target, containing the scattering response of the proud cylinder. A low frequency image.

To compute the three-dimensional wavenumber spectrum, the three-dimensional Fourier transform for the complex image cube is computed. This spectrum is shown in the following image:

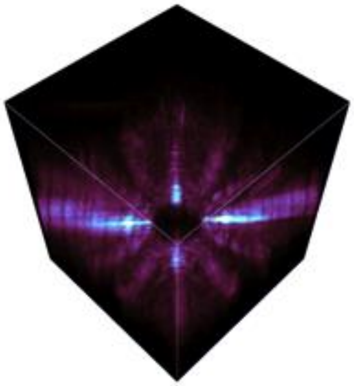

Figure 112. A maximum intensity projection image of the three-dimensional wavenumber spectrum computed for the image cube shown in Fig. 111.

In the previous figure, the broadside and end-on responses appear as spokes radiating from the center of the spectrum. The limited bandwidth results in the circular gap in the center, the edge of which is determined by the lower frequency bound of the signal band. The previous figure is transformed into a 3D acoustic color image by transforming the previous cube into spherical coordinates, where the vertical axis represents the acoustic frequency response as a function of grazing angle, the horizontal axis is aspect angle, and final axis is absolute wavenumber, proportional to temporal frequency:

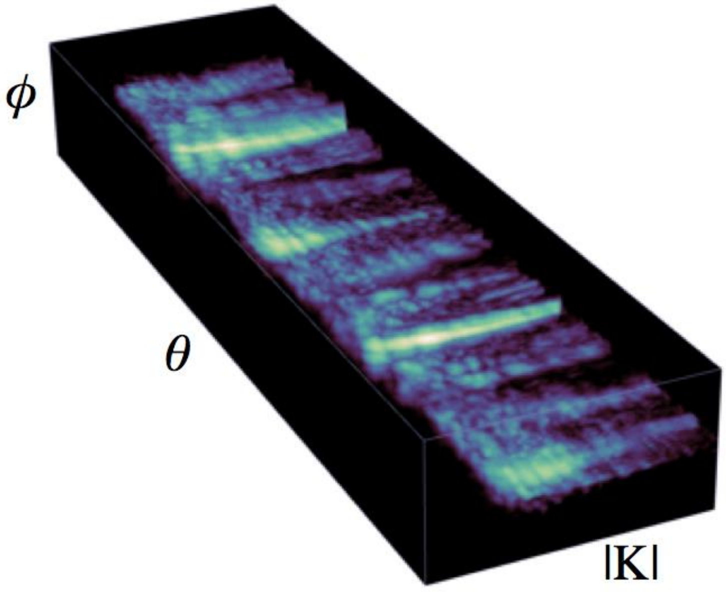

Figure 113. The 3D wavenumber spectrum after a Cartesian to spherical coordinate transform. Phi, the vertical axis, represents the response as a function of grazing angle. Theta is aspect angle and |K| is absolute wavenumber, proportional to temporal frequency.

The wavenumber response, transformed into spherical coordinates, can be sub-sampled to generate target realizations, or generate acoustic color plots for the target at different grazing angles, which can serve as a proxy for target range. Fig. 113 shows maximum intensity projection images in the ϕ and |k| dimensions.

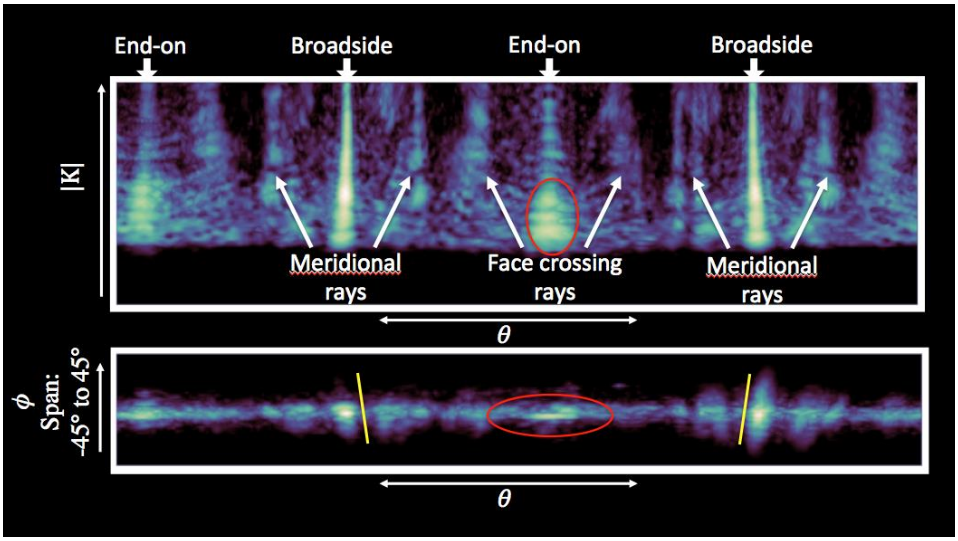

Figure 114. Maximum intensity projections of the spectrum shown in Fig. 113, with various features indicated. The feature contained in the red oval is an end-on backscattering mechanism with a high degree of angular directivity. The yellow lines draw attention to the slope of the broadside response, indicating that the target has a small degree of tilt relative to the sediment. Other elastic scattering mechanisms commonly visible in solid cylinders are also highlighted.

Various features commonly observed in solid aluminum cylinders are highlighted in the previous figure. It can also be observed that scattering off of the end of the cylinder, especially from one side of the cylinder, has a high degree of directivity in the vertical direction. Observation of this type of feature was one of the main motivations for capturing the extended data sets. This directivity can be viewed more directly if linear SAS snapshot images are sampled from the 3D wavenumber spectrum, similar to the previous example of training library generation. This is done in the following figure:

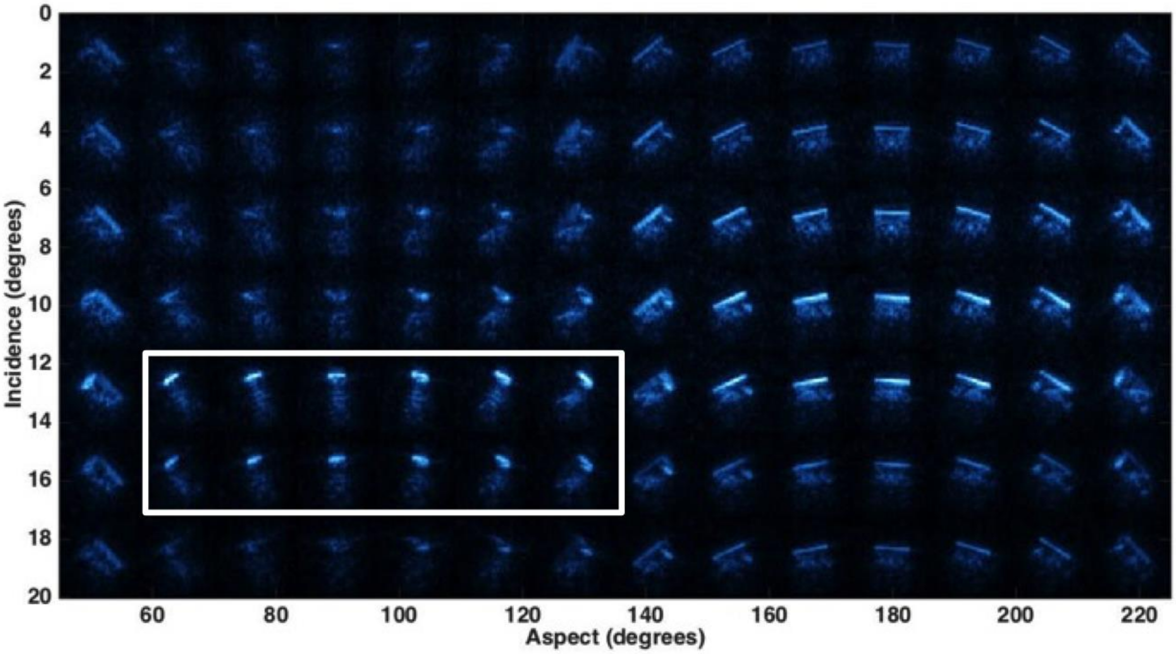

Figure 115. A set of low-frequency linear SAS snapshots, showing the variation in target response as a function of both incidence angle and aspect angle. The white box highlights the regions with enhanced backscattering.

The end-on response shows a very rapid peak at around 13 or 14 degrees. The minimum angle of insonfication in the scan was about 5 degrees, and the samples corresponding to look angles below this threshold are a result of spectral extrapolation from sparse beamforming. Those extrapolated samples do not necessarily accurately reflect the target scattering response.

2-1 Aluminum Cylinder Suspended in Mud Results

The next section discusses the results for the target suspended in mud. Since the mud had a sound speed slower than water, in this case no critical angle was present, and the target was directly visible due to penetration into the mud layer. The following image is the Z-projection through the high frequency data cube, showing the sediment interface:

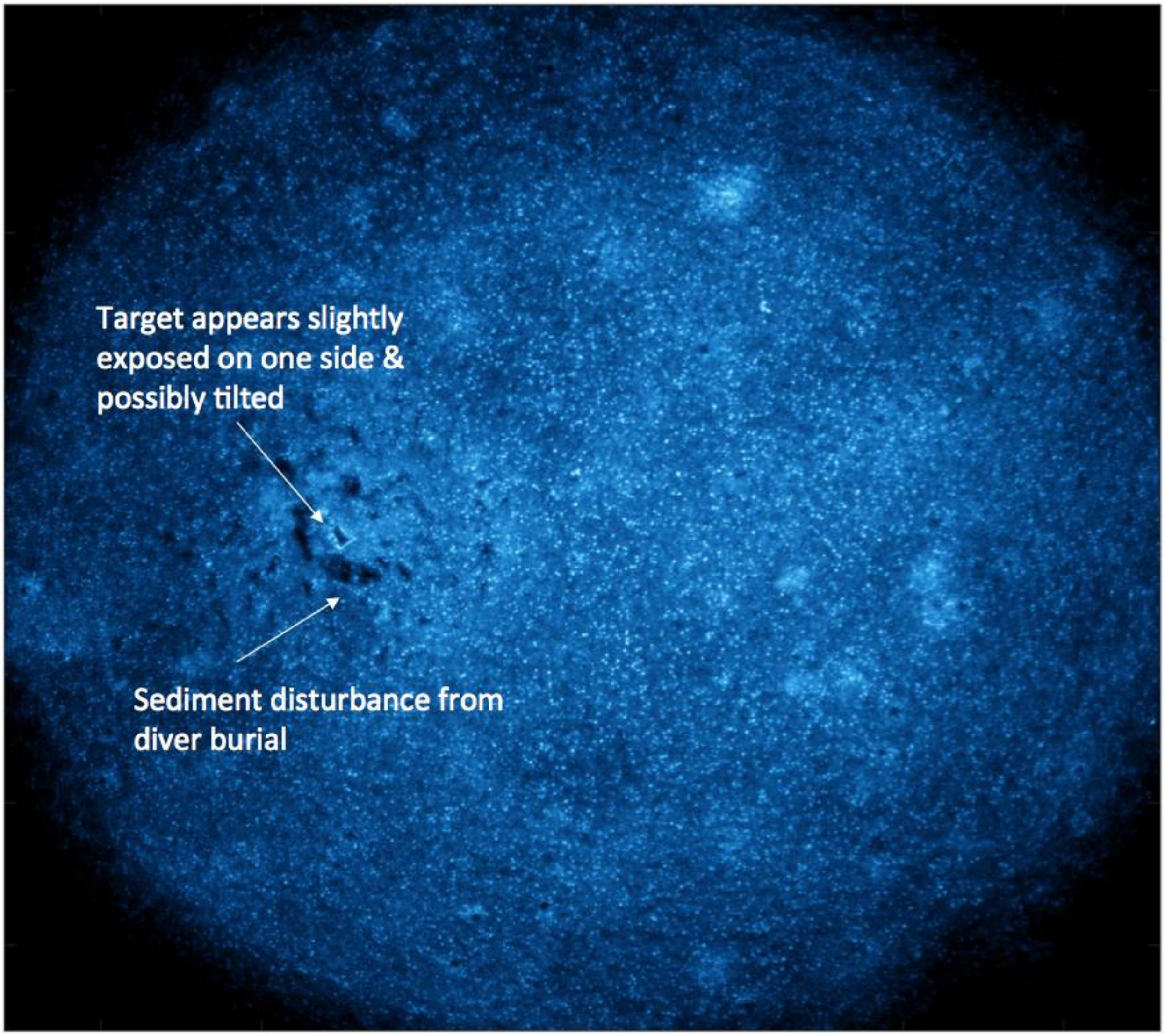

Figure 116. Z-dimension maximum intensity projection through the high frequency image cube containing the flush-buried 2-1 cylinder suspended in the mud layer.

In the HF image, the sediment appears disturbed in the region of the target and one corner of the target appears to be slightly exposed. The target appears to be offset from the center, but not by the same amount as the proud cylinder. The next figure shows the equivalent image, in the low frequency band:

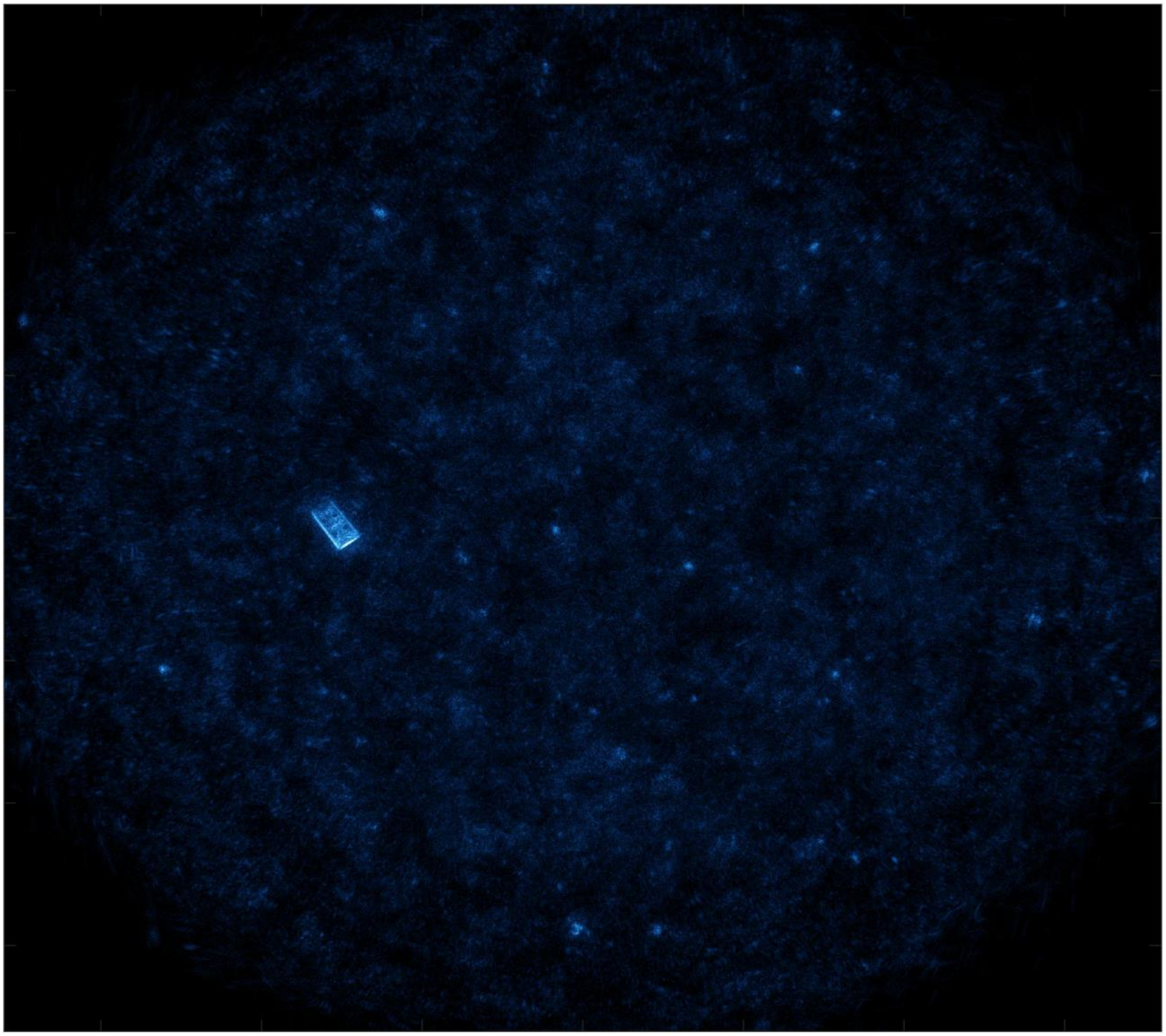

Figure 117. Z-dimension maximum intensity projection through the *low frequency* data cube corresponding to the flush buried cylinder suspended in mud. This is the exact same scene as the previous image but showing the low frequency imaging results.

Note that in the low frequency figure the cylinder is the brightest object in the scene, vs. the high frequency image in which only a corner was visible. Other point-like structures are distributed in the mud as well. This can be further observed by looking at a maximum intensity projection through one of the horizontal dimensions of the image cube. A projection onto the *zy* plane, through the *x* dimension is shown in the following figure.

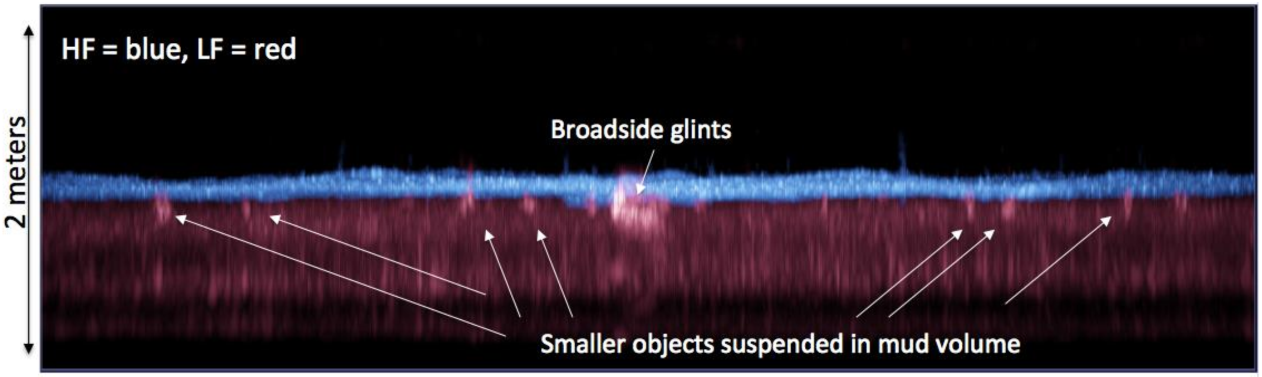

Figure 118. A maximum intensity projection in the *x*-dimension through the composite HF/LF data cube where blue is high frequencies and red is low frequencies. The low frequencies show the burial depth of the suspended target and the presence of many other smaller objects in the mud.

When the patch of the image containing the target is rendered with pixel opacity (i.e., alpha-rendered), the cylinder is occluded when the image is viewed from above the sediment. It is visible, however, if the image cube is viewed from below the sediment, as shown in Fig. 119:

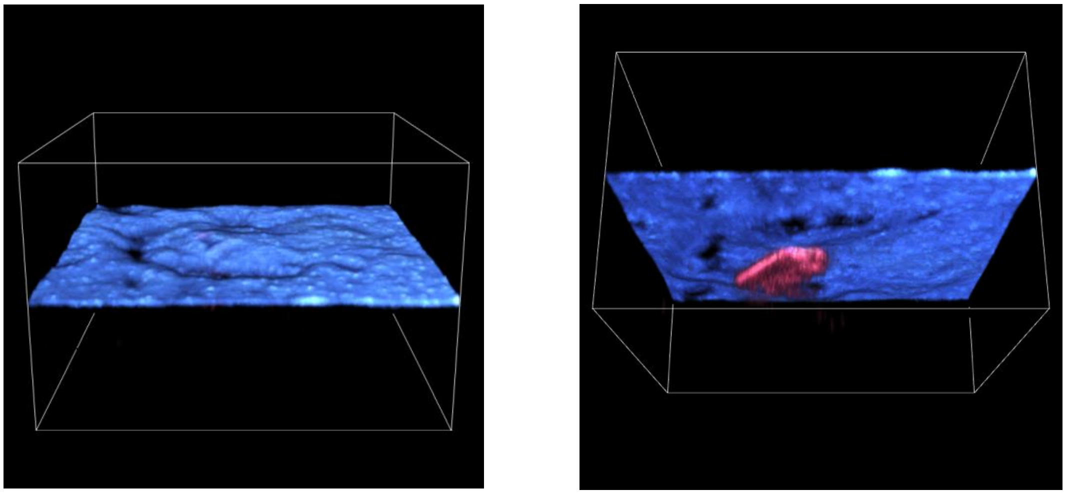

Figure 119. Two views of the same alpha rendered data cube, one view from above (L) and another from below (R) the sediment.

As was done in the proud case, a 3D acoustic color spectrum was extracted from the complex LF 3D image. In this case the bounding box containing the target was 1 x 1 x 2 meters in dimension. The following figure shows the 3D wavenumber spectrum computed for the 3D region of interest containing the target.

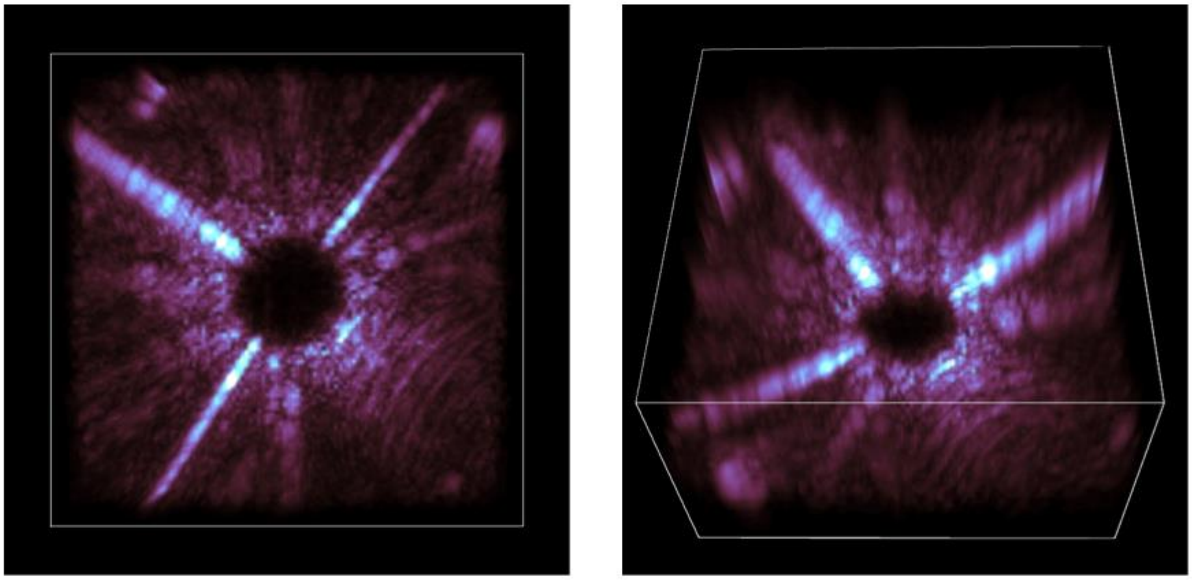

Figure 120. Maximum intensity projections of the 3D wavenumber spectrum

It can be seen in the previous figure that both broadside scattering mechanisms (the two bright, opposing spokes radiating from the center) are visible in the spectrum. Only one end-on spectrum is visible, however. This is consistent with the image for the target shown in figure 117, which only shows one end of the target being visible. Fig. 118, the side-view maximum intensity image, shows that the target has a visible slope. What has probably happened is that the down-tilting side is reflecting the acoustic energy away from the receiver, and hence no backscattering signal is received.

This 3D wavenumber spectrum was converted to a 3D acoustic color spectrum in spherical coordinates. A tilted maximum intensity projection through the data cube is shown in the figure below:

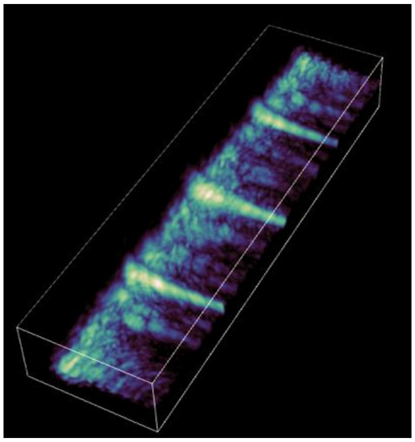

Figure 121. The 3D acoustic color response of the cylinder suspended in mud. As in Fig. 113, the axes represent grazing angle, aspect angle, and frequency.

Interesting features are visible in this domain, and better illustrated using maximum intensity projections directly along the image axes. The figure below is a projection along the frequency axis.

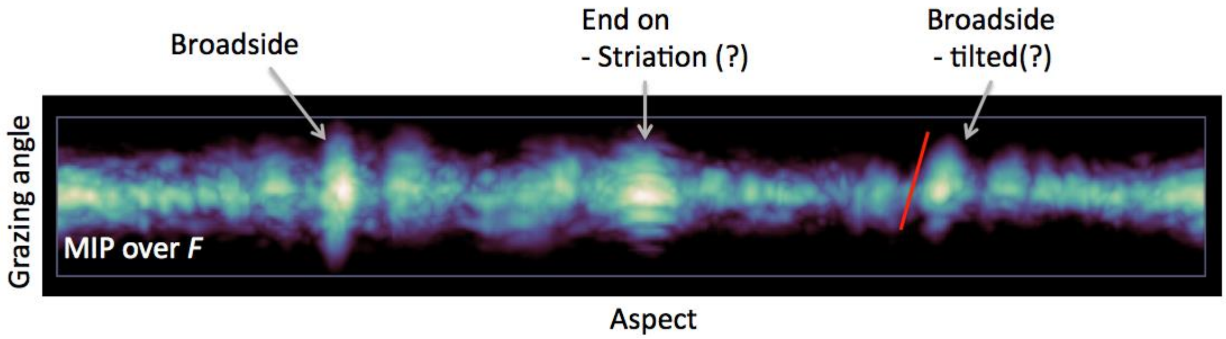

Figure 122. A maximum intensity projection through the 3D acoustic color in the frequency dimension.

One of the broadsides appears to be tilted, and this is possibly due to the sediment locally having a different slope relative to one side of the sediment vs. the other. The end-on scattering from the side tilted up toward the array shows a striation pattern in the vertical dimension. Despite the target being completely buried, elastic features were strongly visible in the target as well, and can be seen in a maximum intensity projection through the phi dimension:

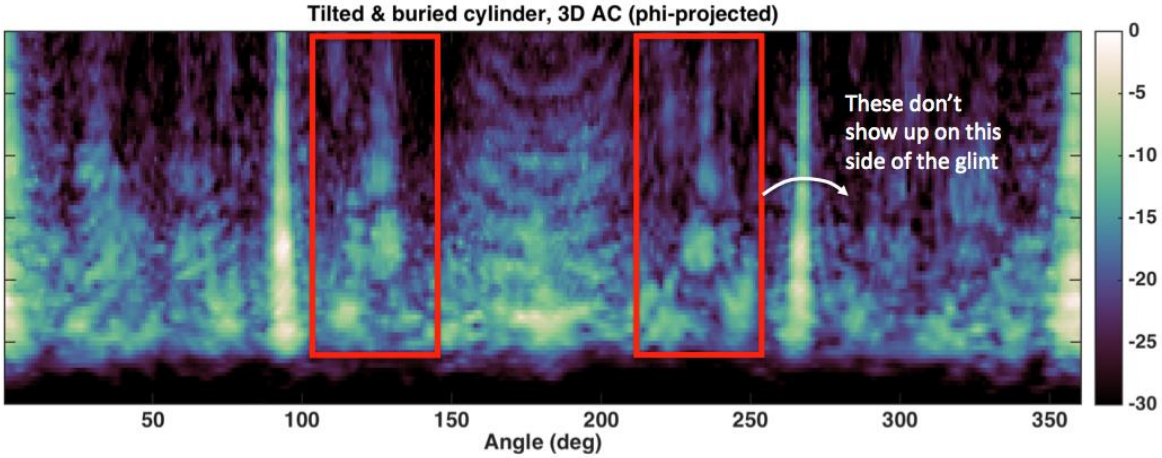

Figure 123. The 3D acoustic color for the flush buried cylinder suspended in mud. Color scale is in dB, vertical axis is proportional to frequency.

In the previous figure, 180 degrees corresponds to down-tilted end of the cylinder. It is interesting to note that the elastic meridional ray contributions [52], highlighted in the red box, symmetrically occur around the down-tilted end, but are absent or highly attenuated on the other side. This may have something to do with the tilt of the target, but it establishes that, in a muddy waveguide, elastic features are can be present and dominant scattering mechanisms.

Boat Wreck: Bow and Stern Results

The last targets scanned in the first set of spiral scan field trials were the bow and stern of a wreck of an abandoned sailboat. As mentioned previously, due to erroneous GPS coordinates, these targets were completely missed (i.e., completely outside the scanned circles). However, the sediment was highly unusual. Randomly distributed over the scene were thousands of almost perfectly isotropic scatterers. Other than bubbles, perfectly isotropic scatterers are rarely encountered in CSAS scans of natural environments – especially scatterers that have dimensions smaller than a wavelength. These scatterers offered a perfect testbed for evaluating the phase accuracy of the multilateration autofocus procedure, and to compare the experimentally realized resolution gains between CSAS and linear SAS scans. The following figures show the CSAS image of the region in which the bow was supposed to have been located, and the real component of the complex beamformed image for zoomed snippets of isotropic scatterers.

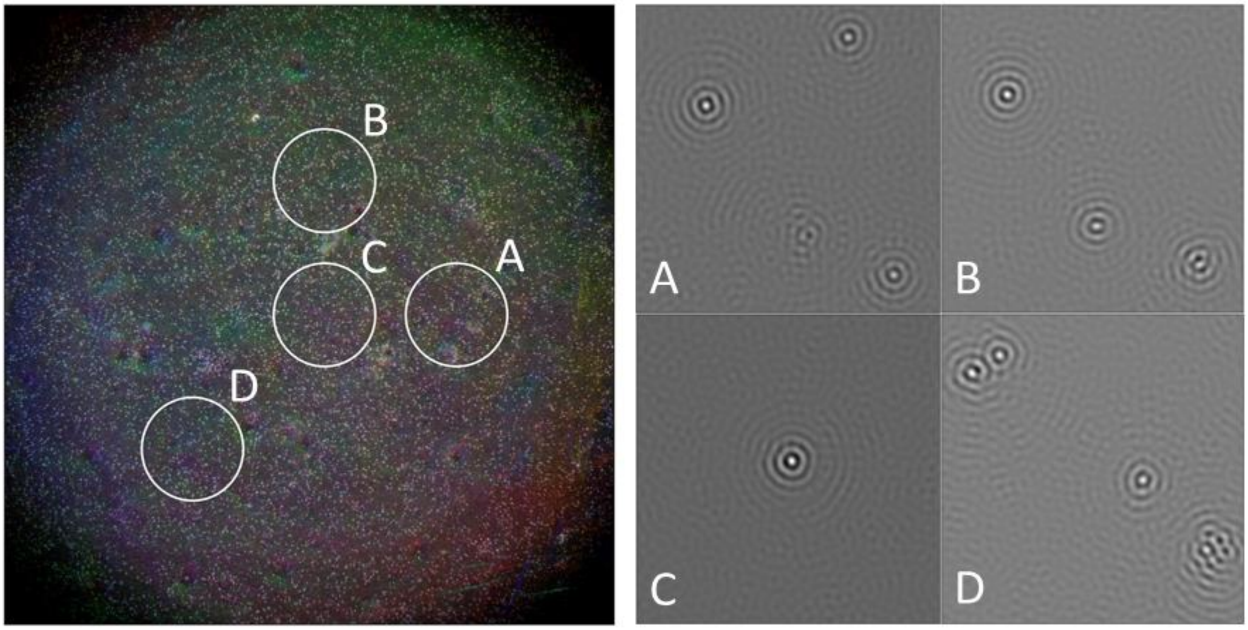

Figure 124. The single pass CSAS scan of the region in which the boat bow was supposed to be located. Multilateration focus regions are shown in the circles labeled A – D. The figure on the right shows the real part of zoomed snippets from each of these locations containing isotropic point scatterers.

As can be seen from the previous image, the scattering signatures from the point-like targets qualitatively behave very similar to the difference – of – Airy function patterns predicted for circular aperture systems scanning ideal point targets [53]. A slice through one of these targets is plotted vs. the same slice through a windowed sub-aperture of the scans, showing the range resolution of the system.

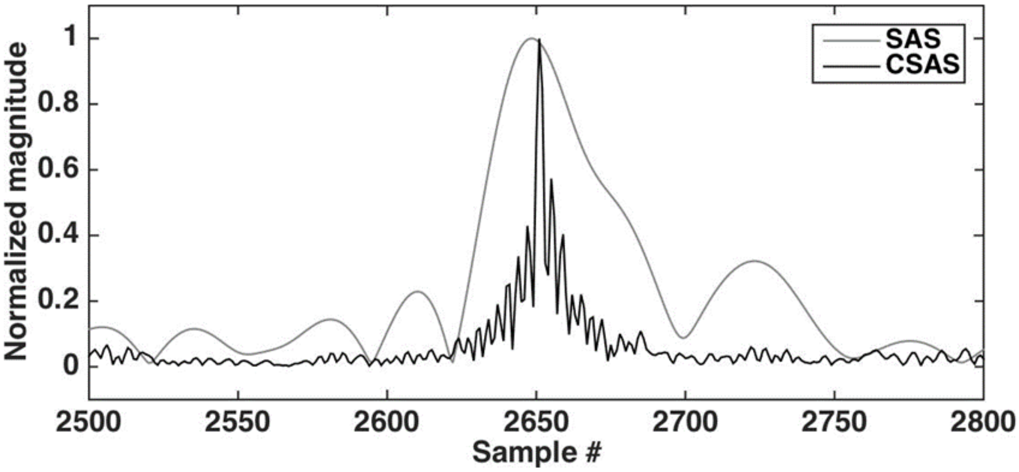

Figure 125. A slice through the same point target for the full-aperture CSAS case and the case in which the target is windowed to behave like an ordinary linear scan. In the latter case, the slice is oriented in the range direction.

Quantitatively, the -3dB peak width ratio between the SAS and CSAS versions of the point target reveal a resolution gain greater than a factor of 12, putting a definitive number of the focusing gain improvements of a real CSAS system scanning sub-wavelength sized targets. This particular data set, then, verified 1) the practical resolution enhancements gained by the circular scan imaging modality, and 2) that multilateration, in contrast to statements implied in [54] (see section on CSAR autofocus), is capable of giving a 3D navigation solution of sufficient quality to fully focus isotropic point scatterers.

8-Foot Step Ladder Results

The major motivation for scanning a ladder was to stretch the beamforming process in regards to the sampling region of support. As mentioned in previous literature [55], [11], the vertical sample rate determines the maximum height extent of a target that can be reconstructed from a given scan. Tighter spacing extends the allowable height distribution of objects. In the present case, the vertical aperture is irregularly sampled, however the tightest spaced samples – the upper and lower interferometric staves of each scan, potentially enable unambiguous beamforming for objects up to approximately 2.5 meters in vertical extent. Though the rest of the array is undersampled, the compressive sensing approach drives down the ambiguities to an acceptable level for imaging. The following figure contains maximum intensity projections through an HF/LF composite image, along with a photograph of the target.

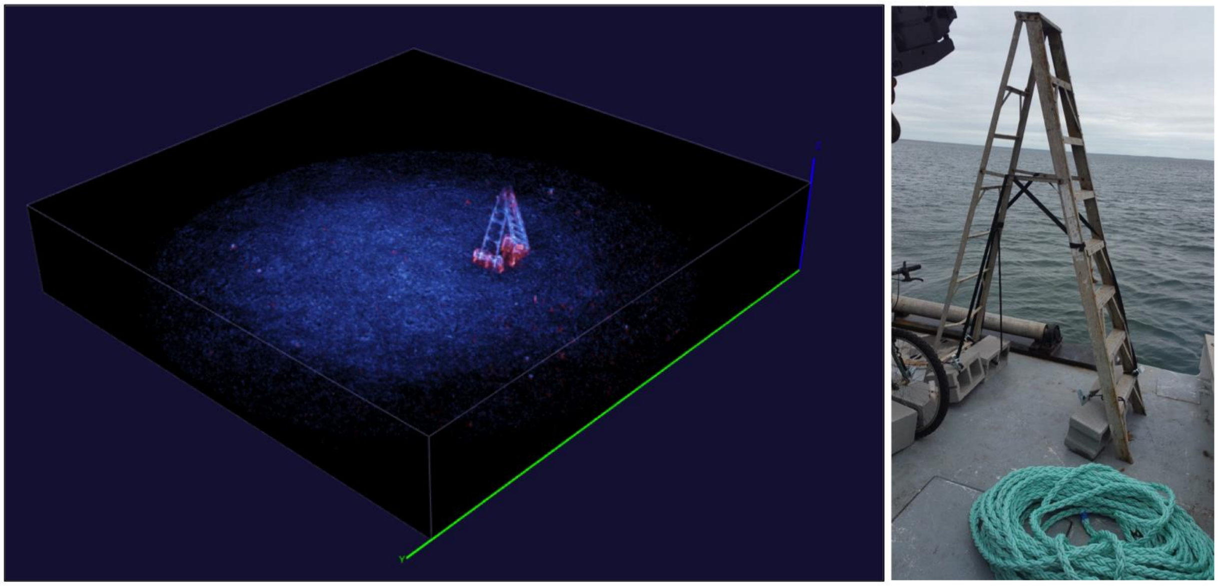

Figure 126. A maximum-intensity-projection image of an HF/LF composite image of the scene with an 8-foot ladder, and a photograph of the same target prior to being placed by divers.

From the photograph on the right of the previous figure it can be seen that cinder-blocks were tied to the bottom of the ladder to weigh it down and stabilize the target. These can be seen much more clearly in the *z*-dimension maximum intensity projection through a zoomed image cube, shown below:

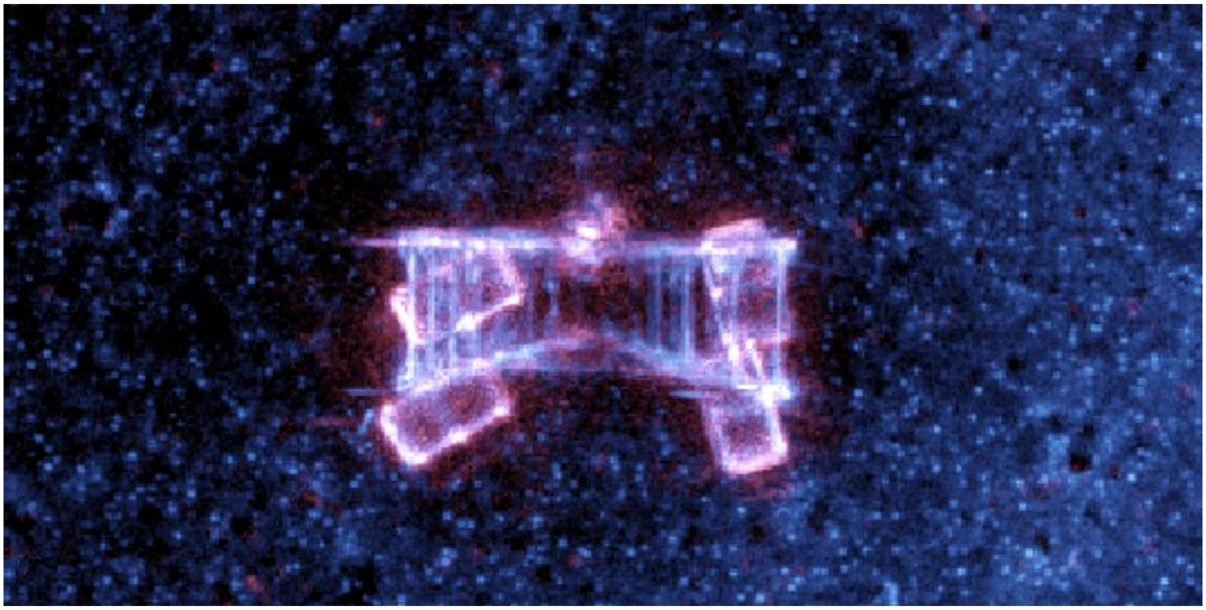

Figure 127. A maximum intensity projection through the Z-dimension of the composite HF/LF image of the ladder.

In the previous figure, the cinder blocks stabilizing the ladder are clearly visible. In fact, these appear to have sunk partially through the water/mud interface, and are predominantly visible in the low-frequency data, as shown in the following images, which show tilted and side projections of the data cube:

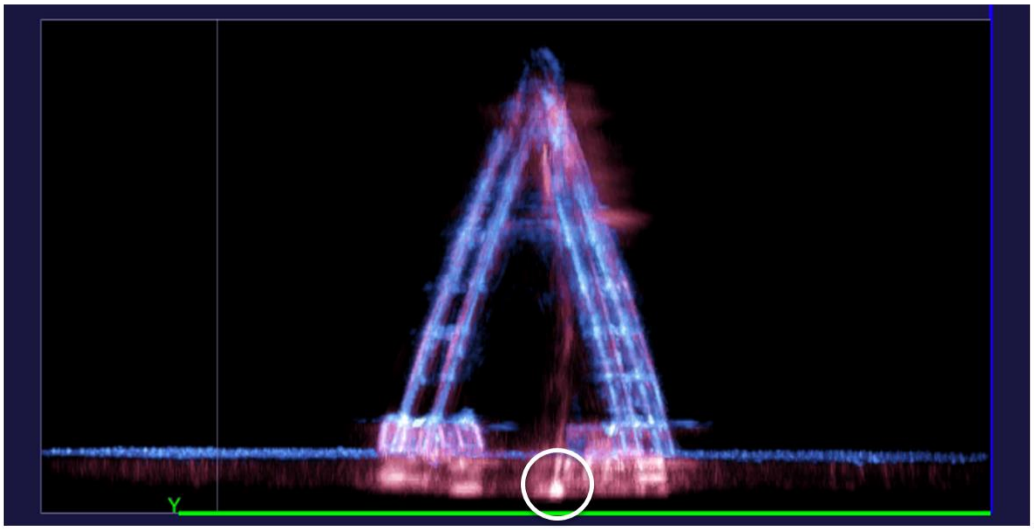

Figure 128. Side view maximum-intensity projection of ladder. A weight or clip suspended from the ladder, sunken in the mud, appears to be visible (inside white circle).

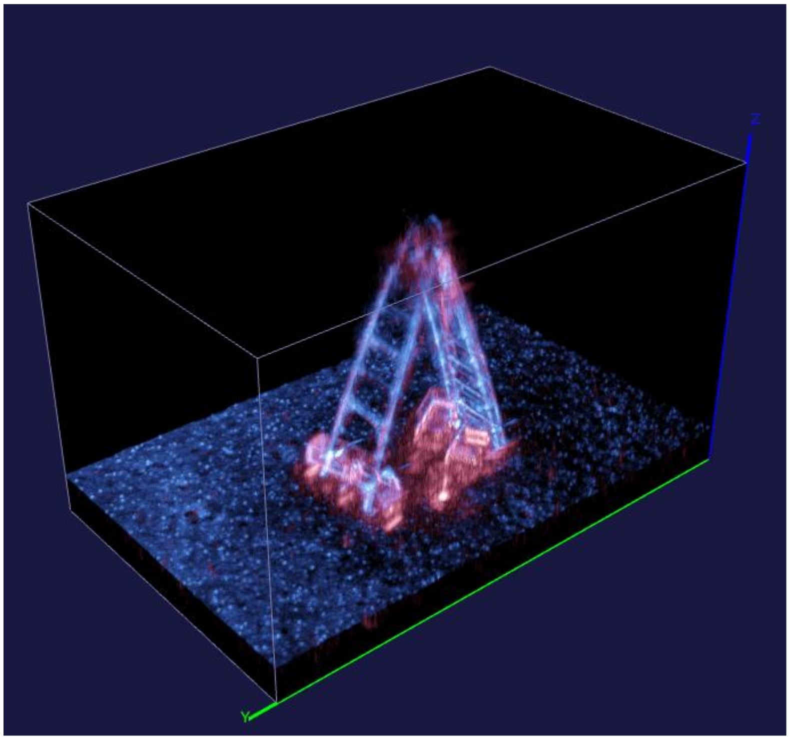

Figure 129. Maximum intensity projection from a different angle. The same sub-sediment scatterer is visible, along with the cinder blocks.

A large number of mud-suspended scatterers are visible in the previous image, along with portions of the cinder blocks. In the previous figure, the decreased image quality near the top of the ladder is also visible. Where the individual rungs of the ladder are visible most of the way up the ladder, near the top the physical features of the ladder become much more difficult to resolve. As previously noted, this target stretches the limits of the reconstruction capability of the current sampling method in the vertical dimension, so this breakdown in image quality is expected.

Bicycle Results

Fig. 130 shows a picture of a bicycle prior to being positioned by a diver in the upright position, on the sediment surface:

Figure 130. Photograph of bicycle used in a spiral scan dataset.

As with the ladder, cinder blocks have been strapped to the ladder to provide stability under water. The purpose of this particular scan was to give researchers an intuitive understanding of the resolution capabilities of the sonar. Most individuals unfamiliar with sonar technology are familiar with UXO shapes, but few have ever actually held or seen a 155 mm. UXO. Most people, however, have ridden bicycles and used ladders, and this object gives an intuitive idea of the capabilities of the current imaging method.

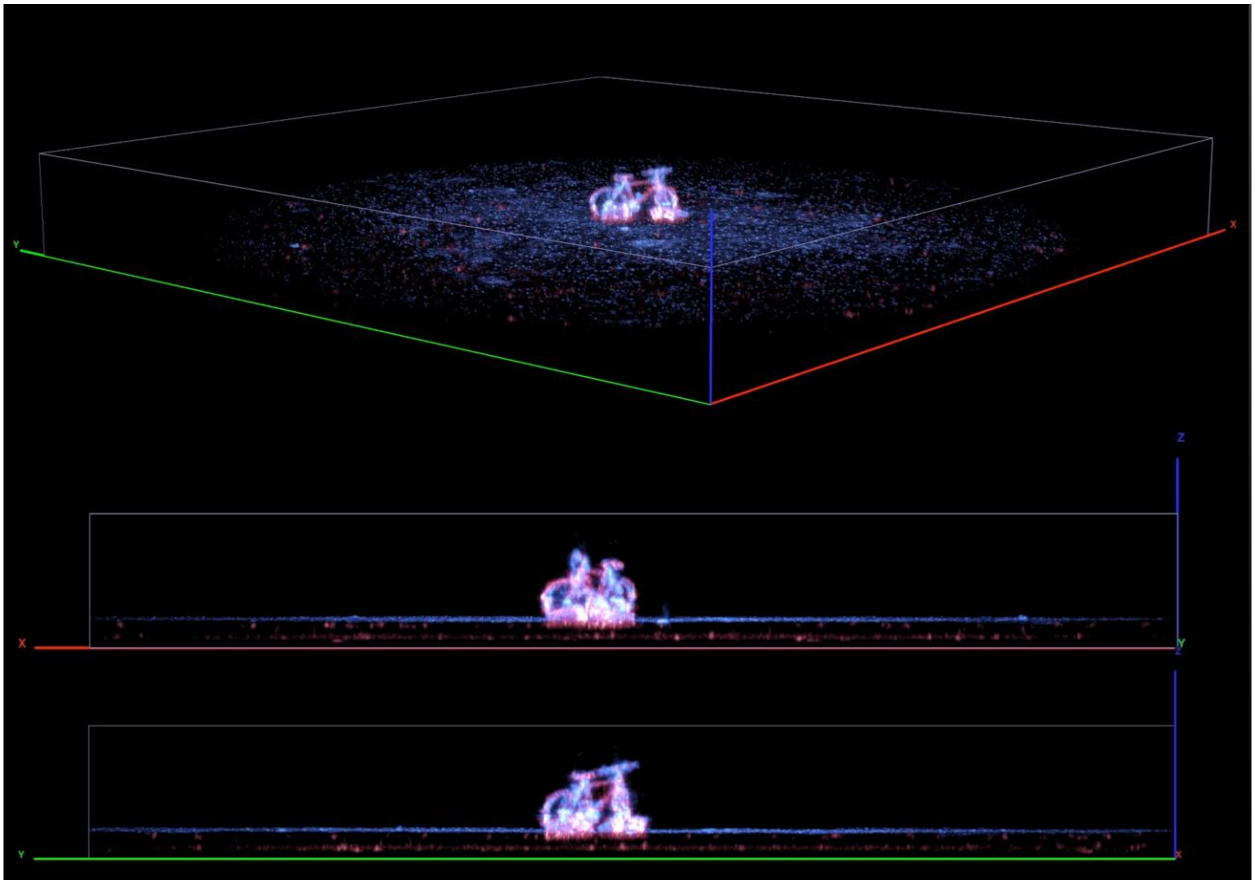

Figure 131. Three maximum intensity projection views of the bicycle.

In the previous figure, the bicycle, many of its features, and cinder blocks are all visible. Perhaps more interestingly, a sub-sediment layer almost as distinct as the mud-water interface is visible in the low frequency below the bicycle. Many discrete scatterers are visible at this interface and suspended in the mud layer.

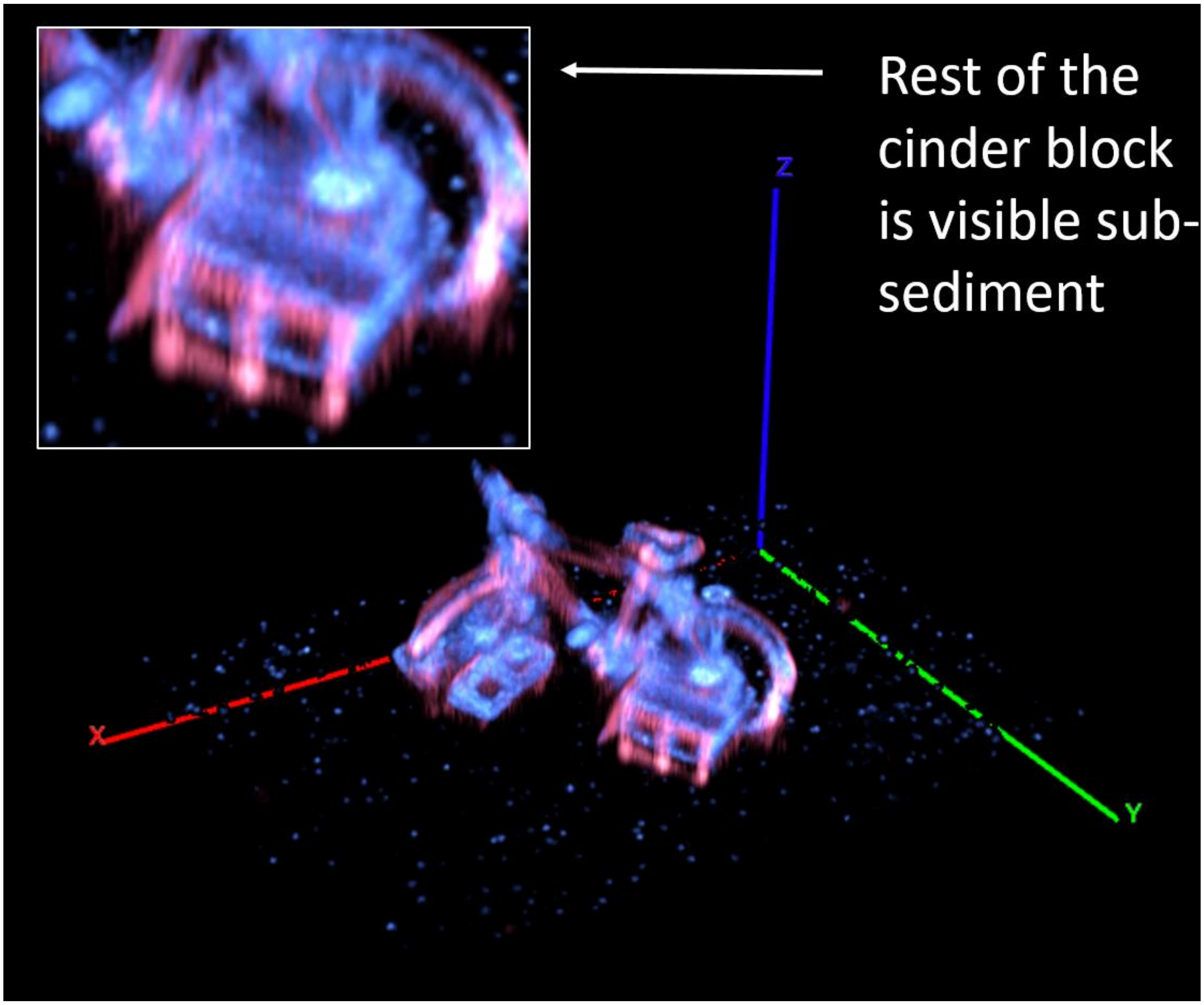

Figure 132. Zoomed in, alpha-rendered view of the bicycle, highlighting the rear wheel and the cinder block.

In the previous figure, the front face of a cinderblock is readily visible. Only the top half is visible at high frequencies, but the full front is visible at low frequencies. The top of the cinderblock is sloped relative to the sediment. The fact that the bottom edge appears parallel to the slop surface implies that the sub-sediment image is actual scattering from the cinderblock, rather than a multipath. No sub-sediment scattering is visible from the cinderblock on the left side of the front wheel, however in the image the slope of the cinderblock indicates that, as with the tilted and buried 2-1 cylinder, the faces of the block may be reflecting energy away from the sonar.

Fig. 133 is a zoomed in cutaway of the top of the bicycle showing various details:

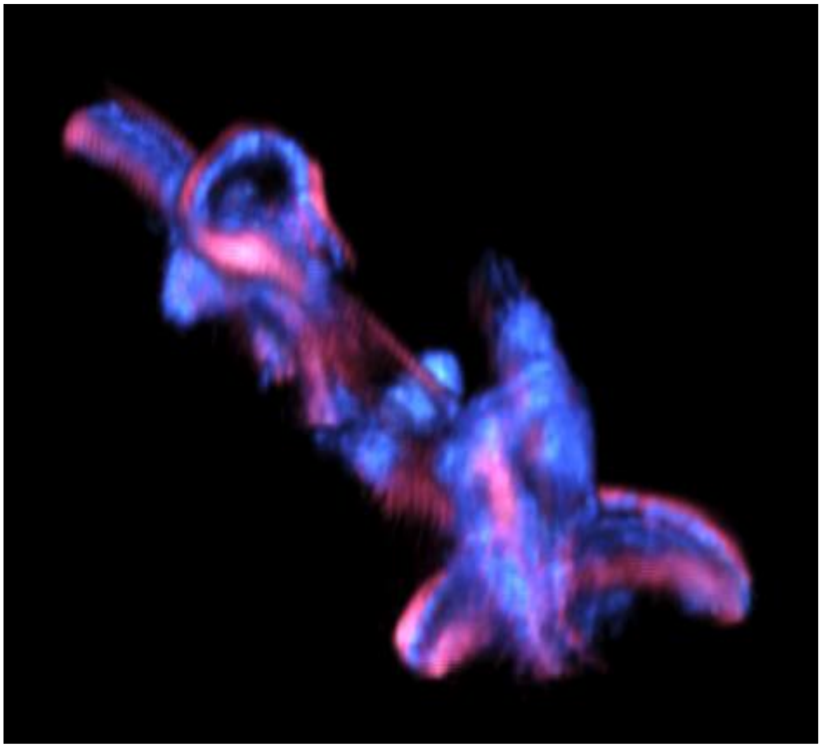

Figure 133. Zoomed in view of the top of the bicycle.

The saddle, front handle bar, stem, fork, and even hints of the gear shifters are visible in the image.

Sailboat Bow Results

The bow of the wreck of an abandoned sailboat was also scanned. This scene had probably the most distinct sub-sediment layer visible of any of the spiral scan sets. A vertical slice through the image cube is show below:

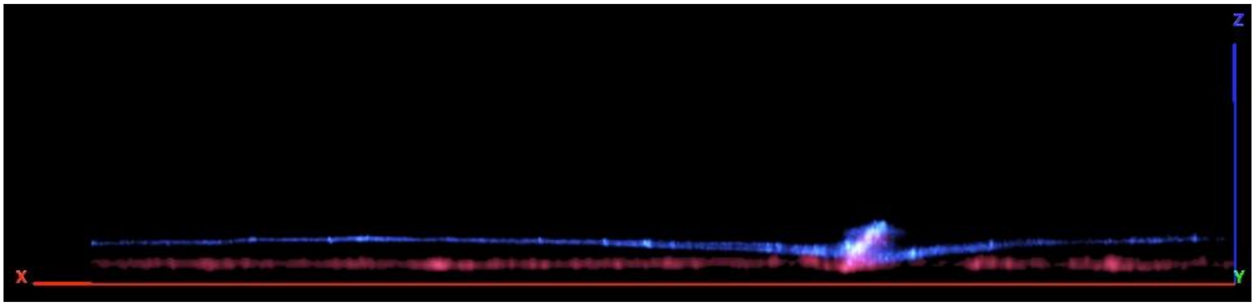

Figure 134. A vertical slice through the image cube of the sailboat bow. This is just a slice, not a maximum-intensity-projection image through the cube, and such strong scattering is occurring off of a sub-sediment interface that it shows up extremely distinctly in the cutaway.

In the previous figure, two sediment interfaces are clearly visible. As in previous cases, almost no scattering occurs off of the mud-water interface in the low frequencies, however unlike previous examples, the scattering off of some sub-sediment boundary is so distinct that the low frequency data demonstrates scattering off of an interface as strongly as the high frequency image. The images below are dual frequency alpha-rendered images of the full scene, in one instance with half of the high-frequency data sliced away:

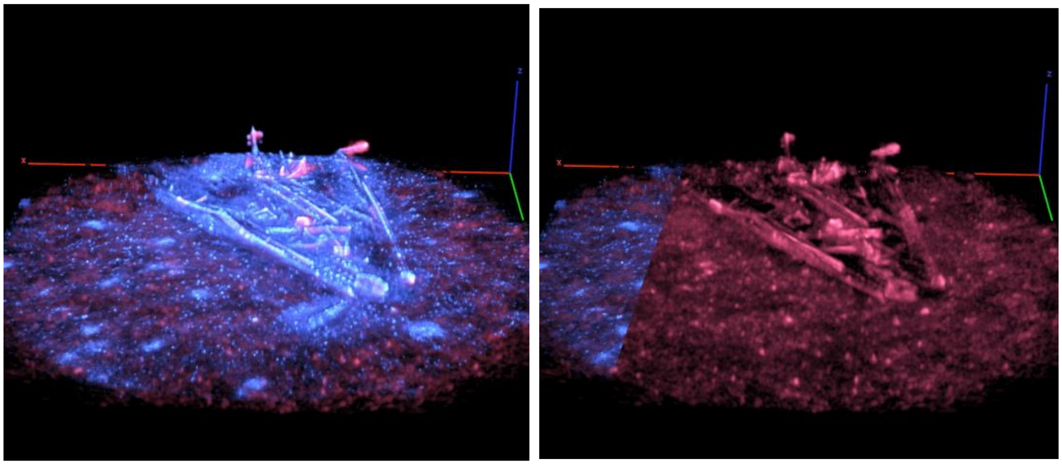

Figure 135. Two views of the boat wreck. The left image shows an alpha-rendered high frequency version of the scene, and the right image shows the same scene with the high frequency image cut away for the dominant portion of the image.

The detail of the wreck is preserved very well in the low frequency image. In the figure below, a portion of the previous alpha-rendered image is viewed from above, and the top is sliced away:

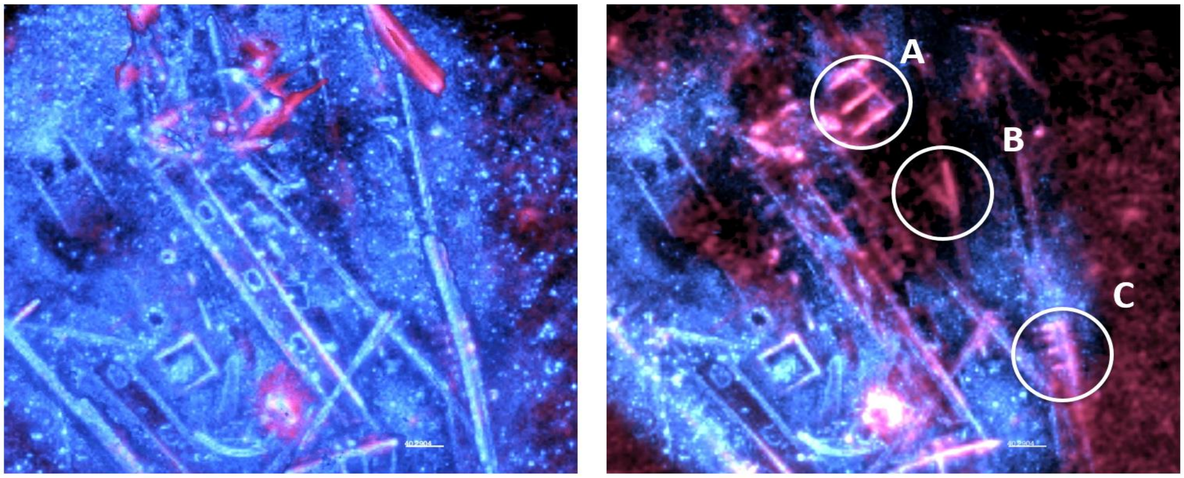

Figure 136. The left plot shows a zoomed patch of the dual-band alpha-rendered image, viewed from above. In the right image, the a portion of the image cube has been sliced off, exposing features (A-C) visible in the LF that are not visible in the HF. Patch A appears to be a derelict crap trap having two chambers. B and C are other miscellaneous debris or boat structural items.

Sailboat Debris Site Results

The final spiral scan analyzed in this project was a debris field of the sunken sailboat. The following images show a side-by-side comparison between high frequency and low frequency maximum intensity projections in the horizontal dimension.

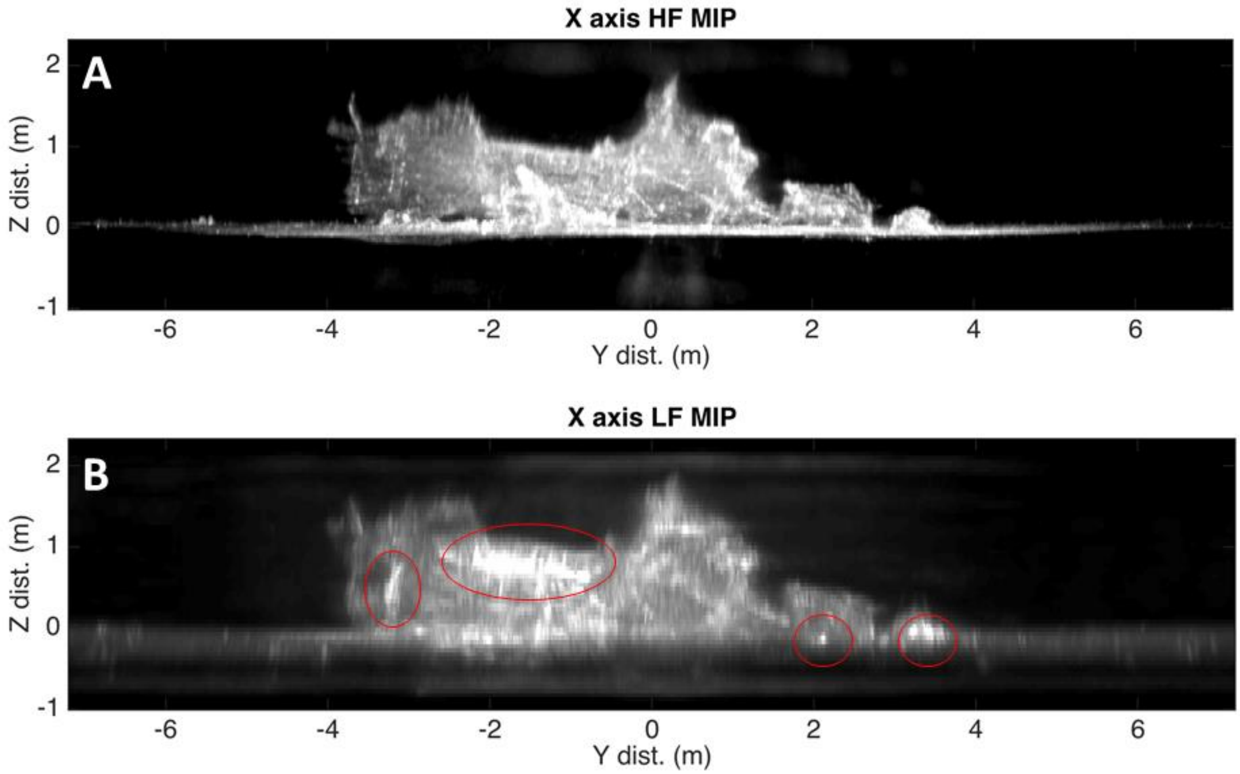

Figure 137. Maximum intensity projections through the debris field. Various structural features visible in the LF and not the HF are circled in red.

As with the airplane, the greater penetration capability of the LF signal seems to penetrate the structures of debris and reveal different features. The following image is an alpha rendered image:

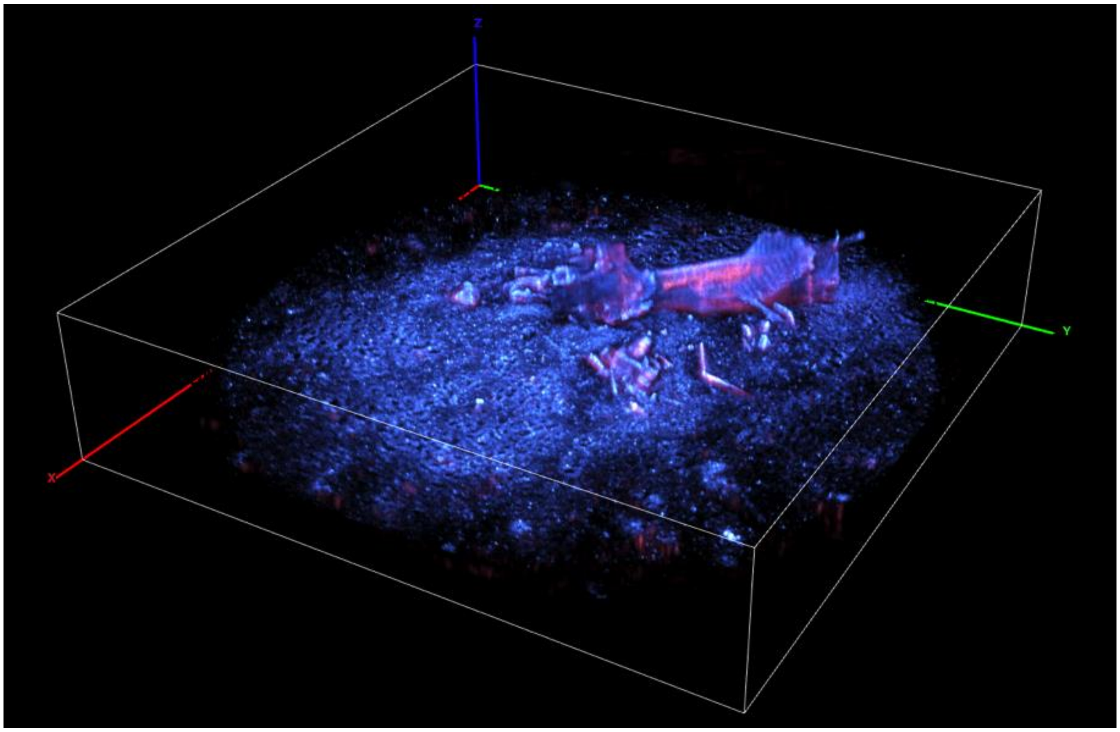

Figure 138. Alpha blended view of the debris field. HF is encoded in blue, LF is encoded in red.

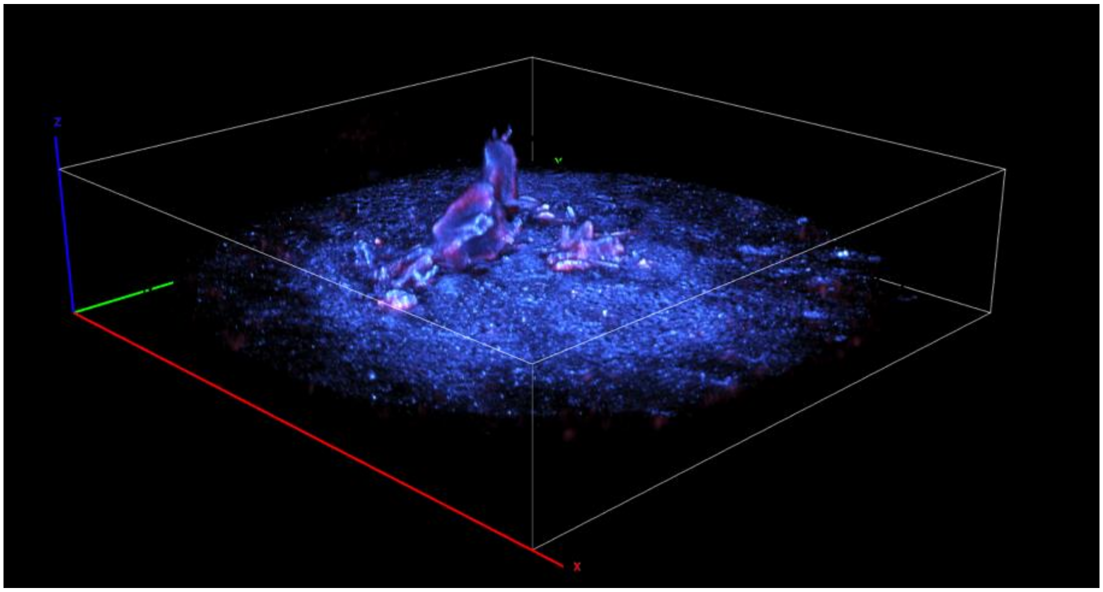

Figure. 139. Alpha blended view of the debris field from a different direction. HF is encoded in blue, LF is encoded in red.

Debris suspended in the mud layer will be viewed in similar manner to the slicing method used to show buried features of the boat bow. The following figure shows an alpha-rendered dual-band image of the debris field from above:

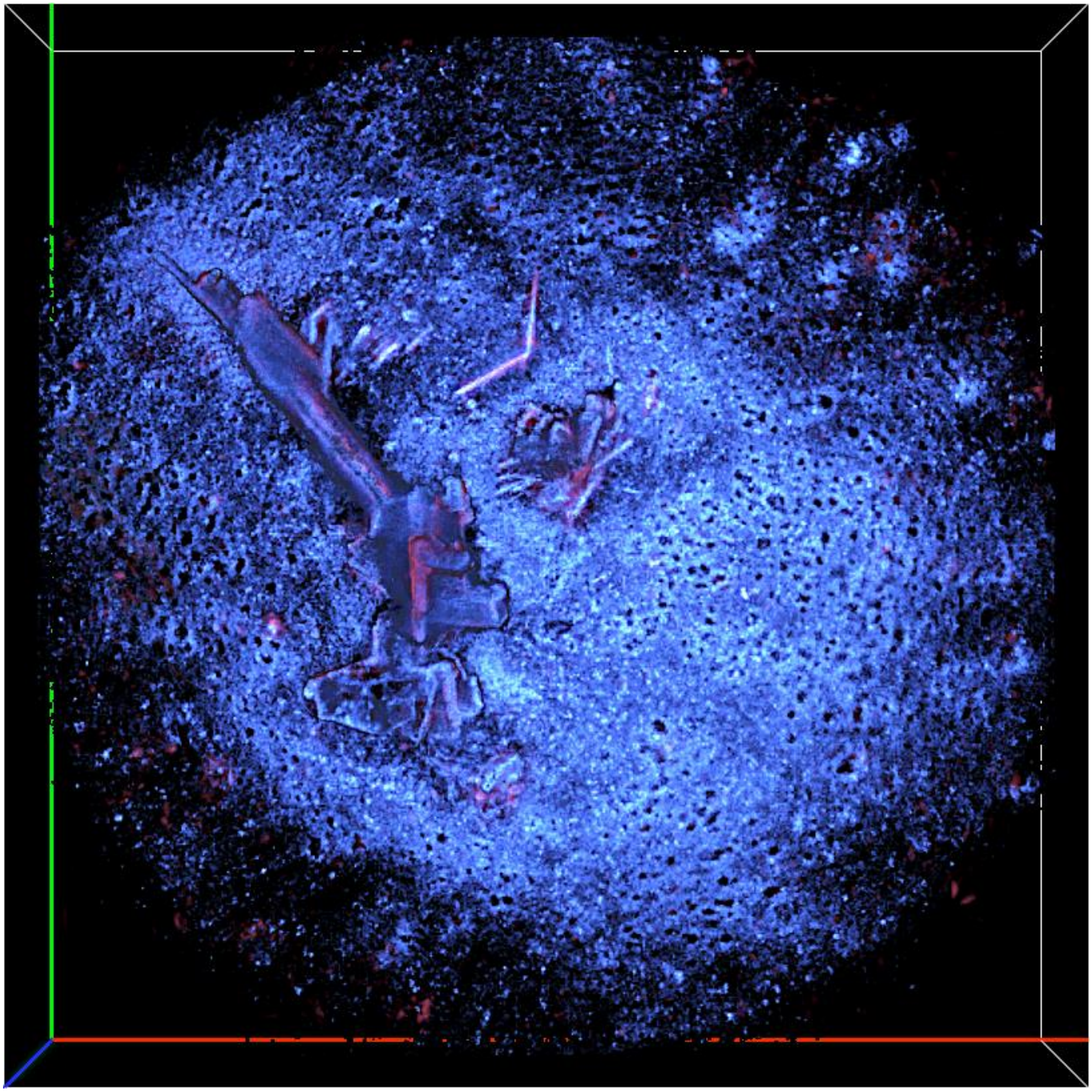

Figure 140. Boat debris field, alpha rendered, dual frequency, viewed from above.

The top of the datacube can be sliced just below the level of the sediment to reveal sub-sediment scatterers and debris. This has been done to the alpha-blended image shown below:

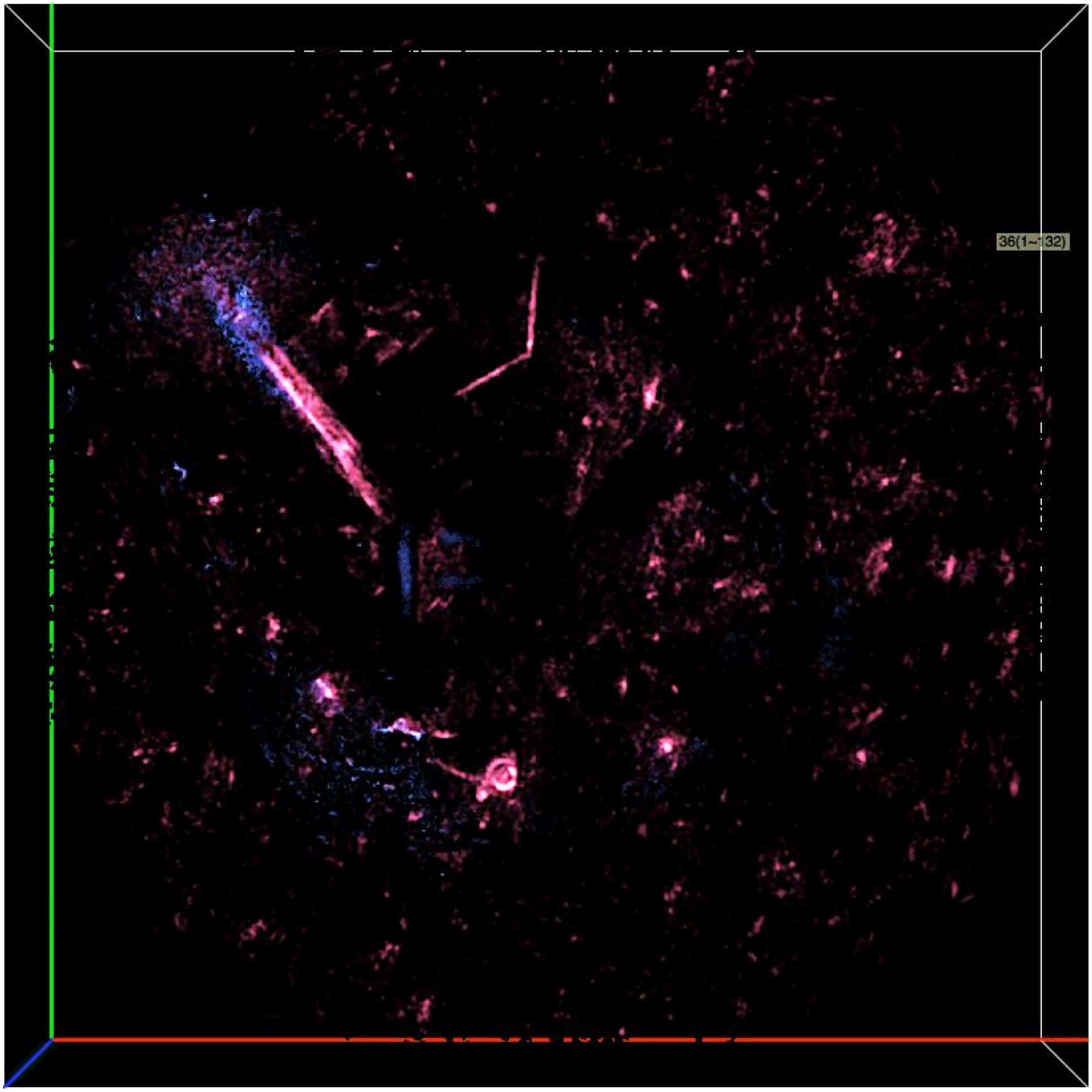

Figure. 141. Debris field of Figure 140, with the top sediment-layer and up sliced off, showing the sub-sediment scatterers.

Comparison of the previous two figures shows that the second is dominated by low frequency scattering (hence the red hue) and a variety of different features and debris are visible.

CONCLUSIONS AND IMPLICATIONS FOR FUTURE RESEARCH

In this project a new data acquisition technique was developed for synthetic aperture sonar systems. The technique generates dataproducts that have potential use for both UXO remediation and other activities of DoD interest, such as mine countermeasures. The technique, multipass aperture synthesis using circular scans, can be used to generate very high resolution 3D images of objects, both proud or suspended in sediments with sound-speeds less than water. As shown from numerous examples in this document, these images have the capability of resolving significant UXO details, such as nose cone transitions and the presence and geometry of end-caps. The precise orientation of the UXO objects relative to the sediment interface (and other, nearby UXO or clutter) can be determined from these images.

The multipass scans also have another important attribute, namely that a significant amount of the three-dimensional acoustic frequency response is captured. Through a set of coordinate transformations, multi-aspect and multi-grazing angle acoustic color characterizations of targets can be made in-situ. This is useful for a number of reasons: 1) in-situ frequency response data for UXO targets has the potential to augment finite element-based models to improve classification algorithm performance, and 2), as was shown in Figs.108 and 115, the spectra can be sub-sampled to generate target realizations that could be used for measuring the performance classification algorithms and identifying key points of failure, or boosting the performance of feature learning classifiers that require large numbers of target realizations (e.g., deep-learning algorithms) to improve robustness.

The data processing methods and results continually improved throughout the course of the project. This is in large part due to the shear amount of experimental data available, which is unique to the present project. In open SAS literature, only one other AUV-based multipass experiment has been divulged, and due to various issues, this set was not successfully processed [56] (a tomography experiment in air was conducted in [57] and 3D tank experiments performed in [58], though no 3D images have yet been constructed from the acquired tank data). Similar spiral scans or stacks of circles have been conducted from airborne systems in the field of SAR, e.g., the GOTCHA SAR data [21], [29], or the DLR scans [34], [56], however these also are individual scans and don’t span a variety of instances or environments. Many papers have been published on the GOTCHA SAR set because of its public availability and interesting nature. Ten years after release publications are still being made (see, e.g., one of the most recent, [59]), and much progress has been made on squeezing information out of multiple scans. To develop a robust *technique*, however, individual instances are not very useful. Complex procedures like multipass aperture synthesis have many potential points of failure, and many instances in different conditions, different environments, and around different objects are necessary for observing these and hardening algorithms. In the present project thirty-three multipass scans were attempted in a variety of environments ranging from flat sand to complex bathymetry at varying levels of wave action, and with different scan geometries. Of these, only two failed from AUV related issues. In fact, the primary point of failure had nothing to do with the co-registration or multipass processing, but rather was a result of poor reacquisition coordinates used for the vehicle mission plan which hampered target placement in the beam. This issue is not related to the performance or reliability of the multipass processing algorithm; in fact, it ought to be stated that for the entirety of the project including the very first AUV trials, *no multipass scan around an appropriately positioned target failed to produce a high quality 3D set of dataproducts.* In this case, a high quality 3D dataproduct is indicated by the generation of an image that shows low phase-error induced blurring or sidelobes in the vertical dimension and a high SNR, indicated by contrast. In total, of the 33 images, 22 3D images were successfully generated. These images, along with the methods used to generate them, ranging from co-registration to 3D beamforming, have been outlined in this document. The general conclusion can be made that the procedures described in this paper can be reliably used to generate 3D data products of reasonably sized target fields (e.g., 15 x 15 x 2.5 meters), under the assumption that the multipass scan can be appropriately placed to insonify the target field.

It must be noted that the method described in this paper has a very low area coverage rate compared to the ordinary, single-scan linear pass apertures. The reasons for this are simple: the scan efficiency is inversely proportional to both the number of scans made of a particular target or target field, and the wavenumber coverage (i.e., additional aperture spent increasing wavenumber coverage on a certain target is less aperture spent increasing the total area scanned). The benefit is that the additional scans and increased wavenumber coverage greatly increase the measured information about targets, improving identification. In the present case, the extra information from multipass circular apertures also has the potential to improve the results of wide-area surveys, which can incorporate the results of these scans via training set generation (e.g., Fig. 108) into their training databases.

Other than the rail system used to acquire multipass data in the initial year of the project, AUV's were used exclusively for multipass data acquisition. It is unclear whether or not AUV's are the optimal technology for UXO remediation operations because of the extra expense and training required to operate the systems. Furthermore, the buried targets may vastly outnumber exposed targets [60], and low grazing angle systems, even low frequency systems, may not be optimal because of the presence of critical angles in many environments. The funding of design studies for towbody systems like MUST (Multi-Sensor Towbody [61]), indicate that down looking, sediment penetrating sonar systems may be more practical for the general submerged UXO detection problem. Even if this is the case, however, much of what was learned in the present project, and many of the processes, are directly applicable to 3D processing from down looking systems like the BOSS [62, 63]. For example, the 3D acoustic color enhancement and extraction technique used in this would be directly applicable to 3D low frequency data captured by other systems, as would the principles behind efficient beamforming (e.g., fast-polar-backprojection) and autofocus. In any case, analysis of the results from two of the experiments (nose up, partially buried howitzer shell and the 2-1 aluminum cylinder, flush buried in mud) indicate that both structural *and* elastic components are significant contributors to the acoustic response of partially or fully buried objects, with certain portions of the wavenumber spectrum being dominated by one or the other of these effects. This result alone is highly suggestive that the efforts for modelling the elastic response of UXO have applications even for down looking systems like BOSS that will be primarily searching for sub-sediment UXO.

LITERATURE CITED

1. Bracewell, R.N. “Strip Integration in Radio Astronomy”. Aust. J. Phys. 9 (2): 198, (1956)

2. B. G. Ferguson and R. J. Wyber, “Application of acoustic reflection tomography” J. Acoust. Soc. Am. 117 (5), pp. 2915-2928, (2005)

3. A.D. Friedman, S.K. Mitchell, T.L. Kooij, K.N. Scarbrough, “Circular synthetic aperture sonar design,” IEEE Oceans, proceedings, p. 1038-1045, June 2005

4. B. G. Ferguson, R. J. Wyber, "Generalized Framework for Real Aperture, Synthetic aperture, and Tomographic Sonar Imaging," IEEE J. Ocean. Eng., 34, (3), p. 225-238 (2009)

5. S. K. Mitchell, K. N. Scarbrough, S. P. Pitt, T. L. Kooij, “High Resolution circular SAS with Controlled Focus”, SAS/SAR proceedings, Lerici, Italy, September 2006

6. H. J. Callow, R. E. Hansen, S. Synnes, and T. O. Saebo, “Circular synthetic aperture sonar without a beacon.” UAM proceedings, June 2009

7. H. J. Callow, S. A. Synnes, T. O. Saebo, R. E Hansen, “Autofocus for Circular Synthetic Aperture Imaging,” SAS/SAR proceedings, Lerici, Italy, September 2010

8. T. M. Marston, “A correlation based autofocus algorithm for coherent circular synthetic aperture sonar,” EUSAR 2012 proceedings, May 2012

9. Daniel D. Sternlicht, Fernandez, J.E., Marston, T. M., "Detecting, Classifying Mines With Synthetic Aperture Acoustic Tomography," SeaTech Magazine, November 2012

10. J. L. Kennedy, T. M. Marston, K. H. Lee, R. Lim, and J. L. Lopes, “A rail system for circular synthetic aperture sonar imaging and acoustic target strength measurements: Design/operation/preliminary results,” Rev. of Sci. Instrum. 85, 4861353 (2014).

11. T. M. Marston and J. L. Kennedy, “Volumetric acoustic imaging via circular multipass aperture synthesis,” IEEE J. Ocean. Eng. vol. 41, no. 4, pp. 852 – 867. (2016)

12. H. Cantalloube and C. Nahum, “Multiscale local map-drift-driven multi-lateration sar autofocus using fast polar format image synthesis,” IEEE Trans. Geosci. Remote Sens. , vol. 49, no. 10, pp. 3730–3736, Oct. 2011

13. S. Tebaldini, F. Rocca, M. M. D'Alessandro, L. Ferro-Famil, "Phase Calibration of Airborne, Tomographic SAR Data via Phase Center Double Localization." IEEE Transactions on Geoscience and Remote Sensing, Vol. 54, no. 3, March 2016

14. D. W. Hawkins, "Synthetic aperture imaging algorithms: With application to wideband sonar," Ph.D. dissertation, Electr. Electron. Eng. Dept., Univ. Canterbury, Christchurch, New Zealand, 1996.

15. D. S. Plotnick, P. L. Marston, and T. M. Marston, "Fast nearfield to farfield conversion algorithm for circular synthetic aperture sonar," J. Acoust. Soc. Am. 136, 4885486 (2014)

16. M. Abramowitz and I. A. Stegun, Handbook of Mathematical Functions, 9th ed. (Dover, New York, 1972), pp. 364–365.

17. D. S. Plotnick, P. L. Marston, D. J. Zartman, and A. R. Smith, "Reversible quasi-holographic line-scan and circular aperture processing for acoustic imaging and feature isolation." J. Acoust. Soc. Am. 134, 3981 (2013).

18. T. M. Marston, J. L. Kennedy, and P. L. Marston, "Coherent and semi-coherent processing of limited-aperture circular synthetic aperture (CSAS) data," in Proceedings of the Oceans Conf. MTS/IEEE 1, 1 (2011).

19. T. M. Marston, J. L. Kennedy, J. L. Prater, "Correction of aperture errors in circular SAS imagery via pseudo-stripmap autofocusing." Proceedings of SAS/SAR, Lerici, (2014)

20. M. Pinheiro, P. Prats, R. Scheiber, M. Nannini, A. Reigber, "Tomographic 3D reconstruction from airborne circular SAR," Proceedings of IEEE IGARSS 2009, July 2009

21. C. H. Casteel, L. A. Gorham, M. J. Minardi, S. Scarborough, and K. D. Naidu, "A challenge problem for 2D/3D imaging of targets from a volumetric data set in an urban environment," in Proc. Algorithms for Synthetic Aperture Radar Imagery XIV. SPIE Defense and Security Symp., Orlando, FL, Apr. 9–13, 2007.

22. T. M. Marston, J. L. Kennedy and P. L. Marston, "Autofocusing circular synthetic aperture sonar imagery using phase corrections modeled as generalized cones," J. Acoust. Soc. Amer., vol. 136, pp. 614-622, August 2014

23. A. Bellettini and M. A. Pinto, "Theoretical accuracy of synthetic aperture sonar micronavigation using a displaced phase-center antenna," IEEE J. Ocean. Eng., vol. 27, no. 4, pp. 780–789, Oct. 2002.

24. D. A. Cook, “Synthetic aperture sonar motion estimation and compensation,” M.S. thesis, Electr. Comput. Eng., Georgia Inst. Technol., Atlanta, GA, 2007.

25. J. L. Kennedy and T. M. Marston, SERDP project MR-2439 FY15 interim report (As of 11/22/2017, publically available at: https://www.serdp-estcp.org/Program-Areas/Munitions-Response/Munitions-Underwater/MR-2439/MR-2439)

26. R. P. Stokey et al., “Development of the REMUS 600 autonomous underwater vehicle,” in Proc. IEEE OCEANS, Washington, DC, Sept. 2005.

27. T. M. Marston and J. L. Kennedy, “TomoSAS in bathymetrically complex environments,” Proceedings of EUSAR 2016: 11th European Conference on Synthetic Aperture Radar, pp. 1-4, Hamburg, (2016)

28. X. Zhu and R. Bamler, “Tomographic SAR inversion by L1-normregularization— The compressive sensing approach,” IEEE Trans. Geosci. Remote Sens., vol. 48, no. 10, pp. 3839–3846, Oct. 2010.

29. C. D. Austin, E. Ertin, and R. L. Moses, “Sparse multipass 3D SAR imaging: Applications to the GOTCHA data set,” in Proc. Algorithms Synthetic Aperture Radar Imagery XVI, SPIE Defense and Security Symp., Orlando, FL, Apr. 13–17, 2009.

30. B. D. Rao, K. Engan, S. F. Cotter, J. Palmer, and K. Kreutz-Delgado, “Subset selection in noise based on diversity measure minimization,” IEEE Trans. Signal Processing, vol. 51, no. 3, pp. 760–770, Mar. 2003.

31. S. F. Cotter, B. D. Rao, K. Engan, and K. Kreutz-Delgado, “Sparse solutions to linear inverse problems with multiple measurement vectors,” IEEE Transactions on Signal Processing, vol. 53, no. 7, pp. 2477-2488, 2005.

32. G. Shippey, S. Banks and J. Pihl, “SAS image reconstruction using Fast Polar Back Projection: comparisons with Fast Factorized Back Projection and Fourier-domain imaging.” Proceedings of IEEE OCEANS 2005, June 2005

33. Ulander, Lars MH, Hans Hellsten, and Gunnar Stenstrom. "Synthetic-aperture radar processing using fast factorized back-projection." IEEE Transactions on Aerospace and electronic systems 39, no. 3 (2003): 760-776.

34. O. Ponce, P. Prats-Iraola, M. Pinheiro, M. Rodriguez-Cassola, R. Scheiber, A. Reigber, and A. Moreira, “Fully polarimetric high-resolution 3-D imaging with circular SAR at L-Band,” IEEE Trans. Geosci. Remote Sens., vol. 52, no. 6, pp. 3074–3090, June 2014

35. J. R. Fienup and J. J. Miller, “Aberration correction by maximizing generalized sharpness metrics,” J. Opt. Soc. Am. A, vol. 20, no. 4, pp. 609 – 620, Apr. 2003.

36. J. Kolman, “Image reconstruction and restoration using constrained optimization algorithms,” Ph.D. dissertation, Purdue Univ., West Lafayette, IN, USA, Aug. 1996.

37. T. M. Marston, D. S. Plotnick, "Semiparametric statistical stripmap synthetic aperture autofocusing", IEEE Trans. Geosci. Remot. Sens., vol. 53, no. 4, pp. 691-700, (2015)

38. M. Pardini, K. Papathanassiou, V. Bianco, A. Iodice, "Phase calibration of multibaseline SAR data based on a minimum entropy criterion", Proc. IEEE IGARSS, pp. 5198-5201, Jul. 2012

39. K. L. Williams, “Reverberation, Sediment Acoustics, and Targets-in-the-Environment,” ONR project report, 2012 (as of 11/22/2017, publically available at: http://www.dtic.mil/get-tr-doc/pdf?AD=ADA575135)

40. G. C. Eastland, T. M. Marston, and P. L. Marston. "Evolution of acoustic feature timing and imaging for different cylinder exposures and applications of reversible SAS filtering," in Proceedings of the Oceans Conference MTS/IEEE 1, 5664581 (2010).

41. K. Baik and P. L. Marston, “Kirchhoff approximation for a cylinder breaking through a plane surface and the measured scattering,” IEEE J. Ocean. Eng., vol. 33, no. 4, pp. 386–396, Oct. 2008.

42. H. Peng et al, “V3D enables real-time 3D visualization and quantitative analysis of large-scale biological image data sets,” Nature Biotechnology, vol. 28, no. 4, p. 348-355, 2010.

43. H. Peng et al., “Extensible visualization and analysis for multidimensional images using Vaa3D,” Nature Protocols, vol. 9, no. 1, pp. 193-208, 2014.

44. D. S. Plotnick, P. L. Marston, K. L. Williams and A. L. Espana, “High frequency backscattering by a solid cylinder with axis tilted relative to a nearby horizontal surface.” J. Acoust. Soc. Am. 137, 470, (2015)

45. G. C. Eastland, “Acoustic scattering boundary effects investigated using reversible synthetic aperture sonar filtering and time delay models,” Ph.D. thesis, Washington State University, Pullman, WA, 2012.

46. T. M. Marston and J. L. Kennedy, “TomoSAS images of acoustically penetrable objects,” Proceedings of EUSAR 2016: 11th European Conference on Synthetic Aperture Radar, pp. 1-4, Hamburg, (2016)

47. J. Perry, “40’s Bomber Found in Sea,” Cape Cod Times, June 1, 2002 (as of 11/22/2017 publically available at: http://www.capecodtimes.com/article/20010601/NEWS01/306019999).

48. D. S. Plotnick, T. M. Marston and J. L. Kennedy, “Utilization of Aspect Angle Information in Synthetic Aperture Images,” submitted to IEEE TGRS (in review)

49. W. G. Carrara, R. S. Goodman, and R. M. Majewski, Spotlight Synthetic Aperture Radar: Signal Processing Algorithms. Norwood, MA, USA: Artech House, 1995.

50. J. L. Prater, T. M. Marston, “Preliminary results from techniques to determine in-situe medium speed of sound using a synthetic aperture sonar,” Proceedings of SAS/SAR, Lerici, (2014)

51. D. Williams, "Underwater Target Classification in Synthetic Aperture Sonar Imagery Using Deep Convolutional Neural Networks," Proceedings of the 23rd International Conference on Pattern Recognition (ICPR), Cancún, Mexico, December 2016

52. K. Gipson and P. L. Marston, “Backscattering enhancements due to reflection of meridional leaky Rayleigh waves at the blunt truncation of a tilted solid cylinder in water: Observations and theory,” J. Acoust. Soc. Am. 106, 1673–1680 (1999)

53. M. Soumekh, “Reconnaissance with slant plane circular SAR imaging,” IEEE Transactions on Image Processing, vol. 5 (8), pp. 1252 – 1265, Aug. 1996

54. O. Ponce Madrigal, “Multicircular Holographic SAR Tomography Over Forested Areas,” Ph.D. Disseration, ETH Zurich. 2017.

55. A. Reigber and A. Moreira, “First demonstration of airborne SAR tomography using multibaseline L-band data,” IEEE Trans. Geosci. Remote Sens., vol. 38, no. 5, pp. 2142–2152, Sep. 2000

56. T. O. Sæbø, R. E. Hansen, and A. Austeng, “Synthetic Aperture Sonar Tomography: A Preliminary Study.” In Proceedings of EUSAR 2014, Berlin, Germany, June 2014

57. J. Jideani and W. Wilkinson, "Air-based synthetic aperture sonar tomography using compressive sensing." IEEE International Ultrasonics Symposium, 2014.

58. V. Bollen, D. S. Plotnick and P. L. Marston, “Circular synthetic aperture sonar images of backscattering enhancements on solid elastic cubes due to Rayleigh waves and other mechanisms,” J. Acoust. Soc. Am. 139, (2019)

59. L. Chen, D. An, X. Huang, and Z. Zhou, “A 3D reconstruction strategy of vehicle outline based on single-pass single-polarization CSAR data.” IEEE Transactions on Image Processing, Vol. 26, (11), Nov. 2017

60. *SERDP/Office of Naval Research Workshop on Acoustic Detection and Classification of UXO in the Underwater Environment*, Sept. 2013. Available at: https://www.serdpestcp.org/content/download/27995/277023/version/2/file/SERDP+Acoustics+Workshop+Report+2013+Final+DistroA.pdf

61. *Limited Scope Design Study for Multi-Sensor Tow Body*, SERDP project MR-2501. Final report available at: https://serdp-estcp.org/Program-Areas/Munitions-Response/Munitions-Underwater/MR-2501

62. Schock, Steven G., Arnaud Tellier, Jim Wulf, Jason Sara, and Mark Ericksen. "Buried object scanning sonar." IEEE journal of oceanic engineering 26, no. 4 (2001): 677-689

63. *Next Generation Buried Object Scanning Sonar (BOSS) for Detecting Buried UXO in Shallow water*, SERDP project MR-2752. Website: https://serdp-estcp.org/Program-Areas/Munitions-Response/Munitions-Underwater/MR-2752

LIST OF SCIENTIFIC/TECHNICAL PUBLICATIONS

1. J. L. Kennedy and T. M. Marston, “3D Volumetric sonar imaging for identification missions,” Sea Technol. 58, 10-14 (2017). [accepted and published]
2. T. M. Marston and J. L. Kennedy, “Volumetric acoustic imaging via circular multipass aperture synthesis,” IEEE J. Ocean. Eng. 41 (4), 852–867 (2016). [accepted and published]
3. D. S. Plotnick and T. M. Marston, “Three-dimensional image reconstruction of objects using synthetic aperture sonar,” J. Acoust. Soc. Am. 140, 3347 (2016). [accepted and published]
4. T. M. Marston and J. L. Kennedy, “TomoSAS images of acoustically penetrable objects,” Proceedings of EUSAR 2016: 11th European Conference on Synthetic Aperture Radar, pp. 1-4, Hamburg, (2016). [accepted and published]
5. T. M. Marston and J. L. Kennedy, “TomoSAS in bathymetrically complex environments,” Proceedings of EUSAR 2016: 11th European Conference on Synthetic Aperture Radar, pp. 1-4, Hamburg, (2016). [accepted and published]
6. T. M. Marston, J. L. Kennedy, J. L. Prater, “Correction of aperture errors in circular SAS imagery via pseudo-stripmap autofocusing.” Proceedings of SAS/SAR, Lerici, (2014). [accepted and published]
7. T. M. Marston, J. L. Kennedy, P. L. Marston, “Autofocusing circular synthetic aperture sonar imagery using phase corrections modeled as generalized cones,” J. Acoust. Soc. Am. 136 (2), 614-622 (2014). [accepted and published]
8. J. L. Kennedy, T. M. Marston, K. H. Lee, R. Lim, and J. L. Lopes, “A rail system for circular synthetic aperture sonar imaging and acoustic target strength measurements: Design/operation/preliminary results,” Rev. of Sci. Instrum. 85, 4861353 (2014). [accepted and published]

OTHER SUPPORTING MATERIALS

Recipient of the SERDP Munitions Response FY16 Project of the Year Award

REPORT DOCUMENTATION PAGE

Form Approved
OMB No. 0704-0188

1. REPORT DATE *(DD-MM-YYYY)* 31-01-2018	**2. REPORT TYPE** Final Technical Report	**3. DATES COVERED** *(From - To)* 14 MAR 2014 to 31 SEP 2017

4. TITLE AND SUBTITLE Multipass and Nonconcentric Target Circular Synthetic Aperture Sonar (CSAS)	**5a. CONTRACT NUMBER**
	5b. GRANT NUMBER
	5c. PROGRAM ELEMENT NUMBER
6. AUTHOR(S) Kennedy, Jermaine, L. (1) Marston, Timothy, M. (2)	**5d. PROJECT NUMBER** MR-2439
	5e. TASK NUMBER
	5f. WORK UNIT NUMBER
7. PERFORMING ORGANIZATION NAME(S) AND ADDRESS(ES) (1) Naval Surface Warfare Center Panama City Division 110 Vernon Ave, Code X11 Panama City, FL 32407 (2) Applied Physics Lab.-UW 1013 NE 40th St. Seattle, WA 98105	**8. PERFORMING ORGANIZATION REPORT**
9. SPONSORING / MONITORING AGENCY NAME(S) AND ADDRESS(ES) SERDP Program Office Dr. Herb Nelson (Munitions Response) 4800 Mark Center Drive, Suite 17D08 Alexandria, VA 22350	**10. SPONSOR/MONITOR'S ACRONYM(S)** SERDP
	11. SPONSOR/MONITOR'S REPORT NUMBER(S)

12. DISTRIBUTION / AVAILABILITY STATEMENT
Distribution A: Approved for public release; distribution is unlimited.

13. SUPPLEMENTARY NOTES
N/A

14. ABSTRACT

In SERDP project MR-2439 research was conducted to enable the in-situ measurement of the aspect and grazing angle dependent scattering response of unexploded ordnance (UXO), clutter, and science targets by conducting circular scans at different heights around identified concentric and non-concentric (i.e. off-center) targets. Methods were developed for coherently fusing the information from all circular scans to generate three-dimensional data products describing spatial reflectivity and impulse response of targets. Showing that these three dimensional (3D) dataproducts could be sampled in the 3D wavenumber spectrum to generate a series of two dimensional (2D) random orientation realizations that have use for target recognition training and/or testing was an additional objective.

15. SUBJECT TERMS
Circular Synthetic Aperture Sonar (CSAS) of UXO, Synthetic Aperture Sonar of UXO, underwater UXO

16. SECURITY CLASSIFICATION OF:			**17. LIMITATION OF ABSTRACT**	**18. NUMBER OF PAGES**	**19a. NAME OF RESPONSIBLE PERSON**
					Dr. Jermaine L. Kennedy
c. REPORT U	**b. ABSTRACT** U	**c. THIS PAGE** U	UU	148	**19b. TELEPHONE NUMBER** *(include area code)* 850-230-7311

Standard Form 298 (Rev. 8-98)
Prescribed by ANSI Std. Z39.18